



**HAL**  
open science

# La spectroscopie de résonance magnétique nucléaire à l'état solide : un outil pour la caractérisation des systèmes poreux de délivrance de médicaments

Marianna Porcino

► **To cite this version:**

Marianna Porcino. La spectroscopie de résonance magnétique nucléaire à l'état solide : un outil pour la caractérisation des systèmes poreux de délivrance de médicaments. Autre. Université d'Orléans, 2020. Français. NNT : 2020ORLE3054 . tel-03209463

**HAL Id: tel-03209463**

**<https://theses.hal.science/tel-03209463>**

Submitted on 27 Apr 2021

**HAL** is a multi-disciplinary open access archive for the deposit and dissemination of scientific research documents, whether they are published or not. The documents may come from teaching and research institutions in France or abroad, or from public or private research centers.

L'archive ouverte pluridisciplinaire **HAL**, est destinée au dépôt et à la diffusion de documents scientifiques de niveau recherche, publiés ou non, émanant des établissements d'enseignement et de recherche français ou étrangers, des laboratoires publics ou privés.

## UNIVERSITÉ D'ORLÉANS

ÉCOLE DOCTORALE

ENERGIE, MATERIAUX, SCIENCE DE LA TERRE ET DE L'UNIVERS

Conditions Extrêmes et Matériaux : Haute Température et Irradiation

CEMHTI UPR 3079 CNRS

**THÈSE** présentée par :

**Marianna PORCINO**

soutenue le : **22 Octobre 2020**

pour obtenir le grade de : **Docteur de l'Université d'Orléans**

Discipline/ Spécialité : Chimie

# Solid state nuclear magnetic resonance spectroscopy: a tool for the characterization of porous drug delivery systems

THÈSE dirigée par :

**M. FLORIAN Pierre**

Ingénieur de Recherche-HDR, CEMHTI-CNRS, Orléans

**Mme MARTINEAU-CORCOS Charlotte**

Maître de Conférences-HDR, UVSQ, Versailles

RAPPORTEURS :

**Mme LAURENCIN Danielle**

Chargée de Recherche-HDR, ICGM-CNRS, Montpellier

**M. AZAÏS Thierry**

Maître de Conférences-HDR, Université Pierre et Marie Curie, Paris

JURY :

**M. DESCHAMPS Michaël**

Président du jury, Professeur, Université d'Orléans, Orléans

**M. AZAÏS Thierry**

Maître de Conférences-HDR, Université Pierre et Marie Curie, Paris

**Mme LAURENCIN Danielle**

Chargée de Recherche-HDR, ICGM-CNRS, Montpellier

**M. ALONSO Bruno**

Directeur de Recherche, ICGM-CNRS, Montpellier

**M. GIRAUD Nicolas**

Professeur, Université Paris Descartes, Paris

**Mme GREF Ruxandra**

Directrice de Recherche, ISMO-CNRS, Orsay

**M. FLORIAN Pierre**

Ingénieur de Recherche-HDR, CEMHTI-CNRS, Orléans

**Mme MARTINEAU-CORCOS Charlotte**

Maître de Conférences-HDR, UVSQ, Versailles

INVITÉ :

**M. BENNETT Thomas**

Associate Professor, Royal Society University, Cambridge



## Table of contents

Abbreviations.....	5
Résumé en Français	
Références .....	20
General Introduction	
References .....	28
Chapter 1- Drug Delivery and Drug Delivery Systems	
1. Drug Delivery.....	31
2. Drug Delivery Systems .....	33
2.1 Liposomes .....	35
2.2 Polymer micelles.....	36
2.3 Microsphere and microcapsules.....	36
2.4 Red blood cells.....	37
2.5 Polymer Nanoparticles.....	37
2.6 Mesoporous Silica Nanoparticles.....	37
2.7 Periodic Mesoporous Organosilica Nanoparticles.....	38
2.8 Metal-Organic Frameworks .....	38
2.8.1 Synthesis and structural characteristics .....	39
2.8.2 Applications.....	41
2.8.3 General techniques for the structural characterization of MOFs.....	41
2.8.4 MOFs as Drug Delivery Systems.....	43
2.8.5 MOFs used in this thesis .....	45
2.8.5.1 Cyclodextrin-based Metal-Organic Frameworks .....	45
2.8.5.2 MIL-100 .....	48
3. Conclusions .....	52
References .....	54
Chapter 2- Solid State Nuclear Magnetic Resonance	
1. The Basics of Nuclear Magnetic Resonance spectroscopy <sup>3,4</sup> .....	61
1.1 The principal interactions in NMR spectroscopy .....	64
1.1.1 Shielding interaction .....	65
1.1.2 Indirect spin-spin ( <i>J</i> ) coupling interaction.....	67
1.1.3 Direct dipole-dipole ( <i>D</i> ) coupling interaction .....	68
1.1.4 Quadrupolar coupling interaction.....	69
1.2 Magic-Angle Spinning (MAS).....	72
2. Pulse Sequences.....	74

2.1	One-pulse .....	74
2.2	Cross Polarization for spin-1/2.....	76
2.3	Triple resonance Cross-Polarization .....	78
2.4	Spin Echo.....	78
2.5	MQMAS.....	79
2.6	Exchange experiments .....	80
2.7	Double Quantum-Single Quantum (DQ-SQ) correlation experiments .....	82
2.7.1	INADEQUATE.....	82
2.7.2	Double-quantum recoupling experiment .....	83
2.8	D-HMQC.....	84
2.9	S-RESPDOR .....	86
2.10	Measurement of relaxation times .....	88
2.10.1	T <sub>1</sub> .....	88
2.10.2	T <sub>2</sub> .....	89
	References .....	90

### Chapter 3- Solid-state NMR spectroscopy of drug delivery systems

1.	Introduction .....	95
2.	1D <sup>1</sup> H solid-state NMR spectroscopy .....	97
3.	<sup>1</sup> H- <sup>1</sup> H 2D NMR .....	100
4.	<sup>1</sup> H-X NMR .....	104
5.	Conclusions .....	114
	References .....	115

### Chapter 4- $\gamma$ -CD-MOFs as drug carriers for Lansoprazole

1.	Introduction .....	119
2.	The system: LPZ@ $\gamma$ -CD-MOF .....	119
3.	Solution-state NMR spectroscopy .....	123
4.	Solid-state NMR spectroscopy.....	125
4.1	$\gamma$ -CD-MOF.....	125
4.2	LPZ@ $\gamma$ -CD-MOFs .....	128
5.	Conclusions .....	136
6.	Experimental ssNMR section .....	137
	References .....	139

### Chapter 5- Surface modified nanoMIL-100(Al) as drug carrier for phosphated drugs

1.	Introduction .....	143
2.	The effect of particle size on MIL-100(Al).....	146

3. CD-P coated nanoMIL-100(Al) .....	151
4. ATP loaded nanoMIL-100(Al) .....	157
5. CD-P coated ATP loaded nanoMIL-100(Al) .....	165
6. Conclusions .....	170
7. Experimental ssNMR section .....	175
References .....	177

## Chapter 6- Surface modified nanoMIL-100(Al) as drug carrier for Doxorubicin

1. Introduction .....	181
2. CD-CO coating on nanoMIL-100(Al) .....	185
3. DOX loaded in nanoMIL-100(Al) .....	193
4. DOX loaded in the CD-CO polymer .....	197
5. DOX loaded CD- <sup>13</sup> CO coated nanoMIL-100(Al) .....	200
6. Conclusions .....	204
7. Experimental ssNMR section .....	205
References .....	208

## Conclusions and Perspectives

References .....	216
------------------	-----

## Publications



## Abbreviations

1D: One dimension

2D: Two dimension

API: Active Pharmaceutical Ingredient

ATP: Adenosine triphosphate

AZT-TP: Azidothymidine 5'-triphosphate

BABA: Back to Back

BET: Brunauer-Emmett-Teller

BTC: Benzene 1,3,5-tricarboxylate

CD: Cyclodextrin

CD-P: Cyclodextrin Phosphate

CO: Citrate

CP: Cross polarization

CTAB: CetylTrimethyl Ammonium Bromide

CUR: Curcumin

CUS: Coordinatively Unsaturated metal Sites

CW: Continuous Waves

DDS: Drug Delivery System

*D*-HMQC: Dipolar Heteronuclear Multi-Quantum Correlation

DOX: Doxorubicin

DQ: Double Quantum

ED: Effective Dose

EXSY: Exchange spectroscopy

GI: Gastro Intestinal

HETCOR: Heteronuclear correlation

Ibu: Ibuprofen

IMC: Indomethacin

INADEQUATE: INcredible Natural Abundance Double QUAntum Transfer Experiment

LPZ: Lansoprazole

LPZS: Lansoprazole sulfide

MAS: Magic Angle spinning

MCM: Mobil Crystalline Materials

MIL: Materials of Lavoisier Institute

MOF: Metal Organic Framework

MQMAS: Multi-Quantum Magic Angle spinning

MSNs: Mesoporous silica nanoparticles

multiCP: multiple Cross Polarization

NMR: Nuclear Magnetic Resonance

NPs: Nanoparticles

PBS: Phosphate Buffer Saline

PEG: Polyethylene glycole

PLA: PolyLactic Acid

PLGA: Polylactic Acid-Glycolic Acid

ppm: part per million

PVP: PolyVynilPyrrolidone

PXRD: powder X-Ray Diffraction

REDOR: Rotational Echo DOuble Resonance

RFDR: Radio-frequency driven dipolar recoupling

s: second

SBA: Santa Barbara Amorphous type material

SEM: Scanning Electron Microscopy

SPINAL-64: Small Phase INcrementation Alteration with 64 steps

SQ: Single Quantum

S-RESPDOR: Symmetric-based Resonance Echo Saturation Pulse DOuble-Resonance

ssNMR: solid state Nuclear Magnetic Resonance

TCP: Triple resonance Cross Polarization

TD: Toxic Dose

TEM: Transmission Electron Microscopy

TGA: Thermogravimetric Analysis

TI: Therapeutic Index

TPPM: Two Pulses Phase Modulation



# Résumé en Français



Le processus d'administration d'un médicament consiste à injecter un produit pharmaceutique dans l'organisme, avec un transport et une distribution contrôlés vers les cellules ou organes cibles. Diverses voies d'administration anatomiques peuvent être utilisées, telles que la voie orale, pulmonaire, transdermique, parentérale, transmuqueuse, colorectal. Le choix de la voie dépend de la maladie, de l'effet souhaité et des caractéristiques du produit. Des matériaux pour l'administration du médicament peuvent être utilisés pour mieux contrôler la dose ou permettre une libération directe du médicament sur la cible. Le matériau idéal pour l'administration d'un médicament doit être biocompatible, non toxique et non immunogène. Il doit avoir des propriétés structurales précises et reproductibles, avec une bio-élimination adéquate, et une surface modifiable. Sa synthèse doit être facile, ne pas employer de solvants toxiques et pouvoir être produite à grande échelle. Les matériaux répondant à ces critères sont appelés systèmes d'administration de médicaments (Drug Delivery Systems (DDSs) en anglais). Les DDSs sont des formulations ou des dispositifs utilisés pour améliorer l'administration de médicaments peu efficaces et peu sûrs. De plus, ils peuvent aider le patient à se sentir plus à l'aise et à se conformer aux prescriptions. D'autres points importants sont la réduction du coût de développement des médicaments, du risque d'échec dans le développement de nouveaux produits et la prolongation de la durée de vie du produit<sup>1</sup>. Il n'existe malheureusement pas de nanovecteurs de médicaments universels, et pour chaque cible médicale, un nouveau vecteur de médicament doit être correctement conçu. Le DDS idéal doit avoir une grande stabilité colloïdale, une capacité de charge élevée du médicament, être préparé sans avoir besoin de solvant toxique, être inerte, biocompatible, mécaniquement fort, biodégradable, confortable pour le patient, sans risque de libération accidentelle, simple à administrer et enfin facile et rentable à fabriquer et à stériliser. La plupart des DDSs sont des systèmes complexes coeur-coquille, composés d'un noyau biodégradable dans lequel le médicament est chargé et d'un enrobage, qui peut être fonctionnalisé avec un ligand spécifique. Le coeur du système accueille le médicament, le protège et le stabilise. Il doit être dégradé pour assurer une libération efficace du médicament. La partie externe du système a pour

but d'augmenter la stabilité colloïdale des nanoparticules, de les rendre furtives pour le système immunitaire et d'assurer une libération spécifique vers la cible biologique.

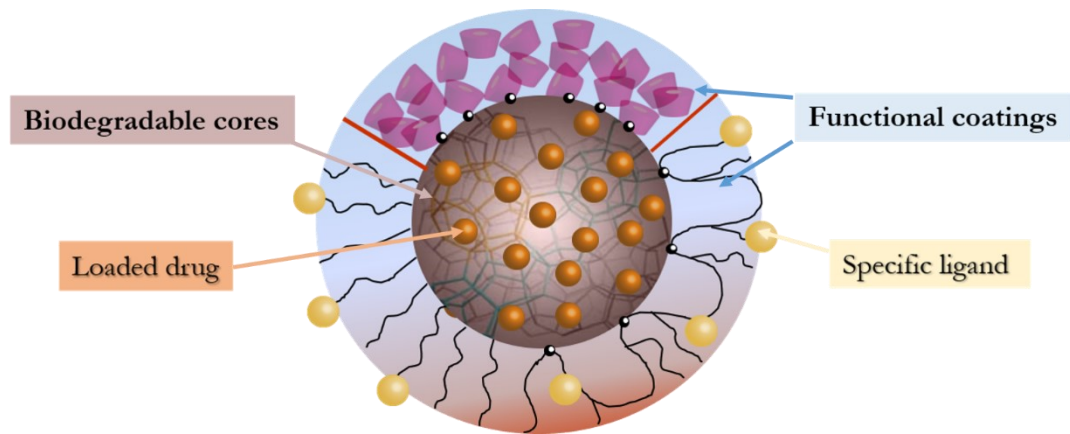


Figure 1: Illustration de la composition d'un système d'administration de médicaments. Le médicament est chargé dans le coeur biodégradable qui doit le protéger et le stabiliser. La couronne est composée d'un revêtement fonctionnel qui peut interagir avec des ligands spécifiques pour assurer l'administration du médicament à la cible.

Il existe différents types de DDSs, tels que les liposomes, les microsphères et microcapsules, les micelles et nanoparticules de polymère, les globules rouges, les nanoparticules de silice mésoporeuse et les composés organique-inorganique appelés 'metal-organique frameworks' (MOF). Les MOFs sont une classe de polymères de coordination comprenant des ligands organiques dans lesquels l'interaction métal-ligand conduit à des structures de réseau cristallin à 2 ou 3 dimensions<sup>2</sup>. La taille, forme et dimensionnalité des pores peuvent être contrôlés par en choisissant judicieusement les briques de construction (le centre métallique et le ligand organique) ainsi que la façon dont ils sont connectés. De plus, il est possible de fonctionnaliser la partie organique, ce qui permet d'ajuster les propriétés des matériaux pour des applications spécifiques<sup>3</sup>. La synthèse biologique, la charge médicamenteuse élevée dans les pores et les modifications de surface permettant une bonne stabilité et un ciblage sélectif ne sont que quelques-uns des avantages des MOFs utilisés comme vecteurs de médicaments<sup>4,5</sup>.

L'analyse de la structure d'un DDS est importante pour comprendre sa stabilité, son mécanisme d'action, son interaction avec le médicament et avec l'organisme et pour effectuer des modifications susceptibles d'augmenter son potentiel. Les techniques analytiques, telles que l'analyse thermique, l'adsorption d'azote, la diffraction des rayons X, fournissent des informations sur la structure cristalline, la morphologie, la porosité, la charge et la libération du médicament.

La résonance magnétique nucléaire à l'état solide (ssNMR) est devenue au cours des dernières décennies un outil physique très puissant pour étudier la structure de différents types de matériaux. Elle donne la possibilité d'observer sélectivement la signature de plusieurs noyaux et d'obtenir des informations structurales très détaillées. Elle est donc très utile non seulement comme outil de diagnostic dans les processus de synthèse, mais elle offre également la possibilité d'étudier la structure locale, de comprendre le niveau moléculaire et la dynamique des cristaux et des solides amorphes et d'étudier l'interaction entre les molécules<sup>6,7</sup>. La RMN a divers avantages, notamment la possibilité de fournir des informations structurales détaillées et d'examiner les défauts et les troubles locaux.

Dans le contexte des DDS, comme de nombreux noyaux RMN actifs sont présents dans le cœur (tels que  $^1\text{H}$ ,  $^2\text{H}$ ,  $^{13}\text{C}$ ,  $^{17}\text{O}$ ,  $^{19}\text{F}$  and  $^{27}\text{Al}$ ), la couronne ( $^1\text{H}$ ,  $^{13}\text{C}$ ,  $^{17}\text{O}$ ,  $^{27}\text{Al}$ ,  $^{29}\text{Si}$ ) et à la surface ( $^{13}\text{C}$ ,  $^{17}\text{O}$ ,  $^{29}\text{Si}$ ,  $^{31}\text{P}$ ) des nanoparticules, ils peuvent fournir des informations sur la localisation, l'état et les interactions du médicament dans le système et sur les interactions cœur/couronne et sur la dégradation de la matrice et donc, la délivrance/libération du médicament. Ces informations peuvent contribuer de manière significative à orienter la conception et le développement de nouveaux DDSs. De plus, cette technique est non destructive, c'est-à-dire que le DDS peut être étudié intact sans avoir besoin d'être dissous, comme cela serait nécessaire pour la RMN liquide, ou d'être modifié chimiquement comme cela serait nécessaire pour la spectroscopie de fluorescence.

Les expériences de RMN 1D  $^1\text{H}$  en rotation à l'angle magique (MAS) sont faciles à réaliser, donnant immédiatement des informations sur l'état du médicament ou la formation de liaisons hydrogène

entre les composants du système. Toutefois, en raison de la complexité de certains systèmes, même en utilisant des hauts champs magnétiques et la rotation MAS très élevée, la RMN du  $^1\text{H}$  ne permet pas toujours d'obtenir des spectres résolus et, par conséquent, d'avoir des informations sur le système. Dans ce cas, des expériences de RMN 2D peuvent être réalisées. En plus de la réalisation des spectres 2D  $^1\text{H}$ - $^1\text{H}$ , mais une solution alternative peut être les expériences  $^1\text{H}$ -X (X = noyau actif en RMN autre que le  $^1\text{H}$ ) pour essayer de tirer profit des hétéronoyaux (X) qui sont présents dans le médicament ou le nanovecteur. Si elles sont informatives dans de nombreux DDS, les expériences  $^1\text{H}$ -X ont également leurs limites dans le cas de systèmes trop complexes. Dans ces cas, des expériences X-Y 2D peuvent être réalisées. Ces types d'expériences constituent une nouvelle approche dans la caractérisation structurale des DDS qui permet de contourner la faible résolution de la RMN du  $^1\text{H}$ .

Dans cette thèse, en étroite collaboration avec le groupe du Dr Ruxandra Gref (DR CNRS ISMO Orsay), nous avons étudié les DDS basés sur les MOFs comme vecteur de médicament en utilisant la spectroscopie RMN à rotation à angle magique. Sur la base de récentes expériences de RMN à base de protons dans des MOF diamagnétiques et paramagnétiques sur des MOF purs, nous voulions initialement aborder ces DDS en utilisant la RMN  $^1\text{H}$  en raison de sa grande sensibilité. Cependant, nous avons rapidement réalisé que si l'utilisation d'un instrument RMN de pointe (aimants à champ magnétique élevé, fréquence de rotation à angle magique ultra-rapide) et de séquences d'impulsions, permettant d'obtenir une très bonne résolution sur des MOF purs, la situation était beaucoup plus difficile sur les systèmes supramoléculaires complexes que sont les DDSs. En outre, les DDSs basés sur les MOFs les plus populaires sont constitués de cations  $\text{Fe}^{3+}$  non toxiques (par exemple, MIL-100(Fe), MIL-88(Fe)). La présence de ces centres paramagnétiques puissants rend les spectres RMN  $^1\text{H}$  MAS encore plus complexes.

Nous avons donc choisi d'étudier les analogues diamagnétiques de MIL-100(Fe) à base d'Al, à savoir MIL-100(Al), en considérant comme hypothèse qu'ils se comporteraient de manière similaire. Nous avons également modifié notre stratégie initiale à base de protons et décidé de concentrer notre

étude sur les hétéronoyaux (tels que  $^{19}\text{F}$ ,  $^{27}\text{Al}$ ,  $^{31}\text{P}$ ,  $^{13}\text{C}$ ,  $^2\text{H}$ ,  $^{17}\text{O}$ , etc.) présents de manière endogène ou ajoutés volontairement dans le médicament ou dans le nanovecteur. Cela s'est fait au prix d'une grande perte de sensibilité (car les hétéronoyaux sont présents en concentration inférieure d'au moins un ordre de grandeur à celle des protons), mais au bénéfice d'une plus grande sélectivité (puisque nous pouvons choisir quel et où chaque hétéronoyau peut être placé, c'est-à-dire sur la surface ou dans le cœur de la nanoparticule, sur le médicament, etc.). Grâce à cette approche, nous avons pu analyser en détail des DDSs supramoléculaires très complexes. En relation constante avec les chimistes, ces informations ont été utilisées pour modifier à leur tour la conception des DDSs, ce qui a permis d'améliorer les performances.

Le premier DDS étudié consistait en un promédicament antituberculeux, le Lansoprazole (LPZ), chargé dans un MOF à base de cyclodextrine- $\gamma$  ( $\gamma$ -CD),  $\gamma$ -CD-MOF. Le LPZ est une molécule fragile qui se dégrade facilement dans des conditions acides<sup>8-10</sup> et basiques, est instable sur une étagère<sup>8,11,12</sup> (même en condition de stockage à 4°C<sup>13</sup>) et a une forte tendance à cristalliser. Le stockage et l'administration de ce médicament sont donc des challenges et le chargement du médicament dans un DDS apparaît comme une solution intéressante pour résoudre ces problèmes.

$\gamma$ -CD-MOF a été choisi comme vecteur du LPZ en raison de sa capacité de chargement élevée pour ce médicament ( $23 \pm 2$  % en poids)<sup>14</sup>. Les  $\gamma$ -CD-MOFs sont des MOFs biocompatibles résultant de la coordination de cations potassium à des unités de *D*-glucopyranosil alternées à liaison  $\alpha$ -1,4 sur les faces primaire et secondaire des CDs. Six unités CDs sont tenues par la coordination de quatre cations  $\text{K}^+$  aux groupes  $\text{C}_6\text{OH}$  et aux atomes d'oxygène du cycle glycosidique sur les faces primaires des  $\gamma$ -CD, tandis que les cubes sont attachés les uns aux autres par la coordination de quatre ions  $\text{K}^+$  aux carbones des groupes OH des faces secondaires de la cyclodextrine. Les  $\gamma$ -CD-MOFs ont une structure poreuse ouverte, avec un grand pore sphérique de 1,7 nm de diamètre situé au centre de chaque cube ( $\gamma$ -CD)<sub>6</sub> et qui est relié par une série de vides plus petits. Six fenêtres de pores de 0,78 nm de diamètre

sont définies par le  $\gamma$ -CD, qui adopte la face du cube. De plus, la structure du canal (avec une ouverture de 0,42 nm) relie les deux types de pores entre eux<sup>15-17</sup>.

Un tensioactif est utilisé dans la synthèse du  $\gamma$ -CD-MOF pour obtenir des particules de MOF de taille homogène. En utilisant des mesures RMN  $^1\text{H}$ - $^1\text{H}$ , nous avons localisé ce tensioactif et montré qu'il restait présent dans les particules finales, un problème potentiel pour l'encapsulation des médicaments. Toutefois, par RMN  $^1\text{H}$ - $^1\text{H}$ ,  $^1\text{H}$ - $^{13}\text{C}$  et  $^1\text{H}$ - $^{19}\text{F}$ - $^{13}\text{C}$ , nous avons montré que la compétition tensioactif/LPZ était favorable au LPZ, qui présente une affinité meilleure avec les CD. L'ensemble des mesures, ainsi que des mesures 15N en abondance naturelle sur ce système, nous ont permis de localiser le médicament dans le MOF, ainsi que son état de protonation, critère important pour la libération.

Le second système à l'étude était un DDS basé sur le nanoMIL-100(Al), choisi comme analogue du nanoMIL-100(Fe) très étudié *in vivo* (préclinique).

Dans une première étape, des groupes fonctionnels de surface et des médicaments contenant des atomes de phosphore ont été sélectionnés parce qu'il a été démontré qu'ils avaient une grande affinité avec l'analogue du MOF à base de Fe, et les liaisons chimiques Al-O-P sont connues pour être énergétiquement favorables. En utilisant les expériences  $^{27}\text{Al}$   $\{^{31}\text{P}\}$  2D *D*-HMQC, nous avons confirmé la grande affinité attendue entre le revêtement phosphaté (phosphate  $\beta$ -CD) et le médicament (adénosine triphosphate) avec les cations aluminium de surface et/ou du cœur des particules de MOF<sup>18</sup>. Grâce à cette méthodologie, la faible résolution de la spectroscopie RMN  $^1\text{H}$  MAS a été contournée et il a été possible de montrer pour la première fois une signature RMN  $^{27}\text{Al}$  à température ambiante des espèces d'aluminium présentes à la surface ou sous la surface des nanoparticules et leur interaction avec le revêtement CD-P. La formation d'une forte liaison covalente P-O-Al entre le CD et le MOF pourrait être la clé pour assurer une grande stabilité des nanoparticules cœur-couronne *in vivo*. Les expériences  $^{27}\text{Al}$   $\{^{31}\text{P}\}$  2D *D*-HMQC ont ensuite été utilisées pour analyser la dégradation du MOF en milieu biologique (tampon phosphate). Il a été constaté que peu de dégradation, et donc

d'administration de médicaments, était obtenue, probablement en raison de la formation d'une couche de type aluminophosphate sur la surface externe du MOF.

C'est pourquoi un autre revêtement de surface plus couvrant a été envisagé : les oligomères de  $\gamma$ -CD-citrate (CD-CO). Ce revêtement a été choisi parce qu'on s'attendait à ce que le  $\gamma$ -CD présente une plus grande affinité pour le médicament que le  $\beta$ -CD (qui est plus petit), ce qui pourrait entraîner une charge utile plus importante. Ici, le médicament choisi est la doxorubicine (DOX) en raison de son affinité connue avec les CD-CO. Dans ce système, aucun atome autre que  $^1\text{H}$  et  $^{13}\text{C}$  n'étaient présent. Par conséquent, la stratégie adoptée a consisté à synthétiser le polymère CD-CO en utilisant le citrate marqué au  $^{13}\text{C}$  comme précurseur. De cette façon, en utilisant  $^{27}\text{Al}\{^{13}\text{C}\}$  2D *D*-HMQC,  $^{13}\text{C}\{^{27}\text{Al}\}$  RESPDOR et  $^1\text{H}\{^{13}\text{C}\}$  *D*-HMQC la bonne interaction du nouveau revêtement avec la surface du nanoMIL-100(Al) a été confirmée par la formation d'une nouvelle résonance sur les spectres RMN  $^{13}\text{C}$  appartenant à la liaison entre le groupe carboxylique du citrate et l'aluminium du MIL-100. La charge du DOX à la fois dans les pores des MOFs et dans le revêtement a été validée par la même approche. Nous avons remarqué que l'interaction de la DOX avec le revêtement réduisait l'interaction du citrate avec l'aluminium de la surface, mais n'affectait pas la stabilité des nanoparticules. L'étude de libération du médicament est toujours en cours.

L'ensemble des données rapportées dans cette thèse a montré que l'utilisation d'hétéroatomes pour étudier des DDS au niveau moléculaire était une bonne alternative à la spectroscopie RMN  $^1\text{H}$ , au prix d'une moindre sensibilité mais avec l'avantage d'une plus grande sélectivité. Cette méthodologie est poursuivie par M. V. D. Le dans sa thèse. En particulier, l'effet de la longueur de la chaîne de phosphate du médicament (mono- vs tri-phosphate) sur son affinité et la délivrance du médicament est en cours d'évaluation. Si seuls quelques noyaux ont été étudiés dans ce travail ( $^{19}\text{F}$ ,  $^{27}\text{Al}$ ,  $^{31}\text{P}$ ,  $^{13}\text{C}$ ,  $^{15}\text{N}$ ), d'autres pourraient être envisagés.

Le deutérium est un nouveau noyau "à la mode" dans le développement des médicaments. La liaison C-D est en effet plus forte que la liaison C-H. Cette liaison plus forte entraîne une moindre

destruction du médicament dans l'organisme, d'où une biodisponibilité accrue et une administration plus faible du médicament. De plus, le remplacement de H par D dans une molécule connue réduit considérablement la durée de développement du médicament. Jusqu'à présent, un seul médicament deutéré a été approuvé par la FDA (Austedo® de Teva), mais une douzaine d'autres sont à l'étude à différents stades (I à III)<sup>19</sup>. D'un point de vue de la spectroscopie RMN, le deutérium dilue les protons, ce qui simplifie les spectres RMN <sup>1</sup>H MAS et permet de modifier les liaisons hydrogène. Le D<sub>2</sub>O peut donc être utilisé pour jouer sur les interactions médicament/porteur. Par exemple, le médicament Vancomycine (VCM) a été chargé à l'intérieur de nanoparticules de PLGA, dans lesquelles le PVA est mélangé à la surface du PLGA. En raison du fort chevauchement des résonances des protons et de la présence de molécules d'eau, une stratégie de deutération a été utilisée pour tenter de simplifier les spectres RMN <sup>1</sup>H. Nous avons comparé l'effet du pH sur le NP chargé avec le médicament avec l'échantillon synthétisé en D<sub>2</sub>O. Si aucune différence n'est perceptible dans les spectres de carbone effectués dans les échantillons à différents pH, dans les spectres de protons, il est possible de remarquer une augmentation de l'intensité des résonances appartenant aux protons de la vancomycine (OH, NH). Ceci peut être mieux remarqué dans l'échantillon synthétisé en D<sub>2</sub>O. On peut remarquer que les résonances appartenant aux OH et NH sont plus intenses dans l'échantillon deutéré et dans celui à pH=7,5. À pH=4, il y a des interactions, créées par les liaisons H, entre le médicament et les polymères. Une fois que nous changeons le pH, en passant à un pH neutre (pH=7,5), le médicament se cristallise à l'intérieur du polymère, et en perdant ces interactions, les pics semblent plus étroits. Les mêmes lignes étroites peuvent être observées dans le spectre de l'échantillon deutéré, car la stratégie de deutération "change" la liaison H et donc les interactions entre le médicament et le polymère.

Enfin, un autre atome très présent dans la DDS est l'oxygène. Le seul isotope de l'oxygène actif en RMN est le <sup>17</sup>O, qui est un spin 5/2 et qui est présent en abondance à 0,037 %. Cette faible abondance naturelle nécessite un enrichissement isotopique (souvent) coûteux. Récemment, de nouvelles stratégies de marquage utilisant une quantité mineure d'eau marquée ont été proposées : i) par

broyage planétaire, ii) par simple imprégnation dans de l'eau marquée en  $^{17}\text{O}$ . Cette dernière a été appliquée avec succès pour les zéolithes<sup>20,21</sup>. Les MOFs présentant des similarités chimiques avec les zéolithes, cette stratégie a également été tentée sur des MOFs. En outre, un MOF à base de scandium, NOTT-400(Sc), qui pu être sélectivement marqué en  $^{17}\text{O}$  sur la position pontante Sc-O-Sc (correspondant au site d'oxygène le plus actif dans le MOF) soit i) en introduisant dans la dernière étape de la synthèse, ii) soit par simple imprégnation du MOF pendant 3 semaines dans une solution  $\text{H}_2^{17}\text{O}$ . Cela montre (ou confirme) que les fonctions oxo des MOFs sont très labiles et peuvent être facilement échangées. Ceci est très important car ces fonctions oxo sont généralement les sites les plus réactifs des MOFs, que ce soit pour la catalyse, l'adsorption de gaz ou l'adsorption de médicaments.

En conclusion, la spectroscopie RMN est un outil analytique important pour comprendre les DDSs au niveau atomique, et représente un guide important pour la conception de DDS avec des performances améliorées.

## Références

- (1) *Drug Delivery Systems*; Jain, K. K., Ed.; Humana Press: Totowa, NJ, 2008.
- (2) Seth, S.; Matzger, A. J. Metal–Organic Frameworks: Examples, Counterexamples, and an Actionable Definition. *Cryst. Growth Des.* **2017**, *17* (8), 4043–4048.
- (3) Corma, A.; García, H.; Lladrós i Xamena, F. X. Engineering Metal Organic Frameworks for Heterogeneous Catalysis. *Chem. Rev.* **2010**, *110* (8), 4606–4655.
- (4) Chen, W.; Wu, C. Synthesis, Functionalization, and Applications of Metal–Organic Frameworks in Biomedicine. *Dalton Trans.* **2018**, *47* (7), 2114–2133.
- (5) McKinlay, A. C.; Morris, R. E.; Horcajada, P.; Férey, G.; Gref, R.; Couvreur, P.; Serre, C. BioMOFs: Metal–Organic Frameworks for Biological and Medical Applications. *Angew. Chem. Int. Ed.* **2010**, *49* (36), 6260–6266.
- (6) Gossert, A. D.; Jahnke, W. NMR in Drug Discovery: A Practical Guide to Identification and Validation of Ligands Interacting with Biological Macromolecules. *Prog. Nucl. Magn. Reson. Spectrosc.* **2016**, *97*, 82–125.
- (7) Martineau-Corcós, C. NMR Crystallography: A Tool for the Characterization of Microporous Hybrid Solids. *Curr. Opin. Colloid Interface Sci.* **2018**, *33*, 35–43.
- (8) DellaGreca, M.; Iesce, M. R.; Previtera, L.; Rubino, M.; Temussi, F.; Brigante, M. Degradation of Lansoprazole and Omeprazole in the Aquatic Environment. *Chemosphere* **2006**, *63* (7), 1087–1093.
- (9) Ngan, Y.; Gupta, M. A Comparison between Liposomal and Nonliposomal Formulations of Doxorubicin in the Treatment of Cancer: An Updated Review. *Arch. Pharm. Pract.* **2016**, *7* (1), 1–13.
- (10) Ekpe, A.; Jacobsen, T. Effect of Various Salts on the Stability of Lansoprazole, Omeprazole, and Pantoprazole as Determined by High-Performance Liquid Chromatography. *Drug Dev. Ind. Pharm.* **1999**, *25* (9), 1057–1065.
- (11) Battu, S.; Pottabathini, V. Hydrolytic Degradation Study of Lansoprazole, Identification, Isolation and Characterisation of Base Degradation Product. *Am. J. Anal. Chem.* **2015**, *6* (2), 145–155.
- (12) Liu, K.-H.; Kim, M.-J.; Jung, W. M.; Kang, W.; Cha, I.-J.; Shin, J.-G. Lansoprazole Enantiomer Activates Human Liver Microsomal CYP2C9 Catalytic Activity in a Stereospecific and Substrate-Specific Manner. *Drug Metab. Dispos.* **2005**, *33* (2), 209–213.
- (13) DiGiacinto, J. L.; Olsen, K. M.; Bergman, K. L.; Hoie, E. B. Stability of Suspension Formulations of Lansoprazole and Omeprazole Stored in Amber-Colored Plastic Oral Syringes. **2000**, *34*, 600–605.
- (14) Li, X.; Guo, T.; Lachmanski, L.; Manoli, F.; Menendez-Miranda, M.; Manet, I.; Guo, Z.; Wu, L.; Zhang, J.; Gref, R. Cyclodextrin-Based Metal–Organic Frameworks Particles as Efficient Carriers for Lansoprazole: Study of Morphology and Chemical Composition of Individual Particles. *Int. J. Pharm.* **2017**, *531* (2), 424–432.
- (15) Rajkumar, T.; Kukkar, D.; Kim, K.-H.; Sohn, J. R.; Deep, A. Cyclodextrin–Metal–Organic Framework (CD–MOF): From Synthesis to Applications. *J. Ind. Eng. Chem.* **2019**, *72*, 50–66.
- (16) Michida, W.; Nagai, A.; Sakuragi, M.; Kusakabe, K. Discrete Polymerization of 3,4-Ethylenedioxythiophene in Cyclodextrin-Based Metal–Organic Framework. *Cryst. Res. Technol.* **2018**, *53* (4), 1700142–1700148.
- (17) Smaldone, R. A.; Forgan, R. S.; Furukawa, H.; Gassensmith, J. J.; Slawin, A. M. Z.; Yaghi, O. M.; Stoddart, J. F. Metal–Organic Frameworks from Edible Natural Products. *Angew. Chem. Int. Ed.* **2010**, *49* (46), 8630–8634.
- (18) Porcino, M.; Christodoulou, I.; Dang Le Vuong, M.; Gref, R.; Martineau-Corcós, C. New Insights on the Supramolecular Structure of Highly Porous Core–Shell Drug Nanocarriers Using Solid-State NMR Spectroscopy. *RSC Adv.* **2019**, *9*, 32472–32475.

- (19) DeWitt, S. H.; Maryanoff, B. E. Deuterated Drug Molecules: Focus on FDA-Approved Deutetrabenazine: Published as Part of the *Biochemistry* Series “Biochemistry to Bedside.” *Biochemistry* **2018**, *57* (5), 472–473..
- (20) Heard, C. J.; Grajciar, L.; Rice, C. M.; Pugh, S. M.; Nachtigall, P.; Ashbrook, S. E.; Morris, R. E. Fast Room Temperature Lability of Aluminosilicate Zeolites. *Nat. Commun.* **2019**, *10* (1), 4690–4697.
- (21) Pugh, S. M.; Wright, P. A.; Law, D. J.; Thompson, N.; Ashbrook, S. E. Facile, Room-Temperature <sup>17</sup>O Enrichment of Zeolite Frameworks Revealed by Solid-State NMR Spectroscopy. *J. Am. Chem. Soc.* **2020**, *142* (2), 900–906.



# General Introduction



Drug delivery systems (DDSs) are formulation or devices used to improve the delivery of drugs with low efficacy and safety<sup>1</sup>. Moreover, they may aid convenience and compliance of the patient. The process of drug delivery consists of administration of a pharmaceutical product into the body, with controlled transport and delivery to the target cells or organs. Most of them are complex core-shell systems, composed by a biodegradable core where the drug is loaded and a coating, which can be functionalized with specific ligand. There are different types of DDSs, such as liposomes, microspheres and microcapsules, polymer micelles and nanoparticles, red blood cells, mesoporous silica nanoparticles and Metal-Organic Frameworks (MOFs). Bio-friendly synthesis, high drug loading in the pores and surface modifications that can increase the stability and have a selective target delivery are only few of the advantages of MOFs used as drug carriers<sup>2,3</sup>.

The analysis of the structure of a DDS is important to understand its stability, its mechanism, its interaction with the drug and with the body and to carry out modification that may increase its potential. Analytical techniques, such as thermal analysis, nitrogen adsorption, X-ray diffraction provide information about the crystal structure, morphology, porosity, drug loading and release.

Solid-state Nuclear Magnetic Resonance (ssNMR) offers information about structural and dynamic properties, probing local environment of the nuclei and short-range order information. This gives rise to various advantages, including the ability to provide detailed structural insights and to examine local defects and disorders. In the context of DDSs, because numerous active NMR nuclei are present in the core (such as <sup>1</sup>H, <sup>2</sup>H, <sup>13</sup>C, <sup>17</sup>O, <sup>19</sup>F and <sup>27</sup>Al), corona (as <sup>1</sup>H, <sup>13</sup>C, <sup>17</sup>O, <sup>27</sup>Al, <sup>29</sup>Si) and surface modification (as <sup>13</sup>C, <sup>17</sup>O, <sup>29</sup>Si, <sup>31</sup>P) of the nanoparticles, it can provide information about drug location, state and interactions in the system and about the core-shell interactions and about the matrix degradation and so, the delivery/release of the drug.

In this thesis, in close collaboration with the group of Dr. Ruxandra Gref (DR CNRS ISMO Orsay), we have investigated DDSs based on MOFs as drug carrier using magic-angle spinning (MAS) NMR spectroscopy.

Based on recent proton-based NMR experiments on diamagnetic and paramagnetic pure MOFs<sup>4</sup>, we initially wanted to address these DDS using <sup>1</sup>H NMR due to its high sensitivity. However, we quickly realized that if using state-of-the-art NMR instrument (high magnetic field magnets, ultra-fast magic-angle spinning frequency) and pulse sequences, very nice resolution can be obtained on pure MOFs, the situation was much more difficult on the complex systems as the DDSs. Furthermore, the most popular MOF-based DDSs are made of non-toxic Fe<sup>3+</sup> cations (e.g., MIL-100(Fe), MIL-88(Fe)). The presence of these strong paramagnetic centers makes the <sup>1</sup>H MAS NMR spectra even more complex.

Therefore, we chose to study the Al-based diamagnetic analogs of MIL-100(Fe), namely MIL-100(Al), considering as hypothesis that they would behave similarly. We also change our initial proton-based strategy and decided to focus our study on heteronuclei (such as <sup>19</sup>F, <sup>27</sup>Al, <sup>31</sup>P, <sup>13</sup>C, <sup>2</sup>H, <sup>17</sup>O, etc) present endogenously or added on purpose in the drug/coating or in the carrier. This was achieved at the expense of great sensitivity loss (as the heteronuclei are present in concentration that are at least an order of magnitude less than the protons), but at the benefit of greater selectivity (since we can choose which and where each heretonuclei can be placed, *i.e.*, on the surface or the bulk of the nanoparticle, on the coating species, on the drug, etc). Using this approach, we have been able to analyze in detail highly complex supramolecular DDSs. In constant relationship with the chemists, these pieces of information were used in turn to modify the design of the DDSs, leading to improved performances.

This thesis starts with a brief introduction on the process of drug delivery and the different route of administration. The different types of DDSs, their use and the main analytical tools that can be used to study their structure are presented. MOFs based drug carriers, notably those studied in this thesis, are describes in more detail. The second chapter contains a basic presentation of the principles of NMR spectroscopy and of the pulse sequences used during this project. In the third chapter, we present a review on the use of ssNMR spectroscopy in the investigation of DDSs. At the end of this chapter, our work is situated as compared to this state-of-the-art review. Results obtained during this

thesis for three different drug/carrier systems are reported in chapters 4 to 6. Conclusions and perspectives to the work end this manuscript.

## References

- (1) *Drug Delivery Systems*; Jain, K. K., Ed.; Humana Press: Totowa, NJ, 2008.
- (2) Chen, W.; Wu, C. Synthesis, Functionalization, and Applications of Metal–Organic Frameworks in Biomedicine. *Dalton Trans.* **2018**, 47 (7), 2114–2133.
- (3) McKinlay, A. C.; Morris, R. E.; Horcajada, P.; Férey, G.; Gref, R.; Couvreur, P.; Serre, C. BioMOFs: Metal–Organic Frameworks for Biological and Medical Applications. *Angew. Chem. Int. Ed.* **2010**, 49 (36), 6260–6266.
- (4) Krajnc, A.; Kos, T.; Zabukovec Logar, N.; Mali, G. A Simple NMR-Based Method for Studying the Spatial Distribution of Linkers within Mixed-Linker Metal–Organic Frameworks. *Angew. Chem. Int. Ed.* **2015**, 54 (36), 10535–10538.

# Chapter 1

## Drug Delivery and Drug Delivery Systems



A brief introduction on the drug delivery process and some of the different types of porous drug delivery systems is presented in this chapter. A particular attention is given to Metal-Organic Frameworks (MOFs) and their application as drug carriers.

## 1. Drug Delivery

The process of drug delivery takes into account the administration of a therapeutic product, the release of the Active Pharmaceutical Ingredient (API) by the product and the transport of this API to the biological target. Nowadays, complex formulations that control the time-release medications and that target specific areas of the body are being developed. Administration of the drug into the human body can occur by various anatomical routes. The choice of the route depends on the disease, the effect desired and the characteristics of the product. Drugs may be given systemically and targeted to the diseased organ or administrated directly to the organ affected<sup>1</sup>.

Briefly, the main routes of delivery are<sup>2,3</sup>:

- **Oral.** The oral route has been the most used drug delivery method in the world, because of the ease of administration and the compliance of the patients. However, many drugs, such as proteins or peptides, are subjected to a massive degradation in the GI (Gastro-Intestinal) tract. As a result, many materials for drug delivery have been developed to protect the drug from the degradation and enhance drug adsorption<sup>2</sup>.
- **Pulmonary.** The pulmonary route is used to treat several illnesses, such as asthma or cystic fibrosis. Because the drug is directly administrated to the lung, systemic side effects can be minimized as well as the dose required. Nevertheless, this route can be useful for systematic therapeutic substances, such as insulin or other proteins.
- **Transdermal.** Delivering of the drug across the skin is useful for local applications, patches, drug carriers and electrotransport. It is an alternative to avoid the drug degradation in the GI

tract and to reduce the systemic side effects. However, the skin is a natural barrier to foreign substances and so, it is important to develop methods to enhance the permeation across it.

- **Parenteral.** The name parenteral route is applied to injections of substances by subcutaneous, intravenous, intramuscular and intra-arterial routes. It is the most used route for systemic drug delivery. It has several advantages such as almost complete bioavailability of the drug and rapid onset of action. However, there are several problems associated with this route among which pain, risk of infections and the involvement of health care coworkers. Improve the injections technologies or develop alternative method of delivery are the two strategies chosen to erase the problems.
- **Transmucosal.** By diffusion several drugs can be introduced at various anatomical sites, thanks to the mucous membranes that covers all the internal passages and orifices of the body. In comparison with parenteral route, there are several advantages, including rapid adsorption and lower cost.
- **Colorectal.** For drug, targeting the small intestine or acting systematically, the colon can be a site for safe and slow adsorption. Adsorption enhancers are required for some hydrophilic drugs (antibiotics or peptide drugs) and other drugs may cause rectal irritations.

The rate of the drug uptake in the administration routes is controlled by the drug properties (solubility, charge, molecular size, etc.) and the characteristics of the site of administration (pH, presence of enzyme or of active transport, etc.). With traditional administrations, the therapeutic index and consequently, the therapeutic window should be taken into consideration. The therapeutic index (TI) is a quantitative measure of the safety of the drug; it is a comparison between the amount of the therapeutic agent causing toxicity, and the amount giving a therapeutic effect in 50% of the subjects tested (respectively  $TD_{50}$  and  $ED_{50}$ ):

$$TI = \frac{TD_{50}}{ED_{50}} \quad (1-1)$$

The therapeutic window of a drug is the range of drug dosages which can treat disease effectively without having toxic effects<sup>3</sup> (Figure 1.1). Each drug has a given TI and some of them are very low and require regular monitoring of drug level.

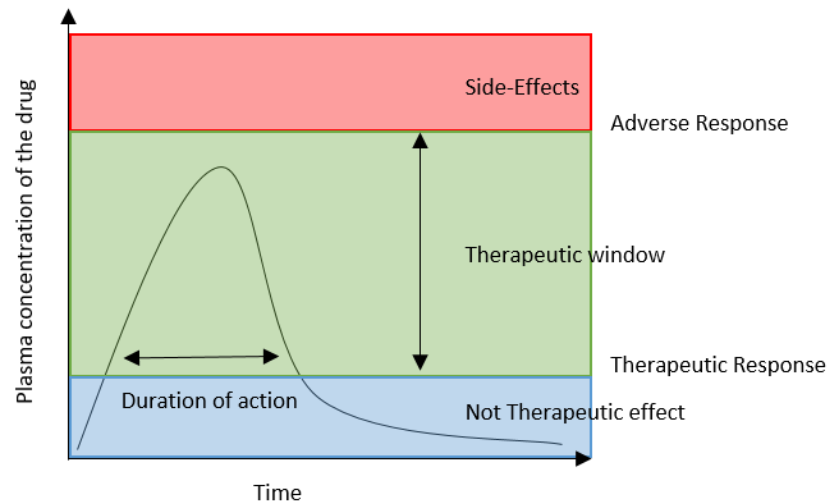


Figure 1.1: Graphic representation of plasma concentration of the drug during the time. The duration of the therapeutic action, correspond to the time in which the concentration stays in the therapeutic window (green zone). Before and after, the concentration is too low to have a therapeutic effect (blue zone). If the concentration goes up of the adverse response, side-effects could be showed (red zone).

Materials for drug delivery can be employed to have a better control of drug level or have a direct release of the drug on the target. An ideal material for drug delivery should be biocompatible, non-toxic and not immunogenic. It should have precise scaffolding properties, with an adequate bioelimination, and a modifiable surface. Its synthesis should be easy and reproducible and it should have a controlled release of the drug. Materials responding to these criteria are called Drug Delivery Systems (DDS).

## 2. Drug Delivery Systems

A nanosized drug delivery system (DDS) is defined as a formulation or a device that enables the introduction of a therapeutic substance in the body<sup>1</sup>. The major objectives to use a DDS are to improve the efficacy and safety of the drug by controlling the rate, time and place of release of the API, as well as to aid convenience and compliance of the patient<sup>4</sup>. Other important points are the reduction of the

cost of drug development, of the risk of failure in new product development and the life extension of the product<sup>1</sup>. There is unfortunately no universal drug nanocarriers, and for each medical target, a new drug carrier has to be properly designed. The ideal DDS should have high colloidal stability, high drug loading capacity, be prepared without need of toxic solvent, be inert, biocompatible, mechanically strong, biodegradable, comfortable for the patient, safe from accidental release, simple to administer, and finally easy and cost effective to fabricate and sterilize. Most DDSs are composed of a very complex core-shell system with different characteristics and functions (Figure 1.2).

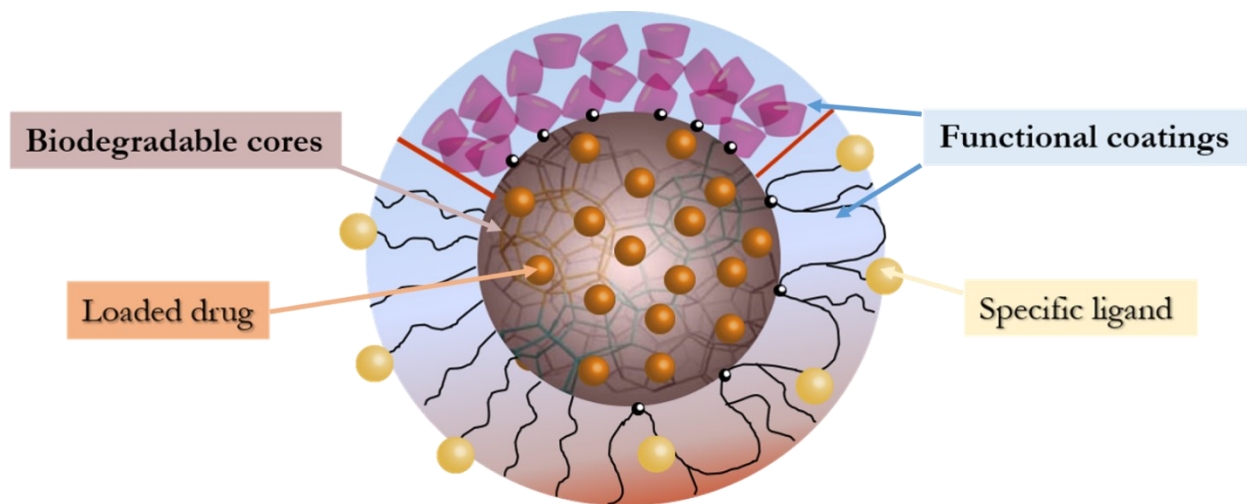


Figure 1.2: Illustration of composition of a Drug Delivery System. The drug is loaded in the biodegradable core that has to protect and stabilize it. The corona is composed by a functional coating that can interact with specific ligands to ensure delivery of the drug to the target.

The core of the system accommodates the drug, protects and stabilizes it. It must be degradable to ensure efficient drug release. The corona part of the system has for goals to increase the colloidal stability of the nanoparticles, to make them furtive to the immune system and to ensure specific delivery to the biological target.

Some of the different types of porous DDSs are summarized in Figure 1.3 and detailed in the next sections.

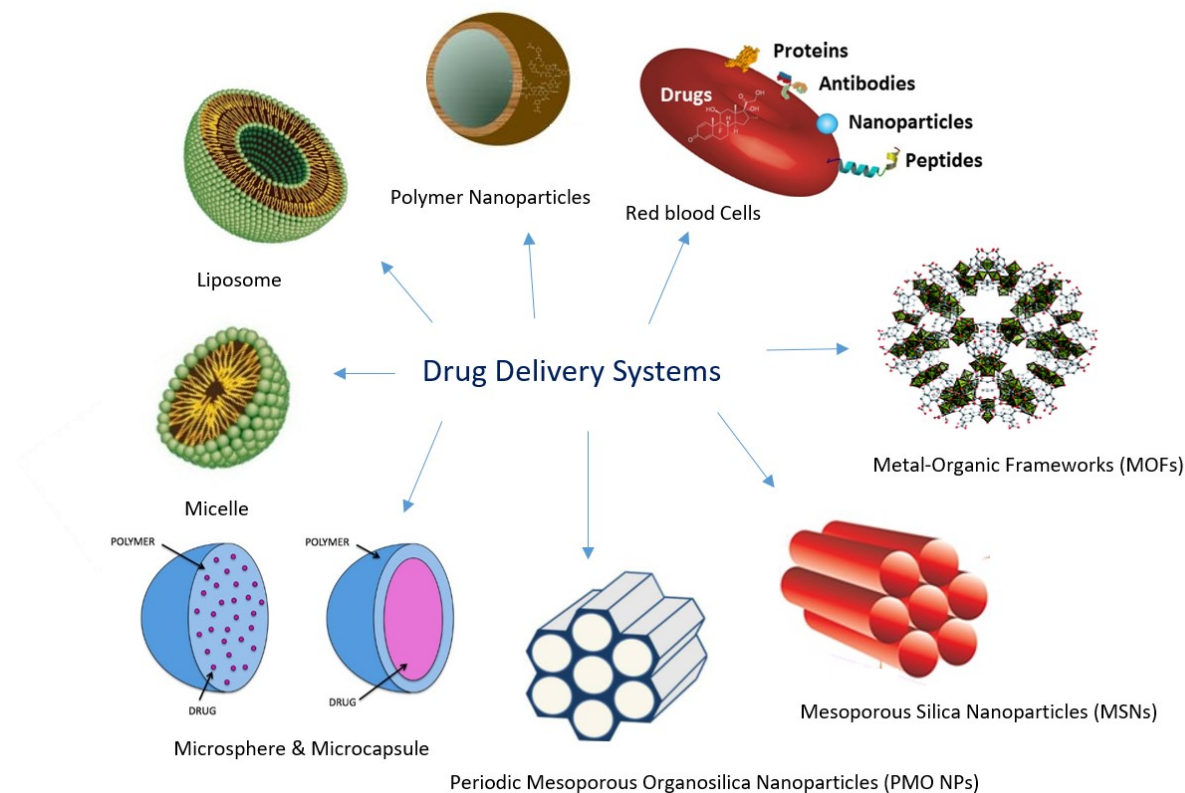


Figure 1.3: Some types of porous Drug Delivery Systems<sup>5-13</sup>.

The choice of the appropriate DDS is based on the physiochemical nature (solubility, molecular weight and size) of the drug as well as the disease for which the system has to be used and so, the administration route chosen to deliver the drug<sup>14</sup>. Moreover, the functional groups of the drug can influence the choice of the DDS, because of the interaction that can form with it.

## 2.1 Liposomes

Liposomes are spherical vesicles formed by phospholipids and similar amphipathic lipids, incorporated with sterols, such as cholesterol<sup>1</sup>. The polar character of their core enables polar drug molecules to be encapsulated, but also lipophilic molecules are solubilized within the phospholipid bilayer. Furthermore, channel proteins can be incorporated and allow passive diffusion of small solutes such as ions, nutrients and antibiotics<sup>15</sup>. Liposomes are classified, depending on the number phospholipidic bilayers, as multilamellar (MLV), small unilamellar (SUVs) or large unilamellar (LUVs)<sup>16</sup>.

The pharmaceutical properties of liposomes depend on the composition of the lipid layer and its permeability and fluidity<sup>1</sup> and they can be formulated and processed to differ size, composition, charge and lamellarity. Drugs with different solubility can be encapsulated in liposomes, hydrophobic drugs have affinity to the phospholipid layer and hydrophilic drugs are entrapped in the aqueous cavity. The liposomes are one of the earliest targeted systems, starting for cancer therapy. Following extensive developments in liposome technology, many liposome-based drug formulations are nowadays used to treat different type of infections, pain management and photodynamic therapy<sup>17</sup>.

## 2.2 Polymer micelles

Polymer micelles are biocompatible nanoparticles varying in size from 50 and 200 nm that are very interesting for drug delivery applications<sup>1</sup>. The drug can be physically entrapped in the core of the micelles and transported in a particular site of the body without being degraded by the enzyme or incur in hydrolysis. This is possible thanks to hydrophilic blocks of the micelles, which can form hydrogen bonds with the aqueous environment and form a tight shell around the micellar core<sup>16</sup>. The size and morphology of the micelles can be easily controlled, since, being composed of polymers, the molecular weight and block length ratio can be changed.

## 2.3 Microsphere and microcapsules

Microspheres and microcapsules are spherical particles with sizes in the range of 1 and 100  $\mu\text{m}$  that are used to encapsulate the active compounds. Microcapsules differ from microspheres in having a barrier membrane surrounding a solid or liquid core. Therefore, in these reservoir systems, a polymer shell surrounds the drug<sup>1</sup>. Microspheres are matrix systems consisting of natural or synthetic polymers in which the agent encapsulated can either molecularly dissolved or heterogeneously dispersed into the matrix polymer<sup>18</sup>. Possible synthetic biodegradable polymers are poly-alkyl-cyanoacrylates that are used as drug carrier for parental, ophthalmic and oral preparations. An example of natural polymer is the protein Albumin that is used for target carrier for anticancer drugs<sup>15</sup>.

## 2.4 Red blood cells

Red blood cells or Erythrocytes have potential carrier capabilities for the delivery of drugs. They are red cells with a biconcave disc form that transport the hemoglobin, a protein that carries oxygen from the lungs to tissues and that consists of four polypeptide subunits, each of which is bound to an iron-containing heme molecule. The red blood cells are biocompatible, biodegradable and non-immunogenic due to their natural presence in the body<sup>1</sup>. By using various physical and chemical methods, cells are broken, and drugs are entrapped into erythrocytes. Finally, the drugs are released and resultant carriers are called as “released erythrocytes”. A broad range of a variety of chemically and biologically drugs can be incorporated in red blood cells, using various chemical and physical methods<sup>15</sup>.

## 2.5 Polymer Nanoparticles

Micro- and nanoparticles based on PLA (Poly(lactic acid)) and PLGA (Poly(lactic acid-glycolic acid))<sup>19</sup> are often used for intravenous administration of a large variety of drugs, such as Docetaxel<sup>20</sup> and Doxorubicin<sup>21</sup>, two anticancer drugs and Estradiol<sup>21</sup>, an hormone that can be used as drug to treat mental disease. Sometimes these particles were covered with Polyethylene glycole (PEG) or chitosan (CS) to improve the stability of the systems and helps the transport of the drugs<sup>1,22,23</sup>.

## 2.6 Mesoporous Silica Nanoparticles

Mesoporous silica nanoparticles (MSNs) are reservoirs with a high capacity to accommodate guest molecules, having uniform and tunable pore size, in the range of 2-50 nm, and which surface can be easy functionalized. Their long-range ordered pore structure with tailorable pore size and geometry facilitates a homogenous incorporation of guest molecules with different sizes and properties. Drug loading is based on the adsorptive properties of MSNs: both hydrophilic and hydrophobic cargos can be adsorbed into the pores. They have greater loading capacity compared to other carriers for their large pore volume. The release profile of drugs from MSNs mainly depends on its diffusion from the pores, which can be tailored by modifying the surface of the MSNs to suit the biological needs. The

decisive factor responsible for controlling the release is the interaction between the surface groups on pores and the drug molecules<sup>9,24</sup>. The two most widely explored materials for drug delivery are MCM-41<sup>25</sup> (Mobil Crystalline Materials) and SBA-15<sup>26</sup> (Santa Barbara Amorphous type material).

## 2.7 Periodic Mesoporous Organosilica Nanoparticles

Periodic Mesoporous Organosilica nanoparticles (PMO NPs), similar to mesoporous silica nanoparticles, are prepared from organo-bridged alkoxysilanes and have tunable mesopores that could be utilized for many applications such as gas and molecule adsorption, catalysis, and drug delivery. Unlike MSNs, the diversity in chemical nature of the pore walls is theoretically unlimited<sup>27</sup>. They have several advantages, such as uniform and tunable pore size, large surface areas, high pore volumes, nontoxic nature and good biocompatibility. PMOs have been explored as drug carriers for different kinds of drugs, such as antiinflammatory, antibiotics or antitumoral drugs. In some cases, the hydrophilic silica walls need to be functionalized with organic groups to allow the loading of hydrophobic drugs. This functionalization seems to be the main controlling factor on the drug adsorption/desorption processes, leading to higher drug loading capacities and slower release kinetics<sup>13</sup>.

## 2.8 Metal-Organic Frameworks

Metal-Organic Frameworks (MOFs) are a class of coordination polymers comprising organic linkers wherein metal-ligand interaction/bonding leads to 2D or 3D crystalline network structures<sup>28</sup> (Figure 1.4). The metal centers act as nodes of the lattice and are held in place by the directionality of their binding to the organic linkers (electrostatic attraction and coordinative metal–ligand interactions). Crystallinity and porosity are the main characteristics of MOFs and these materials hold records in terms of high pore volume (from 0.50 cm<sup>3</sup>/g to 1.5 cm<sup>3</sup>/g), surface area (from 700 m<sup>2</sup>/g to 9000 m<sup>2</sup>/g)<sup>29–31</sup>, and lowest framework density<sup>32</sup>.

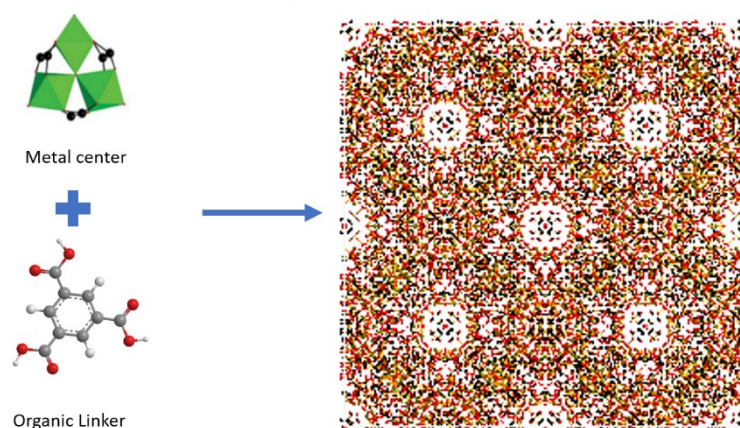


Figure 1.4: Schematic drawing of a metal-organic framework (MOF) structure.

The pore size, shape, dimensionality and chemical environment in the MOFs can be controlled by the selection of their building blocks (metal and organic linker) and how they are connected. Furthermore, the possibility of amending and functionalizing the organic ligand may allow tailoring the material for specific applications<sup>33</sup>.

### 2.8.1 Synthesis and structural characteristics

The synthesis of MOFs is often carried out in the liquid phase by mixing two solutions containing the metal and the organic component, either at room temperature or under solvothermal conditions and with or without the aid of auxiliary molecules. Generally, high-solubility organic solvents, such as dimethyl formamide, ethanol, or methanol, are used in solvothermal reactions. Hydrothermal synthesis of MOFs constitutes a more environmental friendly approach that substitutes the use of organic solvents for water<sup>31</sup>. Formation of crystalline framework takes place by self-assembly of the structural units forming an ordered network of metal-organic coordination bonds. Other synthetic methods are developed such as microwave, electrochemical, ultrasonic processing which reduce the synthesis duration<sup>34</sup>. In Figure 1.5 are summarized all the synthetic methods. After the synthesis, post synthetic modification is a powerful route to introduce functionality into MOFs, and in many cases, is the only way by certain moieties can be incorporated in the molecules without affecting the

underlying structure. Examples of post synthetic methods are covalent modification, surface modification, metalation, linker/metal exchange and modification of inorganic cluster<sup>35</sup>. The nature of the solvent, the ligands, or the presence of guest molecules in the synthesis can have a dramatic effect on the crystal structure of the material obtained<sup>33</sup>.

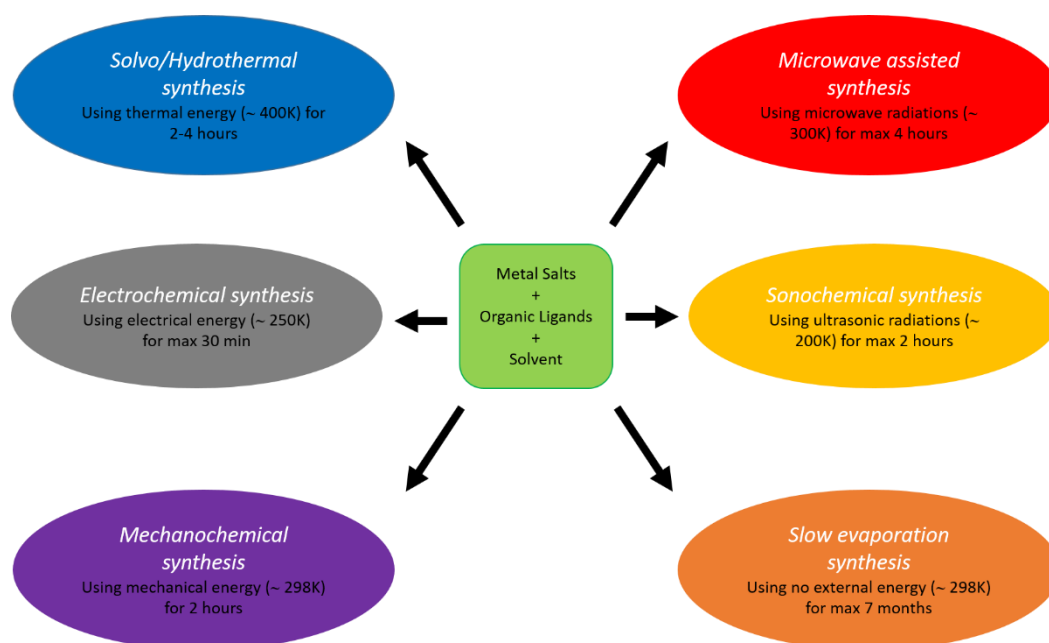


Figure 1.5: Different synthetic methods of MOFs materials<sup>31</sup>.

A large variety of metal atoms in their stable oxidation states, alkaline, alkaline earth, transition metals, main group metals, and rare-earth elements, have been successfully used in the synthesis of MOFs. As organic components, rigid molecules are usually preferred over flexible ones, because they favor the preparation of crystalline, porous, stable MOFs<sup>34</sup>. Different combinations of metal ions and organic linkers lead to an enormous number of MOFs.

MOFs are distinguished by the diversity of the structure, different symmetry, pore sizes and by their characteristics. The carbon chain length or the number of benzene rings of the linker can determine the pore size; therefore, the introduction of different substituents and functional groups

into the linker is responsible for the additional selectivity and unique chemical properties of the pores<sup>36</sup>.

### 2.8.2 Applications

Many potential applications have been explored in strategic domains:

- **Catalysis.** The framework capacity to accommodate catalytic units and the possibility to have the presence of open metal sites are key factors for the catalysis application<sup>33,37</sup>. They are very useful for heterogeneous organic and photocatalytic reactions<sup>38</sup>.
- **Storage and Gas separation.** The large surface-area of MOFs enables them to soak up large amounts of gas or molecules, such as hydrogen, carbon-dioxide and methane<sup>38</sup>. Based on the size/shape of the adsorbent's pore and the binding affinity from the adsorption sites, gas separation can be realized<sup>39,40</sup>.
- **Chemical sensors.** Several chemical functionalities can be incorporated into the coordination nanospace of MOF materials and can show sensing applications for biomolecules, metal ions, explosives, environmental toxins, and others<sup>38,41</sup>.
- **Biomedical applications.** MOFs are used for storage and delivery of gas transmitter such as NO or CO and as well as therapeutic molecules (more details are given in the section 2.8.4)<sup>42</sup>.

### 2.8.3 General techniques for the structural characterization of MOFs

Different techniques can be used for the characterization of the MOFs, regardless of their application. The most common method of analysis of MOF crystal structure is X-ray Diffraction (XRD). Due to the difficulty to grow a single crystal of MOF, powder X-ray diffraction (PXRD) is often used. PXRD patterns allow analyzing the reproducibility of synthesis results or structural differences between samples of the same MOF prepared by different methods; it is useful to determine the structural parameters and crystallinity of the MOFs (Figure 1.6)<sup>31,36,43</sup>. It might be difficult to determine the crystal structure of MOFs from powder diffraction data only. New methods combining PXRD data

with solid-state NMR and molecular modeling were developed, allowing the determination of very complex MOFs<sup>44</sup>.

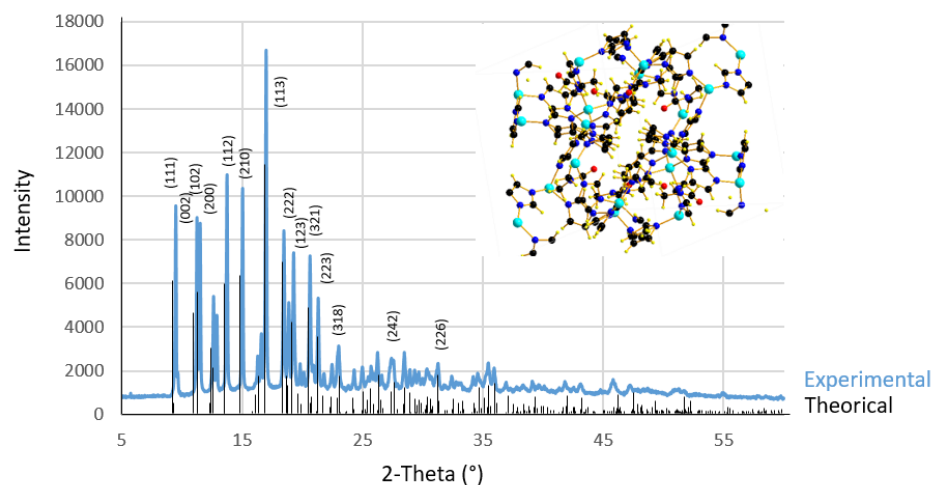


Figure 1.6: Example of experimental (light blue) and theoretical (dark) PXRD patterns of a crystalline MOF, ZIF-45. Some (hkl) indices are given.

For the characterization of the shape of the material, external morphology, dispersion, and mixture of phases, Scanning Electron Microscopy (SEM) technique is routinely used. On the other hand, Transmission Electron Microscopy (TEM) has been widely applied to determine the grain size, particle size, and crystallographic data. This technique is very useful for the characterization of MOFs modified by the incorporation of nanoparticles (NPs), because the collected images provides information about the size and dispersion of those NPs<sup>31</sup>.

Thermal stability of the MOFs is assessed by thermogravimetric analysis (TGA), which measures the mass of the sample as a function of temperature. This technique is not only useful to study the thermal stability but also to estimate solvent-accessible pore volume of the materials<sup>31,36</sup>.

To study surface area, pore volume, average pore size, and pore size distribution, Brunauer-Emmett-Teller (BET) analysis can be used. Nitrogen is the most commonly employed gaseous adsorbate used for surface probing by BET methods. This approach studies the N<sub>2</sub> adsorption over the

surface of a solid at the boiling temperature of liquid nitrogen, resulting in an adsorption isotherm. The shape of the isotherm provides information about the textural composition of the solid<sup>31</sup>.

Among all these techniques, Nuclear Magnetic Resonance (NMR) spectroscopy and in particular, solid-state NMR is becoming an important tool for the characterization of MOFs. Solid-state NMR gives the possibility to analyze the material at atomic level. It can help understanding the synthetic and post-synthetic modifications, performed in order to increase the stability of the material<sup>46,47</sup>. In addition to this, the NMR spectroscopy can reveal interactions between molecules and allows studying, at atomic level the surface of the materials. This makes NMR spectroscopy a promising tool for the study of the MOFs used as drug delivery systems.

#### 2.8.4 MOFs as Drug Delivery Systems

The possibility to synthesize MOFs starting using only non-toxic agents, makes MOFs possible drug carriers. The use of MOFs for biomedical applications indeed requires a biologically friendly composition. To avoid possible toxic side effects, the choice of the appropriate metal and of the linker are critical. Some of appropriate metals are Calcium, Magnesium, Zinc and Iron, but it has to be taken into consideration also the metal daily dose. Regarding the linker, exogenous or endogenous linkers can be used<sup>34</sup>. The endogenous organic spacers, such as cyclodextrin<sup>11</sup>, fumarate<sup>48,49</sup> or aminoacids and peptides<sup>42</sup>, are safer and more biocompatible, but most MOFs used as DDSs are composed of exogenous linkers. In that case, a green synthesis approach is adopted, based on room temperature synthetic reaction in aqueous media, with the use of precursor materials with benign chemical characterizations<sup>50</sup>. Furthermore, it is important to have a study of toxicity of the single components before their use, with cytotoxicity tests and measure of the linker and metal accumulation in the urine.

Among all the porous materials that can be used as DDSs, MOFs have several advantages such as high surface area, the possibility for easy modification of the surface, adjustment of the functional groups of the linkers and tuning of the pore size. In addition, a large number of MOFs with nontoxic metals and biodegradable linkers are available. Another important aspect is the adaptability to host a

large variety of molecules with different chemistry, due to their hydrophilic-hydrophobic internal microenvironment<sup>12,34</sup>.

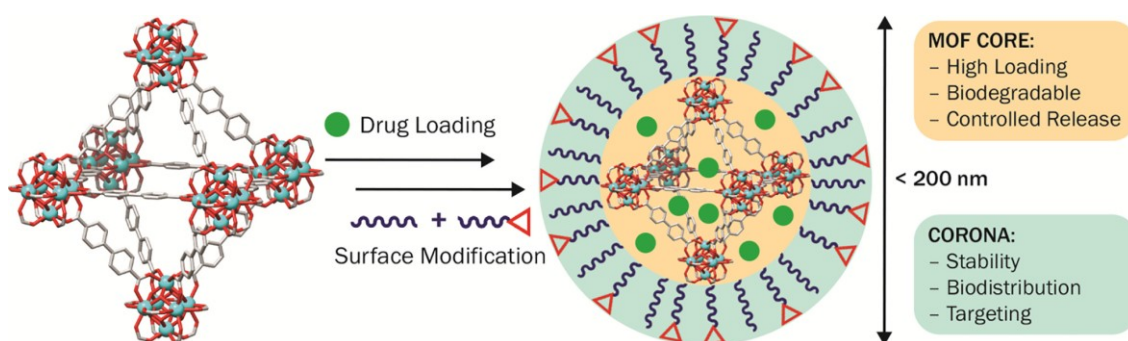


Figure 1.7: Scheme showing the ideal properties of a MOF-based drug delivery system, using the structure of UiO-67,  $[\text{Zr}_6\text{O}_4(\text{OH})_4(\text{bpd})_6]_n$  (bpd = 4,4-biphenyldicarboxylate), as an example. (Source: Abánades Lázaro *et al.*<sup>10</sup>)

The colloidal stability of the MOF in water is another factor that should be taken into consideration in DDS design. It was shown that carefully engineered surface modification of MOF NPs was helpful to increase the colloidal stability in aqueous media and prevent the premature release of the drug<sup>12,34,42</sup> (Figure 1.7). The surface can be modified by coating with a hydrophilic polymer such as PEG,<sup>51</sup> or with larger molecule such as Cyclodextrin (CD)<sup>52</sup>, or with liposomes to have a combination therapy<sup>49</sup>. Moreover, a silica thin layer<sup>53</sup> or nanoparticles made by selenium/ruthenium<sup>54</sup> could be used.

Two other parameters can affect the use of the MOF for biomedical application: size and shape. For some type of administration route, the size is a critical value, for example, nanoparticles with particle size more than 200 nm cannot be administrated by parenteral route. Therefore, it is important to have a homogenous distribution of particle size and the shape of the nanoparticles that compose the DDS<sup>34</sup>.

Up to now, several MOFs have been studied and used as DDSs. Two chromium (despite the potential toxicity of  $\text{Cr}^{3+}$  cations) mesoporous MOFs, MIL-101(Cr) and MIL-100(Cr) (MIL stands for Materials of Lavoisier Institute) were used to encapsulate and deliver Ibuprofen, showing a particularly

high loading capacity and a delivery governed by diffusion processes in *in vitro* experiments<sup>55</sup>. The same drug was loaded in a flexible MOF, MIL-53, with two different types of metal cations ( $\text{Cr}^{3+}$  and  $\text{Fe}^{3+}$ ). The “swelling” effect of the terephthalate linker of this material makes this MOF adaptable to the drug size and can promote the incorporation of different types of drugs<sup>56</sup>. Moreover, several iron-MOFs are used, for example, as caffeine carriers<sup>57-59</sup>. Another example is bio-MOF-1, composed of zinc ions and biphenyl carboxylate and adenine as linkers. It was used to deliver the antiarrhythmic drug, procainamide. Due to the short half-life of the procainamide, a controlled release of this drug was a successfully solution to avoid the administration every 4 hours<sup>60</sup>.

## 2.8.5 MOFs used in this thesis

The porous MOFs-based DDSs used in this thesis, *i.e.*,  $\gamma$ -Cyclodextrin-based Metal-Organic Framework and MIL-100, will be described in the next sections.

### 2.8.5.1 Cyclodextrin-based Metal-Organic Frameworks

CDs are natural cyclic oligosaccharides with 6 ( $\alpha$ -CD), 7 ( $\beta$ -CD) or 8 ( $\gamma$ -CD) glucopyranose units linked by alfa-1,4-glycosilic linkage. The CDs are homogeneous solids with a truncated cone shape (Figure 1.8). They are produced during the degradation of starch by an enzyme, the glycosil transferase. Hydroxyl groups compose the outer surface, that it is the hydrophilic part, while, the internal cavities are hydrophobic and covered by the glycosylic oxygen and the C-H units. This type of structure allows them to form non-covalent inclusion complexes through hydrogen bonding, van der Waals interactions or electrostatic interactions. They are widely used for biomedical applications and showed differently advantage, such as high surface areas, adjustable chemical functionality and structural diversity<sup>50</sup>.

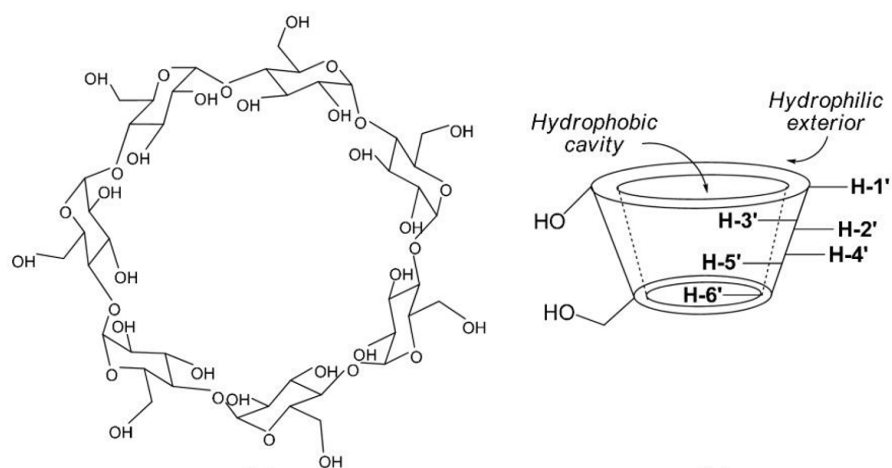


Figure 1.8: Illustration of the structure of  $\gamma$ -CD.

Recently, it was shown that CDs could be used as linker for the formation of porous MOFs, due to the presence of -OCCO- binding groups, which facilitate the formation of complexes with metal ions and the subsequently formation of an extended 3D network<sup>50</sup>. Cyclodextrin based Metal-organic frameworks (CD-MOFs)<sup>61,62</sup> are biologically acceptable types of MOFs, due to their porous and non-toxic nature. They are composed of a biocompatible metal ion, usually potassium or calcium that connect the cyclodextrin molecules to each other.

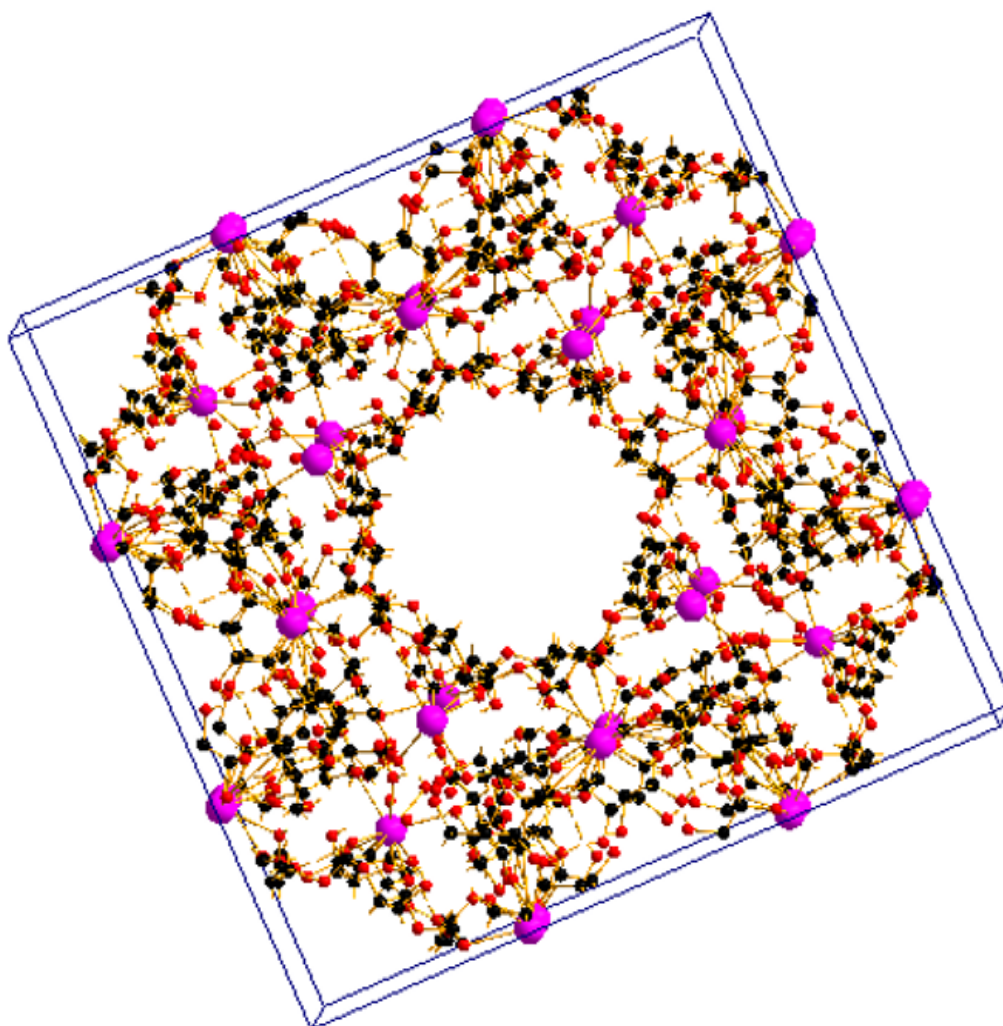


Figure 1.9: 3D cubic structure of  $\gamma$ -CD-MOF<sup>62</sup>. Oxygen, Carbon, Potassium atoms are in red, black and purple, respectively. Hydrogen atoms are omitted for clarity. The formation of the complex with the potassium ions are made through the C<sub>1</sub>O- and C<sub>6</sub>O- moieties.

$\gamma$ -CD-MOFs (Figure 1.9) are generally prepared by a vapor diffusion method<sup>61,62</sup> using methanol or aqueous solution of the hydroxyl metal, such as KOH. Other methods of synthesis can be used, such as hydro/solvothermal method, microwaves-assisted and conventional method<sup>41</sup>.

Post-synthetic modifications can be important to improve the stability of the MOF in the physiological environment. As an example, polymerization of 3,4-ethylenedioxythiophene (EDOT) in  $\gamma$ -CD-MOF was used to increase the thermal stability and the solubility in water of the particles. The

use of functional group, as poly(acrylic acid), incorporated in the MOF was shown to improve its stability in water and enhance drug-loading capacity.<sup>63</sup>

In the field of DDSs,  $\alpha$ -,  $\beta$ - and  $\gamma$ -CD-MOFs have been used.  $\alpha$ - and  $\beta$ -CD-MOFs were used to deliver 5-FU with good release results (93.9 % and 89 % of release rate respectively)<sup>64,65</sup>. Regarding  $\gamma$ -CD-MOFs, which show an homogeneous particle size around 6  $\mu\text{m}$ , they have been used to load several molecules<sup>62,66-68</sup>, including anti-inflammatory drugs, food additives and various pharmaceutical ingredients. Generally, drug molecules are loaded in the CD-MOFs through the principle of host-guest molecular inclusion, as for the pure CDs.

Lanzoprazole<sup>69</sup>, fenbufen<sup>70</sup>, ibuprofen<sup>71</sup> are three examples of drugs loaded in  $\gamma$ -CD-MOF with a loading capacity around 20 wt%, the best ones reported so far. Furthermore, CD-MOF was used to prepare nanoparticles with noble metals for biological applications<sup>50</sup>. CD-MOFs particles can store drugs for long period, since they are stable in air<sup>69</sup>. However, the use of CD-MOFs in the biomedical field is limited because of their high solubility in aqueous media, which may lead to the collapsing of the framework before reaching the target. To overcome this problem, surface modification can be adopted. Li *et al.* showed the utilization of hydrophobic C60 to incorporate  $\gamma$ -CD-MOFs in order to improve their stability without affecting the structural integrity. The new carrier system was used to load Doxorubicin drug, leading to a slower release of the drug<sup>72</sup>.

#### 2.8.5.2 MIL-100

MIL-100 framework is made up of trimesate (benzene 1,3,5-tricarboxylate, BTC) groups linked by trivalent metal (M) trimers. The framework formula is  $\text{M}_3\text{OX}_3(\text{BTC})_2$ , where X represents coordinating ligands on  $\text{M}^{3+}$  (M = Cr, Sc, Fe, Al)<sup>73</sup>. A large variety of potential applications has been proposed for the MIL-100: gas adsorption/storage<sup>74</sup>, catalysis<sup>73,75</sup> as well as in the field of the biomedicine<sup>51,52,76</sup>. In this latter field, synthetic method downsizing the materials to the nanoscale, associated to the low-toxicity of the carboxylate acids and the use of non-toxic metals (notably iron cations) greatly opened the possibility to use the MOFs as nanoparticles for drug delivery systems<sup>77</sup>. These nanoMIL-100(Fe) are

biodegradable and biocompatible and exhibit a crystalline structure with high, regular and controlled porosity. The 3D mesoporous structure of MIL-100(Fe), showed in Figure 1.10, is made of oxocentered trimers of Fe(III) octahedral linked by BTC ligands, resulting in hybrid supertetrahedra with two types of cages: a smaller one (24 Å) and larger one (29 Å), accessible through pentagonal (5.6 Å) and hexagonal windows (8.6 Å), respectively. Fe(III) trimers in MIL-100 possess accessible coordinatively unsaturated metal (CUS) sites, able to coordinate a wide range of polar species and drugs<sup>73,76</sup>.

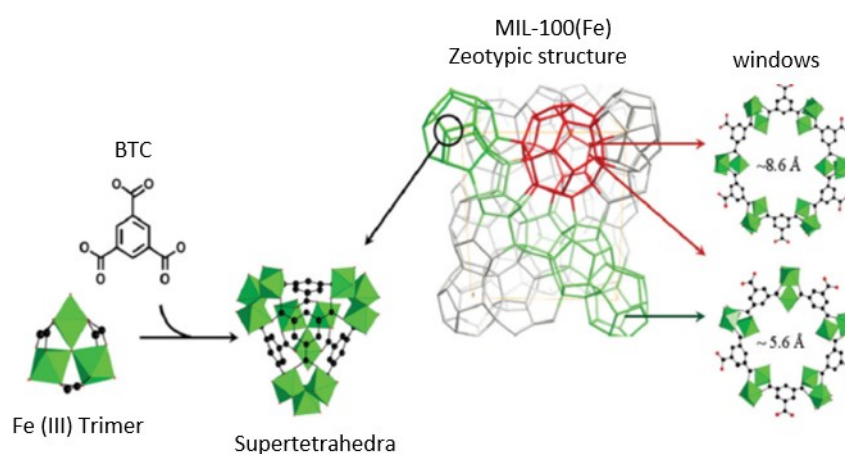


Figure 1.10: NanoMOFs formed by spontaneous coordination between Fe(III) trimers and trimesic acid into hybrid supertetrahedra which further assemble giving rise to a porous zeotypic architecture.

MIL-100(Fe) nanoparticles were synthesized (through a green synthesis approach using microwave-assisted hydrothermal synthesis) and characterized then in terms of biocompatibility, degradability and imaging properties. The efficiency of nanoMIL-100(Fe) was tested with several anticancer and antiviral drugs, such as Busulfan<sup>78</sup> and Doxorubicin<sup>79</sup>. The drugs were loaded in the nanoMOFs by soaking in saturated drug solutions, with a loading amount around 25 wt% for the Busulfan and 9 wt% for the Doxorubicin. The high loading of the Busulfan can reduce the amount of solid required to deliver the needed dose of this drug. Furthermore, the use of nanoMIL-100(Fe) could avoid the use of toxic organic solvents during drug administration and reduce the liver toxicity of the

drug<sup>78</sup>. Regarding Doxorubicin, the drug molecules form stable coordination bonds with the unsaturated iron sites that stabilize the drug and prevent it from the degradation<sup>79</sup>.

Azidothymidine 5'-triphosphate (AZT-TP) was also loaded in MIL-100(Fe) nanoparticles. The drug molecules were adsorbed within the larger pores of the MOF with an amount around 24 wt%. They were believed to interact through their phosphate groups with the unsaturated iron Lewis acid sites. Isothermal titration calorimetry and molecular modelling were performed to evaluate this interaction. The result confirmed the formation of a strong and complex ionocovalent interaction between the drug and the MOF. A comparison with the same drug, but monophosphated (AZT-MP) was made. Even if the encapsulation of AZT-MP was more efficient, the release of the drug was faster, because of the weaker interaction between the monophosphate group and the iron metal compared with the strong ones showed by the triphosphated drug that allow a controlled release of the drug molecules<sup>76</sup>.

The *in vivo* fate of the nanocarrier, such as biodistribution, pharmacokinetics and targeting abilities, depends upon appropriate surface physicochemical properties. With this purpose, engineering of the surface of the nanoparticles should be made. The coating should be obtained in aqueous media without using any toxic addictive, be stable in physiological conditions, confer colloidal stability to the nanoMOF, not interfere with the loading of the drug, and finally should not penetrate inside the porous structure<sup>52</sup>.

Agostoni *et al.*<sup>52</sup> proposed a coating strategy based on the use of aqueous solution of biocompatible bulky molecules, such as CDs. In particular, Phosphate CDs (CD-P) were selected because they are bulkier than the nanoMOF cages and they were already shown to improve the physicochemical properties of the drug. Moreover, the phosphate group of the CD can strongly coordinate with the CUS sites of the nanoMOF located at the surface of the particles, improving the stability of the coating.

The CD-P coating was compared with a coating made of PEG. The CD-P coating reported a good stability in aqueous solution and phosphate buffer saline (PBS). On the contrary, as the PEG chains are smaller than the windows of the nanoMOF, they penetrate into the pores, leading to a partial filling of the pore. As consequence, the amount of the drug loaded decreased and the release of it was not controlled (Figure 1.11)<sup>52</sup>.

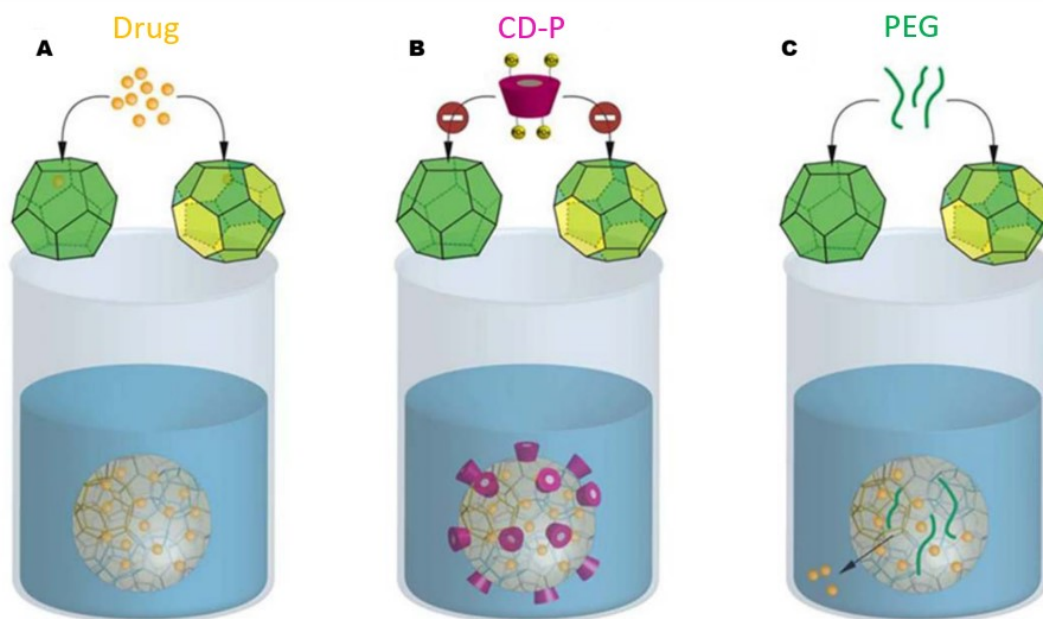


Figure 1.11: Schematic representation of drug loading and surface modification procedures: (A) Drug molecules are absorbed within the porous core interacting by non covalent links with the organic linkers or/and with the Lewis acid Fe(III) sites; (B) CD-P strongly interact with the nanoMOFs by coordination with the available Fe(III) sites at the surface, but cannot penetrate inside the matrix because they are too bulky to cross the nanoparticles microporous windows. (C) PEG coating are able to penetrate within the MOF porosity and lead to uncontrolled drug release. (Source: Agostoni *et al.*<sup>52</sup>)

Going forward, a characterization of the nanoMIL-100(Fe) and CD-P coated nanoMIL-100(Fe) was made to investigate the influence of the coating on the particles structure and on the drug loading. ITC and PXRD analysis showed that the structure of the MOF was not modified by the coating process that increase the colloidal stability of the nanoparticles<sup>52</sup>. Figure 1.12 shows PXRD patterns of coated and uncoated nanoMOFs, evidencing that the nanoparticles crystalline structure was not affected by the surface modification procedure. Studies on the encapsulation of the AZT-TP was made in the coated sample, showing unchanged drug payload. Additionally, drug release in PBS was radically the

same for coated and uncoated nanoMOF and the coated nanoparticles showed a lower toxicity of the uncoated ones.

Solid-state NMR was also used to investigate these DDSs. However, because the  $\text{Fe}^{3+}$  cation is paramagnetic, the study was made on the diamagnetic analog, namely MIL-100(Al), assuming similar behavior between the MOF and the drug<sup>52</sup>.

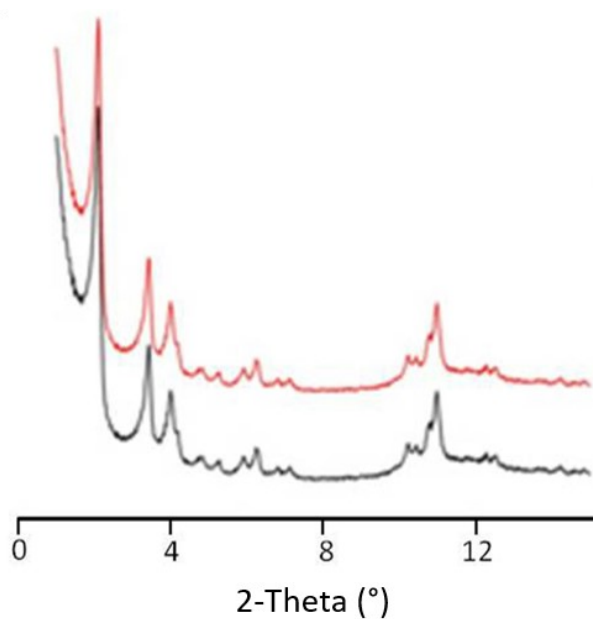


Figure 1.12: PXR D patterns of nanoMOFs before (black) and after impregnation with CD-P (red). (Source: Agostoni *et al.*<sup>52</sup>)

### 3. Conclusions

Drug delivery is a process consisting of administration of a pharmaceutical product into the body, with controlled transport and delivery to the target cells or organs. DDSs are used to improve efficacy and safety of the drug and to aid convenience and compliance of the patient. There are different types of DDSs, such as liposomes, microspheres and microcapsules, polymer micelles and nanoparticles, red blood cells, mesoporous silica nanoparticles, periodic mesoporous organosilica nanoparticles and MOFs, which have been briefly presented.

The porous DDSs used in this thesis, *i.e.*,  $\gamma$ -CD-MOFs and MIL-100, have been described. They were selected because both are biocompatible, showing high loading capacities for different type of drugs, controlled and homogeneous particle sizes and easy surface modification. The usual analytical characterization techniques that provide information about crystal structure, morphology, porosity, etc, have been mentioned. The efficiency of solid-state NMR spectroscopy to go deeper in the structural analysis of these core-shell systems will be presented in details in Chapter 3.

## References

- (1) *Drug Delivery Systems*; Jain, K. K., Ed.; Humana Press: Totowa, NJ, 2008.
- (2) Martín del Valle, E. M.; Galán, M. A.; Carbonell, R. G. Drug Delivery Technologies: The Way Forward in the New Decade. *Ind. Eng. Chem. Res.* **2009**, *48* (5), 2475–2486.
- (3) Katzung, B. G.; Masters, S. B.; Trevor, A. J. *Basic and Clinical Pharmacology*, XI.; McGraw-Hill Companies, 2009.
- (4) Skorupska, E.; Jeziorna, A.; Kazmierski, S.; Potrzebowski, M. J. Recent Progress in Solid-State NMR Studies of Drugs Confined within Drug Delivery Systems. *Solid State Nucl. Magn. Reson.* **2014**, *57–58*, 2–16.
- (5) Bozzuto, G.; Molinari, A. Liposomes as Nanomedical Devices. *Int. J. Nanomedicine* **2015**, *10*, 975–999.
- (6) Villa, C. H.; Anselmo, A. C.; Mitragotri, S.; Muzykantov, V. Red Blood Cells: Supercarriers for Drugs, Biologicals, and Nanoparticles and Inspiration for Advanced Delivery Systems. *Adv. Drug Deliv. Rev.* **2016**, *106*, 88–103.
- (7) Wurm, F. R.; Weiss, C. K. Nanoparticles from Renewable Polymers. *Front. Chem.* **2014**, *2*, 1–12.
- (8) Herrero-Vanrell, R.; Bravo-Osuna, I.; Andrés-Guerrero, V.; Vicario-de-la-Torre, M.; Molina-Martínez, I. T. The Potential of Using Biodegradable Microspheres in Retinal Diseases and Other Intraocular Pathologies. *Prog. Retin. Eye Res.* **2014**, *42*, 27–43.
- (9) Narayan, R.; Nayak, U.; Raichur, A.; Garg, S. Mesoporous Silica Nanoparticles: A Comprehensive Review on Synthesis and Recent Advances. *Pharmaceutics* **2018**, *10* (3), 1–49.
- (10) Abánades Lázaro, I.; Forgan, R. S. Application of Zirconium MOFs in Drug Delivery and Biomedicine. *Coord. Chem. Rev.* **2019**, *380*, 230–259.
- (11) Han, Y.; Liu, W.; Huang, J.; Qiu, S.; Zhong, H.; Liu, D.; Liu, J. Cyclodextrin-Based Metal-Organic Frameworks (CD-MOFs) in Pharmaceutics and Biomedicine. *Pharmaceutics* **2018**, *10* (4), 271–281.
- (12) McKinlay, A. C.; Morris, R. E.; Horcajada, P.; Férey, G.; Gref, R.; Couvreur, P.; Serre, C. BioMOFs: Metal-Organic Frameworks for Biological and Medical Applications. *Angew. Chem. Int. Ed.* **2010**, *49* (36), 6260–6266.
- (13) Esquivel, D.; Van Der Voort, P.; J. Romero-Salguero, F. Designing Advanced Functional Periodic Mesoporous Organosilicas for Biomedical Applications Electrodes. *AIMS Mater. Sci.* **2014**, *1* (1), 70–86.
- (14) Patra, J. K.; Das, G.; Fraceto, L. F.; Campos, E. V. R.; Rodriguez-Torres, M. del P.; Acosta-Torres, L. S.; Diaz-Torres, L. A.; Grillo, R.; Swamy, M. K.; Sharma, S.; Habtemariam, S.; Shin, H.-S. Nano Based Drug Delivery Systems: Recent Developments and Future Prospects. *J. Nanobiotechnology* **2018**, *16* (1), 71–104.
- (15) Bhagwat, R. R.; Vaidhya, I. S. NOVEL DRUG DELIVERY SYSTEMS: AN OVERVIEW. *IJPSR* **2013**, *4*, 970–982.
- (16) Tiwari, G.; Tiwari, R.; Bannerjee, S.; Bhati, L.; Pandey, S.; Pandey, P.; Sriwastawa, B. Drug Delivery Systems: An Updated Review. *Int. J. Pharm. Investig.* **2012**, *2* (1), 1–11.
- (17) Bulbake, U.; Doppalapudi, S.; Kommineni, N.; Khan, W. Liposomal Formulations in Clinical Use: An Updated Review. *Pharmaceutics* **2017**, *9* (4), 1–33.
- (18) Nordstierna, L.; Abdalla, A. A.; Nordin, M.; Nydén, M. Comparison of Release Behaviour from Microcapsules and Microspheres. *Prog. Org. Coat.* **2010**, *69* (1), 49–51.
- (19) Qi, F.; Wu, J.; Li, H.; Ma, G. Recent Research and Development of PLGA/PLA Microspheres/Nanoparticles: A Review in Scientific and Industrial Aspects. *Front. Chem. Sci. Eng.* **2019**, *13* (1), 14–27.

- (20) Musumeci, T.; Ventura, C. A.; Giannone, I.; Ruozi, B.; Montenegro, L.; Pignatello, R.; Puglisi, G. PLA/PLGA Nanoparticles for Sustained Release of Docetaxel. *Int. J. Pharm.* **2006**, *325* (1–2), 172–179.
- (21) Li, J.; Sabliov, C. PLA/PLGA Nanoparticles for Delivery of Drugs across the Blood-Brain Barrier. *Nanotechnol. Rev.* **2013**, *2* (3), 241–257. <https://doi.org/10.1515/ntrev-2012-0084>.
- (22) Lavik, E. B.; Kuppermann, B. D.; Humayun, M. S. Drug Delivery. In *Retina*; Elsevier, 2013; pp 734–745.
- (23) Betancourt, T.; Byrne, J. D.; Sunaryo, N.; Crowder, S. W.; Kadapakkam, M.; Patel, S.; Casciato, S.; Brannon-Peppas, L. PEGylation Strategies for Active Targeting of PLA/PLGA Nanoparticles. *J. Biomed. Mater. Res. A* **2009**, *91A* (1), 263–276.
- (24) Tang, Q.; Yao Xu; Dong Wu; Sun, Y.; Wang, J.; Jun Xu; Feng Deng. Studies on a New Carrier of Trimethylsilyl-Modified Mesoporous Material for Controlled Drug Delivery. *J. Controlled Release* **2006**, *114* (1), 41–46.
- (25) Vallet-Regi, M.; Rámila, A.; del Real, R. P.; Pérez-Pariente, J. A New Property of MCM-41: Drug Delivery System. *Chem. Mater.* **2001**, *13* (2), 308–311.
- (26) Fathi Vavsari, V.; Mohammadi Ziarani, G.; Badiiei, A. The Role of SBA-15 in Drug Delivery. *RSC Adv.* **2015**, *5* (111), 91686–91707.
- (27) Croissant, J. G.; Cattoën, X.; Wong Chi Man, M.; Durand, J.-O.; Khashab, N. M. Syntheses and Applications of Periodic Mesoporous Organosilica Nanoparticles. *Nanoscale* **2015**, *7* (48), 20318–20334.
- (28) Seth, S.; Matzger, A. J. Metal–Organic Frameworks: Examples, Counterexamples, and an Actionable Definition. *Cryst. Growth Des.* **2017**, *17* (8), 4043–4048.
- (29) Khan, N. A.; Hasan, Z.; Jhung, S. H. Beyond Pristine Metal–Organic Frameworks: Preparation and Application of Nanostructured, Nanosized, and Analogous MOFs. *Coord. Chem. Rev.* **2018**, *376*, 20–45.
- (30) Meng, X.; Gui, B.; Yuan, D.; Zeller, M.; Wang, C. Mechanized Azobenzene-Functionalized Zirconium Metal–Organic Framework for on-Command Cargo Release. *Sci. Adv.* **2016**, *2* (8), 1–6.
- (31) Bedia, J.; Muelas-Ramos, V.; Peñas-Garzón, M.; Gómez-Avilés, A.; Rodríguez, J. J.; Bolver, C. A Review on the Synthesis and Characterization of Metal Organic Frameworks for Photocatalytic Water Purification. *Catalysts* **2019**, *9* (1), 52–95.
- (32) Dhakshinamoorthy, A.; Asiri, A. M.; García, H. Metal–Organic Framework (MOF) Compounds: Photocatalysts for Redox Reactions and Solar Fuel Production. *Angew. Chem. Int. Ed.* **2016**, *55* (18), 5414–5445.
- (33) Corma, A.; García, H.; Llabrés i Xamena, F. X. Engineering Metal Organic Frameworks for Heterogeneous Catalysis. *Chem. Rev.* **2010**, *110* (8), 4606–4655.
- (34) Chen, W.; Wu, C. Synthesis, Functionalization, and Applications of Metal–Organic Frameworks in Biomedicine. *Dalton Trans.* **2018**, *47* (7), 2114–2133.
- (35) Marshall, R. J.; Forgan, R. S. Postsynthetic Modification of Zirconium Metal–Organic Frameworks: Postsynthetic Modification of Zirconium Metal–Organic Frameworks. *Eur. J. Inorg. Chem.* **2016**, *2016* (27), 4310–4331.
- (36) Butova, V. V.; Soldatov, M. A.; Guda, A. A.; Lomachenko, K. A.; Lamberti, C. Metal–Organic Frameworks: Structure, Properties, Methods of Synthesis and Characterization. *Russ. Chem. Rev.* **2016**, *85* (3), 280–307.
- (37) Yoon, M.; Srirambalaji, R.; Kim, K. Homochiral Metal–Organic Frameworks for Asymmetric Heterogeneous Catalysis. *Chem. Rev.* **2012**, *112* (2), 1196–1231.
- (38) Jiao, L.; Seow, J. Y. R.; Skinner, W. S.; Wang, Z. U.; Jiang, H.-L. Metal–Organic Frameworks: Structures and Functional Applications. *Mater. Today* **2019**, *27*, 43–68.
- (39) Lin, R.-B.; Xiang, S.; Xing, H.; Zhou, W.; Chen, B. Exploration of Porous Metal–Organic Frameworks for Gas Separation and Purification. *Coord. Chem. Rev.* **2019**, *378*, 87–103.

- (40) Getman, R. B.; Bae, Y.-S.; Wilmer, C. E.; Snurr, R. Q. Review and Analysis of Molecular Simulations of Methane, Hydrogen, and Acetylene Storage in Metal-Organic Frameworks. *Chem. Rev.* **2012**, *112*, 703–723.
- (41) Achmann, S.; Hagen, G.; Kita, J.; Malkowsky, I.; Kiener, C.; Moos, R. Metal-Organic Frameworks for Sensing Applications in the Gas Phase. *Sensors* **2009**, *9* (3), 1574–1589.
- (42) Horcajada, P.; Gref, R.; Baati, T.; Allan, P. K.; Maurin, G.; Couvreur, P.; Férey, G.; Morris, R. E.; Serre, C. Metal–Organic Frameworks in Biomedicine. *Chem. Rev.* **2012**, *112* (2), 1232–1268.
- (43) Chang, Z.; Yang, D.-H.; Xu, J.; Hu, T.-L.; Bu, X.-H. Flexible Metal–Organic Frameworks: Recent Advances and Potential Applications. *Adv Mater* **2015**, *27*, 5432–5441.
- (44) Wang, S.; Xhaferaj, N.; Wahiduzzaman, M.; Oyekan, K.; Li, X.; Wei, K.; Zheng, B.; Tissot, A.; Marrot, J.; Shepard, W.; Martineau-Corcus, C.; Filinchuk, Y.; Tan, K.; Maurin, G.; Serre, C. Engineering Structural Dynamics of Zirconium Metal–Organic Frameworks Based on Natural C4 Linkers. *J. Am. Chem. Soc.* **2019**, *141* (43), 17207–17216.
- (45) Huang, X.-C.; Lin, Y.-Y.; Zhang, J.-P.; Chen, X.-M. Ligand-Directed Strategy for Zeolite-Type Metal–Organic Frameworks: Zinc(II) Imidazolates with Unusual Zeolitic Topologies. *Angew. Chem. Int. Ed.* **2006**, *45* (10), 1557–1559.
- (46) Gossert, A. D.; Jahnke, W. NMR in Drug Discovery: A Practical Guide to Identification and Validation of Ligands Interacting with Biological Macromolecules. *Prog. Nucl. Magn. Reson. Spectrosc.* **2016**, *97*, 82–125.
- (47) Lucier, B. E. G.; Chen, S.; Huang, Y. Characterization of Metal–Organic Frameworks: Unlocking the Potential of Solid-State NMR. *Acc. Chem. Res.* **2018**, *51* (2), 319–330. <https://doi.org/10.1021/acs.accounts.7b00357>.
- (48) Chalati, T.; Horcajada, P.; Gref, R.; Couvreur, P.; Serre, C. Optimisation of the Synthesis of MOF Nanoparticles Made of Flexible Porous Iron Fumarate MIL-88A. *J Mater Chem* **2011**, *21* (7), 2220–2227.
- (49) Illes, B.; Wuttke, S.; Engelke, H. Liposome-Coated Iron Fumarate Metal-Organic Framework Nanoparticles for Combination Therapy. *Nanomaterials* **2017**, *7* (11), 351.
- (50) Rajkumar, T.; Kukkar, D.; Kim, K.-H.; Sohn, J. R.; Deep, A. Cyclodextrin-Metal–Organic Framework (CD-MOF): From Synthesis to Applications. *J. Ind. Eng. Chem.* **2019**, *72*, 50–66.
- (51) Horcajada, P.; Chalati, T.; Serre, C.; Gillet, B.; Sebrie, C.; Baati, T.; Eubank, J. F.; Heurtaux, D.; Clayette, P.; Kreuz, C.; Chang, J.-S.; Hwang, Y. K.; Marsaud, V.; Bories, P.-N.; Cynober, L.; Gil, S.; Férey, G.; Couvreur, P.; Gref, R. Porous Metal–Organic-Framework Nanoscale Carriers as a Potential Platform for Drug Delivery and Imaging. *Nat. Mater.* **2010**, *9* (2), 172–178.
- (52) Agostoni, V.; Horcajada, P.; Noiray, M.; Malanga, M.; Aykaç, A.; Jicsinszky, L.; Vargas-Berenguel, A.; Semiramoth, N.; Daoud-Mahammed, S.; Nicolas, V.; Martineau, C.; Taulelle, F.; Vigneron, J.; Etcheberry, A.; Serre, C.; Gref, R. A “Green” Strategy to Construct Non-Covalent, Stable and Bioactive Coatings on Porous MOF Nanoparticles. *Sci. Rep.* **2015**, *5* (1), 7925–7933.
- (53) Taylor-Pashow, K. M. L.; Della Rocca, J.; Xie, Z.; Tran, S.; Lin, W. Postsynthetic Modifications of Iron-Carboxylate Nanoscale Metal–Organic Frameworks for Imaging and Drug Delivery. *J. Am. Chem. Soc.* **2009**, *131* (40), 14261–14263.
- (54) Chen, Q.; Xu, M.; Zheng, W.; Xu, T.; Deng, H.; Liu, J. Se/Ru-Decorated Porous Metal–Organic Framework Nanoparticles for The Delivery of Pooled siRNAs to Reversing Multidrug Resistance in Taxol-Resistant Breast Cancer Cells. *ACS Appl. Mater. Interfaces* **2017**, *9* (8), 6712–6724.
- (55) Horcajada, P.; Serre, C.; Vallet-Regí, M.; Sebban, M.; Taulelle, F.; Férey, G. Metal–Organic Frameworks as Efficient Materials for Drug Delivery. *Angew. Chem. Int. Ed.* **2006**, *45* (36), 5974–5978.
- (56) Horcajada, P.; Serre, C.; Maurin, G.; Ramsahye, N. A.; Balas, F.; Vallet-Regí, M.; Sebban, M.; Taulelle, F.; Férey, G. Flexible Porous Metal-Organic Frameworks for a Controlled Drug Delivery. *J. Am. Chem. Soc.* **2008**, *130* (21), 6774–6780.

- (57) Cunha, D.; Ben Yahia, M.; Hall, S.; Miller, S. R.; Chevreau, H.; Elkaïm, E.; Maurin, G.; Horcajada, P.; Serre, C. Rationale of Drug Encapsulation and Release from Biocompatible Porous Metal–Organic Frameworks. *Chem. Mater.* **2013**, *25* (14), 2767–2776.
- (58) Devautour-Vinot, S.; Martineau, C.; Diaby, S.; Ben-Yahia, M.; Miller, S.; Serre, C.; Horcajada, P.; Cunha, D.; Taulelle, F.; Maurin, G. Caffeine Confinement into a Series of Functionalized Porous Zirconium MOFs: A Joint Experimental/Modeling Exploration. *J. Phys. Chem. C* **2013**, *117* (22), 11694–11704. <https://doi.org/10.1021/jp402916y>.
- (59) Gaudin, C.; Cunha, D.; Ivanoff, E.; Horcajada, P.; Chev e, G.; Yasri, A.; Loget, O.; Serre, C.; Maurin, G. A Quantitative Structure Activity Relationship Approach to Probe the Influence of the Functionalization on the Drug Encapsulation of Porous Metal–Organic Frameworks. *Microporous Mesoporous Mater.* **2012**, *157*, 124–130.
- (60) An, J.; Geib, S. J.; Rosi, N. L. Cation-Triggered Drug Release from a Porous Zinc–Adeninate Metal–Organic Framework. *J. Am. Chem. Soc.* **2009**, *131* (24), 8376–8377.
- (61) Furukawa, Y.; Ishiwata, T.; Sugikawa, K.; Kokado, K.; Sada, K. Nano- and Microsized Cubic Gel Particles from Cyclodextrin Metal–Organic Frameworks. *Angew. Chem. Int. Ed.* **2012**, *51* (42), 10566–10569. <https://doi.org/10.1002/anie.201204919>.
- (62) Smaldone, R. A.; Forgan, R. S.; Furukawa, H.; Gassensmith, J. J.; Slawin, A. M. Z.; Yaghi, O. M.; Stoddart, J. F. Metal–Organic Frameworks from Edible Natural Products. *Angew. Chem. Int. Ed.* **2010**, *49* (46), 8630–8634.
- (63) Michida, W.; Nagai, A.; Sakuragi, M.; Kusakabe, K. Discrete Polymerization of 3,4-Ethylenedioxythiophene in Cyclodextrin-Based Metal–Organic Framework. *Cryst. Res. Technol.* **2018**, *53* (4), 1700142–1700148.
- (64) Sha, J.-Q.; Zhong, X.-H.; Wu, L.-H.; Liu, G.-D.; Sheng, N. Nontoxic and Renewable Metal–Organic Framework Based on  $\alpha$ -Cyclodextrin with Efficient Drug Delivery. *RSC Adv.* **2016**, *6* (86), 82977–82983.
- (65) Liu, J.; Bao, T.-Y.; Yang, X.-Y.; Zhu, P.-P.; Wu, L.-H.; Sha, J.-Q.; Zhang, L.; Dong, L.-Z.; Cao, X.-L.; Lan, Y.-Q. Controllable Porosity Conversion of Metal–Organic Frameworks Composed of Natural Ingredients for Drug Delivery. *Chem. Commun.* **2017**, *53* (55), 7804–7807.
- (66) Michida, W.; Ezaki, M.; Sakuragi, M.; Guan, G.; Kusakabe, K. Crystal Growth of Cyclodextrin-Based Metal–Organic Framework with Inclusion of Ferulic Acid: Crystal Growth of Cyclodextrin-Based Metal–Organic Framework with Inclusion of Ferulic Acid. *Cryst. Res. Technol.* **2015**, *50* (7), 556–559.
- (67) Moussa, Z.; Hmadeh, M.; Abiad, M. G.; Dib, O. H.; Patra, D. Encapsulation of Curcumin in Cyclodextrin–Metal Organic Frameworks: Dissociation of Loaded CD–MOFs Enhances Stability of Curcumin. *Food Chem.* **2016**, *212*, 485–494.
- (68) Liu, B.; Li, H.; Xu, X.; Li, X.; Lv, N.; Singh, V.; Stoddart, J. F.; York, P.; Xu, X.; Gref, R.; Zhang, J. Optimized Synthesis and Crystalline Stability of  $\gamma$ -Cyclodextrin Metal–Organic Frameworks for Drug Adsorption. *Int. J. Pharm.* **2016**, *514* (1), 212–219.
- (69) Li, X.; Guo, T.; Lachmanski, L.; Manoli, F.; Menendez-Miranda, M.; Manet, I.; Guo, Z.; Wu, L.; Zhang, J.; Gref, R. Cyclodextrin-Based Metal–Organic Frameworks Particles as Efficient Carriers for Lansoprazole: Study of Morphology and Chemical Composition of Individual Particles. *Int. J. Pharm.* **2017**, *531* (2), 424–432.
- (70) Liu, B.; He, Y.; Han, L.; Singh, V.; Xu, X.; Guo, T.; Meng, F.; Xu, X.; York, P.; Liu, Z.; Zhang, J. Microwave-Assisted Rapid Synthesis of  $\gamma$ -Cyclodextrin Metal–Organic Frameworks for Size Control and Efficient Drug Loading. *Cryst. Growth Des.* **2017**, *17* (4), 1654–1660.
- (71) Hartlieb, K. J.; Ferris, D. P.; Holcroft, J. M.; Kandela, I.; Stern, C. L.; Nassar, M. S.; Botros, Y. Y.; Stoddart, J. F. Encapsulation of Ibuprofen in CD–MOF and Related Bioavailability Studies. *Mol. Pharm.* **2017**, *14* (5), 1831–1839.
- (72) Li, H.; Hill, M. R.; Huang, R.; Doblin, C.; Lim, S.; Hill, A. J.; Babarao, R.; Falcaro, P. Facile Stabilization of Cyclodextrin Metal–Organic Frameworks under Aqueous Conditions via the Incorporation of C<sub>60</sub> in Their Matrices. *Chem. Commun.* **2016**, *52* (35), 5973–5976.

- (73) Mitchell, L.; Williamson, P.; Ehrlichová, B.; Anderson, A. E.; Seymour, V. R.; Ashbrook, S. E.; Acerbi, N.; Daniels, L. M.; Walton, R. I.; Clarke, M. L.; Wright, P. A. Mixed-Metal MIL-100(Sc,M) (M=Al, Cr, Fe) for Lewis Acid Catalysis and Tandem C-C Bond Formation and Alcohol Oxidation. *Chem. - Eur. J.* **2014**, *20* (51), 17185–17197.
- (74) Mali, G.; Mazaj, M.; Arčon, I.; Hanžel, D.; Arčon, D.; Jagličić, Z. Unraveling the Arrangement of Al and Fe within the Framework Explains the Magnetism of Mixed-Metal MIL-100(Al,Fe). *J. Phys. Chem. Lett.* **2019**, 1464–1470. <https://doi.org/10.1021/acs.jpcclett.9b00341>.
- (75) Haouas, M.; Volkringer, C.; Loiseau, T.; Férey, G.; Taulelle, F. Monitoring the Activation Process of the Giant Pore MIL-100(Al) by Solid State NMR. *J. Phys. Chem. C* **2011**, *115* (36), 17934–17944.
- (76) Agostoni, V.; Anand, R.; Monti, S.; Hall, S.; Maurin, G.; Horcajada, P.; Serre, C.; Bouchemal, K.; Gref, R. Impact of Phosphorylation on the Encapsulation of Nucleoside Analogues within Porous Iron(III) Metal–Organic Framework MIL-100(Fe) Nanoparticles. *J. Mater. Chem. B* **2013**, *1* (34), 4231–4242.
- (77) Simon-Yarza, T.; Mielcarek, A.; Couvreur, P.; Serre, C. Nanoparticles of Metal–Organic Frameworks: On the Road to In Vivo Efficacy in Biomedicine. *Adv. Mater.* **2018**, *30* (37), 1707365–1707380.
- (78) Horcajada, P.; Chalati, T.; Serre, C.; Gillet, B.; Sebrie, C.; Baati, T.; Eubank, J. F.; Heurtaux, D.; Clayette, P.; Kreuz, C.; Chang, J.-S.; Hwang, Y. K.; Marsaud, V.; Bories, P.-N.; Cynober, L.; Gil, S.; Férey, G.; Couvreur, P.; Gref, R. Porous Metal–Organic-Framework Nanoscale Carriers as a Potential Platform for Drug Delivery and Imaging. *Nat. Mater.* **2010**, *9* (2), 172–178.
- (79) Anand, R.; Borghi, F.; Manoli, F.; Manet, I.; Agostoni, V.; Reschiglian, P.; Gref, R.; Monti, S. Host–Guest Interactions in Fe(III)-Trimesate MOF Nanoparticles Loaded with Doxorubicin. *J. Phys. Chem. B* **2014**, *118* (29), 8532–8539.

## Chapter 2

# Solid-State Nuclear Magnetic Resonance



Solid-state Nuclear Magnetic Resonance (ssNMR) has over the past decades become a very powerful physical tool to investigate the structure of different types of materials. It gives the possibility to observe selectively the signature of several nuclei and to obtain very detailed structural information. Therefore, it is very useful not only as diagnostic in synthetic processes, but it also offers the opportunity to investigate the local structure, understanding the molecular level and the dynamics of crystal and amorphous solids<sup>1</sup> and for studying interaction between molecules<sup>2</sup>.

In this chapter, the basic concepts of NMR spectroscopy are explained, with particular attention on the interactions, parameters and techniques that can influence the solid-state NMR spectra. The pulse sequences used during this thesis are described and illustrated in the second part of this chapter.

## 1. The Basics of Nuclear Magnetic Resonance spectroscopy<sup>3,4</sup>

Nuclear Magnetic Resonance (NMR) is based on the manipulation of nuclear spins. The nuclear spin is an intrinsic property of the particles (protons, neutrons, electrons etc.), noted  $\vec{I}$ . The spin is very closely linked to the magnetism. All substances with  $\vec{I} \neq 0$  are magnetic, so they have the ability to interact with magnetic fields. This interaction is expressed in term of magnetic moment ( $\vec{\mu}$ ). The magnetic moment is proportional to the spin angular momentum (Symmetric theorem) by the equation:

$$\vec{\mu} = \gamma \hbar \vec{I} \quad (2-1)$$

where  $\gamma$  is gyromagnetic ratio (characteristics of each nucleus).

The equation of the motion of a wave function  $|\psi(t)\rangle$  at some time  $t$  for a spin system is given by the Schrödinger equation:

$$\frac{d}{dt} |\psi(t)\rangle = -i\hbar^{-1} \hat{H} \psi(x, t) \quad (2-2)$$

where  $\hat{H}$  is a hermitian operator, called Hamiltonian and represents the energy of the system. The eigenvalues of the Hamiltonian are the energy levels available to the system and the eigenfunctions are the associated wave functions.

Particles with spin  $I$  have  $(2I+1)$  energy sublevels. In the absence of a magnetic field, each sublevel is degenerated and the spins polarizations are uniformly distributed pointing in all directions in space, hence the total magnetic moment of the sample is close to zero. Application of a strong external magnetic field  $B_0$  on the z-axis of the laboratory frame breaks the degeneracy, causing each of the  $(2I+1)$  sublevel to have different energy. This phenomenon is called the Zeeman Effect. The energy separation between the sublevels is called nuclear Zeeman splitting. The interaction between the nuclear spin and the magnetic field is called Zeeman interaction (Figure 2.1).

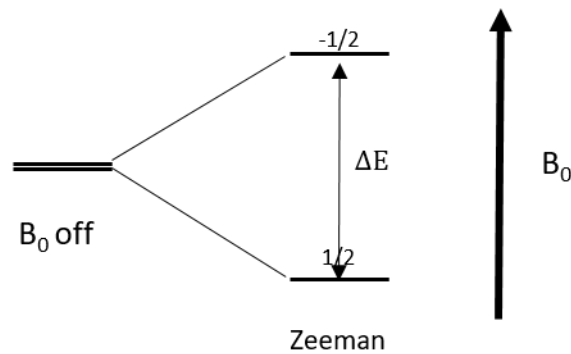


Figure2.1: Zeeman effect for a spin  $I = \frac{1}{2}$ .

The Hamiltonian describes the Zeeman interaction is:

$$\hat{H}_Z = \omega_0 \hat{I}_Z \quad (2-3)$$

where  $\hat{I}_Z$  is the projection of the operator of the spin in the z-axis and  $\omega_0$  is the frequency of the spin precession, given by:

$$\vec{\omega}_0 = -\gamma \vec{B}_0 \quad (2-4)$$

where  $B_0$  is the external magnetic field.

For nuclear spin,  $\omega_0$  is called the nuclear Larmor Frequency. The Larmor frequency has a sign that indicates the sense of the spin precession around the applied field.

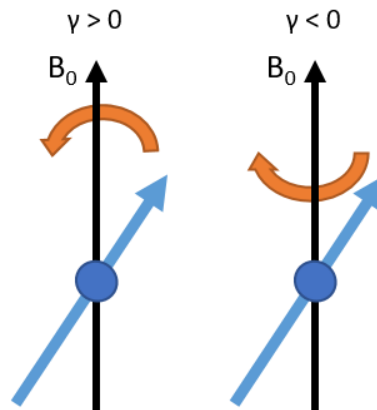


Figure 2.2: Most nuclei have  $\gamma > 0$ , consequently  $\vec{\omega}_0 < 0$  and the precession of the spin is in anticlockwise direction. The nuclei with a negative gyromagnetic ratio (as  $^{15}\text{N}$  and  $^{29}\text{Si}$ ) have a  $\vec{\omega}_0 > 0$ . In this case, the precession is in clockwise direction<sup>3</sup>.

When a magnetic field at the Larmor frequency ( $B_1$ ) (Radio-Frequency (RF) field) of the atom is applied, this interacts with the spins of a sample and there is a perturbation of the equilibrium state of the spins and a creation of a transverse magnetization (perpendicular to the field,  $B_0$ ). When the radio frequency is turned off, the spins resume their precessional motion (Figure 2.2), start to relax and the transverse magnetization decays slowly. The spin magnetization relaxes back to the equilibrium state with a signal oscillating at the Larmor frequency that is registered by the spectrometer via the FID (Free Induction Decay) on the time domain.

During the relaxation process to the equilibrium state, the magnetization  $\vec{M} = (M_X M_Y M_Z)$  is described by:

$$M_X(t) = (M_X(t=0) \cos(\omega_0 t) + M_Y(t=0) \sin(\omega_0 t)) e^{-t/T_2} \quad (2-5)$$

$$M_Y(t) = (M_Y(t=0) \cos(\omega_0 t) - M_X(t=0) \sin(\omega_0 t))e^{-t/T_2} \quad (2-6)$$

$$M_Z(t) = M_Z(t=0)e^{-t/T_1} + M_0(1 - e^{-t/T_1}) \quad (2-7)$$

where  $M_0$  is the magnetization at the equilibrium,  $T_1$  is the time constant describing the relaxation in the z-direction that leads to restoration of the equilibrium state,  $T_2$  is the time constant describing the rate of the decay of the magnetization within the x-y plane.

$T_1$  relaxation is known as *spin-lattice relaxation time constant* or *longitudinal relaxation time constant* and describes the rate of transfer of energy from the nuclear spin system to the neighboring molecules. Instead,  $T_2$  relaxation is known as *transverse relaxation time constant* or *spin-spin relaxation time constant*. These two types of relaxation describe the magnetization behavior (Figure 2.3).

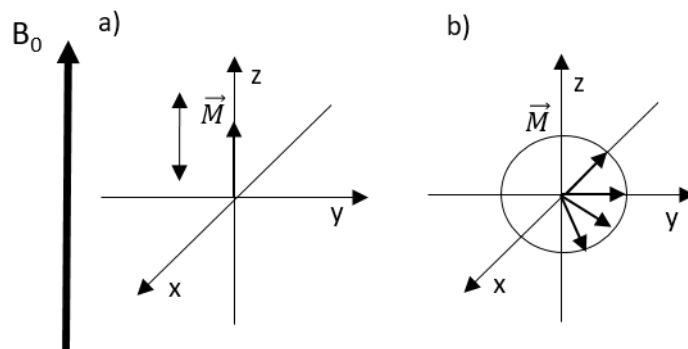


Figure 2.3: Magnetization in the axis for the  $T_1$  relaxation (a) and the  $T_2$  relaxation (b).

## 1.1 The principal interactions in NMR spectroscopy

The real samples studied by NMR are not composed of isolated spins, therefore the interactions that arise between the spin and their environment (internal interactions) are to be taken into consideration. These interactions can be electric or magnetic and the Hamiltonian that summarizes all the total energy of the interaction of the system is given by:

$$\hat{H} = \hat{H}_Z + \hat{H}_i \quad (2-8)$$

where  $H_z$  is the Hamiltonian for the Zeeman interaction and the  $H_i$  for all the internal interactions of the spin system.

In usual NMR experiments, the Zeeman interaction is several orders of magnitude larger than the other interactions, which can therefore be seen as perturbation of the Zeeman interaction.

The Hamiltonian of the internal interaction is given by:

$$\hat{H}_i = \hat{H}_{CS} + \hat{H}_{DD} + \hat{H}_J + \hat{H}_Q \quad (2-9)$$

where  $\hat{H}_{CS}$  is the Hamiltonian of the Shielding interaction,  $\hat{H}_{DD}$  is the Hamiltonian of the direct dipole dipole (D) coupling interaction,  $\hat{H}_J$  is the Hamiltonian of the indirect spin-spin (J) coupling interaction and the  $\hat{H}_Q$  is the Hamiltonian for the quadrupolar interaction.

Interactions	Nature	Information	Order of Magnitude (Hz)	Dependence from magnetic field	MAS
Zeeman	Interaction with magnetic field	Nucleus selection	$10^7$ - $10^9$	yes	-
Chemical Shielding	Modification of the magnetic field by the electrons	Neighboring environment and orientation	$\sim 0$ - $10^4$	yes	CSA is averaged out
J-Coupling	Interaction spin-spin by chemical bond	Chemical bonds and distances	$\sim 0$ - $10^5$	no	The anisotropic part is averaged out
Dipolar Coupling	Interaction spin-spin by the space	Spatial proximities and distances	$\sim 0$ - $10^4$	no	It is averaged out
Quadrupolar Coupling	Interaction of quadrupolar moment with the electric magnetic field	Geometry and local symmetry	$\sim 0$ - $10^6$	No for the 1 <sup>st</sup> order; Yes for the 2 <sup>nd</sup> order	The 1 <sup>st</sup> order is averaged out

Table 2-1: Summary of the principal interactions in NMR spectroscopy.

A description of these different interactions is given below.

### 1.1.1 Shielding interaction

When a molecule is placed in a magnetic field, the electrons develop a magnetic field, that it is called induced field ( $\vec{B}$ ). And it is given by:

$$\vec{B} = \vec{B}_0(1 - \sigma) \quad (2-10)$$

where  $\sigma$  is the shielding tensor that is mathematically represented by a matrix of 3x3 (three dimensions of space). Only the diagonal values are important in NMR, due to the fact that in the principal axes system (PAS) the off-diagonal tensor elements are all equal to zero.

The shielding interaction has an isotropic component that expresses the average chemical surrounding of a spin and anisotropy component, which reflects the geometry of the chemical surrounding of the spin in a solid (Figure 2.4). The isotropic component is given by:

$$\sigma_{iso} = \frac{1}{3} (\sigma_{XX} + \sigma_{YY} + \sigma_{ZZ}) \quad (2-11)$$

The Chemical Shift Anisotropy (CSA), that quantifies the deviation from the isotropic value, is described by:

$$\sigma_{CSA} = \sigma_{ZZ} - \sigma_{iso} \quad (2-12)$$

with the convention:  $|\sigma_{YY} - \sigma_{iso}| \leq |\sigma_{XX} - \sigma_{iso}| \leq |\sigma_{ZZ} - \sigma_{iso}|$ , the different components of the shielding interaction are depicted.

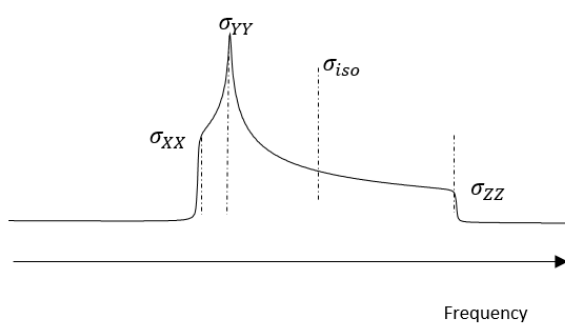


Figure 2.4: Visual representation of the different components of the shielding interaction.

The difference between the other two principal values is quantified by the asymmetry  $\eta_{CS}$ :

$$\eta_{CS} = \frac{(\sigma_{XX} - \sigma_{YY})}{\sigma_{iso}} \quad (2-13)$$

Experimentally, the spectrometer is able to measure frequencies of precession and not directly shielding tensor. Therefore, it is important to define the chemical shift of a nucleus  $i$  ( $\delta_i$ ):

$$\delta_i(\text{in ppm}) = \frac{\nu_i - \nu_{ref}}{\nu_{ref}} 10^6 \quad (2-14)$$

where  $\nu_i$  and  $\nu_{ref}$  are the frequencies of precession of the nucleus and the reference, respectively<sup>4</sup>.

It is possible to define the chemical shift starting, also, from the shielding tensor:

$$\delta_i = \sigma_{ref} - \sigma_i \quad (2-15)$$

where  $\sigma_{ref}$  is the shielding tensor of the reference and  $\sigma_i$  is the shielding tensor of the nucleus  $i$ .

The Hamiltonian of the Chemical Shift (CS) is:

$$\widehat{H}_{CS} = \gamma I_z B_0 \left[ \sigma_{iso} + \frac{\sigma_{CSA}}{2} (3 \cos^2 \theta - 1 + \eta_{CS} \sin^2 \theta \cos 2\phi) \right] \quad (2-16)$$

where  $\theta$  and  $\phi$  are the polar angles and  $\gamma$  is the gyromagnetic ratio of the nucleus.

One can notice that this interaction is proportional to the external magnetic field  $B_0$  and that the anisotropic parameter of the CS is proportional to the  $3\cos^2\theta - 1$ . This equation is going to be zero, when the angle  $\theta$  will be equal to the Magic Angle (Section 1.2).

### 1.1.2 Indirect spin-spin ( $J$ ) coupling interaction

It is an intramolecular interaction of the nuclear spin with each other with the involvement of the electron. If the chemical shift indicates the local electronic environment, the  $J$ -coupling (Figure 2.5) gives a spectral manifestation of the chemical bond. The measure of the  $J$ -coupling between two spins is possible only if they are linked together through bonds. Usually,  $J$ -coupling are small in the range of few Hertz. The Hamiltonian for a  $J$ -coupling between two nuclei  $i$  and  $s$  is given by:

$$\widehat{H}_J = 2\pi\widehat{I}_i J_{is} \widehat{I}_s \quad (2-17)$$

where  $J_{is}$  is the  $J$ -coupling tensor, a 3x3 real matrix.

Similar to the nuclear magnetic shielding interaction, the  $J$  coupling Hamiltonian consists of a non-zero isotropic ( $J_{iso}$ ) and anisotropic ( $\Delta J$ ) component. In solution, rapid molecular tumbling averages out the anisotropic contribution, and the isotropic component gives rise to the resonance splitting that is well known in solution phase NMR. In a solid, the anisotropic portion is preserved; nevertheless, it is difficult to measure since it is often small and inseparable from dipolar coupling interaction.

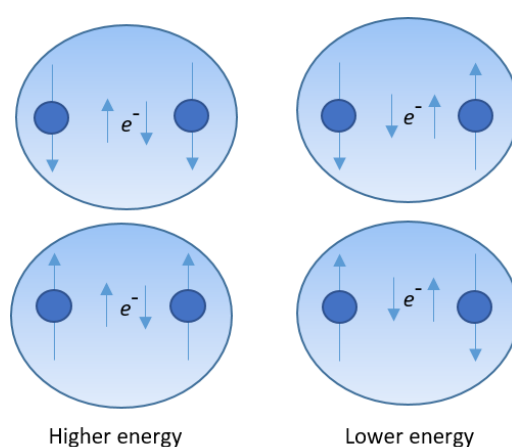


Figure 2.5: Schematic representation of the  $J$ -coupling interaction between two nuclei<sup>3</sup>.

### 1.1.3 Direct dipole-dipole ( $D$ ) coupling interaction

The  $D$ -coupling interaction (Figure 2.6) is a direct magnetic interaction of the nuclear spin with each other. This is also called through-space dipole-dipole coupling and it is a mutual interaction that can be either intramolecular or intermolecular.

Each nuclear spin generates a magnetic field. A second nuclear spin interacts with this magnetic field. At the same time, the first nuclear spin also feels the field generated by the second one. The fields between the nuclear spins propagate through the space, without the involving of the electrons.

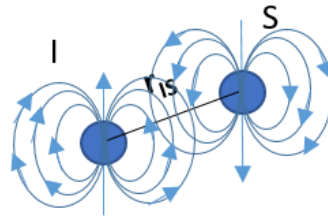


Figure 2.6: Schematic representation of the  $D$ -coupling interaction between two nuclei.

The Hamiltonian of the dipolar heteronuclear interaction between two nuclei  $i$  and  $s$  is:

$$\hat{H}_{DD}^{Hetero} = -d(3 \cos^2 \theta - 1) \hat{I}_{iZ} \hat{I}_{sZ} \quad (2-18)$$

where  $d$  is the dipolar coupling constant which is equal to:

$$d = \frac{\mu_0 \gamma_i \gamma_s}{4\pi r_{is}^3} \hbar \quad (2-19)$$

where  $\mu_0$  is the permeability in the vacuum,  $\hbar$  is the reduced Planck's constant,  $\gamma_i$  and  $\gamma_s$  are the gyromagnetic ratio of the two nuclei and  $r_{is}$  is the internuclear radius.

In the case of two spins of the same isotropic species (homonuclear case) is:

$$\hat{H}_{DD}^{Homo} = \frac{1}{2} d(3 \cos^2 \theta - 1) (\hat{I}_{iZ} \hat{I}_{sZ} - \hat{I}_i \hat{I}_s) \quad (2-20)$$

In both cases, the dipolar coupling depends on the molecular orientation.

In addition, this interaction is proportional to the  $3 \cos^2 \theta - 1$ , as the  $\hat{H}_{DD}^{Homo}$  is going to be zero at the magic angle.

#### 1.1.4 Quadrupolar coupling interaction

More of the 75% of the nuclei are characterized by a spin with  $I > \frac{1}{2}$ . (Figure 2.7) and they are called quadrupolar nuclei.

Figure 2.7: Periodic Table of elements. In color, the nuclei that can be observed by NMR spectroscopy ( $I \geq \frac{1}{2}$ ). Nuclei with  $I > \frac{1}{2}$  are called “quadrupolar nuclei”.

The quadrupolar interaction involves:

- a nuclear property: quadrupolar moment ( $Q$ ) of the nucleus (intrinsic property)
- a molecular property: Electric Field Gradient (EFG) created by the local charge distribution.

The nuclear quadrupolar coupling Hamiltonian,  $\hat{H}_Q$ , is:

$$\hat{H}_Q = \frac{eQ}{2I(2I - 1)\hbar} \hat{V} \hat{I}^2 \quad (2-21)$$

where  $e$  is an elemental charge and  $V$  is the tensor of EFG, having three values ( $V_{xx}$ ,  $V_{yy}$ ,  $V_{zz}$ ).

In solution, the quadrupolar coupling interaction has no influence in the resonance frequency.

In solid-state NMR, this interaction is important and two parameters are used:

- the quadrupolar coupling constant ( $C_Q$ ), in the order of MHz, that is expressed by the equation:

$$C_Q = \frac{eQV_{zz}}{h} \quad (2-22)$$

- the asymmetric parameter,  $\eta_Q$  (value between 0 and 1), given by:

$$\eta_Q = \frac{V_{XX} - V_{YY}}{V_{ZZ}} \quad (2-23)$$

Due to the large size of this interaction, the  $\hat{H}_Q$  can be divided in two parts:

$$\hat{H}_Q = \hat{H}_Q^{(1)} + \hat{H}_Q^{(2)} \quad (2-24)$$

where  $(\hat{H}_Q^{(1)})$  and  $(\hat{H}_Q^{(2)})$  are the first and second order terms of the quadrupolar interaction, respectively.

The effect of this interaction on the spectra depends on its magnitude in comparison to the Zeeman interaction (Figure 2.8). When the quadrupolar interaction is much smaller than the Zeeman one, only the first –order quadrupolar Hamiltonian is sufficient. When the quadrupolar interaction is larger, the second-order term has to be used.

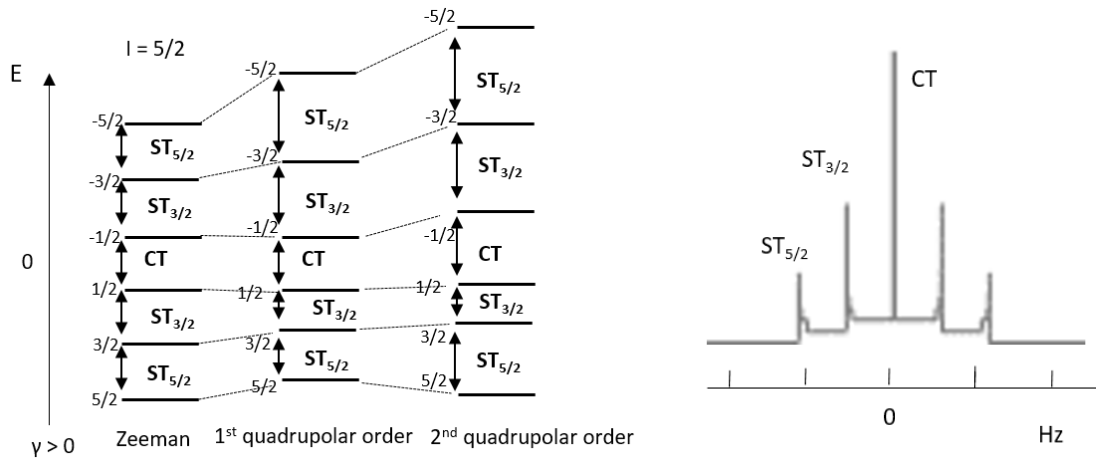


Figure 2.8: Effect of 1<sup>st</sup> and 2<sup>nd</sup> quadrupolar order interactions on the Zeeman energy level for a spin-5/2. (CT= Central Transition; ST= Satellite Transition).

The first-order quadrupolar interaction is not dependent on the external magnetic field and perturbs the Zeeman energy level only on the satellite transitions (STs).

In the case of a uniaxial electric field gradient tensor ( $\eta_Q = 0$ ), the first-order quadrupolar coupling is given by:

$$\omega_Q^{(1)} = \frac{3\pi C_Q}{I(2I-1)} \frac{1}{2} (3 \cos^2 \theta_Q - 1) \quad (2-25)$$

where  $\theta_Q$  is the angle between the z-axis of the EFG tensor and the external magnetic field.

Therefore, the dependence of the equation to the  $3\cos^2\theta-1$ , gives that the first-order quadrupolar interaction will be zero at the magic angle.

On the contrary, the second-order quadrupolar interaction perturbs all the transitions and it is inversely proportional to the external magnetic field,  $B_0$  and is given by:

$$\begin{aligned} \omega_Q^{(2)} = & \frac{\omega_Q^2}{6\omega_0} (I(I+1) - \frac{3}{4}) \left[ \left( -\frac{27}{8} + \frac{9}{4}\eta_Q \cos 2\theta - \frac{3}{8}\eta_Q^2 \cos^2 2\phi \right) \cos^4 \beta \right. \\ & + \left( -\frac{30}{8} + \frac{\eta_Q^2}{2} - 2\eta_Q \cos 2\phi \right) \cos^2 \theta \\ & \left. + \left( -\frac{3}{8} + \frac{\eta_Q^2}{3} - \frac{\eta_Q}{4} \cos 2\phi - \frac{3}{8}\eta_Q^2 \cos^2 2\phi \right) \right] \end{aligned} \quad (2-26)$$

## 1.2 Magic-Angle Spinning (MAS)

In a solid powder sample, each part of it has a different orientation relative to the external magnetic field.

The inhomogeneity is due to the dipolar interaction, chemical shift anisotropy and, for the spin with  $I > \frac{1}{2}$ , the quadrupolar interaction. This leads to a broad spectrum due to an overlapping of the signals.

Andrew *et al.*<sup>5</sup> showed that a rotation of the sample around an angle of 54.74° (Magic-Angle) with respect the external magnetic field  $B_0$ , leads to an increase of the resolution of the spectra.

The magic-angle is given by:

$$P_2(\cos \theta) = \frac{1}{2} (3 \cos^2 \theta - 1) = 0 \quad (2-27)$$

$$\theta = 54.74^\circ$$

$P_2 \cos \theta$  is a Legendre polynomial of 2<sup>nd</sup> degree.

The technique of spinning the sample in a rotor at the magic-angle is called Magic-Angle Spinning (MAS) (Figure 2.9).

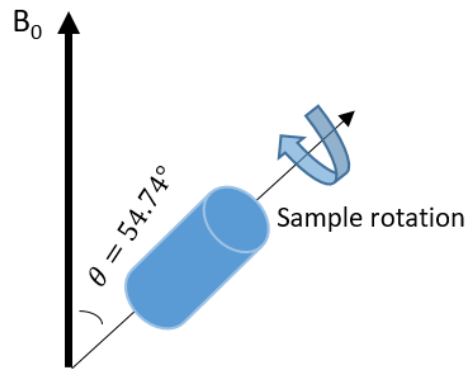


Figure 2.9: Representation of the Magic-angle spinning.  $\theta$  corresponds to the magic-angle.

Thanks to this technique the dipolar interaction, chemical shift anisotropy and the first order term of the quadrupolar interaction can be averaged out since their contributions to solid-state NMR spectra are scaled by  $(3 \cos^2 \theta - 1)$ , where  $\theta$  is the angle between the  $B_0$  and the z-axis of the relevant NMR interaction tensor.

If the spinning frequency is large enough, it is possible to obtain spectra with a resolution approach of a liquid state. If the MAS is not sufficiently large compared with the anisotropy interaction, the spectrum will contain extra peaks, called *Spinning Sidebands (ssb)* (Figure 2.10).

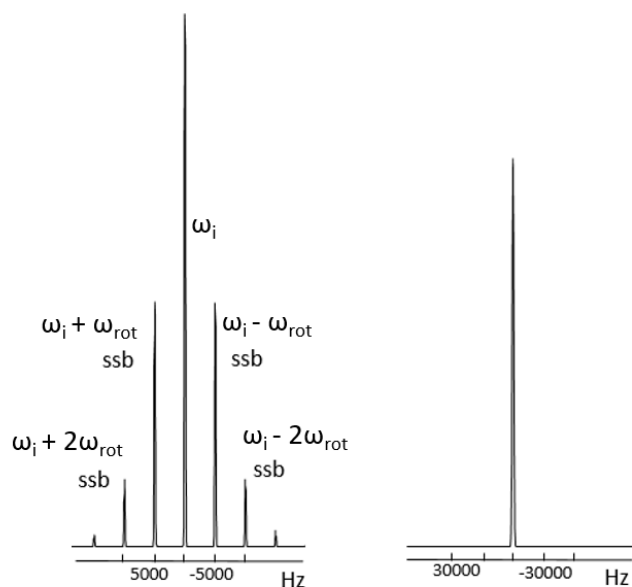


Figure 2.10: MAS NMR spectrum recorded at 5 kHz (left). The presence of the spinning sidebands (ssb) means that higher spinning speed has to be used to average completely the anisotropy interaction, as shown on the right with a MAS NMR spectrum recorded at 30 kHz. One can notice that the ssb peaks appeared at frequencies given by  $\omega_i \pm k\omega_{rot}$ . Where  $\omega_i$  is the isotropic chemical shift frequency of the nucleus,  $k$  is an integer number and  $\omega_{rot}$  is the spinning frequency.

## 2. Pulse Sequences

All the pulse sequence reported below have been utilized under Magic-Angle spinning conditions in order to improve spectral resolution and sensitivity.

### 2.1 One-pulse

The simplest experiment that can be realized is the application of a single radiofrequency (RF) pulse on a single channel (S), followed by a signal detection (Figure 2.11).

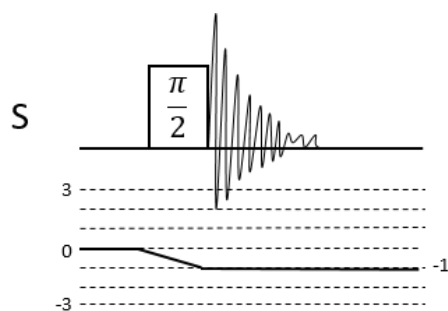


Figure 2.11: Scheme of the One-pulse sequence.

Heteronuclear decoupling can be applied during signal acquisition to remove dipolar and scalar interactions. A high power RF is required to average out the effect of the dipolar coupling, while to remove the  $J$ -coupling effect only a low power decoupling can be used.

Choice of decoupling for the different experiments:

- Decoupling during acquisition: **SPINAL-64 (Small Phase INcrementation Alteration with 64 steps)**<sup>6,7</sup>, designed by changing the phase angles in the **TPPM**<sup>8</sup>(**Two Pulses Phase Modulation**) sequence stepwise and then combining the basic cycles into supercycles (Figure 2.12). This decoupling sequence is particularly robust with respect to radio-frequency (RF) inhomogeneity and pulse width imperfection and has better compensation for resonance offsets, arising from the compensatory super cycles<sup>9</sup>.
- Decoupling during recoupling experiment: **CW (Continuous Waves)**<sup>10,11</sup>, consisting on the application of a continuous RF pulse at the frequency of the non-detected nucleus. The performance of the decoupling sequence is limited by the maximum power that the probe can tolerate. More important CW decoupling limits interactions between rotor synchronized recoupling schemes and finite pulses of decoupling.

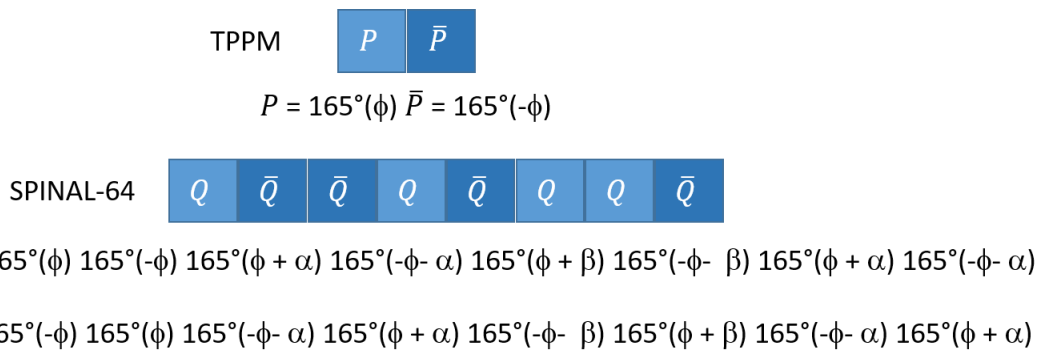


Figure 2.12: Decoupling sequence SPINAL-64, based on TPPM and composed by eight Q pulses, characterized by phases, with  $\alpha=5^\circ$   $\beta=10^\circ$  and  $\phi=10^\circ$ .

## 2.2 Cross Polarization for spin-1/2

The **cross-polarization (CP)**<sup>12</sup> (Figure 2.13a) is a very useful sequence, with which it is possible to resolve two problems of ssNMR:

- the low sensitivity of some nuclei due to their low natural abundance, with a theoretic gain of signal of  $\frac{|\gamma_I|}{|\gamma_S|}$  (such as  $\frac{|\gamma_{1H}|}{|\gamma_{13C}|} \cong 4$ , for example).

- the long  $T_1$  of rare nuclei.

Classical description of CP is based on the concept of spin-temperature or spin-thermodynamics<sup>13</sup>. A  $90^\circ$  pulse is applied on the I channel (abundant spin), followed by a spin-lock pulse. As the magnetization is larger than would be expected from Boltzmann statistics, the system is said to have a low spin-temperature (subcooled state). Simultaneously, a second spin-lock pulse is applied on the S channel (less abundant spin). Since no net magnetization is present, the system is said to be in a high spin-temperature. If the two spin-lock pulses (contact pulses) are adjusted to have identical nutation frequencies, the magnetization is transferred from the abundant to the less abundant spin, for a period called contact time ( $t_{cp}$ ). This is referred to as the Hartmann-Hahn matching condition<sup>14</sup>. In the thermodynamic point of view, the Hartmann-Hahn condition brings the hot and cold spin-reservoirs

into thermal contact, allowing the flow of polarization and the equilibration of the spin-temperature. Under MAS conditions, to have an efficient transfer, the RF fields applied on both I and S channels should fulfill the equation<sup>14</sup>:

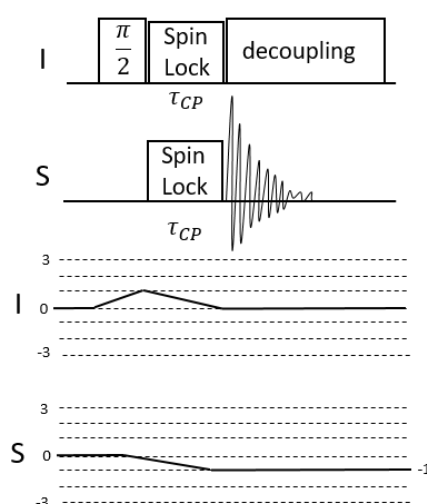
$$|\omega_S| = |\omega_I| \pm n\omega_{rot} \quad (2-28)$$

with  $n = 1, 2$  and  $\omega_{rot}$  is MAS frequency.

A decoupling may be applied to I channel, during acquisition on S channel, to remove heteronuclear dipolar interactions.

The CP is not a quantitative experiment, because of the signal loss due to the  $T_1$  relaxation of I nucleus. To overcome this, the **multiple Cross Polarization (multi-CP)**<sup>15</sup> (Figure 2.13b) can be used. The approach of this sequence is to repeat blocks of CP separated by periods of  $\tau$  duration, during which the magnetization on I channel can recover to a near-equilibrium value. During  $\tau$ , I magnetization undergoes  $T_1$  relaxation towards its thermal-equilibrium value, which reverses most of the I magnetization loss by  $T_1$  during the preceding CP period. In addition, the local magnetization loss of I spins near S due to the polarization transfer to S will be canceled by I spin diffusion from the surrounding spins. This allows acquiring a quantitative spectrum.

a)



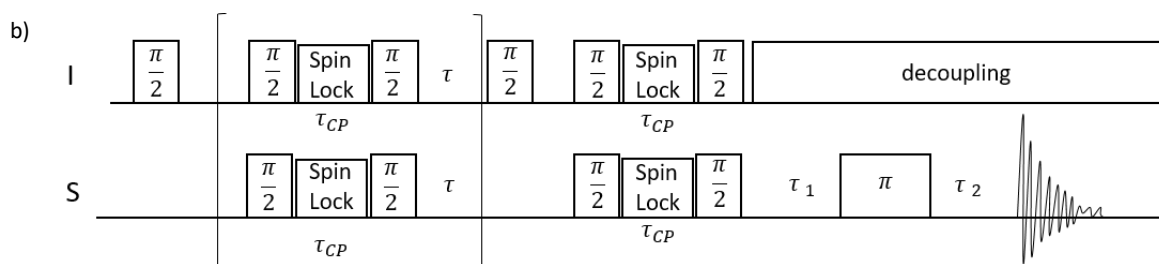


Figure 2.13: Scheme of the CP (a), multi-CP (b) pulse sequences.

### 2.3 Triple resonance Cross-Polarization

The **Triple resonance Cross Polarization (TCP)**<sup>16,17</sup> (Figure 2.14), in which the transfer of the polarization is done sequentially to two nuclei, was used. This experiment allows to filter the signal obtained by a heteronuclear spin and to determine the connectivity between the spins, thanks to experiments with different contact time.

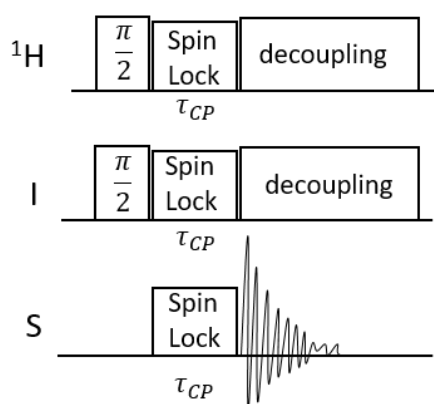


Figure 2.14: Scheme of the TCP pulse sequence.

### 2.4 Spin Echo

The **spin echo** pulse sequence<sup>18</sup> (Figure 2.15) is characterized by a 180° pulse that allows to refocalize of the magnetization after a time,  $\tau$ . This sequence is used in particular to remove the probe

signal that leads to a distortion of the baseline (mostly for  $^1\text{H}$  and  $^{19}\text{F}$  NMR), but which is a non-coherent signal, hence is not refocused.

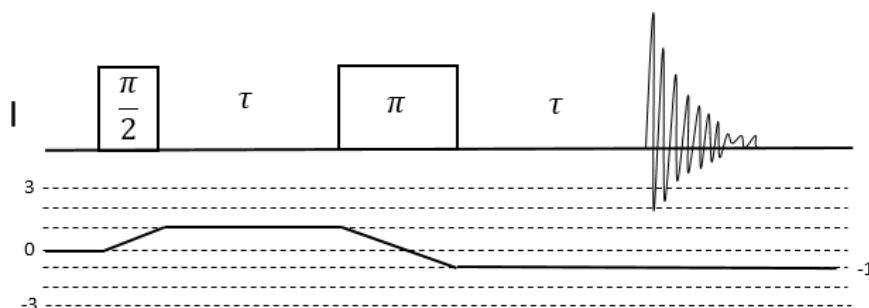


Figure 2.15: Scheme of the Echo pulse sequence.

## 2.5 MQMAS

Second order quadrupolar interaction not averaged by MAS, need additional technique to gain resolution. The **Multi-Quantum MAS (MQMAS)** experiment (Figure 2.16) allows separating the isotropic interactions from the anisotropic interactions in a quadrupolar nucleus. The resulting 2D MQMAS NMR spectrum is composed of a classic MAS dimension (horizontal dimension) and an isotropic dimension (vertical dimension) in which the quadrupolar effect is suppressed. Several variants of MQMAS experiments have been reported<sup>19,20</sup>.

In this thesis, for the study of  $^{27}\text{Al}$  species, the **MQMAS Z-filter** pulse sequence was used<sup>21</sup>. This experiment is composed of three pulses. The first one leads to the excitation of the triple-quantum (3Q) coherences, which evolves during  $t_1$ . The second pulse convert the 3Q to zero-quantum coherence, and the third pulse is a  $90^\circ$  pulse selective on the central transition that allows the acquisition.

The Z-filter method is robust and efficient because the dispersive component in the 2D spectrum, noticed in other type of MQMAS experiments<sup>21</sup>, are cancelled without any pulse setting, thanks to the

symmetrical pathways. Moreover, the pulse optimization is easier and any missetting of the three pulses is much less critical since efficiencies in both pathways always remain equal.

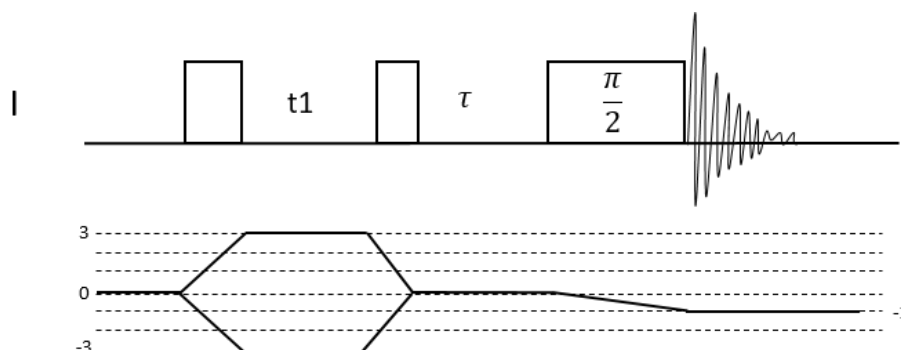


Figure 2.16: Scheme of the MQMAS pulse sequence.

## 2.6 Exchange experiments

The **Exchange spectroscopy (EXSY)** experiment<sup>12</sup> (Figure 2.17) is a two dimensional experiment that gives information about the chemical exchange in a solid. In this experiment, the exchange between regions with different chemical shifts manifests itself in the appearance of cross-peaks between the signals from the sites in exchange.

After an excitation  $90^\circ$  pulse, transverse magnetization evolves during a free variable evolution  $t_1$  period. A  $90^\circ$  pulse creates longitudinal magnetization and during the mixing time, magnetization transfer via chemical exchange can take place. A final  $90^\circ$  proton pulse creates transverse magnetization, which is detected.

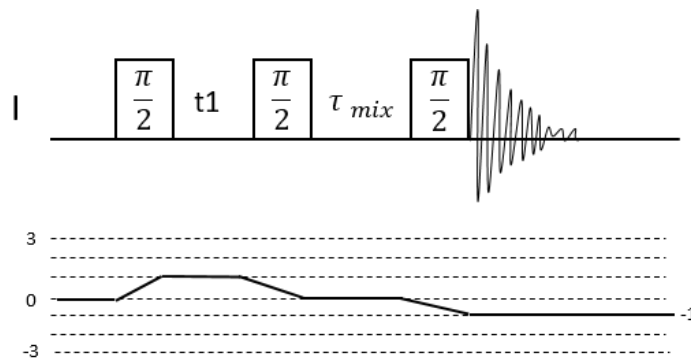


Figure 2.17: Scheme of the EXSY sequence.

During  $\tau_{mix}$ , either true chemical exchange (i.e., atoms physically exchanging positions in a molecule or a solid) or spin diffusion (self or driven) can occur.

The second case exploits the homonuclear dipolar interaction. **Radio-frequency driven dipolar recoupling (RFDR)**<sup>8</sup> sequence (Figure 2.18) was used. The difference with the normal exchange experiment is the presence of a  $180^\circ$  pulse in the middle of the mixing time (that it is divided in two).

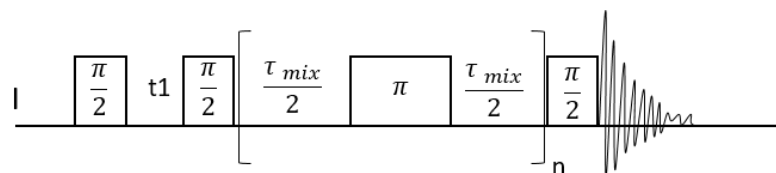


Figure 2.18: Scheme of the RFDR pulse sequence.

It could be interesting to compare the results obtained with the exchange and RFDR (single quantum-single quantum, SQ/SQ) with a DQ-SQ (double quantum-single quantum) pulse sequence (Figure 2.19), as **Back to Back (BABA)**<sup>22</sup>(general DQ/SQ pulse sequence is showed in Figure 2.21). In the SQ/SQ correlation experiment, if magnetization is exchanged between two nuclei during the mixing time, cross peaks between two SQ frequencies are observed. Diagonal signals, mostly consist of non-exchanged magnetization. The magnetization can diffuse farther than 100 nm. In a DQ/SQ

correlation experiment, a pair of  $^1\text{H}$  gives DQ/SQ correlation peaks on the indirect dimension and SQ in the direct dimension. All the correlation that appear in the DQ/SQ spectrum go through the DQ filtering, isolated nuclei do not give any signal at the diagonal lines. Compared to the SQ/SQ spectra, the presence of a diagonal peak clearly shows the autocorrelation between two spins having the same chemical shift. In addition the weaker interaction are truncated by the stronger interaction, so the DQ/SQ correlation appear only between neighboring spins with distance shorter than  $4\text{-}5 \text{ \AA}^{13}$ .

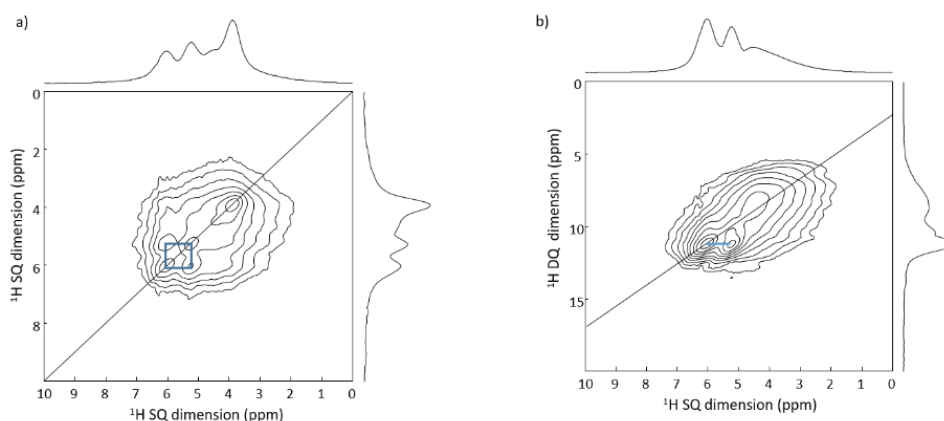


Figure 2.19: 2D  $^1\text{H}$ - $^1\text{H}$  RFDR (a) and BABA (b) NMR experiments of MIL-140, recorded at 30 kHz on 11.6 T spectrometer. One can notice that both experiments show the same correlation peaks.

## 2.7 Double Quantum-Single Quantum (DQ-SQ) correlation experiments

### 2.7.1 INADEQUATE

**INcredible Natural Abundance Double QUAntum Transfer Experiment (INADEQUATE)**<sup>3</sup> is a homonuclear correlation experiment (double quantum-single quantum) through  $J$ -coupling. It gives information about the directly bonded nuclei of the same type.

The pulse sequence used was the **CP-INADEQUATE refocused**<sup>23</sup> (Figure 2.20), characterized an initial CP scheme, instead of the initial  $90^\circ$  pulse. The CP is followed by a  $180^\circ$  pulse after a delay  $\tau$ . The conversion to the double coherence is done by the subsequent  $90^\circ$  pulse and evolves during  $t_1$ . Another  $90^\circ$  pulse converts the double quantum in single quantum coherence. Before the acquisition, a refocusing pulse is applied.

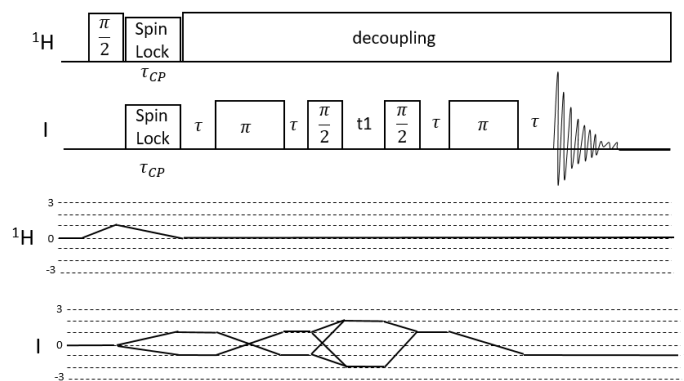


Figure 2.20: Scheme of the INADEQUATE pulse sequence.

### 2.7.2 Double-quantum recoupling experiment

The homonuclear dipolar **Double Quantum-Single Quantum (DQ-SQ) correlation experiment** (Figure 2.21) gives information about the proximities, of two nuclei of the same type, in space. The sequence starts with a cross-polarization to transfer the I-spin magnetization to the nucleus of interest. After a  $90^\circ$  pulse that converts the magnetization into longitudinal one, a DQ excitation pulse sequence (first recoupling block,  $R$ ) of duration  $\tau_{exc}$  is applied to convert the longitudinal magnetization in DQ coherence. The DQ coherences evolve during a time  $t_1$ , and are reconverted into longitudinal magnetization thanks to another recoupling block,  $R$  with duration  $\tau_{rec}$ . A last  $90^\circ$  pulse converts the magnetization into an observable one. The time between the two blocks,  $t_1$  has to be incremented in integer multiples of the rotational period.

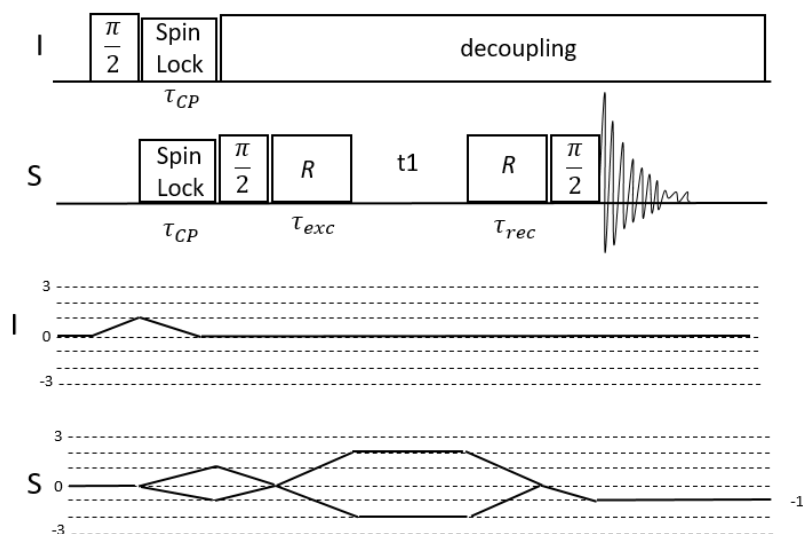


Figure 2.21: Scheme of a general homonuclear recoupling experiment pulse sequence.

Two types of recoupling sequence had used in this thesis:  $S_3$ <sup>24,25</sup> and **SC14**<sup>26</sup>.

In the context of this thesis  $S_3$  for  $^{31}\text{P}$ - $^{31}\text{P}$  correlation experiments, SC14 for  $^{13}\text{C}$ - $^{13}\text{C}$  correlation experiments. These experiments were recorded to try to get some resolution and identify the single resonances belongs to the different parts of the system and to have information about the proximities of the different molecules. Low power is required for RF field of both the recoupling sequence (half of the spinning speed for  $S_3$  and 3.5 times the spinning speed for SC14), allowing the use of fast MAS and the possibility to have high decoupling power on the I channel to avoid heteronuclear interactions. In the SC14, the chemical shifts perturbations are well compensated and it is less dependent of the resonance offset. For this last reason, this sequence was preferred to the  $S_3$  sequence for the  $^{13}\text{C}$ - $^{13}\text{C}$  homonuclear recoupling correlation experiments (large  $^{13}\text{C}$  chemical shift range (~200 ppm)).

## 2.8 D-HMQC

The 2D **Dipolar Heteronuclear Multi-Quantum Correlation (D-HMQC)** experiment (Figure 2.22) is a heteronuclear correlation experiment that allows obtaining a 2D map of the correlation through space between quadrupolar nuclei and spins-1/2. Considering the need of through-space correlation

schemes performed at high field in materials science, it appears that the limitation of CP for quadrupolar nuclei, as the strong offset irradiation dependence, had to be overcome using different techniques, such as *D*-HMQC<sup>27</sup>.

The *D*-HMQC is characterized by the reintroduction of the dipolar interaction thanks to a series of 180° pulses synchronized with the MAS (**Recoupling**). An echo sequence takes place in the I channel, while on the S channel the two recoupling blocks (*R*) are separated by a delay *t*<sub>1</sub> between two 90° pulses. The signal is acquired on the I channel.

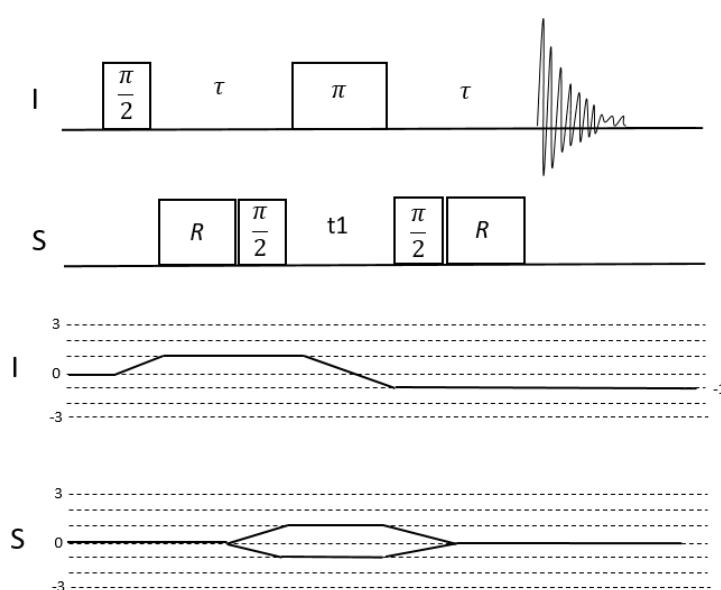


Figure 2.22: Scheme of the *D*-HMQC pulse sequence.

The recoupling sequence used is  $R4_1^{2,28,29}$ .  $R4_1^2$  is a symmetry-based sequence, that requires RF field strength to be only twice the spinning frequency. It is composed of four pulses with alternating phases ( $\pm 90^\circ$ ) per rotor period and has a very robustness to RF inhomogeneities. This sequence is very well suited to recouple heteronuclear dipolar interactions in the presence of strong  $^1\text{H}$  homonuclear dipolar couplings. It is also demonstrated that HMQC is useful for correlations between spin-1/2 (as  $^1\text{H}$ ,  $^{13}\text{C}$  and  $^{31}\text{P}$ ) and quadrupolar nuclei (as  $^{27}\text{Al}$ ), as only two pulses are applied on the quadrupolar nuclei, alleviating the sensitivity loss associated to large quadrupolar coupling. Moreover, it is very

easy and fast to optimize<sup>27,29,30</sup>. In Figure 2.23, 2D CPMAS and HMQC experiments, recorded on MIL-100(Al), are shown. One can see that in the HMQC experiment, the mobile protons of the water are not visible, on the other hand in the CP experiment both correlation with <sup>1</sup>H resonance of the aromatic ring of the MIL-100(Al) and of the water are detected. This can be another advantage to study dipolar interaction without the influence of mobile protons, which can have the same chemical shift of other <sup>1</sup>H resonances of interest.

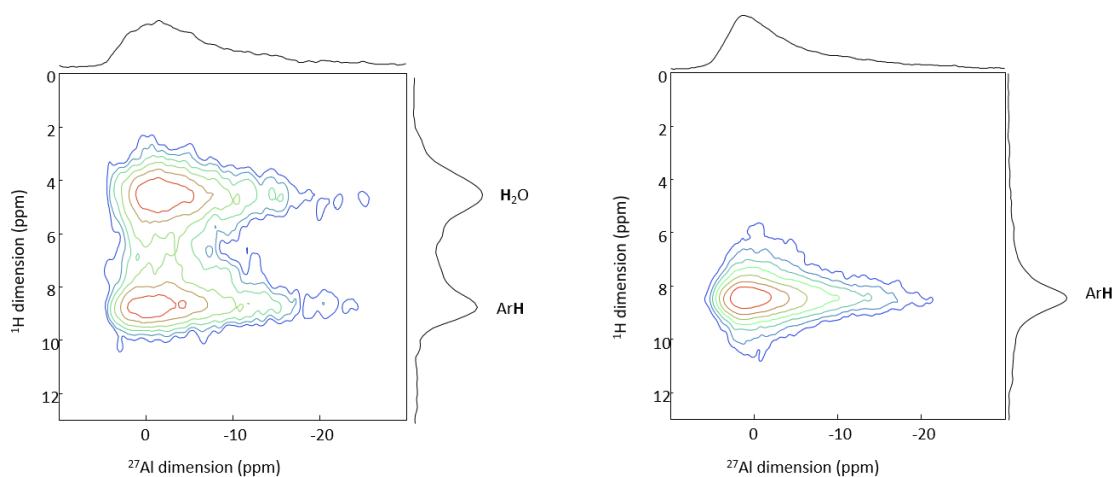


Figure 2.23: <sup>27</sup>Al-<sup>1</sup>H 2D CP (contact time of 3 ms, recorded at 10 kHz on a 9.4 T spectrometer) (left) and HMQC (recoupling time of 1.25 ms, recorded at 60 kHz on a 20 T spectrometer) (right) MAS NMR spectra of MIL-100(Al).

## 2.9 S-RESPDOR

The most popular NMR method to determine distance is the **Rotational Echo Double Resonance (REDOR)**<sup>31</sup>. This technique consists of rotor-synchronized  $\pi$ -pulses, which invert the spin magnetization, requiring RF fields larger than internal spin interactions. This condition is usually fulfilled for spin-1/2 nuclei, but, for the nuclei with spin  $I > 1/2$ , the quadrupole interaction generally exceeds the RF field<sup>32</sup>. Another technique has to be used for quadrupolar nuclei.

The **Symmetric-based Resonance Echo Saturation Pulse Double-Resonance (S-RESPDOR)**<sup>32,33</sup> experiment (Figure 2.24) is a method used to measure internuclear distance between spin-1/2 and quadrupolar nuclei. This sequence employs a saturation pulse on the quadrupolar channel S and a symmetric based recoupling scheme on the observed I channel (spin-1/2). A CP sequence is added, to

take advantage of the shorter  $T_1$  of the proton. The recoupling sequence used is  $R4_1^2$ . The recoupling block is split into two parts of equal duration  $\tau/2$ .

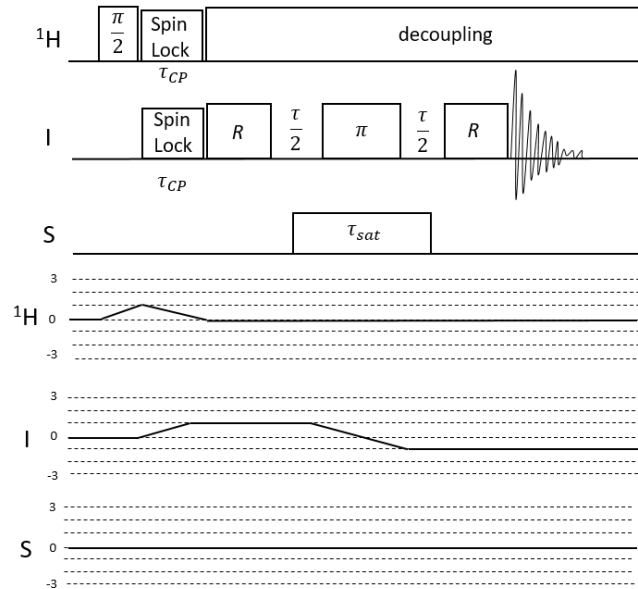


Figure 2.24: Scheme of the S-RESPDOR pulse sequence.

The distance determination requires the acquisition of two signals as function of the dipolar time  $\tau$ . One (S) recorded with the sequence showed in the figure 2.24 and a reference signal recorded omitting the saturation block on the quadrupolar nucleus ( $S_0$ ). The influence of dipolar interaction is measured via normalization of the S signal with the reference signal,  $S_0$  through the ratio:

$$\Delta S/S_0 = (S_0 - S)/S_0 \quad (2-29)$$

In Figure 2.25 is showed an example of RESPDOR curve.

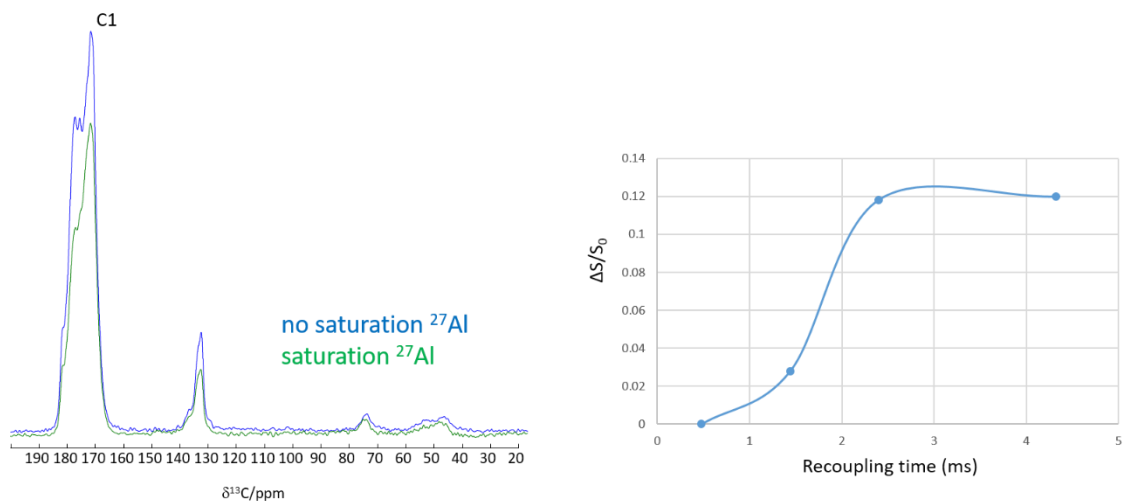


Figure 2.25: Example of  $^{27}\text{Al}$   $\{^{13}\text{C}\}$  RESPDOR experiment (recoupling time 2.4 ms, recorded at 12.5 kHz on a 9.4 T spectrometer) (left) and RESPDOR experimental curve of C1  $^{13}\text{C}$  resonance (right).

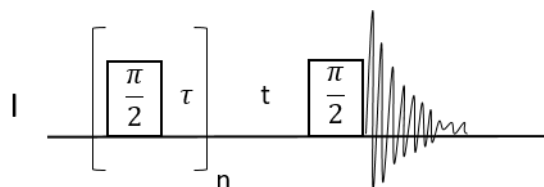
## 2.10 Measurement of relaxation times

### 2.10.1 $T_1$

The experiment used for the measurement of the **spin-lattice relaxation time  $T_1$**  is the Saturation-Recovery (Figure 2.26). It is composed by a series  $90^\circ$  pulses (saturation), which allows to annul the magnetization and, after a delay of recovery  $\tau$ , another  $90^\circ$  pulse. And the resulting acquisition of the signal.

The  $T_1$  is given by:

$$M_Z(t) = M_0(1 - e^{-t/T_1}) \quad (2-30)$$



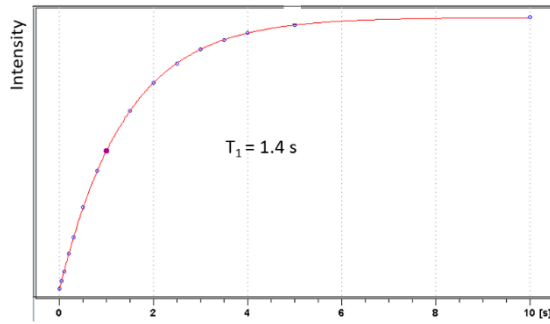


Figure 2.26: Scheme of the Saturation-Recovery pulse sequence (top) and example of  $^1\text{H}$   $T_1$  measurement curve of Cefadroxyl drug(bottom).

### 2.10.2 $T_2$

The measurement of the **spin-spin relaxation time  $T_2$**  is given using an Echo sequence, detailed in section 2.4. The experiment is repeated with different value of  $\tau$  and the equation to determine  $T_2$  is

$$M_Y(t) = M_0 e^{-t/T_2} \quad (2-31)$$

In Figure 2.27 is showed an example of  $T_2$  measurement curve.

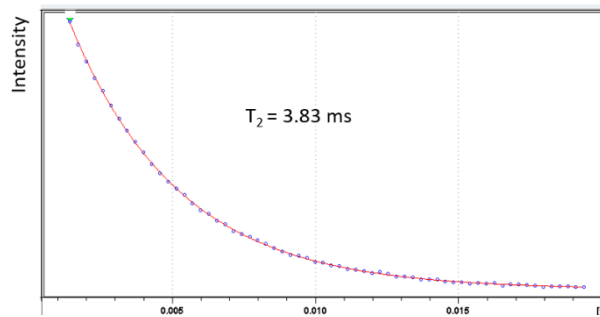


Figure 2.27: Example of  $^{27}\text{Al}$   $T_2$  measurement curve of nanoMIL-100(Al).

## References

- (1) Martineau-Corcus, C. NMR Crystallography: A Tool for the Characterization of Microporous Hybrid Solids. *Curr. Opin. Colloid Interface Sci.* **2018**, *33*, 35–43.
- (2) Gossert, A. D.; Jahnke, W. NMR in Drug Discovery: A Practical Guide to Identification and Validation of Ligands Interacting with Biological Macromolecules. *Prog. Nucl. Magn. Reson. Spectrosc.* **2016**, *97*, 82–125.
- (3) Levitt, M. H. *Spin Dynamics*, Second.; Wiley, 2008.
- (4) Keeler, James. *Understanding NMR Spectroscopy*; Wiley, 2012.
- (5) Andrew, E.R.; Bradbury, A.; Eades, R.G. Removal of Dipolar Broadening of Nuclear Magnetic Resonance Spectra of Solids by Specimen Rotation. *Nature* **1959**, *183*, 1802–1803.
- (6) Fung, B. M.; Khitrin, A. K.; Ermolaev, K. An Improved Broadband Decoupling Sequence for Liquid Crystals and Solids. *J. Magn. Reson.* **2000**, *142* (1), 97–101.
- (7) Bräuniger, T.; Wormald, P.; Hodgkinson, P. Improved Proton Decoupling in NMR Spectroscopy of Crystalline Solids Using the S PINAL -64 Sequence. *Monatshefte Fr Chem. Chem. Mon.* **2002**, *133* (12), 1549–1554.
- (8) Bennett, A. E.; Rienstra, C. M.; Griffiths, J. M.; Zhen, W.; Lansbury, P. T.; Griffin, R. G. Homonuclear Radio Frequency-Driven Recoupling in Rotating Solids. *J. Chem. Phys.* **1998**, *108* (22), 9463–9479.
- (9) Comellas, G.; Lopez, J. J.; Nieuwkoop, A. J.; Lemkau, L. R.; Rienstra, C. M. Straightforward, Effective Calibration of SPINAL-64 Decoupling Results in the Enhancement of Sensitivity and Resolution of Biomolecular Solid-State NMR. *J. Magn. Reson.* **2011**, *209* (2), 131–135.
- (10) Ernst, R. R.; Bodenhausen, G.; Wokaum, A. *Principles of Nuclear Magnetic Resonance in One and Two Dimensions*; Clarendon Press., 1987.
- (11) Reich, H. J.; Jautelat, M.; Messe, M. T.; Weigert, F. J.; Roberts, J. D. Nuclear Magnetic Resonance Spectroscopy. Carbon-13 Spectra of Steroids. *J. Am. Chem. Soc.* **1969**, *91* (26), 7445–7454.
- (12) *Solid-State NMR Spectroscopy Principles and Applications: Duer/Solid-State*; Duer, M. J., Ed.; Blackwell Science Ltd: Oxford, UK, 2001.
- (13) Miyoshi, T.; Sun, P.; Zhang. *NMR Methods for Characterization of Synthetic and Natural Polymers*; Royal Society of Chemistry, 2019.
- (14) Hartmann, S.R.; Hahn, E.L. Nuclear Double Resonance in the Rotating Frame. *Phys. Rev.* **1962**, *128* (5), 2042–2053.
- (15) Johnson, R. L.; Schmidt-Rohr, K. Quantitative Solid-State <sup>13</sup>C NMR with Signal Enhancement by Multiple Cross Polarization. *J. Magn. Reson.* **2014**, *239*, 44–49.
- (16) Akbey, Ü.; Camponeschi, F.; van Rossum, B.-J.; Oschkinat, H. Triple Resonance Cross-Polarization for More Sensitive <sup>13</sup>C MAS NMR Spectroscopy of Deuterated Proteins. *ChemPhysChem* **2011**, *12* (11), 2092–2096.
- (17) Yu, C.; Bourrelly, S.; Martineau, C.; Saidi, F.; Bloch, E.; Lavrard, H.; Taulelle, F.; Horcajada, P.; Serre, C.; Llewellyn, P. L.; Magnier, E.; Devic, T. Functionalization of Zr-Based MOFs with Alkyl and Perfluoroalkyl Groups: The Effect on the Water Sorption Behavior. *Dalton Trans.* **2015**, *44* (45), 19687–19692.
- (18) Hahn, E.L. Spin Echoes. *Phys. Rev.* **1950**, *80* (4), 580–594.
- (19) Medek, A.; Harwood, J. S.; Frydman, L. Multiple-Quantum Magic-Angle Spinning NMR: A New Method for the Study of Quadrupolar Nuclei in Solids. *J. Am. Chem. Soc.* **1995**, *117* (51), 12779–12787.
- (20) Wu, G.; Rovnyak, D.; Griffin, R. G. Quantitative Multiple-Quantum Magic-Angle-Spinning NMR Spectroscopy of Quadrupolar Nuclei in Solids. *J. Am. Chem. Soc.* **1996**, *118* (39), 9326–9332.
- (21) Amoureux, J.-P.; Fernandez, C.; Steuernagel, S. ZFiltering in MQMAS NMR. *J. Magn. Reson. A* **1996**, *123* (1), 116–118.

- (22) Feike, M.; Demco, D. E.; Graf, R.; Gottwald, J.; Hafner, S.; Spiess, H. W. Broadband Multiple-Quantum NMR Spectroscopy. *J. Magn. Reson. A* **1996**, *122* (2), 214–221.
- (23) Borisov, A. S.; Hazendonk, P.; Hayes, P. G. Solid-State Nuclear Magnetic Resonance Spectroscopy: A Review of Modern Techniques and Applications for Inorganic Polymers. *J. Inorg. Organomet. Polym. Mater.* **2010**, *20* (2), 183–212.
- (24) Teymoori, G.; Pahari, B.; Edén, M. Low-Power Broadband Homonuclear Dipolar Recoupling in MAS NMR by Two-Fold Symmetry Pulse Schemes for Magnetization Transfers and Double-Quantum Excitation. *J. Magn. Reson.* **2015**, *261*, 205–220.
- (25) Teymoori, G.; Pahari, B.; Stevenson, B.; Edén, M. Low-Power Broadband Homonuclear Dipolar Recoupling without Decoupling: Double-Quantum  $^{13}\text{C}$  NMR Correlations at Very Fast Magic-Angle Spinning. *Chemical Physics Letters* **2012**, *547*, 103–109.
- (26) Brinkmann, A.; Edén, M.; Levitt, M. H. Synchronous Helical Pulse Sequences in Magic-Angle Spinning Nuclear Magnetic Resonance: Double Quantum Recoupling of Multiple-Spin Systems. *J. Chem. Phys.* **2000**, *112* (19), 8539–8554.
- (27) Tricot, G.; Trébosc, J.; Pourpoint, F.; Gauvin, R.; Delevoye, L. The D-HMQC MAS-NMR Technique. In *Annual Reports on NMR Spectroscopy*; Elsevier, 2014; Vol. 81, pp 145–184.
- (28) Brinkmann, A.; Kentgens, A. P. M. Proton-Selective  $^{17}\text{O}$ - $^1\text{H}$  Distance Measurements in Fast Magic-Angle-Spinning Solid-State NMR Spectroscopy for the Determination of Hydrogen Bond Lengths. *J. Am. Chem. Soc.* **2006**, *128* (46), 14758–14759.
- (29) Levitt, M. H. *Advances in NMR*; Grant, D. M., Harris, R. K., Eds.; Encyclopedia of nuclear magnetic resonance; Wiley: Chichester, 2002; Vol. 9.
- (30) Hu, B.; Trébosc, J.; Amoureux, J. P. Comparison of Several Hetero-Nuclear Dipolar Recoupling NMR Methods to Be Used in MAS HMQC/HSQC. *J. Magn. Reson.* **2008**, *192* (1), 112–122.
- (31) Schaefer, J. “Development of REDOR Rotational-Echo Double-Resonance NMR” by Terry Gullion and Jacob Schaefer [J. Magn. Reson. 81 (1989) 196–200]. *J. Magn. Reson.* **2011**, *213* (2), 421–422.
- (32) Chen, L.; Lu, X.; Wang, Q.; Lafon, O.; Trébosc, J.; Deng, F.; Amoureux, J.-P. Distance Measurement between a Spin-1/2 and a Half-Integer Quadrupolar Nuclei by Solid-State NMR Using Exact Analytical Expressions. *J. Magn. Reson.* **2010**, *206* (2), 269–273.
- (33) Lu, X.; Lafon, O.; Trébosc, J.; Amoureux, J.-P. Detailed Analysis of the S-RESPDOR Solid-State NMR Method for Inter-Nuclear Distance Measurement between Spin-1/2 and Quadrupolar Nuclei. *J. Magn. Reson.* **2012**, *215*, 34–49.



# Chapter 3

## Solid-state NMR spectroscopy of drug delivery systems



## 1. Introduction

To improve the performance of the drug and reduce the side effects, one efficient strategy is to employ a DDS. In the last decades, numerous porous nano-sized DDSs were developed. Nanoscale sized systems exhibit unique chemical and biological properties that can facilitate the uptake of the drug and increase the drug delivery. As mentioned in Chapter 1, most DDSs are composed of a very complex core-shell system with different characteristics and functions (Figure 3.1). The core of the system accommodates the drug, protects and stabilizes it. It must be degradable to ensure efficient drug release. The corona part of the system has for goal to increase the colloidal stability of the nanoparticles, to make itfurtive to the immune system and to ensure specific delivery to the biological target. DDSs are hence very complex particles, and to guide the design of improved DDSs, it is essential to have at hand analytical tools able to yield information at the atomic scale about the structure of the DDS, the host-drug interactions, dynamics, etc.

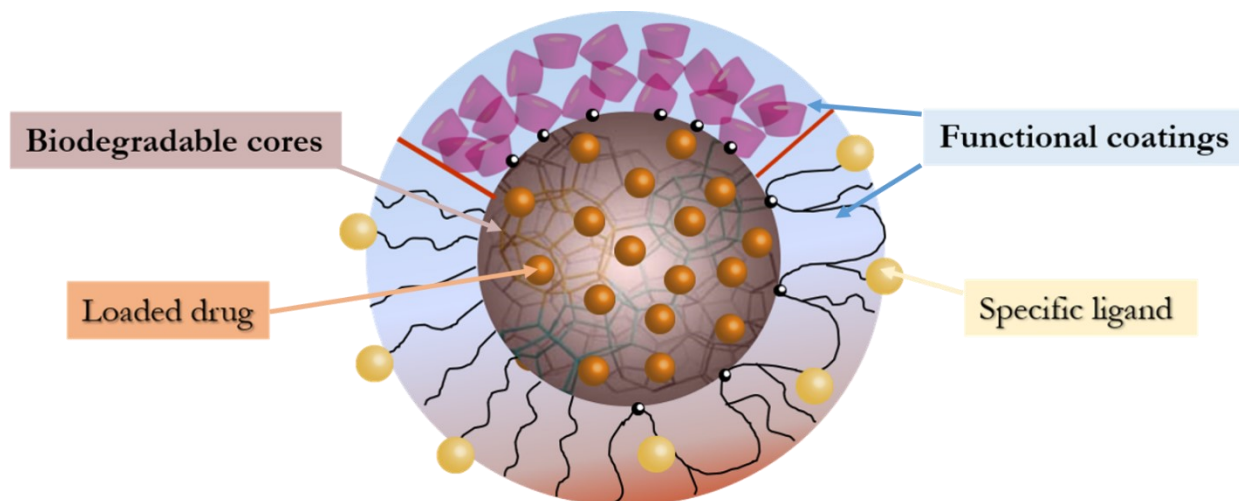


Figure 3.1: Illustration of composition of a Drug Delivery System. The drug is loaded in the biodegradable core that has to protect and stabilize it. The corona is composed by a functional coating that can interact with specific ligands to ensure delivery of the drug to the target.

A variety of techniques have been used so far, the most frequently employed being thermal analysis and nitrogen sorption, which can both give qualitative and quantitative information about

bulk structural and thermodynamical properties of the incorporated drugs. Unfortunately, the two techniques do not provide any knowledge about the microscopic properties of the embedded drugs and in particular about the crucial drug–drug and drug–host interactions. PXRD, which is the usual method of choice for the investigation of the atomic-level structural properties, is also often inapplicable because of the lack of long-range order in phases confined to mesopores. The alternative technique is solid-state nuclear magnetic resonance (ssNMR), which through spectroscopy and relaxation measurements offers valuable information about structural and dynamical properties of the embedded compound and which is not limited to the materials or forms that exhibit long-range order<sup>1</sup>. Solid-state NMR experiments probe the local environment of the nucleus and short-range order. This gives rise to various advantages, including the ability to provide detailed structural insights from polycrystalline samples and to examine local defects and disorders<sup>2</sup>. In the context of DDSs, because numerous active NMR nuclei are present in the core (such as <sup>1</sup>H, <sup>2</sup>H, <sup>13</sup>C, <sup>17</sup>O, <sup>19</sup>F and <sup>27</sup>Al), corona (as <sup>1</sup>H, <sup>13</sup>C, <sup>17</sup>O, <sup>27</sup>Al, <sup>29</sup>Si) and surface modification (as <sup>13</sup>C, <sup>17</sup>O, <sup>29</sup>Si, <sup>31</sup>P) of the nanoparticles, it can provide information about drug location, state and interactions in the system and about the core-shell interactions and about the matrix degradation and so, the delivery/release of the drug (Figure 3.2). These information can significantly contribute to guide the design and development of new DDSs. Moreover, this technique is non destructive, *i.e.* the DDS can be studied intact without need for dissolution, as would be required for liquid NMR, or chemical modification as would be required for fluorescence spectroscopy. Furthermore, the sample preparation is easy, consisting only in grinding the sample into powder and packing it into a zirconia rotor of the appropriate size.

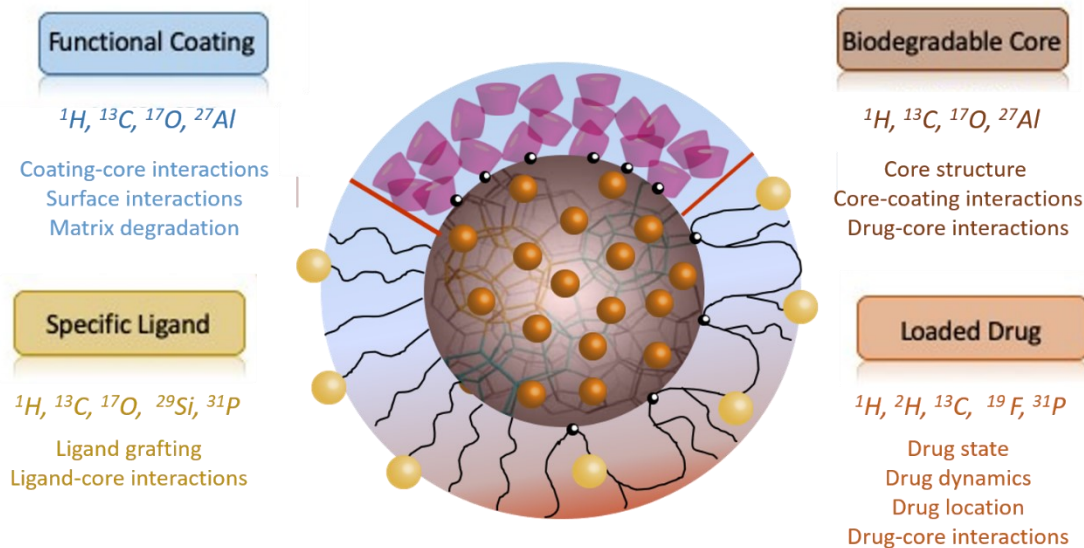


Figure 3.2: Scheme of a DDS nanoparticle containing a core, in which the drug is loaded, functional coating and specific ligand. The nuclei of interest in ssNMR and the information that can be extracted from these measurements are indicated for each part for the system.

In this chapter, a review of the most recent applications of ssNMR spectroscopy in the field of DDSs is presented. The review is only focused on DDSs based on porous inorganic and hybrid inorganic-organic particles. SsNMR experiments based on one-dimensional (1D) NMR spectroscopy, then two-dimensional (2D) NMR starting from the simpler  $^1\text{H}$ - $^1\text{H}$  spin pair, then moving towards  $^1\text{H}$ -X pairs are reported. For each case, the efficiency and limits of the ssNMR technique are described.

## 2. 1D $^1\text{H}$ solid-state NMR spectroscopy

$^1\text{H}$  is the most obvious nucleus that can be used for the characterization of DDSs as the majority of drugs are protonated, as are the drug carriers.  $^1\text{H}$  1D MAS NMR are simply and fast experiments that may readily give information about the state of the drug in the DDS and the formation of hydrogen bonds, thanks to a shift of the proton resonance. The  $^1\text{H}$  MAS NMR spectra are known to be dominated by large homonuclear dipolar interactions; hence, techniques based on fast MAS are usually preferred to get high-resolution data. Due to the small chemical shift dispersion of  $^1\text{H}$  NMR spectra (below 20

ppm in most diamagnetic systems), it is preferable to perform measurements at high magnetic field to optimize the signal resolution.

Fast MAS techniques are very useful to clarify the structure of pure drugs or pristine molecular systems. Two examples of  $^1\text{H}$  MAS NMR spectra recorded on pure drug samples (an antibiotic, Cefadroxyl monohydrate and a neurotransmitter, Adenosin Triphosphate) are shown Figure 3.3. In both samples, one can clearly see the increase of resolution of the  $^1\text{H}$  MAS NMR spectra starting from spectra recorded on 9.4 T and going to high field (20 T) and fast MAS (60 kHz). Higher resolution facilitates the interpretation of the spectra and the assignments of the  $^1\text{H}$  resonances, potentially providing information about intra or inter-molecular interactions, the purity of the drug, their state and their stability.

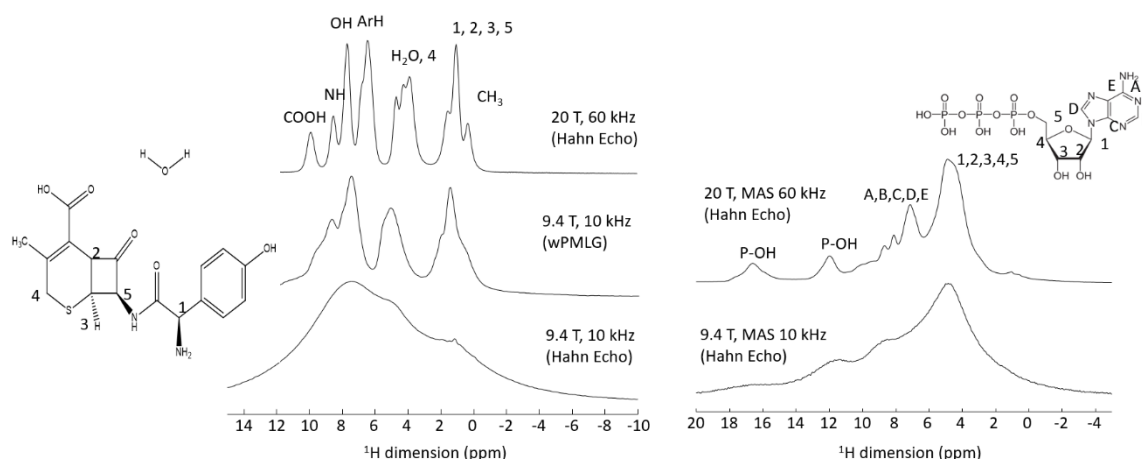


Figure 3.3:  $^1\text{H}$  NMR spectra of Cefadroxyl (left) and Adenosin Triphosphate (right) drugs, recorded on different spectrometers and at different spinning speed.

Going forward on analysis of drug in DDS, T. Ukmar *et al.*<sup>1</sup> studied by ssNMR the composition and structure of nonfunctionalized and functionalized SBA-15 (Santa Barbara Amorphous type material) mesoporous silica matrices in which were loaded different amounts of Indomethacin (IMC) molecules. On the  $^1\text{H}$  MAS NMR spectra (Figure 3.4), a decrease of the signal intensity of the water resonance

when the amount of the drug increases was detected. Furthermore, the appearance of a new resonance revealed the formation of hydrogen bonds between the drug and the silica matrix. Measurements of spin-spin relaxation times  $T_2$  were performed, showing a decreasing of the  $T_2$  with the increase of the amount of the drug in the silica matrix. These were evidences of the reduced mobility of the drug and increased density of the protons, because of the close contact in the pores with the silica matrix.

If this study nicely illustrates the power of  $^1\text{H}$  MAS NMR, most DDSs are much more complex and lack long-range order, leading to broad overlapping  $^1\text{H}$  resonances which cannot be prevented even using the fastest available MAS probes and highest static magnets<sup>3</sup>. In this case, 2D  $^1\text{H}$ - $^1\text{H}$  MAS NMR is a first step towards increased resolution.

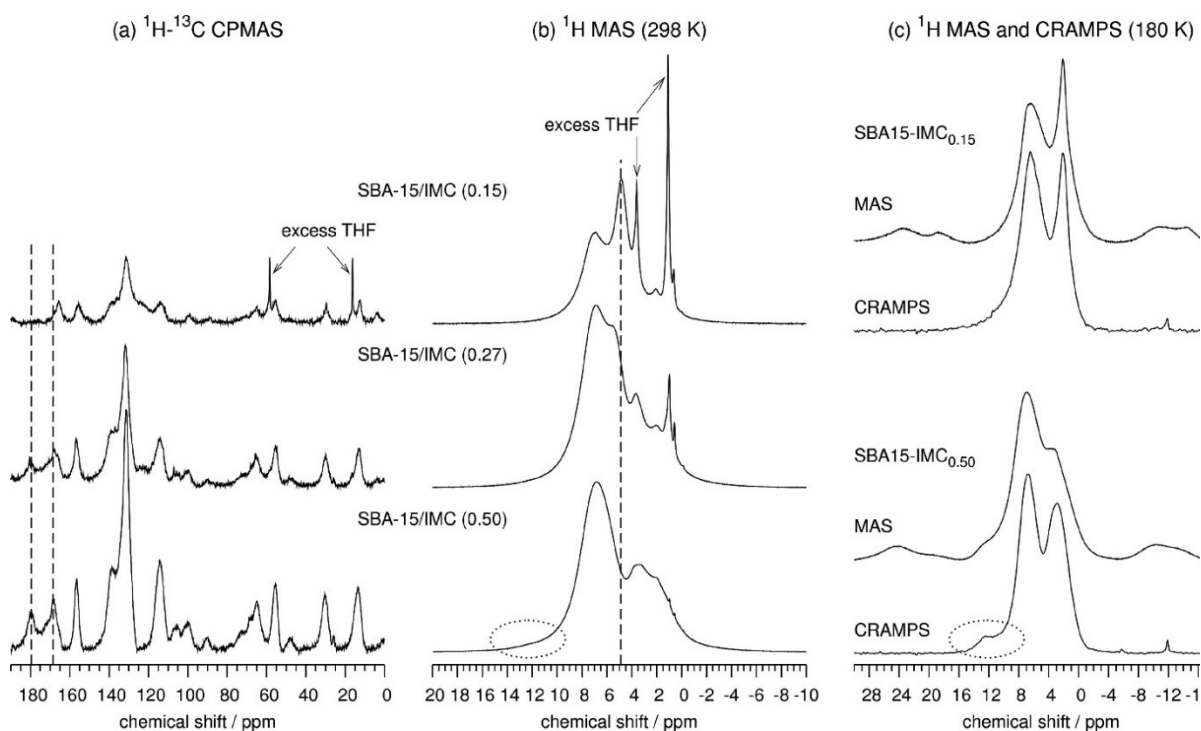


Figure 3.4:  $^1\text{H}$ - $^{13}\text{C}$  CPMAS (a),  $^1\text{H}$  MAS (b),  $^1\text{H}$  MAS and CRAMPS(c) experiments of SBA-15 in which were loaded different amount of Indomethacin. (Source: Ukmar *et al.*<sup>1</sup>)

### 3. $^1\text{H}$ - $^1\text{H}$ 2D NMR

The amount of information from 1D NMR spectra is sometimes limited due to potential overlap on the resonances. 2D NMR spectroscopy can give detailed information about the crystal structure of molecules, as example for pure drug and MOFs. Cefadroxyl monohydrate, which  $^1\text{H}$  1D MAS NMR spectra were shown in Figure 3.3, was analyzed using 2D  $^1\text{H}$ - $^1\text{H}$  DQ-SQ (BABA) experiment. The 2D spectrum was recorded on a 850 MHz spectrometer with a spinning speed of 60 kHz (Figure 3.5). On this spectrum, it is possible to have information about intermolecular distances (around 5 Å). One can clearly see correlation peaks between  $\text{H}_1$  and protons of aromatic rings, but also cross-peaks between  $\text{H}_1$  and  $\text{CH}_3$  and between  $\text{H}_4$  and OH and protons of the phenol, confirming the proximity between the two rings of the molecule, seen on crystal structure data<sup>4</sup>.

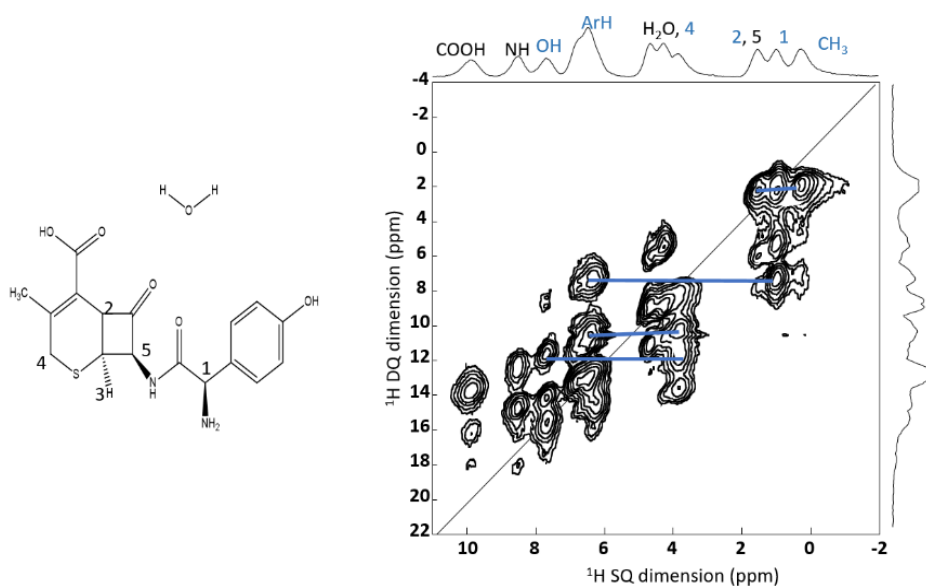
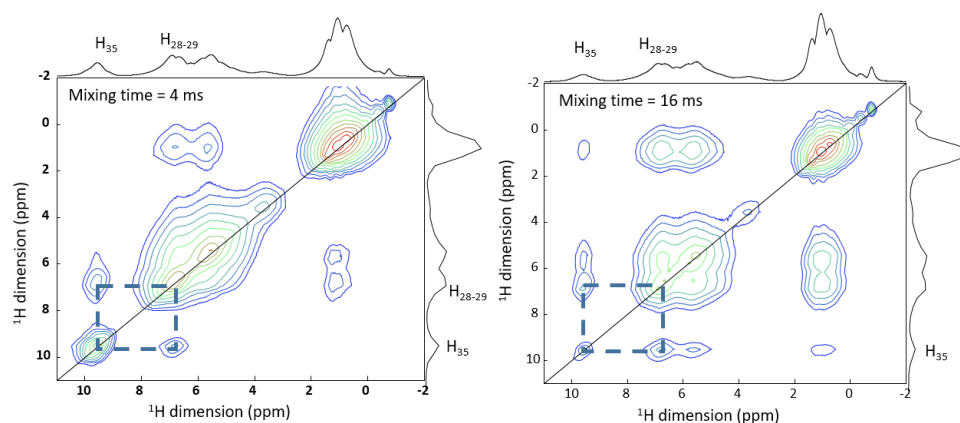


Figure 3.5:  $^1\text{H}$ - $^1\text{H}$  DQ-SQ 2D NMR spectrum of Cefadroxyl monohydrate, recorded at 60 kHz (20 T). The blues lines show the correlation between the different protons.

$^1\text{H}$ - $^1\text{H}$  SQ-SQ experiments can also be recorded. They allow probing longer proton-proton distances. In Figure 3.6a, two 2D  $^1\text{H}$ - $^1\text{H}$  homonuclear correlation spectra (proton spin diffusion experiments) of MIL-154, recorded with a RFDR pulse sequence on a 20 T spectrometer, at different mixing times are shown. MIL-154 is a Zr-based MOF with and salicylic and gallic acid as linkers. Proton spin diffusion

(PSD) build-up curves were traced and compared with simulated build-up, obtained by extraction of  $^1\text{H}$ - $^1\text{H}$  distances from the crystal structure<sup>5-7</sup>. In Figure 3.6b, one of this curve for  $\text{H}_{28-29}$  of gallic acid and  $\text{H}_{35}$  of salicylic acid linkers of MIL-154 is shown. This can allow refining the theoretical crystal structure of the MOF with experimental data. And, in general, it can help to design the unknown structure of several materials.

a)



b)

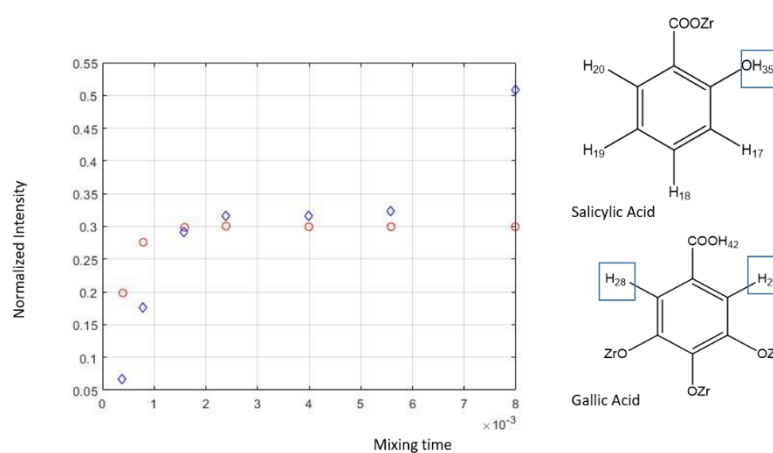


Figure 3.6: a)  $^1\text{H}$ - $^1\text{H}$  2D MAS NMR spectra of MIL-154, recorded at 20 kHz (20 T) at two different mixing times ( $\circ$ ). The dash lines indicate spatial proximity between the protons; b) PSD Build-up curves

2D homonuclear NMR spectroscopy can also be used for the characterization in formulated pharmaceutical materials<sup>8</sup>. As an example, it was employed to study flurbiprofen, an anti-inflammatory drug, incorporated in 200-400 nm silica capsules filled with Pluronic P123 (polyethylene oxide-polypropylene oxide-polyethylene oxide triblock copolymer). After confirmation of the

confinement of the drug in the capsules, thanks to  $^1\text{H}$  and  $^{13}\text{C}$  1D NMR spectra,  $^1\text{H}$ - $^1\text{H}$  2D SQ-SQ NMR experiments (Figure 3.7) were recorded using RFDR. These experiments revealed the close proximity between the protons of flurbiprofen molecules and those of polypropyleneoxide part of the P123 chains (that form the core of the micelle), confirming the solubilization of the flurbiprofen inside the micelles<sup>9</sup>.

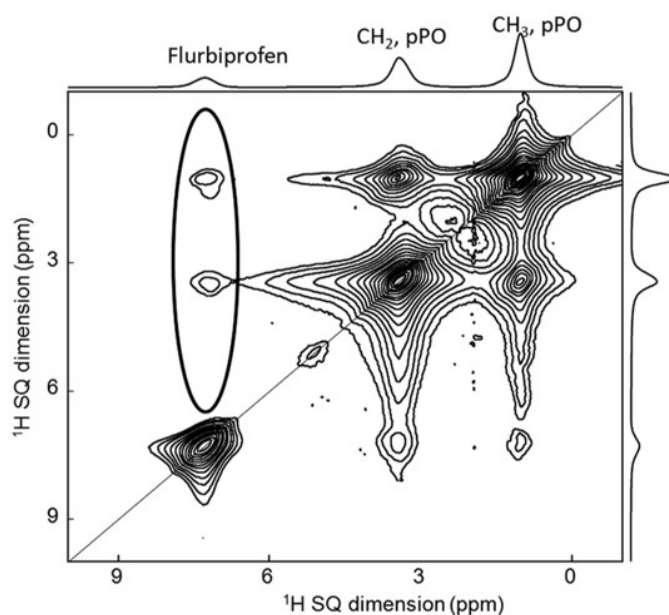


Figure 3.7:  $^1\text{H}$ - $^1\text{H}$  2D SQ-SQ MAS NMR of Flurbiprofen incorporated in silica capsules filled with Pluronic P123. In evidence (ringed) the cross-peaks presented between the protons of the drug and the ones of the DDS. (Source: Kerkhofs *et al.*<sup>9</sup>)

Another class of potential candidate as DDS are Metal Organic Frameworks (MOFs)<sup>10</sup>, based on cation clusters linked to each other through organic linkers, they offer highly porous structures that can accommodate and release drugs. The most promising MOFs are based on non-toxic paramagnetic  $\text{Fe}^{3+}$  cations, which limits the NMR investigations<sup>11</sup>. SsNMR gives more information when diamagnetic compounds are studied. As an example, UiO-66(Zr), where UiO stands for University of Oslo, has been tested as carrier for caffeine<sup>12</sup> (Figure 3.8a). The terephthalate linker can be functionalized with different polar/apolar groups, which can allow tuning the host/guest interactions.  $^1\text{H}$  and  $^{13}\text{C}$  ssNMR experiments were performed to investigate these interactions. Combining density functional theory

(DFT) calculations and  $^1\text{H}$ - $^1\text{H}$  DQ-SQ MAS NMR experiments on different functionalized UiO-66(Zr) samples (-H, -NH<sub>2</sub>, -2OH, -Br) loaded with caffeine (Figure 3.8b), the authors clearly identified the interactions between the MOF and the drug<sup>12</sup>. Another evidence of the encapsulation of the caffeine in the pores was given by measurement of the T<sub>1</sub> spin-lattice relaxation time of the  $^1\text{H}$  of caffeine that strongly decreases compared with the encapsulation of the caffeine. Indeed, the decrease of the T<sub>1</sub> shows that caffeine molecules are more mobile in the pores of the MOF than when they are packed in a pure phase. Notably, they show that the functional groups had little impact on the drug as no specific interaction between the caffeine and the functional group was found on the NMR spectra<sup>12</sup>.

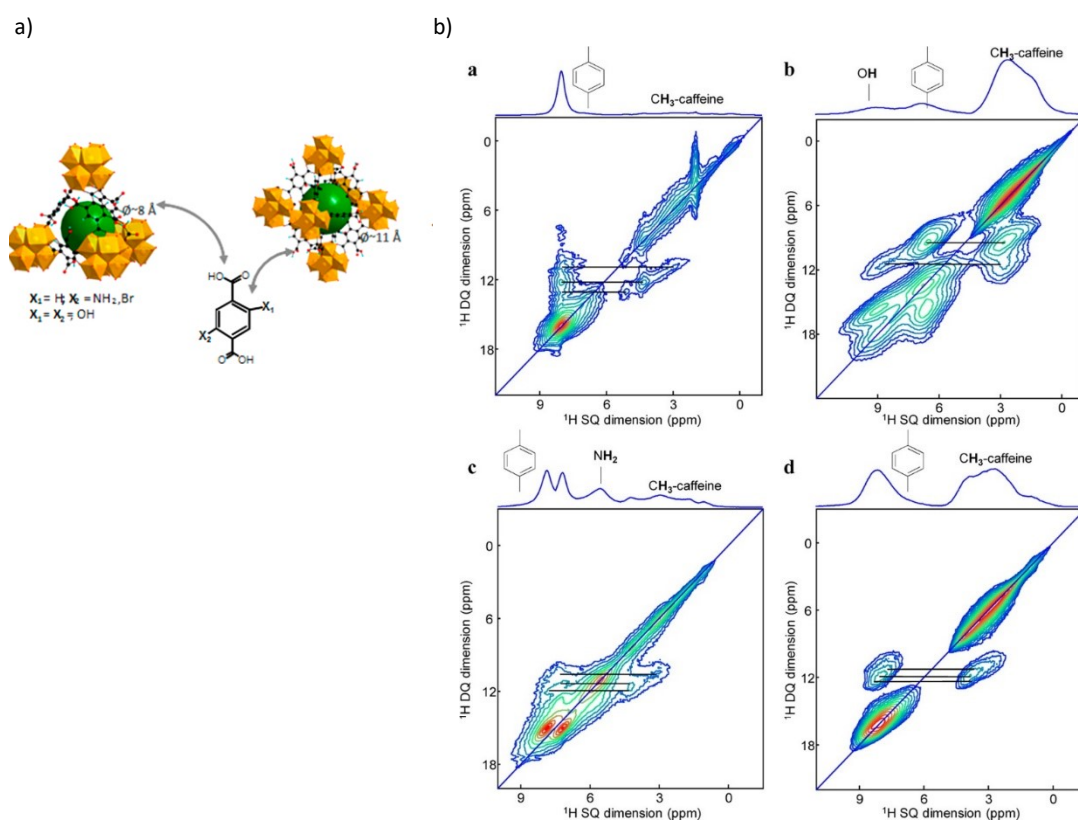


Figure 3.8: a) Schematic view of the tetrahedral (left) and octahedral (center) cages of the dehydrated UiO-66(Zr). Zirconium polyhedra and carbon atoms are in orange and black, respectively. Hydrogen atoms are omitted for clarity; b)  $^1\text{H}$ - $^1\text{H}$  DQ-SQ MAS NMR experiments on different functionalized UiO-66(Zr) samples (-H, -NH<sub>2</sub>, -2OH, -Br) loaded with caffeine. The lines indicate the correlation between the protons of the linker of the MOF and the ones of the CH<sub>3</sub> group of the caffeine. (Source: Devautour-Vinot *et al.*<sup>12</sup>)

## 4. $^1\text{H-X}$ NMR

An alternative solution to analyze the structure of the system is to take advantage of the heteroatoms (*i.e.*, non hydrogen atoms) that can be present in the drug or in the host.

$^{13}\text{C}$  nucleus is the second most obvious nucleus, as most drugs but also numerous DDSs contain carbon atoms, either as pore modification or in the host structure itself (*e.g.*, organic DDSs, MOFs or functionalized porous silica). Solid dispersion can be analyzed by  $^{13}\text{C}$  ssNMR to probe the association between amorphous drug and polymers, remarking difference in NMR spectra that are not visible in PXRD pattern<sup>13,14</sup>. For example, in solid dispersions formed by  $\alpha$ -,  $\beta$ -,  $\gamma$ -CD in PEG6000 with or without addition of 5% w/w Indomethacin (IM), the  $^{13}\text{C}$  CPMAS NMR spectra of the  $\alpha$ - and  $\beta$ -CD solid dispersions gave spectra that are essentially superpositions of the spectra from the pure phases. On the contrary, for the  $\gamma$ -CD based dispersion, the spectral resolution was somewhat better, and therefore several chemical shift data for C-1, C-4 and C-6 were obtained. They concluded from these data that a structure might have been formed where the PEG molecules or their hydroxyl end groups interact with the cyclodextrin, changing the chemical shift in a way similar to that obtained when water is present. It can be possible also that the part of the PEG penetrates in the cavities of the cyclodextrins. In the PEG/IM (Figure 3.9a), PEG/ $\alpha$ -CD/IM (Figure 3.9b), and PEG/ $\beta$ -CD/IM (Figure 3.9c) samples as in pure indomethacin, C-13 and C-10 are of the same magnitude, while the C-10 peak has almost disappeared in the  $\gamma$ -CD dispersion (PEG/ $\gamma$ -CD/IM) (Figure 3.9d). For  $\gamma$ -CD, all the carbons resonances are shifted compared with the pure cyclodextrin. In particular, the C-6 carbon located at the exterior of the torus also showed a shift of 2 ppm upfield. From these results, the authors showed that indomethacin may interact with  $\gamma$ -CD not only at the interior of the cavity but can also form hydrogen bonds at the top of the torus where C-6 is located<sup>15</sup>.

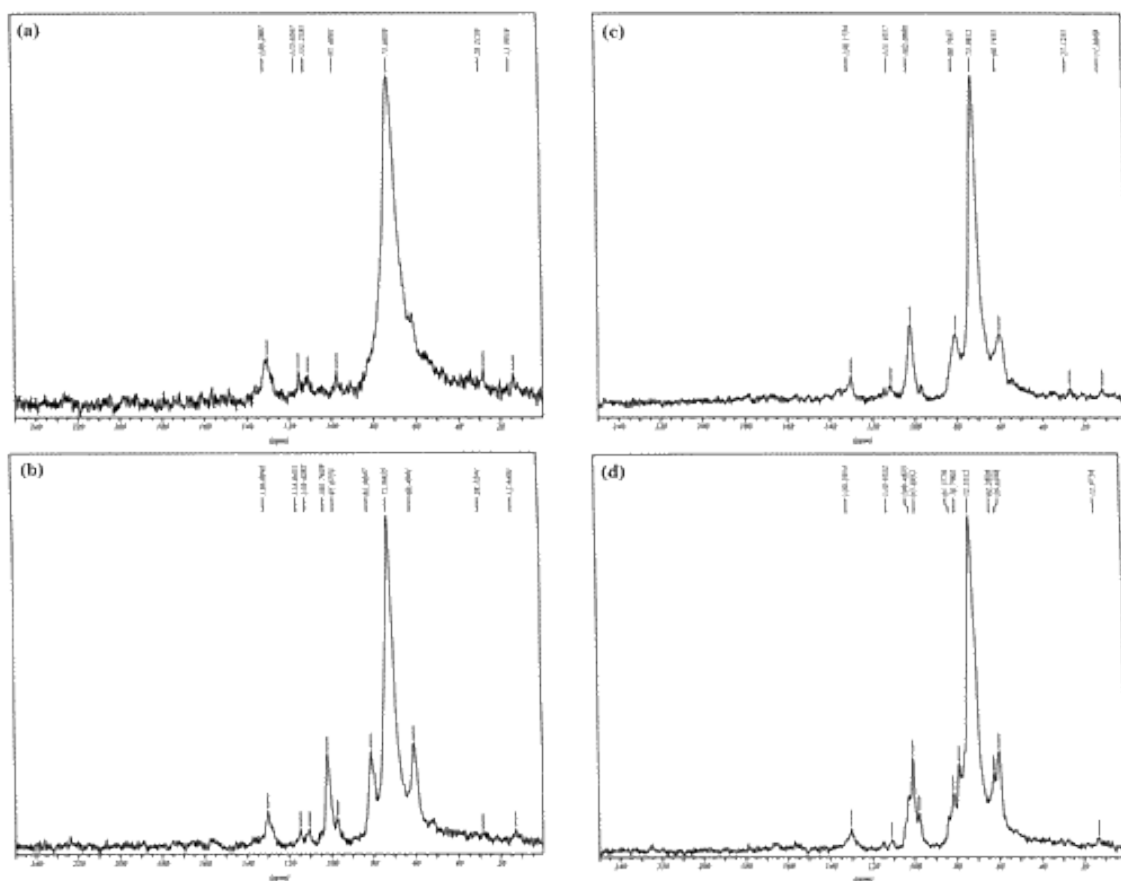


Figure 3.9:  $^{13}\text{C}$  MAS NMR spectra of PEG/IM (a), PEG/ $\alpha$ -CD/IM (b), PEG/ $\beta$ -CD/IM (c) and PEG/ $\gamma$ -CD/IM (d) samples. (Source: Wulff *et al.*<sup>15</sup>)

The surface of MCM-41 can be modified with silane or other organic or amino groups<sup>8–11</sup> with the aim to better control the drug release. T. Azaïs *et al.*<sup>16</sup> reported a study on a model drug (ibuprofen), which was loaded in MCM-41 with pore sizes ranging from 35 to 116 Å (Figure 3.10a). Using  $^1\text{H}$ ,  $^{13}\text{C}$  and  $^{29}\text{Si}$  ssNMR experiments recorded at room or low temperature ( $-50^\circ\text{C}$ ), the authors clearly showed the local interactions between the drug and the host, which they could relate to the drug release profile. Figure 3.10b displays the  $^{13}\text{C}$  CPMAS NMR spectra of Ibu-116 (Ibuprofen loaded in the pores of size 116 Å) and Ibu-35 (Ibuprofen loaded in the pores size of 35 Å) recorded at  $-50^\circ\text{C}$ . The two spectra are very distinct. In particular, if the spectrum of Ibu-116 is close to the one of the crystalline ibuprofen, the one of Ibu-35 presents broader peaks. The pores of Ibu-116 are large enough to allow nucleation of crystallites, but in the second size of pores a vitrification process occurs and it is clearly

demonstrated in the  $^{13}\text{C}$  NMR spectrum (Figure 3.10b), in which the quaternary carbons are now clearly detected, due a solidification of the molecules<sup>16</sup>.

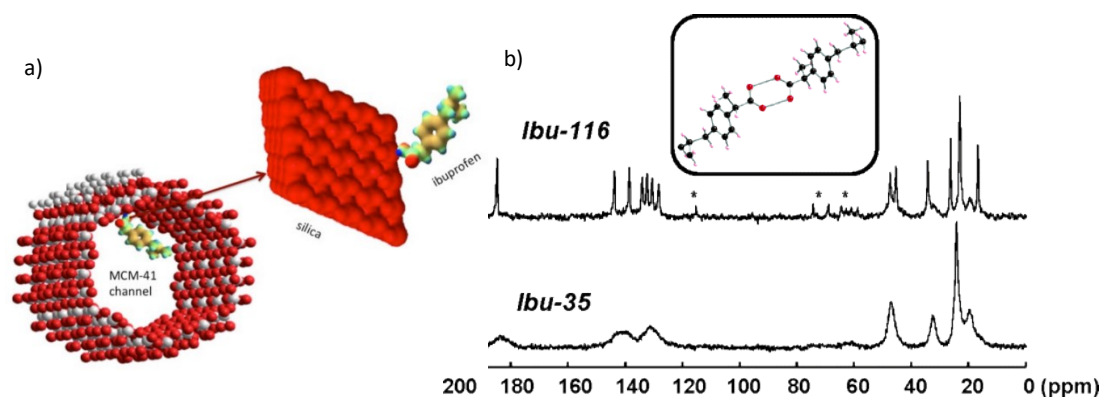
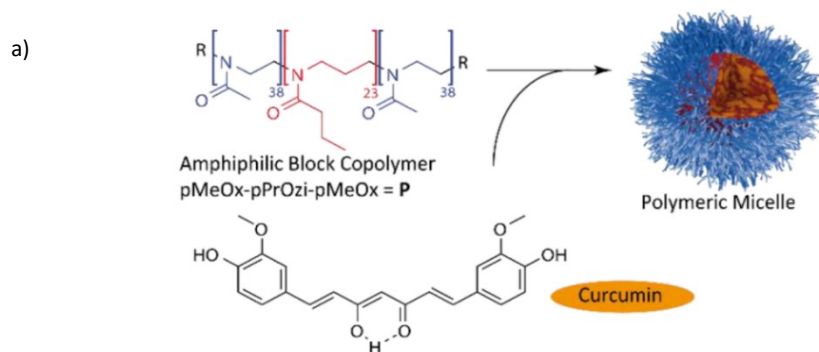


Figure 3.10: a) Adsorption of a molecule of ibuprofen within the MCM-41 channels; b)  $^{13}\text{C}$  CPMAS NMR spectra of Ibu-116 (a) and Ibu-35 (b). \* denote spinning sidebands. (Source: Azais *et al.*<sup>16</sup>)

In a copolymers based on poly(2-oxazoline) and poly(2-oxazines) was loaded different amount of curcumin drug (Figure 3.11a) and  $^1\text{H}$ - $^{13}\text{C}$  2D HETCOR spectra with long contact time (5 ms) were recorded to probe the intermolecular interaction between the polymer and the drug. On this 2D spectrum, it was possible to easily distinguish the different  $^{13}\text{C}$  resonances belonging to the core block (hydrophobic pPrOzi) and the interface block (hydrophilic pMeOx). In the formulation with the lowest concentration of curcumin (CUR-2-P), the HETCOR experiment showed only cross-peaks between the drug and the block present in the core due to a formation of hydrogen bond between the phenolic OH moieties and the amide moiety of this hydrophobic block. Increasing the amount of the drug (CUR-6-P), the core became saturated and the curcumin now is located in the amphipatic interfaces (interaction with pMeOx block showed in the 2D spectrum). Another evidence of this interaction was obtained by the decrease of the dissolution properties with the increase of the amount of the drug for the high amount of H-bonds formed. In the last formulation, CUR-11-P, due to the high amount of drug presented also the hydrophilic amid units are saturated and there is a formation of physically crosslinking of the hydrophilic corona with a strongly decrease of the dissolution rate<sup>17</sup>.



b)

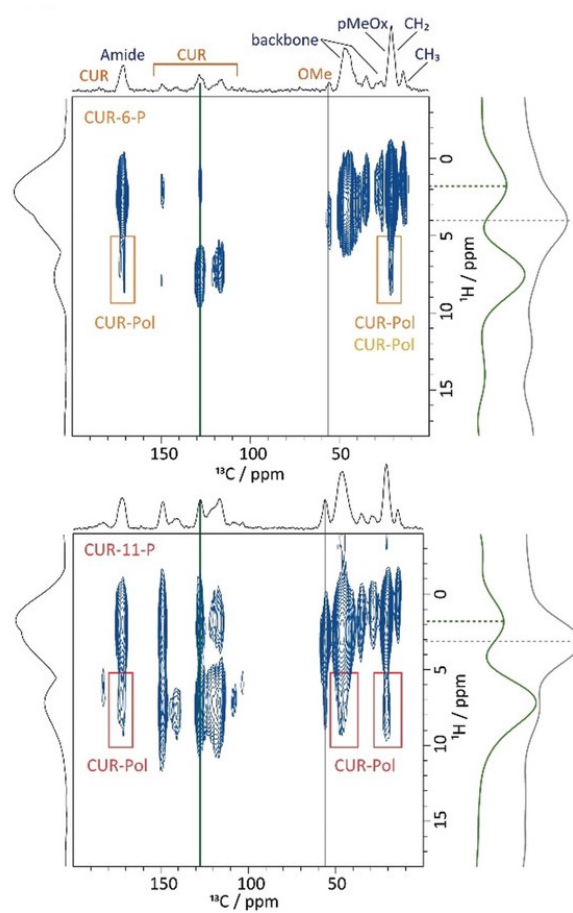


Figure 3.11: a) Structural formula of CUR-6-P and CUR-11-P; b)  $^1\text{H}$ - $^{13}\text{C}$  FSLG HETCOR spectra of CUR-6-P and CUR-11-P alongside the vertical slices extracted as highlighted by the colored bars. Colored boxes indicate cross-peaks originating from CUR-Pol intermolecular contacts. (Source: Pöpler *et al.*<sup>17</sup>)

In Figure 3.11b, HETCOR spectra of the CUR-6-P and CUR-11-P are shown. In both the spectra one can clearly see correlation between the protons of the drug and the carbon (amide) of the polymer.

An increase of the correlation peak intensity can be noticed in the aliphatic part of carbon spectrum when the amount of the drug increases.

In another example,  $\beta$ -IMC (Indomethacin), which is a crystalline solvate of tetrahydrofuran, was loaded in the cavities of MIL-101(Al)-NH<sub>2</sub> and in mesoporous silicate SBA-15. Detailed inspection of the <sup>1</sup>H-<sup>13</sup>C CPMAS NMR spectra (Figure 3.12) leads to several interesting observations. First, in the spectrum of SBA-15/IMC, the resonances are broadened, but the majority of them is not shifted. Instead, on the spectrum of the MOF with the Indomethacin, one can clearly distinguish regions in which the signals of the drug and the MOF are strongly overlapped while in some other parts, as around 150 ppm, the resonances are clearly separated. Second, unlike the spectrum of SBA-15/IMC the spectrum of MIL-101(Al)-NH<sub>2</sub>/IMC clearly confirms the presence of tetrahydrofuran (THF) within the pores. The reason of this difference can be explained by the different geometry of the pores. The SBA-15 has cylindrical channels that cannot confine the solvent. On the contrary, MIL-101 has spherical cavities interconnected and the migration of the molecules of solvent is more difficult. Third, the carboxylic carbon peak at 173 ppm (L2, L3) narrows substantially. This suggests that the metal-organic framework undergoes structural ordering when it is filled with IMC molecules, enabling extensive loading of the drug. In fact, when the MIL is immersed into the solution of IMC in THF, the framework can rearrange and open up the pores. Thanks to the analysis of carbon spectra and other experiments, the authors had information about the state of the drug in the two different delivery systems and the influence of the solvent in the loading process<sup>18</sup>.

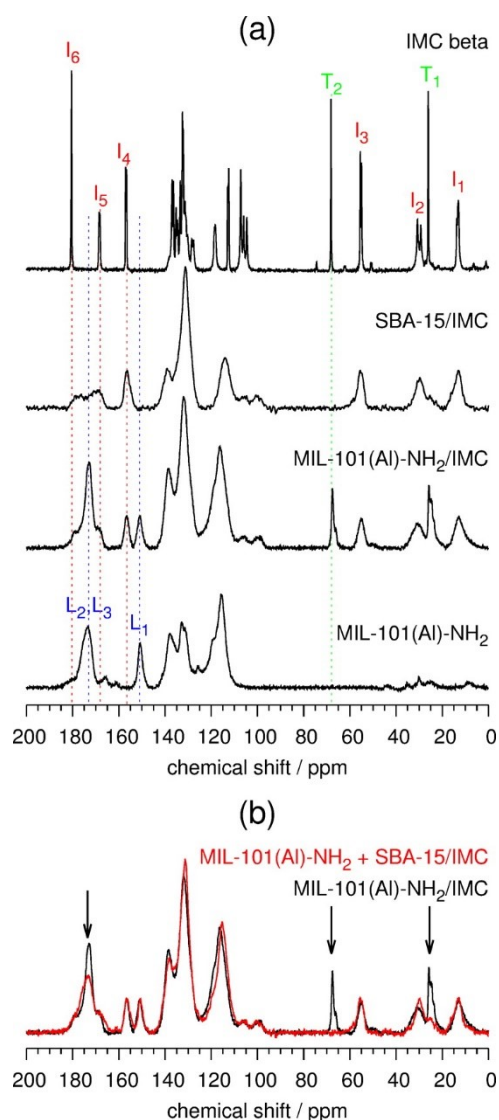


Figure 3.12: (a)  $^1\text{H}$ - $^{13}\text{C}$  CPMAS NMR spectra of bulk crystalline  $\beta$ - IMC, SBA-15/IMC, loaded and empty MIL-101(Al)-NH<sub>2</sub>. Peak labels correspond to selected carbon atoms within IMC molecule (I1–I6), THF molecule (T1, T2), and BDC-NH<sub>2</sub> linker (L1–L3). Vertical dotted lines enable easier comparison of signal positions. (b) Comparison of the  $^1\text{H}$ - $^{13}\text{C}$  CPMAS NMR spectrum of MIL-101(Al)-NH<sub>2</sub>/IMC with the sum of the spectra of SBA-15/IMC and MIL-101(Al)-NH<sub>2</sub>. Arrows indicate details where the differences are the most pronounced. (Source: Čendak *et al.*<sup>18</sup>)

Another interesting nucleus is  $^{19}\text{F}$ , as about 25% of APIs present on the market contain a fluorine atom in their structure. With a sensitivity close to the one of proton,  $^{19}\text{F}$  is highly attractive from an NMR point of view. It is usually present in little quantity in the API (often less than 2 or 3 fluorine groups), leading to  $^{19}\text{F}$  MAS NMR spectra with a limited number of resonances. Furthermore, the chemical shift dispersion (but also the chemical shift anisotropy) is much larger than that of proton,

leading to less signal overlap. It can provide information also on the molecular orientation inside a drug delivery system<sup>19</sup>.

T.N. Pharm *et al.*<sup>13</sup> performed  $^1\text{H}$ - $^{19}\text{F}$  CP-HETCOR and LGCP-HETCOR experiments on diflunisal amorphous dispersion in PolyVinylPyrrolidone (PVP) to confirm the formation of an amorphous glass solution (Figure 3.13). Correlations are observed between the fluorine signal and both types of protons (aromatic and aliphatic). The aliphatic ones can only be associated with the polymer. Increasing the contact time (from 0.1 ms to 2 ms), the correlation increases as expected from spin diffusion. To confirm spin diffusion effects the authors performed LGCP-HETCOR experiments, which greatly reduces spin diffusion during the  $^1\text{H}$  spin lock period. (Figure 3.13b). As shown by the relative intensity of the correlations, the build-up of spin diffusion was eliminated and the remaining correlation between the fluorine signals and aliphatic protons could then be assigned to a direct through-space dipolar interaction. The  $^1\text{H}$ - $^{19}\text{F}$  CP-HETCOR and LGCP-HETCOR experiments were useful to prove glass solution formation, evaluating the signal intensity variations caused by spin-diffusion to proton-rich polymers.

On a complex made by diflunisal and  $\beta$ -CD (Figure 3.14a), a 2D  $^1\text{H}$ - $^{19}\text{F}$  CP-HETCOR spectrum was performed to verify the incorporation of the drug in the cavities. In the spectrum shown in Figure 3.14b, correlations can be seen between the protons of the cyclodextrin and the two components representing the included and free diflunisal, which can be clearly distinguished. A strong correlation arises between the aliphatic  $\beta$ -CD protons (3.5 ppm) and the more deshielded fluorine position at approximately -111 ppm. It is more difficult to observe the expected correlation between aromatic proton resonances and included fluorine resonances, because of a combination of the lower concentration of this component and the loss of signal from spin diffusion to aliphatic  $\beta$ -CD protons. However, the presence of this expected correlation is evidenced by a deshielded shoulder between -105 and -110 ppm in the 1D row extraction shown for the free component. This experiment can be a quickly and easy approach to detect the presence of free drug during process development of, in this case, diflunisal-CD complexes<sup>20</sup>.

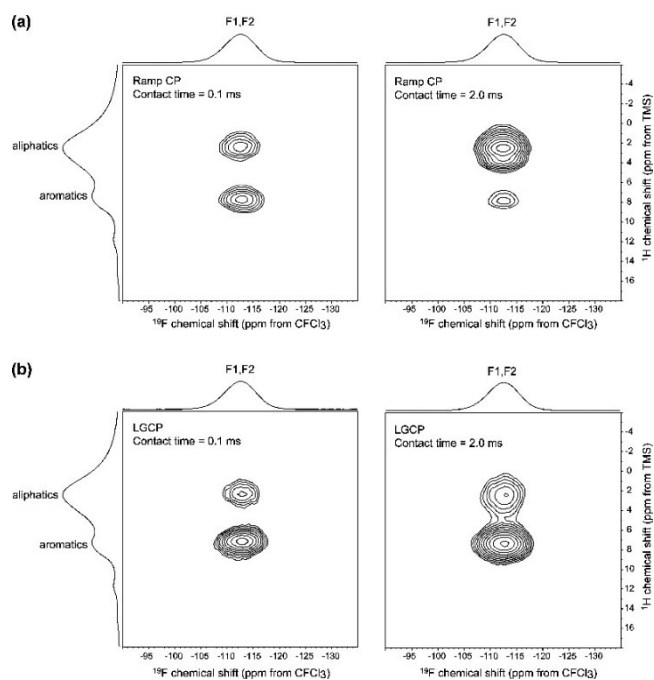


Figure 3.13: (a)  $^1\text{H}$ - $^{19}\text{F}$  CP-HETCOR spectra of a 30% w/w amorphous dispersion of diflunisal in PVP; (b)  $^1\text{H}$ - $^{19}\text{F}$  LGCP-HETCOR spectra obtained under the same conditions, except with the use of LGCP to suppress spin diffusion. The difference in relative correlation intensity with a 2.0 ms contact time between the two CP methods highlights the magnitude of the spin diffusion effects between drug and PVP in the dispersion. The F2 projections are the  $^{19}\text{F}$  CP-MAS spectra recorded at 15 kHz), and the F1 projections are the  $^1\text{H}$  MAS spectra recorded at 35 kHz). (Source: Pharm *et al.*<sup>13</sup>)

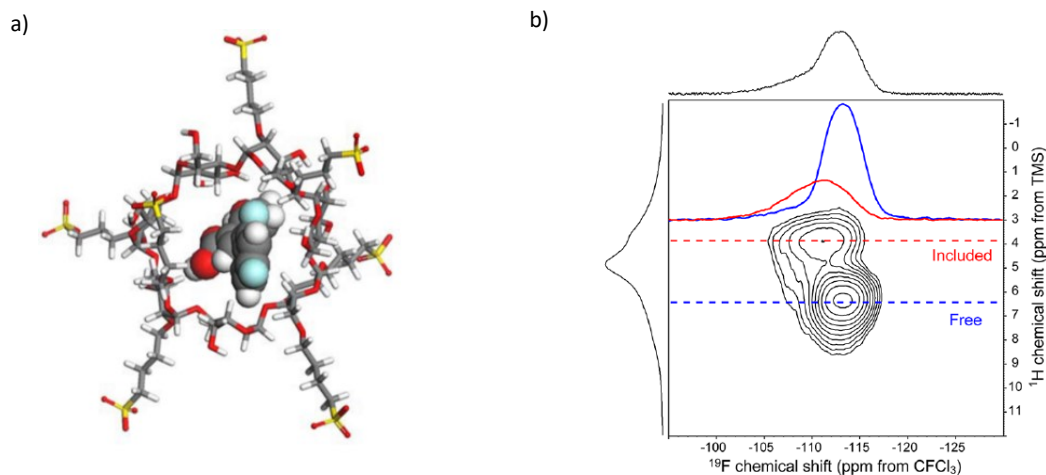


Figure 3.14: a) Crystal structure of Diflunisal on  $\beta$ -CD complex; b)  $^1\text{H}$ - $^{19}\text{F}$  CP HETCOR spectrum showing a mixture of bound and unbound diflunisal. In the F2 axis dimension is plotted the  $^{19}\text{F}$  CP-MAS spectrum (at 14 kHz) and the  $^1\text{H}$  DP-MAS spectrum (at 35 kHz) is plotted along the F1 axis dimension. Extracted rows are shown. (Source: Vogt *et al.*<sup>20</sup>)

For mesoporous silica,  $^{29}\text{Si}$  proves an interesting nucleus. It is quite useful to study the influence of mesoporous structure on the uptake of the drug<sup>21</sup>, on the drug-silica<sup>22,23</sup> interactions, on the drug delivery properties<sup>24</sup>, to study the different connectivity in the silica network<sup>25</sup> and explore the proton chemical environments around the silica<sup>26</sup>.

Zeolites are also potential drug carriers. A  $^1\text{H}$ - $^{29}\text{Si}$  HETCOR spectrum of a zeolite beta-based drug formulation containing Ag and Sulfadiazine (SD) can give details into the incorporation of the drug within the zeolite matrix, as shown by Shestakova *et al.*<sup>27</sup>. On the 2D spectrum shown in Figure 3.15, a strong correlation peak between the Si(OAl) sites and SD aromatic and NH protons was detected. This peak evidenced the localization of the drug near the Si(OSi)<sub>4</sub> sites. A second correlation peak with lower intensity was observed between the aromatic protons of SD and the signal, corresponding to [Si(1OH) + Si(1Al)] sites, at 103 ppm. Furthermore, an amorphization of the drug when incorporate in the silica matrix was evidenced from  $^1\text{H}$  T<sub>1</sub> and T<sub>2</sub> measurements<sup>27</sup>.

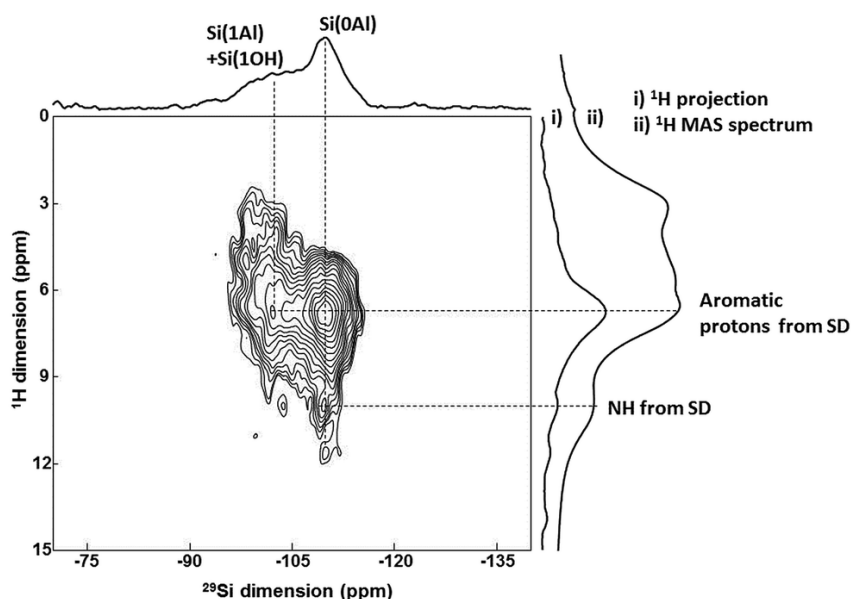


Figure 3.15:  $^1\text{H}$ - $^{29}\text{Si}$  CP-HETCOR NMR correlation spectrum of SD/AgB. (Source: Shestakova *et al.*<sup>27</sup>)

One last nucleus to take into consideration is  $^{31}\text{P}$  (nuclear spin  $\frac{1}{2}$ , 100% natural abundance), as it yields NMR spectra very sensitive to hydrogen bonding (chemical shift range from -180 to 250 ppm). Numerous drugs contain minimum a phosphorous atom in the form of phosphonate, phosphinate or phosphate groups. Phosphorous groups can also be incorporated in the drug carrier. One example is

a drug carrier made of MCM-41 containing Phosphorous (P-MCM-41). In that case, the  $^{31}\text{P}$  MAS-NMR experiments were performed to evaluate the amount of phosphorous and its impact in the structure of the material used as DDS. In the spectrum shown in Figure 3.16, two groups of signals around 0 and -11 ppm are observed, which could be assigned to phosphate units  $-\text{PO}_4$  not bonded to silicon ( $\text{Q}_0$ ) or bonded to one silicon atom ( $\text{Q}_1$ ) through one P-O-Si bond. The relative intensities between both signals give a  $\text{Q}_0/\text{Q}_1$  molar ratio = 1:2, which indicates that at least 66% of the P atoms are bonded to the silica framework. The phosphorus MCM-41 showed good bioactive properties, not showed by the pure MCM-41, that can be important for the application of this material for bone reconstruction and that can be combined with the fact that it is already used as DDS.<sup>28</sup>

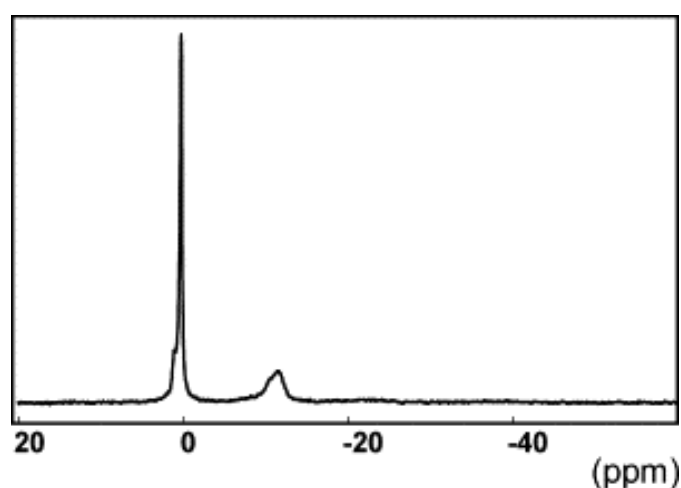


Figure 3.16:  $^{31}\text{P}$  MAS-NMR spectrum of MCM-41 phosphate. (Source: Vallet-Regí *et al.*<sup>28</sup>)<sup>1</sup>

<sup>1</sup>Extrait de: Vallet-Regí, M.; Izquierdo-Barba, I.; Rámila, A.; Pérez-Pariente, J.; Babonneau, F.; González-Calbet, J. M. Phosphorous-Doped MCM-41 as Bioactive Material. *Solid State Sci.* **2005**, 7 (2), 233–237. Copyright © 2005, publié par Elsevier Masson SAS. Tous droits réservés.

## 5. Conclusions

Atomic level understanding of the drug delivery systems is very important to get insight the structure of the drug and its carrier<sup>17</sup>.

In this chapter, several examples of ssNMR experiments, used to analyze the DDSs, were reported. It was showed how ssNMR offers valuable information about structural and dynamical properties of the encapsulated compound and how it can get insight into the intermolecular or intramolecular interactions between the pharmaceutical molecules and between these molecules and their delivery systems. This technique can be useful, also, in the investigations of drug polymorphism<sup>1</sup>. The 1D <sup>1</sup>H MAS NMR experiments give suddenly information about the state of the drug or the formation of hydrogen bonds between the components of the system. Because of the complexity of some systems, even going at high field and using fast MAS spinning, it does not allow obtaining resolved spectra and, therefore, have information about the system. In that case, 2D NMR experiments can be performed. <sup>1</sup>H-<sup>1</sup>H 2D spectra can be performed, but an alternative solution can be <sup>1</sup>H-X experiments to try to take advantages of the heteronuclei (X) that are present in the drug or the carrier. Even performing <sup>1</sup>H-X experiments, the information obtained do not give a real advantage to analyze the structure of complex delivery system, because of the presence of too broader <sup>1</sup>H spectra. In those cases, X-Y 2D experiments can be performed. These types of experiments are a new approach in the structural characterization of the DDSs that allow to circumvent the low resolution of the <sup>1</sup>H ssNMR. In this thesis, taking advantage of the different heteronuclei of the drugs and the carriers, we tried to find the best approach to have as much as possible information not only on the interactions taking place in the interphases of the core-shell structure of the DDS, but also on how they can influence the release of the drug once the carrier is degraded.

## References

- (1) Ukmar, T.; Čendak, T.; Mazaj, M.; Kaučič, V.; Mali, G. Structural and Dynamical Properties of Indomethacin Molecules Embedded within the Mesopores of SBA-15: A Solid-State NMR View. *J. Phys. Chem. C* **2012**, *116* (4), 2662–2671. Figure 3.4: Reprinted with permission from T. Ukmar, T. Čendak, M. Mazaj, V. Kaučič, G. Mali, *J. Phys. Chem. C* **2012**, *116*, 2662. Copyright © 2012, American Chemical Society.
- (2) Wong, Y. T. A.; Martins, V.; Lucier, B. E. G.; Huang, Y. Solid-State NMR Spectroscopy: A Powerful Technique to Directly Study Small Gas Molecules Adsorbed in Metal–Organic Frameworks. *Chem. – Eur. J.* **2019**, *25* (8), 1848–1853.
- (3) Porcino, M.; Christodoulou, I.; Dang Le Vuong, M.; Gref, R.; Martineau-Corcós, C. New Insights on the Supramolecular Structure of Highly Porous Core–Shell Drug Nanocarriers Using Solid-State NMR Spectroscopy. *RSC Adv.* **2019**, *9*, 32472–32475.
- (4) Shin, W.; Cho, S. W. Structure of Cefadroxil Monohydrate. *Acta Crystallogr. C* **1992**, *48* (8), 1454–1456.
- (5) Dumez, J.-N.; Butler, M. C.; Salager, E.; Elena-Herrmann, B.; Emsley, L. Ab Initio Simulation of Proton Spin Diffusion. *Phys. Chem. Chem. Phys.* **2010**, *12* (32), 9172–9175.
- (6) Elena, B.; Emsley, L. Powder Crystallography by Proton Solid-State NMR Spectroscopy. *J. Am. Chem. Soc.* **2005**, *127* (25), 9140–9146.
- (7) Krajnc, A.; Kos, T.; Zabukovec Logar, N.; Mali, G. A Simple NMR-Based Method for Studying the Spatial Distribution of Linkers within Mixed-Linker Metal–Organic Frameworks. *Angew. Chem. Int. Ed.* **2015**, *54* (36), 10535–10538.
- (8) Brown, S. P. Applications of High-Resolution  $^1\text{H}$  Solid-State NMR. *Solid State Nucl. Magn. Reson.* **2012**, *41*, 1–27.
- (9) Kerkhofs, S.; Saïdi, F.; Vandervoort, N.; Van den Mooter, G.; Martineau, C.; Taulelle, F.; Martens, J. A. Silica Capsules Enclosing P123 Triblock Copolymer Micelles for Flurbiprofen Storage and Release. *J. Mater. Chem. B* **2015**, *3* (15), 3054–3061.
- (10) Horcajada, P.; Chalati, T.; Serre, C.; Gillet, B.; Sebrie, C.; Baati, T.; Eubank, J. F.; Heurtaux, D.; Clayette, P.; Kreuz, C.; Chang, J.-S.; Hwang, Y. K.; Marsaud, V.; Bories, P.-N.; Cynober, L.; Gil, S.; Férey, G.; Couvreur, P.; Gref, R. Porous Metal–Organic-Framework Nanoscale Carriers as a Potential Platform for Drug Delivery and Imaging. *Nat. Mater.* **2010**, *9* (2), 172–178.
- (11) Mali, G. Looking into Metal–Organic Frameworks with Solid-State NMR Spectroscopy. In *Metal–Organic Frameworks*; Zafar, F., Sharmin, E., Eds.; InTech: London, United Kingdom, 2016.
- (12) Devautour-Vinot, S.; Martineau, C.; Diaby, S.; Ben-Yahia, M.; Miller, S.; Serre, C.; Horcajada, P.; Cunha, D.; Taulelle, F.; Maurin, G. Caffeine Confinement into a Series of Functionalized Porous Zirconium MOFs: A Joint Experimental/Modeling Exploration. *J. Phys. Chem. C* **2013**, *117* (22), 11694–11704. ] Figure 3.8: Reprinted with permission from S. Devautour-Vinot, C. Martineau, S. Diaby, M. Ben-Yahia, S. Miller, C. Serre, P. Horcajada, D. Cunha, F. Taulelle, G. Maurin, *J. Phys. Chem. C* **2013**, *117*, 11694. Copyright © 2013, American Chemical Society.
- (13) Pham, T. N.; Watson, S. A.; Edwards, A. J.; Chavda, M.; Clawson, J. S.; Strohmeier, M.; Vogt, F. G. Analysis of Amorphous Solid Dispersions Using 2D Solid-State NMR and  $^1\text{H}$   $T_1$  Relaxation Measurements. *Mol. Pharm.* **2010**, *7* (5), 1667–1691. Figure 3.13: Reprinted with permission from T. N. Pham, S. A. Watson, A. J. Edwards, M. Chavda, J. S. Clawson, M. Strohmeier, F. G. Vogt, *Mol. Pharm.* **2010**, *7*, 1667. Copyright © 2010, American Chemical Society.
- (14) Ito, A.; Watanabe, T.; Yada, S.; Hamaura, T.; Nakagami, H.; Higashi, K.; Moribe, K.; Yamamoto, K. Prediction of Recrystallization Behavior of Troglitazone/Polyvinylpyrrolidone Solid Dispersion by Solid-State NMR. *Int. J. Pharm.* **2010**, *383* (1–2), 18–23.
- (15) Wulff, M.; Aldén, M.; Tegenfeldt, J. Solid-State NMR Investigation of Indomethacin–Cyclodextrin Complexes in PEG 6000 Carrier. *Bioconjug. Chem.* **2002**, *13* (2), 240–248. Figure 3.9: Reprinted with permission from M. Wulff, M. Aldén, J. Tegenfeldt, *Bioconjug. Chem.* **2002**, *13*, 240. Copyright © 2002, American Chemical Society.

- (16) Azaïs, T.; Tourné-Péteilh, C.; Aussenac, F.; Baccile, N.; Coelho, C.; Devoisselle, J.-M.; Babonneau, F. Solid-State NMR Study of Ibuprofen Confined in MCM-41 Material. *Chem. Mater.* **2006**, *18* (26), 6382–6390. Figure 3.10: Reprinted with permission from T. Azaïs, C. Tourné-Péteilh, F. Aussenac, N. Baccile, C. Coelho, J.-M. Devoisselle, F. Babonneau, *Chem. Mater.* **2006**, *18*, 6382. Copyright © 2006, American Chemical Society.
- (17) Pöppler, A.-C.; Lübtow, M. M.; Schlauersbach, J.; Wiest, J.; Meinel, L.; Luxenhofer, R. Loading-Dependent Structural Model of Polymeric Micelles Encapsulating Curcumin by Solid-State NMR Spectroscopy. *Angew. Chem. Int. Ed.* **2019**, *58*, 1–8.
- (18) Čendak, T.; Žunkovič, E.; Godec, T. U.; Mazaj, M.; Logar, N. Z.; Mali, G. Indomethacin Embedded into MIL-101 Frameworks: A Solid-State NMR Study. *J. Phys. Chem. C* **2014**, *118* (12), 6140–6150. Figure 3.12: Reprinted with permission from T. Čendak, E. Žunkovič, T. Ukmar Godec, M. Mazaj, N. Zabukovec Logar, G. Mali, *J. Phys. Chem. C* **2014**, *118*, 6140. Copyright © 2014, American Chemical Society.
- (19) Lau, S.; Stanhope, N.; Griffin, J.; Hughes, E.; Middleton, D. A. Drug Orientations within Statin-Loaded Lipoprotein Nanoparticles by <sup>19</sup>F Solid-State NMR. *Chem. Commun.* **2019**, *55* (88), 13287–13290.
- (20) Vogt, F. G.; Strohmeier, M. 2D Solid-State NMR Analysis of Inclusion in Drug–Cyclodextrin Complexes. *Mol. Pharm.* **2012**, *9* (11), 3357–3374. Figure 3.14: Reprinted with permission from F. G. Vogt, M. Strohmeier, *Mol. Pharm.* **2012**, *9*, 3357. Copyright © 2012, American Chemical Society
- (21) Manzano, M.; Aina, V.; Areán, C. O.; Balas, F.; Cauda, V.; Colilla, M.; Delgado, M. R.; Vallet-Regí, M. Studies on MCM-41 Mesoporous Silica for Drug Delivery: Effect of Particle Morphology and Amine Functionalization. *Chem. Eng. J.* **2008**, *137* (1), 30–37.
- (22) Mellaerts, R.; Roeffaers, M. B. J.; Houthoofd, K.; Van Speybroeck, M.; De Cremer, G.; Jammaer, J. A. G.; Van den Mooter, G.; Augustijns, P.; Hofkens, J.; Martens, J. A. Molecular Organization of Hydrophobic Molecules and Co-Adsorbed Water in SBA-15 Ordered Mesoporous Silica Material. *Phys Chem Chem Phys* **2011**, *13* (7), 2706–2713.
- (23) Azaïs, T.; Hartmeyer, G.; Quignard, S.; Laurent, G.; Tourné-Péteilh, C.; Devoisselle, J.-M.; Babonneau, F. Solid-State NMR Characterization of Drug-Model Molecules Encapsulated in MCM-41 Silica. *Pure Appl. Chem.* **2009**, *81* (8), 1345–1355.
- (24) Gao, L.; Sun, J.; Zhang, L.; Wang, J.; Ren, B. Influence of Different Structured Channels of Mesoporous Silicate on the Controlled Ibuprofen Delivery. *Mater. Chem. Phys.* **2012**, *135* (2–3), 786–797.
- (25) Möller, K.; Bein, T. Degradable Drug Carriers: Vanishing Mesoporous Silica Nanoparticles. *Chem. Mater.* **2019**, *31* (12), 4364–4378.
- (26) Folliet, N.; Roiland, C.; Bégu, S.; Aubert, A.; Mineva, T.; Goursot, A.; Selvaraj, K.; Duma, L.; Tielens, F.; Mauri, F.; Laurent, G.; Bonhomme, C.; Gervais, C.; Babonneau, F.; Azaïs, T. Investigation of the Interface in Silica-Encapsulated Liposomes by Combining Solid State NMR and First Principles Calculations. *J. Am. Chem. Soc.* **2011**, *133* (42), 16815–16827.
- (27) Shestakova, P.; Martineau, C.; Mavrodinova, V.; Popova, M. Solid State NMR Characterization of Zeolite Beta Based Drug Formulations Containing Ag and Sulfadiazine. *RSC Adv.* **2015**, *5* (100), 81957–81964.
- (28) Vallet-Regí, M.; Izquierdo-Barba, I.; Rámila, A.; Pérez-Pariente, J.; Babonneau, F.; González-Calbet, J. M. Phosphorous-Doped MCM-41 as Bioactive Material. *Solid State Sci.* **2005**, *7* (2), 233–237. Figure 3.16: Extrait de: Vallet-Regí, M.; Izquierdo-Barba, I.; Rámila, A.; Pérez-Pariente, J.; Babonneau, F.; González-Calbet, J. M. Phosphorous-Doped MCM-41 as Bioactive Material. *Solid State Sci.* **2005**, *7* (2), 233–237. Copyright © 2005, publié par Elsevier Masson SAS. Tous droits réservés.

## Chapter 4

$\gamma$ -CD-MOFs as drug carriers for

Lansoprazole



## 1. Introduction

In this chapter, we focus on a  $\gamma$ -CD-MOF-based DDS. The synthesis and initial characterizations of the system, are first shortly described. In the second part, the solid-state NMR strategy employed to understand these supramolecular assemblies, the role of each components (in particular the competition between the surfactant used in the MOF synthesis and the loaded drug) as well as the fate of the drug once incorporated in the particles are presented. This study has been published in 2020<sup>1</sup>. (“Efficient incorporation and protection of lansoprazole in cyclodextrin metalorganic frameworks”, Xue Li, Marianna Porcino, Charlotte Martineau-Corcus, Tao Guo, Ting Xiong, Weifeng Zhu, Gilles Patriarche, Christine Péchoux, Barbara Perrone, Alia Hassan, Rainer Kümmerle, Alexandre Michelet, Anne Zehnacker-Rentien, Jiwen Zhange, Ruxandra Gref, International Journal of Pharmaceutics, 585 (2020) 119442.)

## 2. The system: LPZ@ $\gamma$ -CD-MOF

Lansoprazole (LPZ) (Figure 4.1) is a proton-pump inhibitor used to reduce the production of acid in the stomach to treat ulcers of the stomach and duodenum and that has been recently identified as an antitubercular prodrug<sup>2</sup>. In more detail, LPZ is a relatively unstable compound that can be modified in both enzymatic and non-enzymatic reactions. Its activity consists in decreasing the acid secretion through the inhibition of human H<sup>+</sup>K<sup>+</sup>-Adenosine triphosphatase (H<sup>+</sup>K<sup>+</sup>-ATPase), the proton pump of the gastric parietal cells, and requires conversion to a sulfenic acid or sulfonamide intermediate in the acidic environment of the stomach. LPZ is also converted in lansoprazole sulfide (LPZS) that shows an anti-bacterial activity, targeting cytochrome bc<sub>1</sub> and inhibiting the growth of *Mycobacterium Tuberculosis*<sup>2</sup>. The cytochrome bc<sub>1</sub> is a key enzyme of the mycobacterial respiratory transfer chain and has a key role in adaptive processes during intracellular growth. Its inhibition arrests the growth of the mycobacterium, but the mechanism of action is still unknown.

LPZ is a fragile molecule which readily degrades in both acidic<sup>3-5</sup> and basic conditions, is unstable on a shelf<sup>3,6,7</sup> (even during stored at 4 °C<sup>8</sup>) and has a strong tendency to crystallize. The storage and

administration of this drug are therefore a challenging and loading the drug in a DDS appears as an interesting solution to solve these issues.  $\gamma$ -CD-MOF was selected as the drug carrier because of its high loading capacity for this drug ( $23 \pm 2$  wt %)<sup>9</sup>.

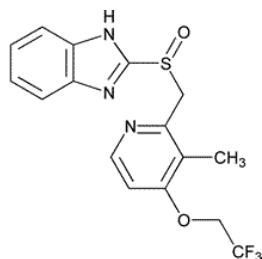


Figure 4.1: Chemical structure of Lansoprazole.

As detailed in Chapter 1,  $\gamma$ -CD-MOFs are biocompatible MOFs resulting from the coordination of potassium cations to alternating  $\alpha$ -1,4-linked *D*-glucopyranosil units on the primary and secondary faces of the CDs. Six CDs units are held by the coordination of four  $K^+$  cations to the C<sub>6</sub>OH groups and the glycosylic ring oxygen atoms on the primary faces of the  $\gamma$ -CD, whereas the cubes are attached to one another by the coordination of four  $K^+$  ions to the oxygen of the OH groups of the secondary faces of the cyclodextrins (Figure 4.2).  $\gamma$ -CD-MOFs have open porous frameworks, with a large spherical pore of 1.7 nm diameter resides at the center of each ( $\gamma$ -CD)<sub>6</sub> cube and that is connected by a series of smaller voids. Six pore windows of 0.78 nm diameter are defined by the  $\gamma$ -CD, which adopt the face of the cube. Further, the channel structure (with an aperture of 0.42 nm) links the two types of pore together<sup>10-12</sup>.

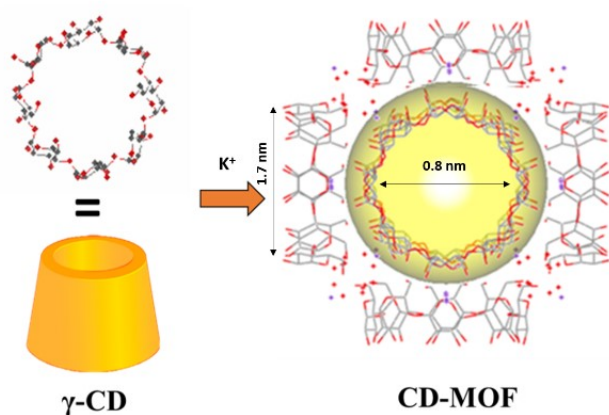


Figure 4.2: Schematic representation of  $\gamma$ -CD-MOF structure. K ions are indicated as purple spots

Two samples are studied in this chapter:  $\gamma$ -CD-MOF(K) as synthesized and loaded with LPZ (LPZ@ $\gamma$ -CD-MOF). Both samples were synthesized by Dr. Lisa Xue in the group of Prof. Ruxandra Gref (Institut des Sciences Moléculaires d'Orsay) and are obtained as polycrystalline powders. Both samples were synthesized following a green route, showed in Figure 4.3, called vapor diffusion method:  $\gamma$ -CD reacts with KOH in aqueous solution, followed by vapor diffusion of methanol (MeOH) into the solution (Figure 4.3). To create nanocrystals around 200-300 nm, cetyltrimethyl ammonium bromide (CTAB) has to be added during the synthesis procedure<sup>13</sup>. It allows a good control on the particle size distribution.

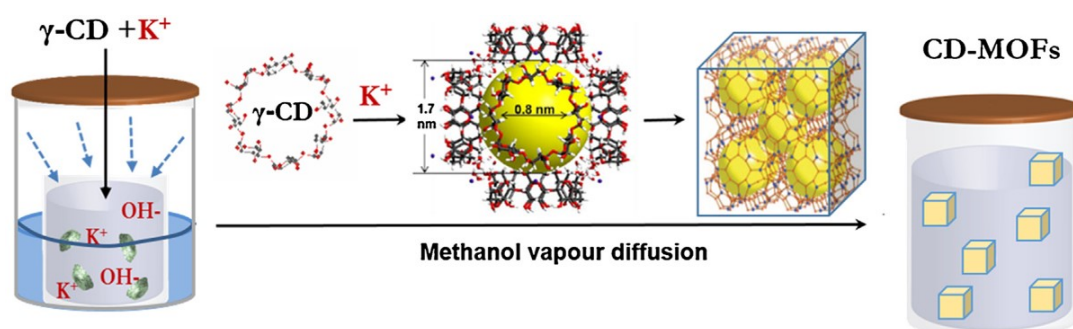


Figure 4.3: Schematic representation of CD-MOF synthesis and structure. (Source: Li *et al.*<sup>9</sup>)

The same procedure was used to obtain the loaded samples, LPZ @ $\gamma$ -CD-MOFs<sup>9</sup>, adding LPZ in the initial mixture. The payload reached around 20 wt%. Although it was not understood why, the CTAB did not affect the drug loading.

SEM analysis shows that the morphology and shape of the particles are the same for loaded and not loaded samples, while the Raman spectrum of LPZ @ $\gamma$ -CD-MOF crystals provides evidence for the drug entrapment. Additionally, PXRD of the particles (Figure 4.4) do not contain any diffraction peaks corresponding to the crystalline LPZ, showing that the drug is incorporated in amorphous state<sup>9</sup>.

These initial characterizations gave information about the drug loading and the overall incorporation of the drug, further atomic level characterization are needed to better understand the DDS.

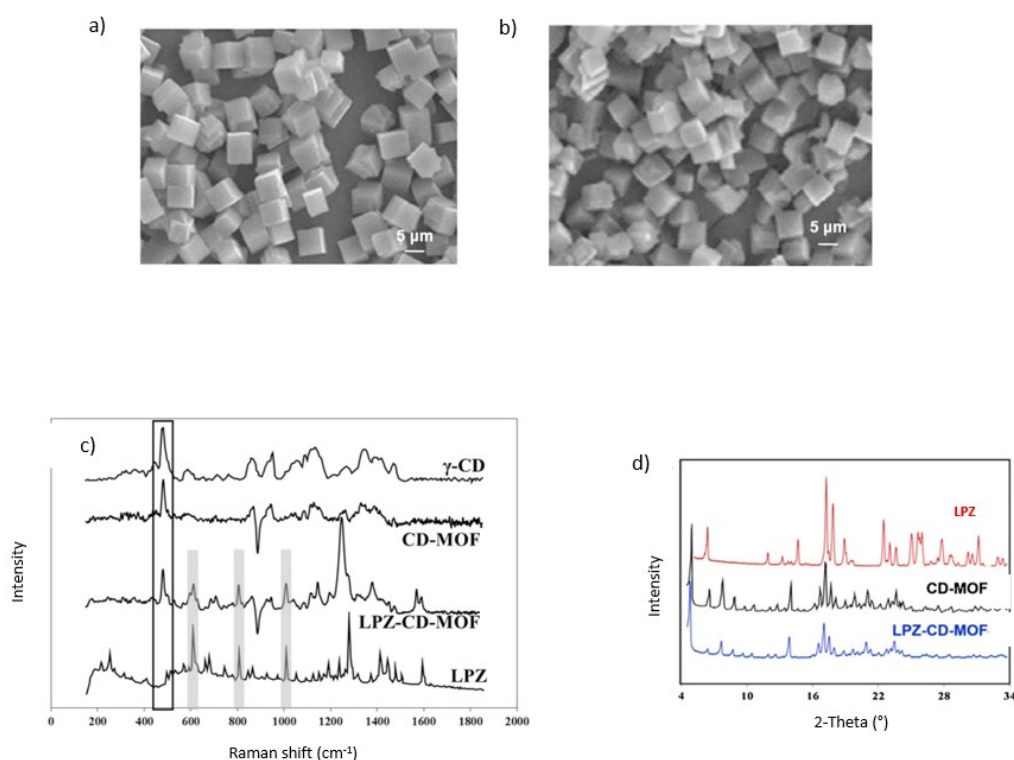


Figure 4.4: a) SEM micrograph of CD-MOFs and b) SEM micrograph of LPZ loaded CD-MOFs; c) Raman spectra of CD-MOF crystals containing or not LPZ were recorded and compared to the spectra of LPZ and CD; d) PXRD patterns of LPZ, CD-MOFs and LPZ loaded CD-MOFs. (Source: Li *et al.*<sup>9</sup>)

### 3. Solution-state NMR spectroscopy

First, we chose to go for solution-state NMR spectroscopy. It is a well-known as technique to analyze CD-drug inclusions<sup>14,15</sup>, as CDs are highly soluble in aqueous solutions.  $\gamma$ -CD-MOFs turned out to also dissolve partially in D<sub>2</sub>O, hence <sup>1</sup>H and <sup>13</sup>C liquid NMR could be performed at ILV by Dr. Mohamed Haouas. The <sup>13</sup>C NMR spectrum of 4 year old LPZ@ $\gamma$ -CD-MOF particles (Figure 4.5b) confirms that the LPZ molecules are still intact, even after this long storage period at room temperature. Notably, the <sup>13</sup>C resonances of the known degradation product<sup>3</sup> were not observed. Slight shifts are observed between the LPZ resonances resulting from the dissolution of the CD-MOF and pure LPZ, because of the LPZ-CD interaction that persists in solution, as attested by the <sup>1</sup>H NMR spectrum (Figure 4.5a). These data show the potential of CD-MOF to store for long period of time drugs that readily degraded on a shelf.

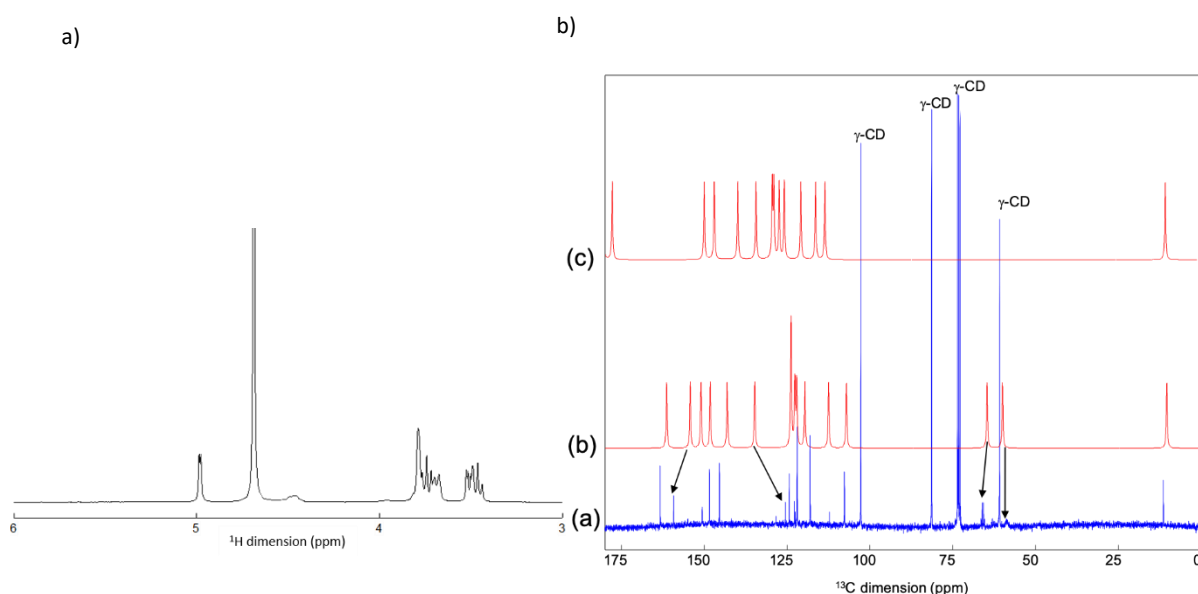


Figure 4.5: a) <sup>1</sup>H liquid NMR spectrum of LPZ loaded CD-MOF dissolved in D<sub>2</sub>O; b) (a)<sup>13</sup>C liquid- NMR spectrum of LPZ loaded CD-MOF dissolved in D<sub>2</sub>O. Simulated spectra of (b) pure LPZ and (c) degraded LPZ molecules. The lines of the  $\gamma$ -CD are assigned. The other lines belong to the LPZ molecule. Some lines are shifted between (a) and (b), because of the  $\gamma$ -CD/LPZ interaction in solution.

If these first NMR results were encouraging, they did not provide any information about the fate of the drug in the solid particles, hence ssNMR spectroscopy was further employed. DDSs based on CD-MOFs present some difficulties for ssNMR, which are illustrated below: i) the massive presence of

protons both in the carrier and in the drug lead to strong  $^1\text{H}$  resonance overlap that makes the  $^1\text{H}$  NMR line assignment ambiguous (Figure 4.6), ii) the particles contain some degree of disorder that strongly broaden the NMR resonances in the solid-state, reducing further the spectrum resolution. Fortunately, heteroatoms are present in the drug ( $^{19}\text{F}$  and  $^{15}\text{N}$ ), hence, we choose methods based on these heteroatoms to better understand the host-drug interactions.

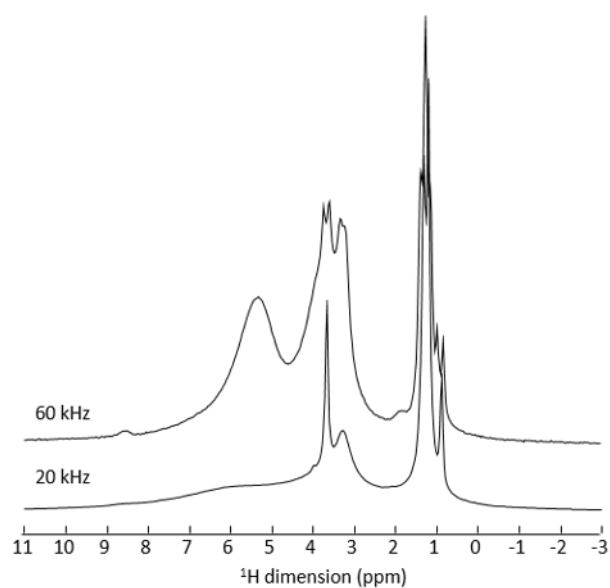


Figure 4.6:  $^1\text{H}$  MAS NMR spectra at 20 kHz and 60 kHz of LPZ@CD-MOF (20 T).

## 4. Solid-state NMR spectroscopy

### 4.1 $\gamma$ -CD-MOF

As reported by Furukawa *et al.*<sup>13</sup>, addition of CTAB (Figure 4.7) during the synthesis of the particles is needed to control the size and achieve a regular cubic morphologies. Elemental analysis indicates a residual amount of the CTAB around 15 % in the particles ssNMR spectroscopy was used to characterize the CD-MOF particles, to validate the presence and to find out the position and the interactions of the CTAB in/with the particles.

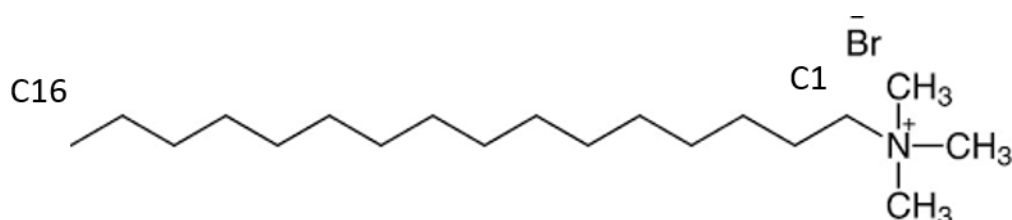


Figure 4.7: Chemical structure of CTAB.

The most obvious nuclei in these systems to start the NMR investigation are of course  $^1\text{H}$  and  $^{13}\text{C}$  as they are present everywhere in the samples. The  $^1\text{H}$  MAS spectrum of  $\gamma$ -CD shows a single broad featureless resonance while the spectrum of the CD-MOF, acquired under the same experimental conditions, contains three sets of peaks: the hydroxyl protons at 5.20 ppm, the CH and the  $\text{CH}_2$  groups at 3.49 and 3.06 ppm respectively. The lines corresponding to the  $\gamma$ -CD appear narrower on the CD-MOF. This might be due to the intrinsic porosity of the CD-MOF, which increases the  $^1\text{H}$ - $^1\text{H}$  distances, hence reduces the homonuclear dipolar interaction and the linewidth. An additional set of peaks is noticed at 1 ppm, which corresponds to the aliphatic protons of the CTAB used in the CD-MOF synthesis and trapped in the product (Figure 4.8a). This unambiguously confirms that, although this was not initially expected, the CTAB molecules are indeed trapped in the final MOF. Note that CD-MOF can be obtained without CTAB, but this yields to highly polydisperse particle sizes.

The presence of CTAB is also confirmed by the  $^{13}\text{C}$  CPMAS spectrum, which contains, in addition to the peaks of the  $\gamma$ -CD (at 102.2, 82.3, 73.5 and 61.8 ppm), peaks of smaller intensity that corresponds to the CTAB (Figure 4.8b) in the region of 60-0 ppm.

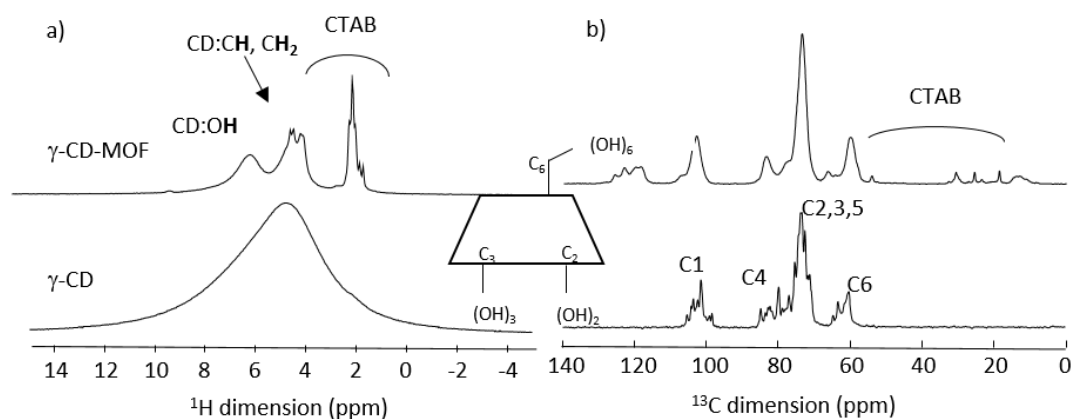


Figure 4.8:  $^1\text{H}$  MAS (a) and  $^{13}\text{C}$  CPMAS (b) NMR spectra of CD-MOF and CD at 60 kHz (20 T). The lines are assigned based on liquid-state and solid-state NMR data respectively for the CTAB<sup>16</sup> and the CD<sup>17</sup>.

To go further in the characterization and find out the location of the CTAB in the MOF, 2D  $^1\text{H}$ - $^1\text{H}$  MAS NMR homonuclear correlation experiments were performed. Two spectra were recorded using the EXSY experiment using a short (5 ms, to probe short proton-proton distances) and a longer (10 ms) mixing time (Figure 4.9). They provide information about spatial proximity between protons in the sample. One can notice cross-correlation peaks of high intensity between the CTAB and the CH/CH<sub>2</sub> of the CD in the spectrum recorded with the short mixing time, while the cross-peaks between the CTAB and the OH of the CD have a much smaller intensity. This evidences a shorter distance of the protons of CTAB with the inside protons of the  $\gamma$ -CD, which in turn indicates that the CTAB molecules are in strong interaction with the CD and part of the molecules are very likely located inside the cavities of the  $\gamma$ -CDs.

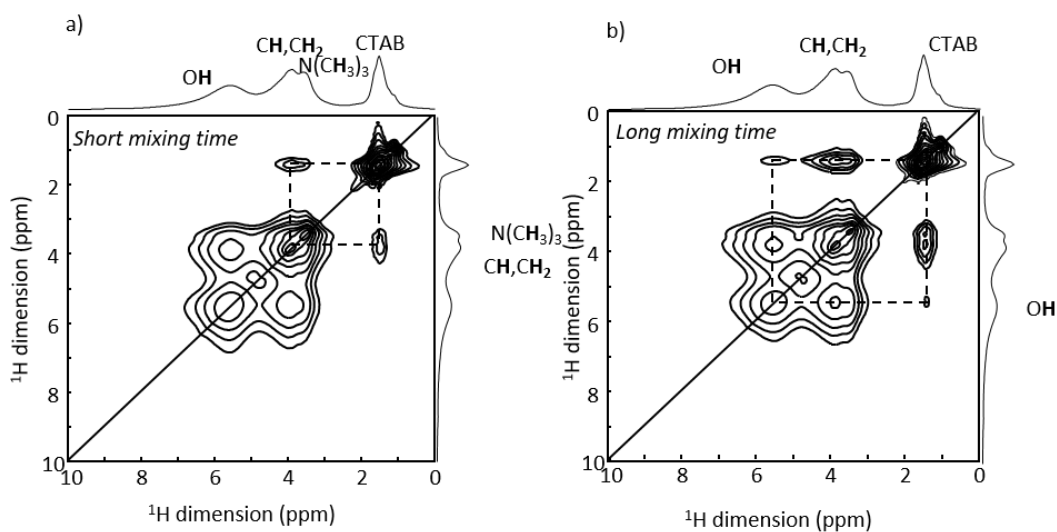


Figure 4.9:  $^1\text{H}$ - $^1\text{H}$  2D MAS NMR correlation spectra of CD-MOF recorded with mixing time of 5 ms (A) and 10 ms (B) at 60kHz (20 T). The dash lines indicate spatial proximity between the protons of the CTAB and those of the  $\gamma$ -CD.

This was confirmed by molecular simulations performed using the Gaussian code by Prof. Jiwen Zhang (Center of Drug Delivery Systems, Shanghai Institute of Materia Medica) and showed in Figure 4.10.

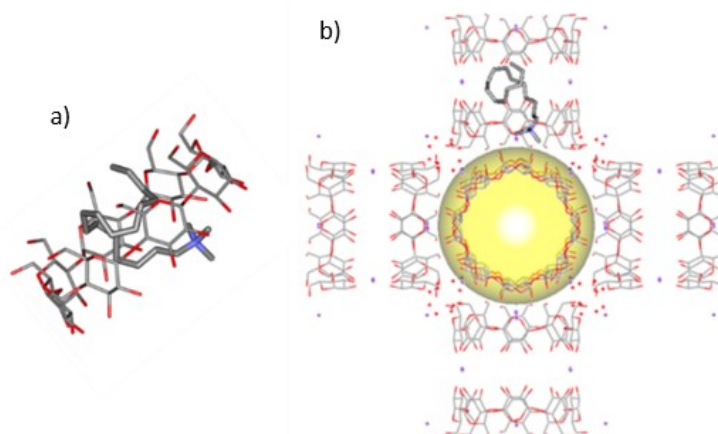


Figure 4.10: Simulated configurations of CTAB in monomeric  $\gamma$ -CD (a) and in  $\gamma$ -CD-MOF (b). K ions are indicated as purple spots in the structure of the CD-MOF.

Figure 4.11 shows 2D  $^{13}\text{C}$ - $^1\text{H}$  CP-HETCOR NMR spectra recorded with two different contact times: the shortest one (0.5 ms) allows the identification and assignment of  $^1\text{H}$  resonances of the CD and the CTAB, while the second one (2 ms) shows the interaction between the proton of the CTAB and the  $^{13}\text{C}$  resonance at 73.5 ppm of the  $\gamma$ -CD, corresponding to the carbon atoms located in the cavity of the CD. This confirms the strong interaction between CTAB and CD and the partial inclusion of CTAB in the CD cavity.

This ensemble of data gives some hints about the potential templating role of CTAB. It also raises questions as to why it is possible to load a drug inside these particles when the CDs are already in interaction with the CTAB molecules.

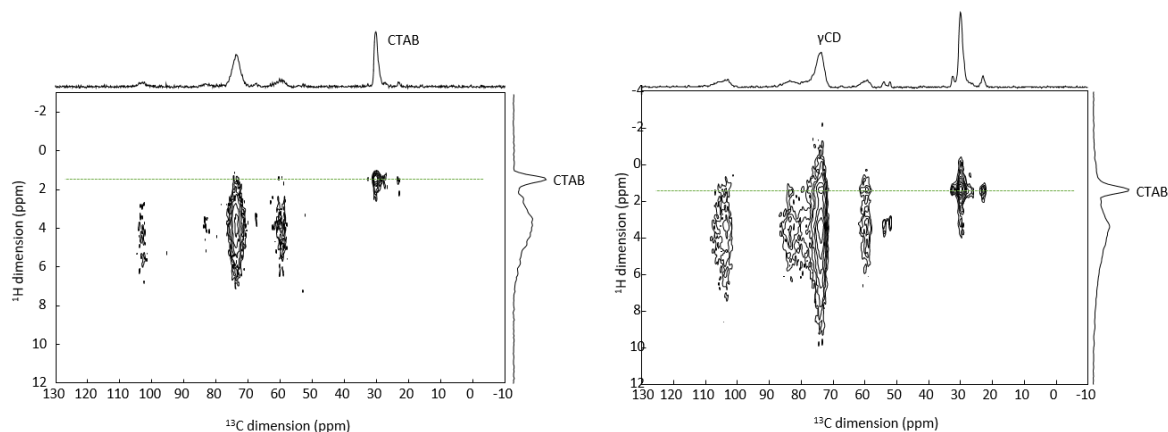


Figure 4.11:  $^{13}\text{C}$ - $^1\text{H}$  CPMAS 2D NMR spectra (recorded at 20 kHz, 20 T) at two different contact time: 0.5 ms (left) and 2 ms (right) of CDMOF sample.

## 4.2 LPZ@ $\gamma$ -CD-MOFs

Similarly to the  $\gamma$ -CD-MOFs,  $^1\text{H}$  and  $^{13}\text{C}$  nuclei are first investigated. The  $^1\text{H}$  and  $^{13}\text{C}$  MAS NMR spectra of LPZ loaded CD-MOF are displayed in Figure 4.12 along with those of pure LPZ. The first observation was that the intensity of the CTAB resonances has strongly decreased (in  $^{13}\text{C}$  MAS NMR spectra in the 25 ppm region and slightly above 50 ppm), indicating that the drug loading process has expelled most CTAB molecules from the system. One could hence expect a much stronger affinity of the  $\gamma$ -CD with LPZ rather than CTAB, this was confirmed by molecular simulation (Figure 4.13), which

shows that while both LPZ and CTAB preferred to crouch in the hydrophobic cavity of  $\gamma$ -CD, LPZ possessed a stronger interaction free energy with  $\gamma$ -CD than CTAB. This gave explanation why LPZ successfully replace CTAB during the drug loading.

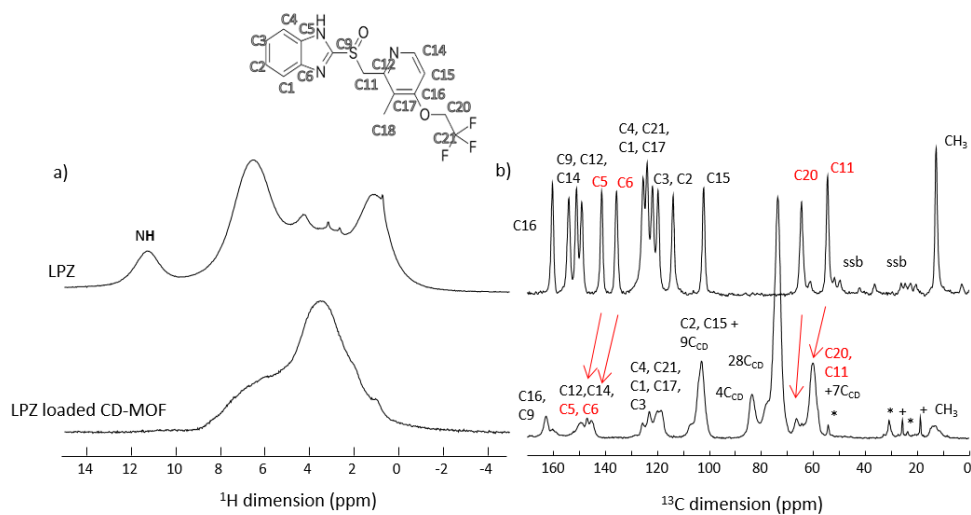


Figure 4.12:  $^1\text{H}$  MAS (a) and  $^{13}\text{C}$  CPMAS (b) NMR spectra of LPZ and LPZ loaded CD-MOF. The lines are assigned comparing with solutions NMR studies<sup>18</sup>. The lines are assigned. \* indicate traces of CTAB, + traces of ethanol, ssb indicate the spinning sidebands.

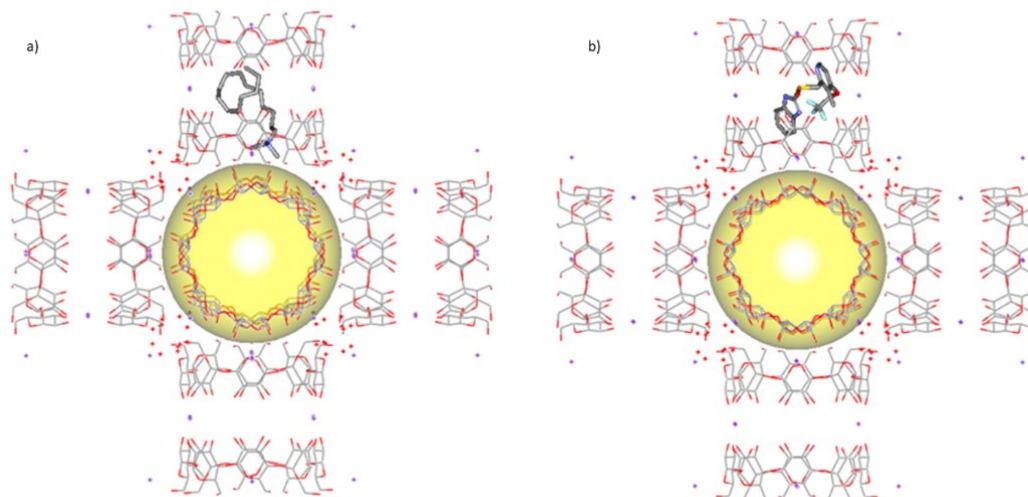


Figure 4.13: Simulated configurations of CTAB (a) and LPZ (b) in  $\gamma$ -CD-MOF. K ions are indicated as purple spots in the structure of the CD-MOF. For the simulation, two LPZ molecules were placed in contact with two CD cavities of the CD-MOFs.

Several  $^{13}\text{C}$  NMR experiments were performed to identify and quantify the various carbon atoms, the goal being to validate the integrity of the drug inside the particles (Figure 4.14): a  $^{13}\text{C}$  CPMAS NMR spectrum with a short contact time (50  $\mu\text{s}$ ) allows selection of the proton bearing carbon atoms while a quantitative CP allowed the determination of the number of carbon atoms contributing to each  $^{13}\text{C}$  resonance (which can arise from the overlap of several C atoms).

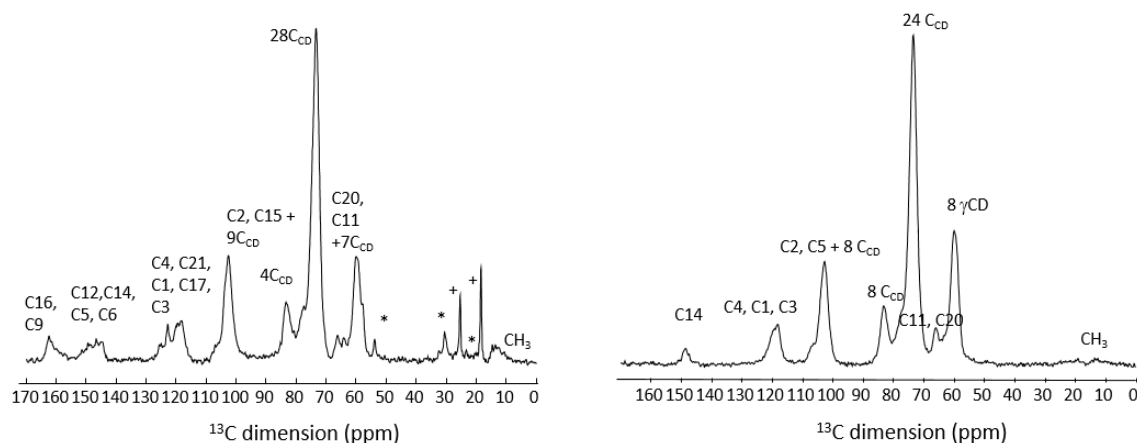


Figure 4.14: Quantitative  $^{13}\text{C}$  CPMAS (left) and CPMAS with a contact time of 50  $\mu\text{s}$  (right) NMR spectra, recorded at 10 kHz (9.4 T), of LPZ loaded  $\gamma$ -CD-MOF. The lines are assigned. \* indicate traces of CTAB, + traces of ethanol.

Careful analysis of these experiments shows that all  $^{13}\text{C}$  resonances of the drug are found in the LPZ loaded CD-MOF sample, indicating that the drug remained intact after the encapsulation process, and is stabilized inside the MOF particles. These results hence confirm the results from liquid-state NMR, which indicated that encapsulation provides a stabilization of the LPZ. The quantitative analysis indicates a ratio between the LPZ and  $\gamma$ -CD close to 1:1, corroborating with elemental analysis and HPLC data.

One can notice that the  $^{13}\text{C}$  resonances corresponding to the carbon atoms C5, C6, C9, C11 and C20 of the LPZ have different chemical shifts in the pure and loaded drug (Figures 4.12B and 4.15). Notably, C11 and C20 are flexible  $\text{sp}^3$  carbon atoms, the observed shifts hence very likely correspond to a bending of the drug inside the MOF, as hinted by the molecular simulation<sup>19</sup>, showed in Figure 4.13. Note that the shift of  $^{13}\text{C}$  resonances of C5, C6 and C9, which belong to the imidazole ring, are

correlated to the disappearance of the N-H proton of the pure drug (11.5 ppm), when it is loaded in the CD-MOF.

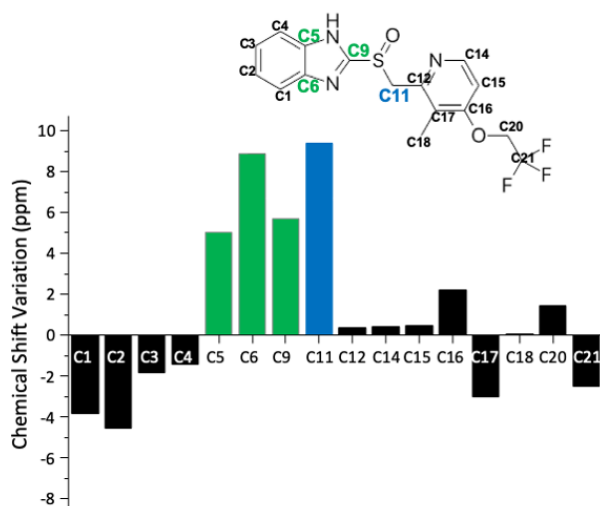


Figure 4.15:  $^{13}\text{C}$  chemical shift variation (ppm) of the carbon atoms of LSP pure and loaded in the MOF.

$^1\text{H}$ - $^1\text{H}$  exchange and  $^{13}\text{C}$ - $^1\text{H}$  CPMAS 2D experiments were recorded to get more information of the interaction of the drug (Figure 4.16). The CPMAS 2D experiment, gives the possibility to identify two protons that belong to the Lansoprazole (the  $\text{H}_{18}$  and  $\text{H}_{14}$  at 1.02 ppm and 6.55 ppm, respectively). A comparison between the 1D MAS spectrum of the pure lansoprazole, pure cyclodextrin, LPZ loaded CD-MOF and positive 1D projections from the  $^1\text{H}$ - $^1\text{H}$  2D exchange experiment was made, leading to a confirmation of this assignment. In the 2D CPMAS spectrum, one can notice also, the proximity between the proton 14 of the Lansoprazole and the C2, located inside the cavity, of the cyclodextrin. This is another confirmation of the location of the lansoprazole inside the cavity of the  $\gamma$ -CD.

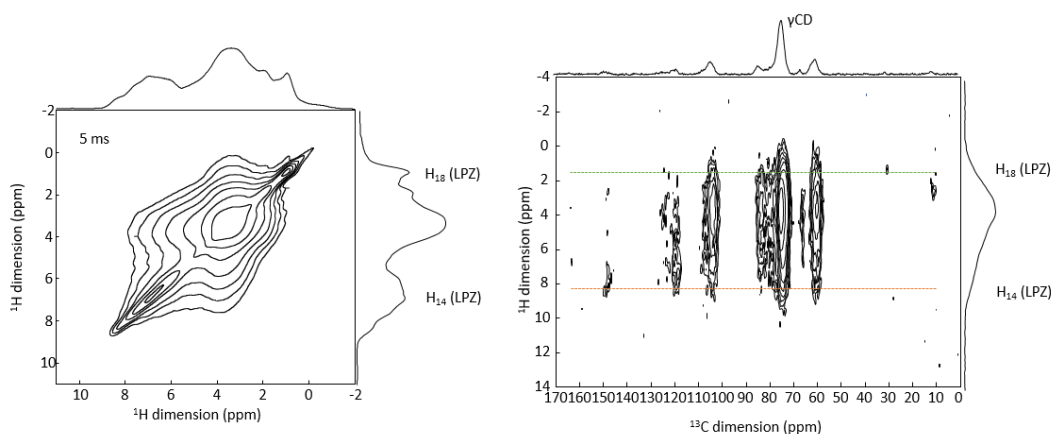


Figure 4.16:  $^1\text{H}$ - $^1\text{H}$  exchange (mixing time of 5 ms) and  $^{13}\text{C}$ - $^1\text{H}$  CPMAS (contact time of 2 ms) 2D NMR spectra of LPZ loaded CDMOF, recorded at 60 kHz (20 T).

Although some indications about LPZ and CD interaction were guessed from the  $^1\text{H}$  MAS NMR data, the strong signal overlap makes the data interpretation somewhat ambiguous.  $^{15}\text{N}$  and  $^{19}\text{F}$  were therefore considered.

$^{19}\text{F}$  nucleus is an interesting spy in these materials as there is only one fluorine atom in the compound ( $^{19}\text{F}$  1D spectrum shows in Figure 4.17), which belongs to the drug. A shift of the resonance is observed upon drug loading, indicating interactions between the drug and the carrier.

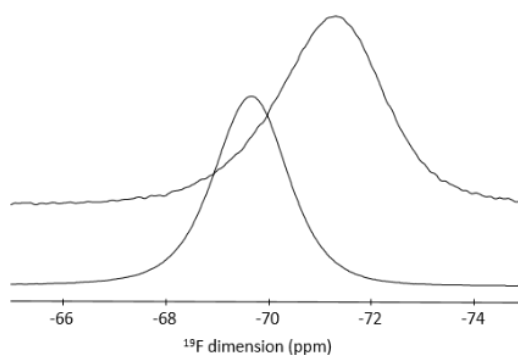


Figure 4.17:  $^{19}\text{F}$  MAS NMR spectra of LPZ (below) and LPZ loaded CD-MOF (above), recorded at 30 kHz (11.6 T).

Another nucleus of interest is  $^{15}\text{N}$ , also because it is present only in the drug. However, the low natural abundance of  $^{15}\text{N}$  (< 1%) and little amount of drug loaded (< 25 wt%) makes the NMR measurements highly challenging. Indeed, while a  $^{15}\text{N}$  CPMAS NMR spectrum of the pure LPZ could be obtained in a 4 mm room temperature MAS probe in a couple of hours (Figure 4.18), no signal was detected for the LPZ@ $\gamma$ -CDMOFs after 2.5 days of acquisition time.

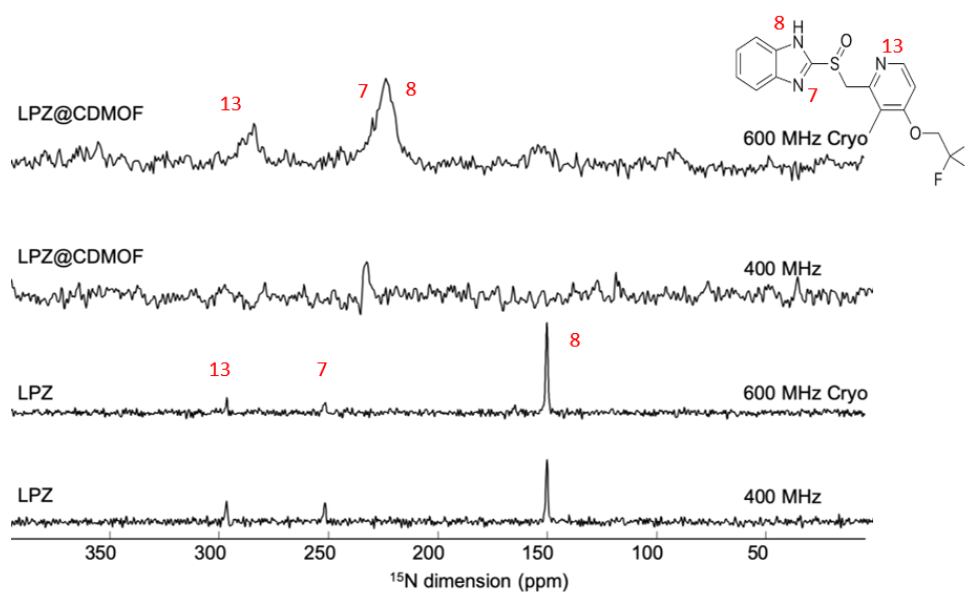


Figure 4.18:  $^{15}\text{N}$  CPMAS NMR spectra of LPZ and LPZ@ $\gamma$ -CDMOF recorded on a 400 MHz NMR spectrometer using a 4 mm probehead and on a 600 MHz NMR spectrometer using a CPMAS CryoProbe.

In formulated drugs, significant  $^{15}\text{N}$  NMR sensitivity gain have been obtained using dynamic nuclear polarization (DNP-MAS) NMR<sup>20</sup>. However, CD-MOFs are unstable in the solvents that are required for DNP-MAS to work. Hence, we chose an alternative emerging solution: the cryoprobe technology developed by Bruker Biospin. Up to now, the CPMAS CryoProbe has mostly been used for biomolecules<sup>21,22</sup>. The principle of the solide CryoProbe is similar to the liquid one: the goal is to cool to liquid nitrogen temperature all electronic components, notably the probe and preamp circuits, while keeping the sample at room temperature. In liquid, this allows a strong reduction of the noise, hence a sensitivity gain of 4.

The  $^{15}\text{N}$  CPMAS NMR spectra of L郑 and the LPZ loaded  $\gamma$ -CDMOFs were recorded at Bruker Biospin (Falläden, Switzerland) by P. Florian and Drs. Alian Hassan and Barbara Perrone. Despite the relatively small amount of drug loaded (below 25%) and broadness of the signals (due to chemical shift distributions), the  $^{15}\text{N}$  CPMAS NMR spectrum of the drug-loaded sample could be obtained at natural abundance in about 2 days due to significant signal enhancement provided by the novel cryogenically cooled 3.2 mm HCN CPMAS probe. On this spectrum, a strong shift of one  $^{15}\text{N}$  resonance is observed, which unambiguously confirms that the LPZ molecules are deprotonated when loaded in the CD-MOFs, possibly because of their basic inner microenvironment.

Despite using a high magnetic field (20 T) and fast MAS (60 kHz), the  $^1\text{H}$  MAS NMR spectrum of LPZ loaded CD-MOF only shows broad peaks with extremely low resolution (Figure 4.8a), hence 2D  $^1\text{H}$ - $^1\text{H}$  NMR was, as mentioned above, of limited use.

Using a dedicated  $^1\text{H}$ - $^{19}\text{F}$ -X probe, a  $^1\text{H}$ - $^{19}\text{F}$ - $^{13}\text{C}$  triple CPMAS NMR experiment was performed at ILV Versailles. The initial  $^1\text{H}$ - $^{19}\text{F}$  is used to benefit from the shorter relaxation  $T_1$  of  $^1\text{H}$  (shorter than 1 s) compared to the one of  $^{19}\text{F}$  (> 5 s). This experiment allows the selection of the carbon atoms in the proximity of the fluorine atom. The resulting  $^{13}\text{C}$  NMR spectrum (Figure 4.19) is compared to the  $^1\text{H}$ - $^{13}\text{C}$  CP NMR spectrum, in which all  $^{13}\text{C}$  atoms are present (since both the drug and the CD have protons to transfer magnetization to the carbon atoms), the spectra are normalized to the CD peak at 73 ppm. In the  $^{19}\text{F}$ - $^{13}\text{C}$  CPMAS, one can notice that the  $\text{CF}_3$  and C20 carbons of the LPZ have higher intensity, expected as these are the closest C atoms to the  $^{19}\text{F}$  nuclei. There is also significant signal for the  $^{13}\text{C}$  of the  $\gamma$ -CD, indicating its close spatial proximity to the drug. Among the  $^{13}\text{C}$  of the  $\gamma$ -CD, the one labeled C6 (which corresponds to the  $\text{CH}_2\text{OH}$ ) has higher intensity than the other  $\gamma$ -CD carbon atoms. This indicates that the  $\text{CF}_3$  is in close contact with the  $\text{CH}_2\text{OH}$  of the CD. The drug is most probably bend and the  $\text{CF}_3$  group is located outside of the CD cavity. This experiment validates the molecular model, showed in Figure 4.13, in which the  $\text{CF}_3$  is found between two CDs (zoom on the  $\text{CF}_3$  in the molecular simulation showed in Figure 4.20).

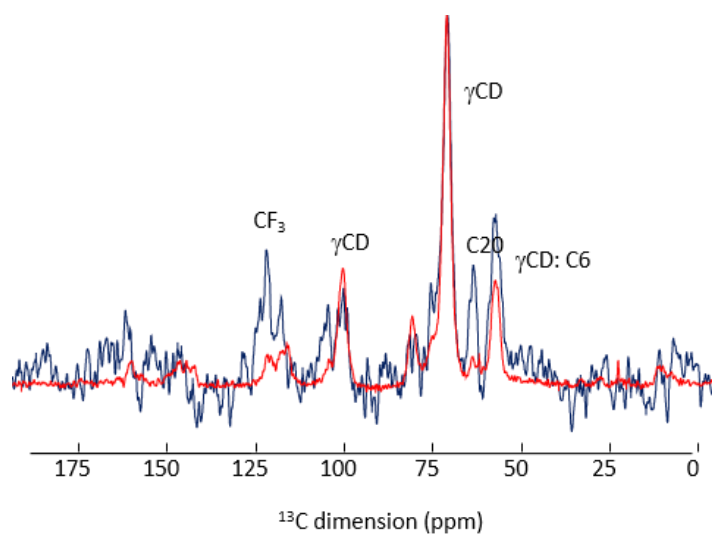


Figure 4.19:  $^1\text{H} \rightarrow ^{13}\text{C}$  (red) and  $^{19}\text{F} \rightarrow ^{13}\text{C}$  (blue) CPMAS NMR spectra of LPZ loaded CD-MOF. The spectra are normalized to the  $^{13}\text{C}$  resonance of  $\gamma$ -CD at 73 ppm. The lines are assigned.

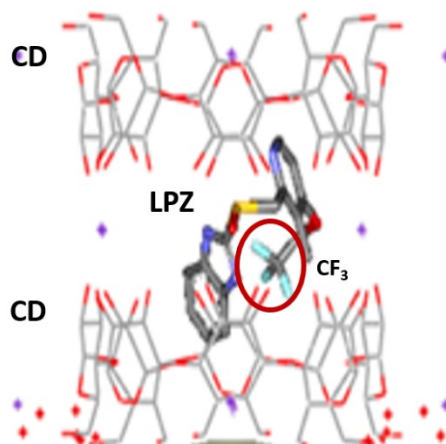


Figure 4.20: Simulated configurations of LPZ in  $\gamma$ -CD-MOF.

## 5. Conclusions

Lansoprazole, a proton-pump inhibitor used to reduce the production of acid in the stomach and which has been also recently identified as an antitubercular prodrug, is a drug that presents long-term stability problems and that readily degrades in non-neutral pH. Development of new DDS are particularly important for these drugs.  $\gamma$ -CD-MOFs, which represent an environment-friendly and biocompatible class of MOFs, have been selected as they show high payload. Crystalline LPZ-loaded CD-MOFs with homogeneous sizes and high payload were successfully synthesized via co-crystallization.

Using ssNMR spectroscopy, new atomic-level insights about the interactions between CTAB/LPZ and CD-MOFs as well as the localization and configuration of CTAB and LPZ in CD-MOFs have been obtained. The limited information obtained by  $^1\text{H}$  MAS NMR spectra were supported performing a  $^{13}\text{C}$  triple CPMAS experiment, thanks to the use of a particular  $^1\text{H}$ - $^{19}\text{F}$ - $^{13}\text{C}$  triple-resonance probe. Moreover, the possibility to perform  $^{15}\text{N}$  NMR experiments at natural abundance with the cryoprobe in Zurich complemented the study of the structure. These data were further supported by molecular simulation, which also confirmed a much stronger interaction between LPZ and CD-MOFs than that between CTAB and CD-MOFs. This ensemble of experimental data and simulation explains why LPZ successfully replaces CTAB during the drug loading inside the cavity of  $\gamma$ -CD.

## 6. Experimental ssNMR section

All the samples were finely ground into powders and packed into a zirconia rotor of the appropriate size. Then, the full rotor was dried at 40° C under vacuum for at least 12 h prior to the NMR experiments.

The NMR spectra were acquired using TopSpin 3.5 Bruker Software and processed with the Dmfit program<sup>23</sup>. The chemical shift are referenced to <sup>1</sup>H and <sup>13</sup>C of TMS at 0 ppm, to CFC<sub>3</sub> at 120 ppm for <sup>19</sup>F.

<i>Nucleus/i</i>	<i>Probe and MAS</i>	<i>Pulse sequence</i>	<i>Main Parameters</i>	<i>Time required</i>
<sup>19</sup> F	<sup>1</sup> H- <sup>19</sup> F-X triple-resonance 2.5 mm probe <sup>24</sup> , with a spinning rate of 30 kHz	CP-MAS	Recycle delay of 3 s; 90° pulse on <sup>1</sup> H of 3 μs; contact time of 1 ms; 1H CW decoupling applied during acquisition.	Around 50 minutes
<sup>1</sup> H- <sup>19</sup> F- <sup>13</sup> C		triple CP-MAS		5 days

Table 4.1: NMR spectra recorded on a Bruker 500 MHz (11.6 T) WB NMR spectrometer.

<i>Nucleus/i</i>	<i>Probe and MAS</i>	<i>Pulse sequence</i>	<i>Main Parameters</i>	<i>Time required</i>
<sup>13</sup> C	HX 4 mm probe, with a spinning rate of 10 kHz.	CP-MAS	Recycle delay of 3 s; 90° pulse on <sup>1</sup> H of 3.5 μs; contact time of 3.5 ms; <sup>1</sup> H SPINAL-64 decoupling applied during acquisition (RF field of 70 kHz).	Around 50 minutes
<sup>15</sup> N		CP-MAS	Recycle delay of 3.5 s; 90° pulse on <sup>1</sup> H of 3 μs; contact time of 6 ms; <sup>1</sup> H SPINAL-64 decoupling applied during acquisition.	9 hours-2 days

Table 4.2: NMR spectra were recorded on a 400 MHz (9.4 T) Bruker NMR spectrometer.

<i>Nucleus/i</i>	<i>Probe and MAS</i>	<i>Pulse sequence</i>	<i>Main Parameters</i>	<i>Time required</i>
$^1\text{H}$	HXY 1.3 mm probe in double mode, with a spinning rate of 60 kHz	Hahn Echo	Recycle delay of 3 s; 90° pulse of 2.5 $\mu\text{s}$ (RF field of 100 kHz); an inter-pulse delay synchronized with one rotor period.	less than 1 minute
$^1\text{H}\text{-}^1\text{H}$		Exchange	Recycle delay of 2s; 90° pulse of 2.5 $\mu\text{s}$ (RF field of 100 kHz); two different mixing times (5 and 10 ms); States procedure.	7 hours
$^{13}\text{C}\text{-}^1\text{H}$		CP-MAS	Recycle delay of 2 s; two different contact times (0.5 and 2 ms); $^1\text{H}$ SPINAL-64 decoupling during acquisition; States procedure.	14 hours

Table 4.3: NMR spectra recorded on a 850 MHz (20 T) WB Bruker NMR spectrometer.

<i>Nucleus/i</i>	<i>Probe and MAS</i>	<i>Pulse sequence</i>	<i>Main Parameters</i>	<i>Time required</i>
$^{15}\text{N}$	novel cryogenically cooled 3.2 mm HCN CPMAS probe (Biosolids CryoProbe™) <sup>21</sup> , with a spinning rate of 8 kHz (at 15°C).	CP-MAS	Recycle delay of 3 s; 90° pulse on $^1\text{H}$ of 3.2 $\mu\text{s}$ ; contact time of 5 ms; $^1\text{H}$ SPINAL-64 decoupling applied during acquisition.	30 minutes-2 days

Table 4.4: NMR spectra recorded on a Bruker 600 MHz (14 T) SB NMR spectrometer.

## References

- (1) Li, X.; Porcino, M.; Martineau-Corcus, C.; Guo, T.; Xiong, T.; Zhu, W.; Patriarche, G.; Péchoux, C.; Perrone, B.; Hassan, A.; Kümmerle, R.; Michelet, A.; Zehnacker-Rentien, A.; Zhang, J.; Gref, R. Efficient Incorporation and Protection of Lansoprazole in Cyclodextrin Metal-Organic Frameworks. *International Journal of Pharmaceutics* **2020**, *585*, 119442–119453.
- (2) Rybniker, J.; Vocat, A.; Sala, C.; Busso, P.; Pojer, F.; Benjak, A.; Cole, S. T. Lansoprazole Is an Antituberculous Prodrug Targeting Cytochrome Bc1. *Nature Communications* **2015**, *6* (1), 1–8.
- (3) DellaGreca, M.; Iesce, M. R.; Previtera, L.; Rubino, M.; Temussi, F.; Brigante, M. Degradation of Lansoprazole and Omeprazole in the Aquatic Environment. *Chemosphere* **2006**, *63* (7), 1087–1093.
- (4) Ngan, Y.; Gupta, M. A Comparison between Liposomal and Nonliposomal Formulations of Doxorubicin in the Treatment of Cancer: An Updated Review. *Archives of Pharmacy Practice* **2016**, *7* (1), 1–13.
- (5) Ekpe, A.; Jacobsen, T. Effect of Various Salts on the Stability of Lansoprazole, Omeprazole, and Pantoprazole as Determined by High-Performance Liquid Chromatography. *Drug Development and Industrial Pharmacy* **1999**, *25* (9), 1057–1065.
- (6) Battu, S.; Pottabathini, V. Hydrolytic Degradation Study of Lansoprazole, Identification, Isolation and Characterisation of Base Degradation Product. *AJAC* **2015**, *6* (2), 145–155.
- (7) Liu, K.-H.; Kim, M.-J.; Jung, W. M.; Kang, W.; Cha, I.-J.; Shin, J.-G. Lansoprazole Enantiomer Activates Human Liver Microsomal CYP2C9 Catalytic Activity in a Stereospecific and Substrate-Specific Manner. *Drug Metab Dispos* **2005**, *33* (2), 209–213.
- (8) DiGiacinto, J. L.; Olsen, K. M.; Bergman, K. L.; Hoie, E. B. Stability of Suspension Formulations of Lansoprazole and Omeprazole Stored in Amber-Colored Plastic Oral Syringes. **2000**, *34*, 600–605.
- (9) Li, X.; Guo, T.; Lachmanski, L.; Manoli, F.; Menendez-Miranda, M.; Manet, I.; Guo, Z.; Wu, L.; Zhang, J.; Gref, R. Cyclodextrin-Based Metal-Organic Frameworks Particles as Efficient Carriers for Lansoprazole: Study of Morphology and Chemical Composition of Individual Particles. *International Journal of Pharmaceutics* **2017**, *531* (2), 424–432.
- (10) Rajkumar, T.; Kukkar, D.; Kim, K.-H.; Sohn, J. R.; Deep, A. Cyclodextrin-Metal–Organic Framework (CD-MOF): From Synthesis to Applications. *Journal of Industrial and Engineering Chemistry* **2019**, *72*, 50–66.
- (11) Michida, W.; Nagai, A.; Sakuragi, M.; Kusakabe, K. Discrete Polymerization of 3,4-Ethylenedioxythiophene in Cyclodextrin-Based Metal-Organic Framework. *Crystal Research and Technology* **2018**, *53* (4), 1700142–1700148.
- (12) Smaldone, R. A.; Forgan, R. S.; Furukawa, H.; Gassensmith, J. J.; Slawin, A. M. Z.; Yaghi, O. M.; Stoddart, J. F. Metal-Organic Frameworks from Edible Natural Products. *Angewandte Chemie International Edition* **2010**, *49* (46), 8630–8634.
- (13) Furukawa, Y.; Ishiwata, T.; Sugikawa, K.; Kokado, K.; Sada, K. Nano- and Microsized Cubic Gel Particles from Cyclodextrin Metal-Organic Frameworks. *Angew. Chem. Int. Ed.* **2012**, *51* (42), 10566–10569.
- (14) Garcia, A.; Leonardi, D.; Salazar, M. O.; Lamas, M. C. Modified B-Cyclodextrin Inclusion Complex to Improve the Physicochemical Properties of Albendazole. Complete In Vitro Evaluation and Characterization. *PLoS ONE* **2014**, *9* (2), 1–8.
- (15) Ye, Y.; Sun, Y.; Zhao, H.; Lan, M.; Gao, F.; Song, C.; Lou, K.; Li, H.; Wang, W. A Novel Lactoferrin-Modified  $\beta$ -Cyclodextrin Nanocarrier for Brain-Targeting Drug Delivery. *International Journal of Pharmaceutics* **2013**, *458* (1), 110–117.
- (16) Ulmius, J.; Lindman, B.; Lindblom, G.  $^1\text{H}$ ,  $^{13}\text{C}$ ,  $^{35}\text{Cl}$ , and  $^{81}\text{Br}$  NMR of Aqueous Hexadecyltrimethylammonium Salt Solutions: Solubilization, Viscoelasticity, and Counterion Specificity. *Journal of Colloid and Interface Science* **1978**, *65* (1), 88–97.

- (17) Upreti, M.; Strassburger, K.; Chen, Y. L.; Wu, S.; Prakash, I. Solubility Enhancement of Steviol Glycosides and Characterization of Their Inclusion Complexes with Gamma-Cyclodextrin. *International Journal of Molecular Sciences* **2011**, *12* (11), 7529–7553.
- (18) Ramulu, K.; Rao, B. M.; Rao, N. S. Identification, Isolation and Characterization of Potential Degradation Product in Lansoprazole Drug Substance. *RJC* **2013**, *6*, 274–283.
- (19) Kritskiy, I.; Volkova, T.; Surov, A.; Terekhova, I.  $\gamma$ -Cyclodextrin-Metal Organic Frameworks as Efficient Microcontainers for Encapsulation of Leflunomide and Acceleration of Its Transformation into Teriflunomide. *Carbohydrate Polymers* **2019**, *216*, 224–230.
- (20) Ni, Q. Z.; Yang, F.; Can, T. V.; Sergeyev, I. V.; D’Addio, S. M.; Jawla, S. K.; Li, Y.; Lipert, M. P.; Xu, W.; Williamson, R. T.; Leone, A.; Griffin, R. G.; Su, Y. In Situ Characterization of Pharmaceutical Formulations by Dynamic Nuclear Polarization Enhanced MAS NMR. *J. Phys. Chem. B* **2017**, *121* (34), 8132–8141.
- (21) Hassan, A.; Quinn, C. M.; Struppe, J.; Sergeyev, I. V.; Zhang, C.; Guo, C.; Runge, B.; Theint, T.; Dao, H. H.; Jaroniec, C. P.; Berbon, M.; Lends, A.; Habenstein, B.; Loquet, A.; Kummerle, R.; Perrone, B.; Gronenborn, A. M.; Polenova, T. Sensitivity Boosts by the CPMAS CryoProbe for Challenging Biological Assemblies. *Journal of Magnetic Resonance* **2020**, *311*, 106680–106691.
- (22) Gibbs, E.; Perrone, B.; Hassan, A.; Kummerle, R.; Kriwacki, R. NPM1 Exhibits Structural and Dynamic Heterogeneity upon Phase Separation with the P14ARF Tumor Suppressor. *Journal of Magnetic Resonance* **2020**, *310*, 106646–106653.
- (23) Massiot, D.; Fayon, F.; Capron, M.; King, I.; Le Calvé, S.; Alonso, B.; Durand, J.-O.; Bujoli, B.; Gan, Z.; Hoatson, G. Modelling One- and Two-Dimensional Solid-State NMR Spectra: Modelling 1D and 2D Solid-State NMR Spectra. *Magn. Reson. Chem.* **2002**, *40* (1), 70–76.
- (24) Martineau, C.; Engelke, F.; Taulelle, F. Multiple Resonance Heteronuclear Decoupling under MAS: Dramatic Increase of Spectral Resolution at Moderate Magnetic Field and MAS Frequencies. *Journal of Magnetic Resonance* **2011**, *212* (2), 311–319.

## Chapter 5

Surface modified nanoMIL-100(Al) as  
drug carrier for phosphated drugs



## 1. Introduction

MIL-100(Fe) nanoparticles based on benzene tricarboxylate (BTC) as linker and  $\text{Fe}^{3+}$  ions as metal center, have emerged as a new class of biodegradable and non-toxic materials of high interest for biomedical application. The particles showed an important drug loading capacity due to their high pore volume and surface area<sup>1-3</sup>. The nanoparticles of MIL-100(Fe), nanoMIL-100(Fe), however showed a strong tendency to aggregate in aqueous medium, requiring storage of the particles in an ethanol solution. The aggregation process was a problem not only for the long term stability of the nanoparticles, but also for their use as drug delivery system, as the body is an aqueous medium itself.

As reported in Chapter 1, surface modification is a common strategy to improve the colloidal stability of nanoparticles. This strategy was employed for nanoMIL-100(Fe) particles, which were coated with CD derivatives. The coated particles proved very stable and the CD coating did not seem to enter into the pores of the nanoMOF, contrary to what was observed with PEG coating, because of its size is larger than the pore windows of the MIL-100 framework<sup>4</sup>. The potential applications of these coated nanoparticles have been clearly demonstrated, but little information are known about the interaction at the atomic level between the coating and the nanoparticles surface sites. Solid-state NMR spectroscopy is in principle an ideal spectroscopic technique to access this type of information. However, the presence of strong paramagnetic centers in nanoMIL-100(Fe) strongly reduces the relaxation time and hence the amount of information that the NMR analysis can give. Therefore, we chose to investigate the diamagnetic analog of nanoMIL-100(Fe), namely nanoMIL-100(Al), assuming similar drug/host interactions could occur in both systems<sup>5</sup>.

NanoMIL-100(Al) particles are a diamagnetic analog of the MIL-100(Fe)<sup>6</sup>, they have similar crystalline topology, formed by hybrid supertetrahedra which assemble giving rise to a porous zeotypic architecture. Similarly to nanoMIL-100(Fe), nanoMIL-100(Al) particles present two different types of mesoporous cages (25 Å and 29 Å) delimited by microporous windows (5.6 Å and 8.6 Å,

respectively). It was shown that large amount of drugs can be incorporated, also, in these Al-based nanoparticles. Drug loading was made by simple impregnation with aqueous drug solutions overnight.

Interestingly, the coating approach used for the nanoMIL-100(Fe) could be successfully applied to MIL-100(Al) nanoparticles<sup>4</sup>. The coatings were made in the same way by a green synthesis approach, simply mixing the coating particles with the MOF particles overnight in aqueous solution. Phosphate-Cyclodextrins (CD-P) were used for the coating, because of the possibility of coordination with the available Al (III) CUS sites at the surface. CD-Ps are too bulky to bypass pores windows of the MOF and they remain adsorbed on the surface of the MOF (Figure 5.1).

Adenosine triphosphate (ATP) was chosen as drug of interest. It is a neurotransmitter with a crucial role in metabolism, which is believed to have a strong affinity with the aluminum species of the nanoMOF framework. The samples were synthesized by Ioanna Christodoulou in the group of Prof. Ruxandra Gref (Institut des Sciences Moléculaires d'Orsay).

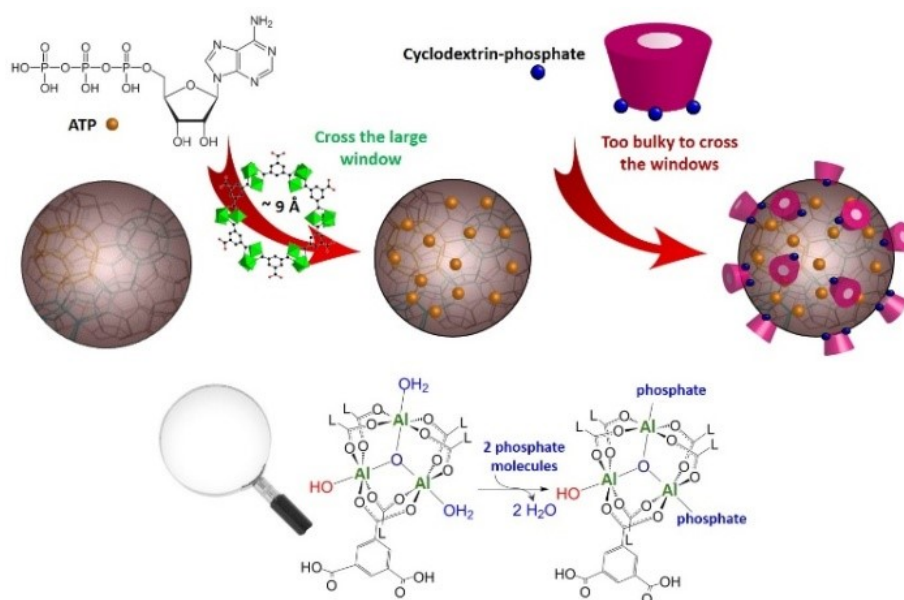


Figure 5.1: Schematic representation of MIL-100(Al) nanoparticles loaded with ATP and then coated with CD-P. On the bottom, there is a focus on Al trimers coordinated to trimesate ligands (L). Two molecules of bound water can be replaced either by phosphates from the drug or by phosphate grafted on the cyclodextrin molecules<sup>7</sup>.

Morphology and size of the solids were observed by Transmission Electron Microscopy (TEM) (Figure 5.2), under a JEOL JEM-1400 microscope with acceleration voltage of 120 kV. Nanoparticle suspensions were deposited on copper grids, left to dry and observed without further staining. All TEM images showed no dissolution of the nanoparticles.

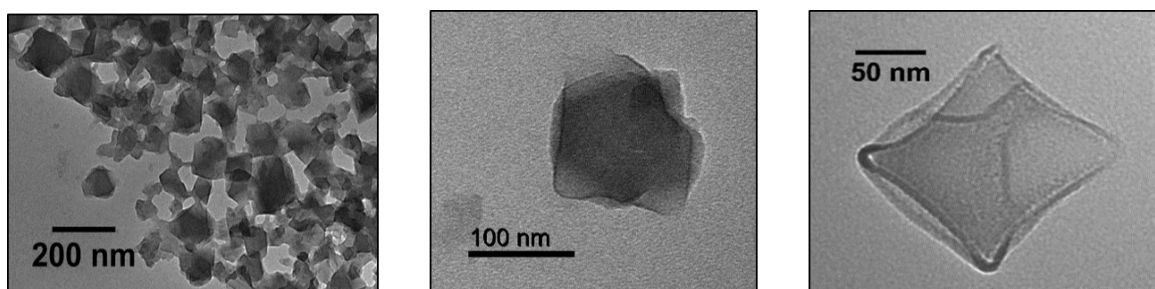


Figure 5.2: TEM images of CD-P coated nanoMIL-100(Al).

nanoMOF carries should be stable until the delivery of the drug on the target. The nanoparticles should be biodegraded, i.e. decomposed in non-toxic degraded products that should be removed from the body without any toxic effects. Degradation reaction of original MOF in mimetic physiological medium, as phosphate buffer PBS, as shown by M. Vuong in her Master thesis<sup>8</sup>, seems to occur through substitution of water ligand and trimesate ligand by phosphate ions<sup>9</sup>. Consequently, free linker is produced in the form of trimesic acid. Study of nanoMIL-100(Al) morphology after degradation are made by TEM (Figure 5.3). The faceted shape and the size are retained, but the degradation seems occur through formation of holes in the nanoparticles.

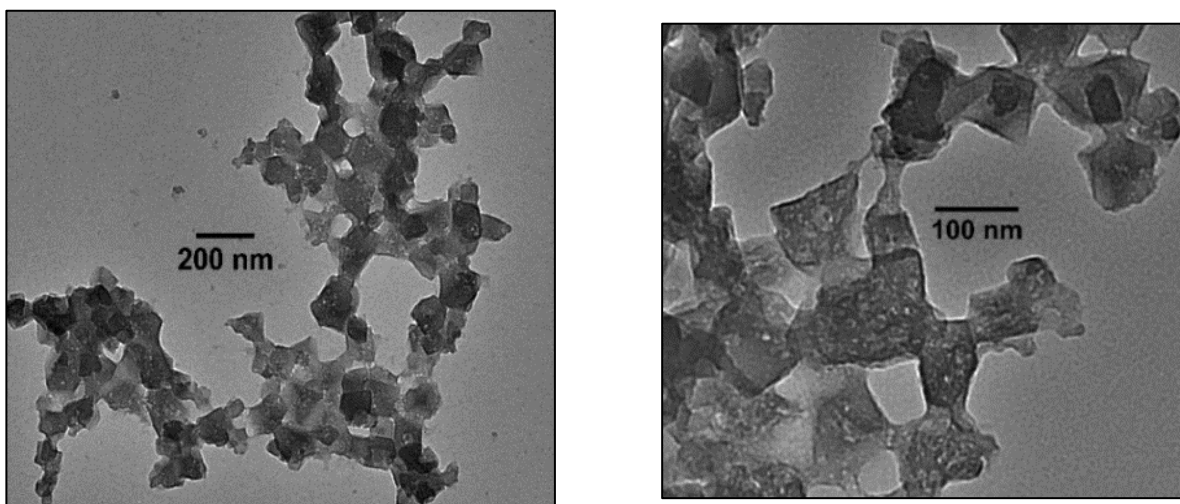


Figure 5.3: TEM images of nanoMIL-100(Al) degraded 48 hours in PBS solution.

Understanding this system to the atomic level and studying the interactions between the coating and the surface of the MOF, and further drug loaded inside the pores can help guide the engineering of further surface modifications and better understanding the delivery process of the drug<sup>7</sup>, thanks to the use of solid-state NMR. During the investigation, several challenges were to be fight and the best approach had to be found and will be shown in detail. This study has been published in 2019<sup>7</sup> (“New insights on the supramolecular structure of highly porous core–shell drug nanocarriers using solid-state NMR spectroscopy”, Marianna Porcino, Ioanna Christodoulou, Mai Dang Le Vuong, Ruxandra Gref, and Charlotte Martineau-Corcos, RSC Adv., 9 (2019), 32472).

## 2. The effect of particle size on MIL-100(Al)

Before to start the investigation of the DDS, it is important to focus a little bit on the MOF used: nanoMIL-100(Al). If lots of structural information are available for microMIL-100(Al)<sup>6,10</sup>, nanoMIL-100(Al) is still an unexplored material. In this section, a comparison from atomic level point of view, thanks to ssNMR experiments, of micro- and nano-size MIL-100(Al) is given.

<sup>1</sup>H and <sup>13</sup>C nuclei are first investigated. No differences could be noticed in the spectra recorded and showed in Figure 5.4. Both <sup>1</sup>H MAS NMR spectra show resonances around 9.11 ppm belong to the aromatic protons of the MOF. The different hydration state of the micro- and nano- MIL-100(Al) can

be noticed by the different intensity of the  $^1\text{H}$  resonance belonging to the water molecules around 5 ppm. The  $^{13}\text{C}$  CPMAS NMR spectra performed on both samples are quite similar, showing  $^{13}\text{C}$  resonances around 170 ppm, belonging to carboxyl groups and around 135 ppm belonging to aromatic carbons.

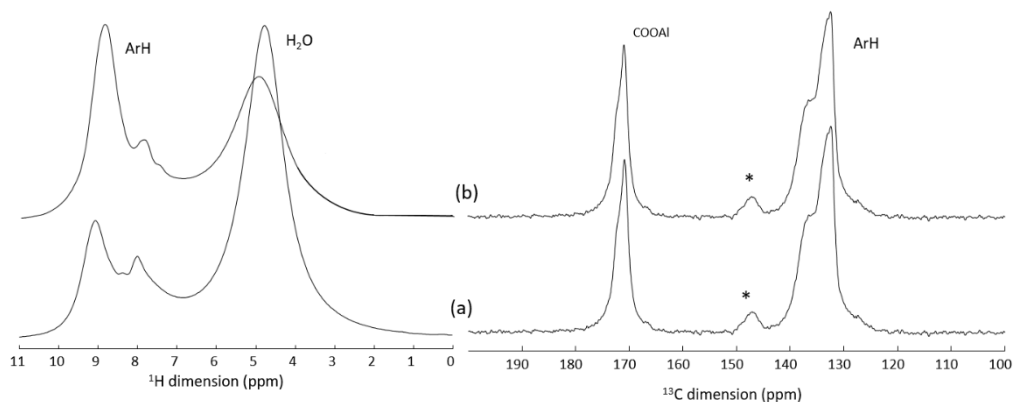


Figure 5.4:  $^1\text{H}$  (left) (20 T, 20 kHz) and  $^{13}\text{C}$  (right) (9.4 T, 10 kHz) MAS NMR spectra microMIL-100(Al) (a) and nanoMIL-100(Al) (b). The lines are assigned. \* indicate traces of impurities.

Noticing any difference on the  $^1\text{H}$  and  $^{13}\text{C}$  environment point of view,  $^{27}\text{Al}$  MAS NMR experiments were performed. The 1D NMR spectra do not show any significant difference, except for a slight modification on the right part of the spectrum of the nanoMIL-100(Al) (Figure 5.5).

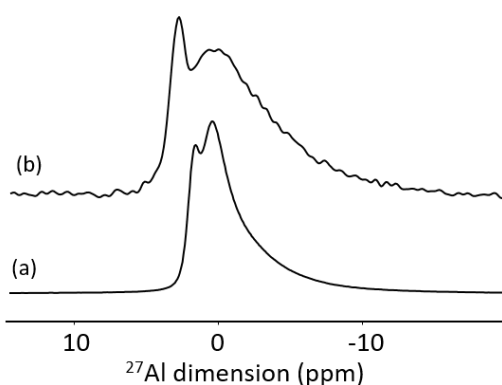


Figure 5.5:  $^{27}\text{Al}$  MAS NMR of microMIL-100(Al) (a) and nanoMIL-100(Al) (b) recorded at 20 kHz on a 20 T spectrometer.

To go further in the analysis of the aluminum environment,  $^{27}\text{Al}$  species of the MIL-100(Al) were identified and compared with the information already present in the literature<sup>6,10</sup>, using Multiple-

quantum MAS (MQ-MAS) NMR experiments. This pulse sequence can be useful to separate quadrupolar nuclei (such as  $^{27}\text{Al}$ ) species in the indirect dimension. The  $^{27}\text{Al}$  MQMAS NMR spectra of the nanoMIL-100(Al) were compared with the ones of the microMIL-100(Al), recorded in the same conditions at the same magnetic fields (9.4 T and 20 T) (Figure 5.6 and Figure 5.7).

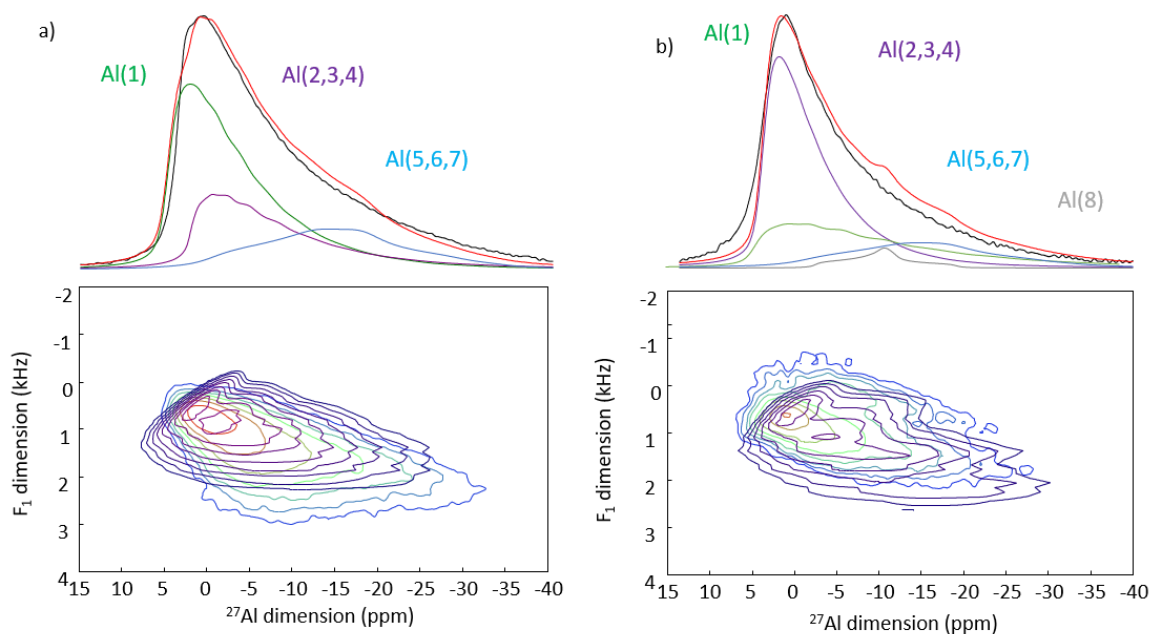


Figure 5.6:  $^{27}\text{Al}$  MQMAS NMR spectra of the microMIL-100(Al) (a) and nanoMIL-100(Al) (b), recorded at 25 kHz (on a 9.4 T spectrometer). The simulation were made using Czezik and QMAS1/2 mode on Dmfit program<sup>11</sup>.

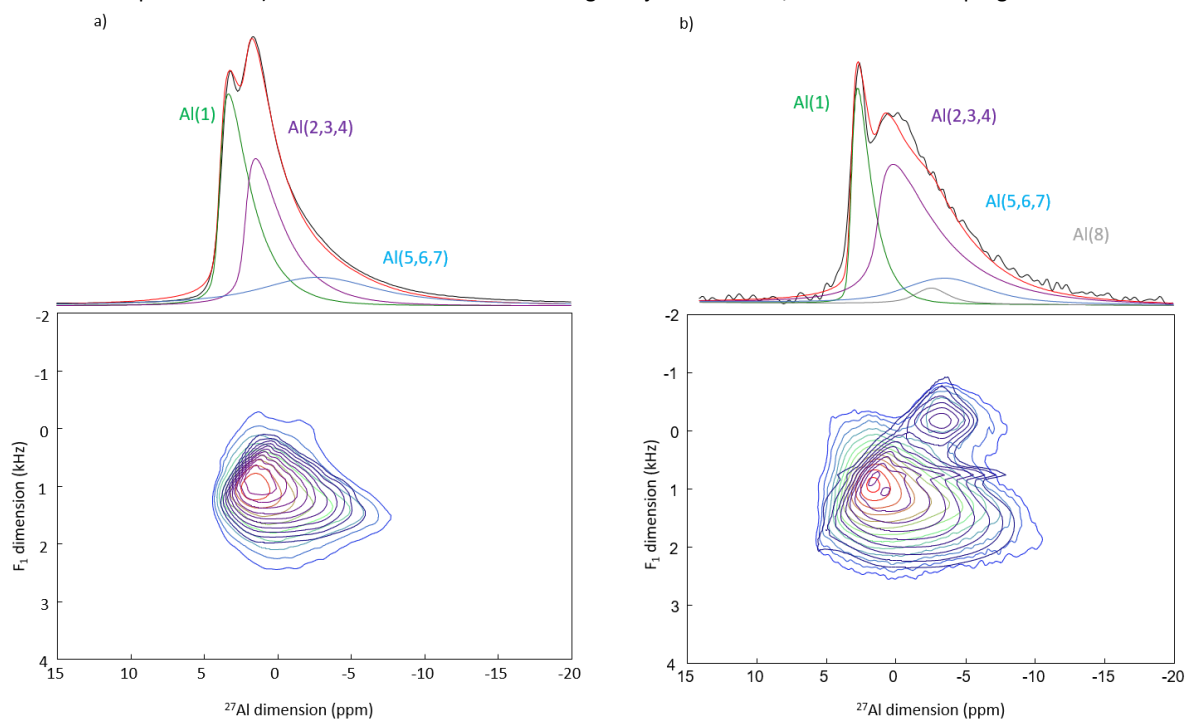


Figure 5.7:  $^{27}\text{Al}$  MQMAS NMR spectra of the microMIL-100(Al) (a) and nanoMIL-100(Al) (b), recorded at 20 kHz (on a 20 T spectrometer). The simulation were made using Czezik and QMAS1/2 mode on Dmfit program<sup>11</sup>.

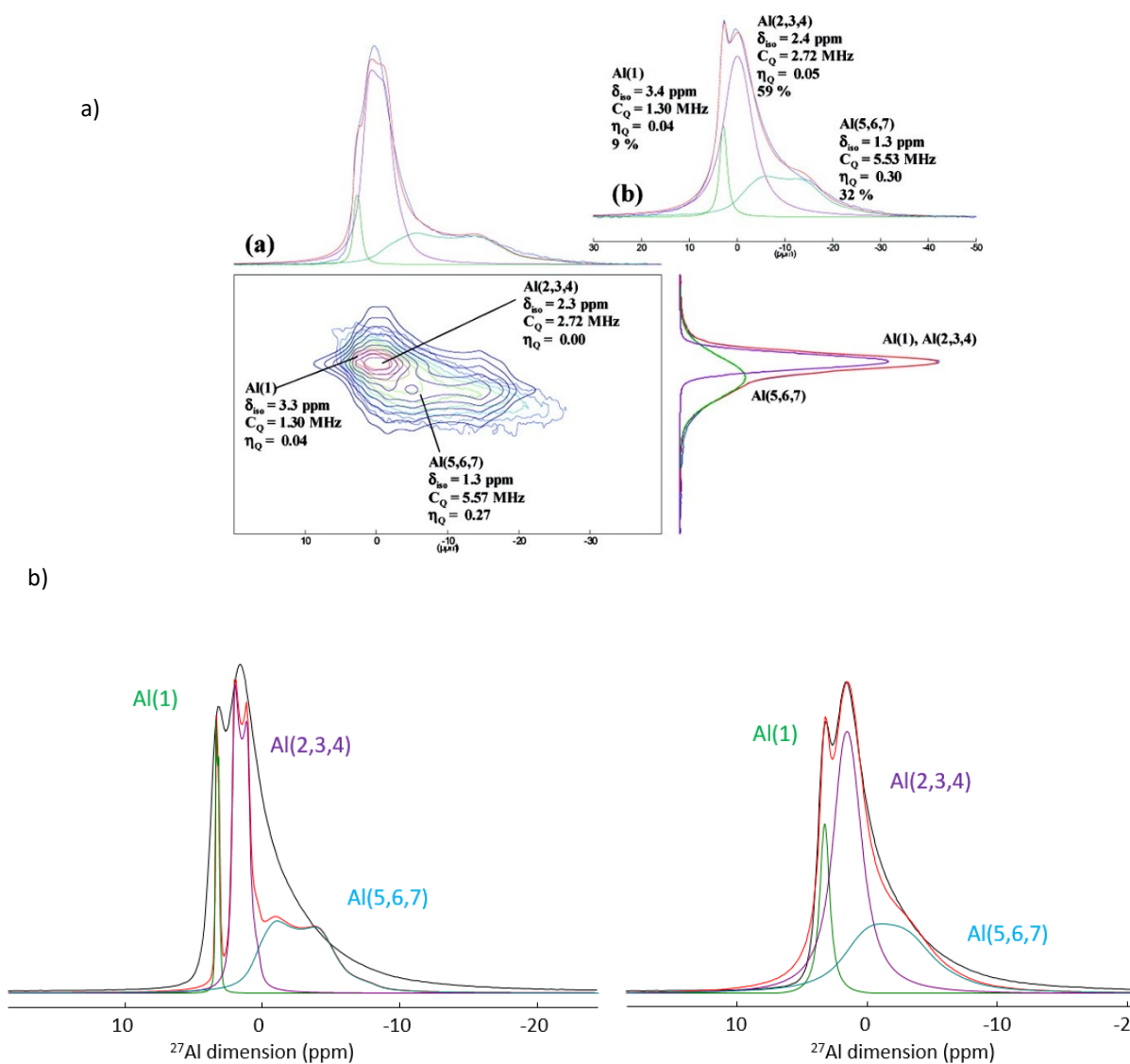


Figure 5.8: a)  $^{27}\text{Al}$  MQMAS (a) and 1D MAS (b) NMR spectra of the microMIL-100(Al) (Source: Volklinger *et al.*<sup>6,10</sup>); b)  $^{27}\text{Al}$  1D MAS NMR of micro MIL-100(Al), fitted with the parameters of the literature (left) and increasing the broadening parameter (right).

Both spectra show three overlapping isotropic six coordinated  $^{27}\text{Al}$  resonances (the name of the species is taken by the crystal structure of the microMIL-100(Al)<sup>6,10</sup>, details are given in Table 5.1) with contrasted anisotropic line-shapes due to the difference in quadrupolar parameters, as reported previously by Volklinger *et al.*<sup>6,10</sup> (shown in Figure 5.8). One can notice the presence of an additional resonance located in the region around -1 and -5 ppm, present only in the spectrum of the nanoMIL-100(Al) and never identified before.

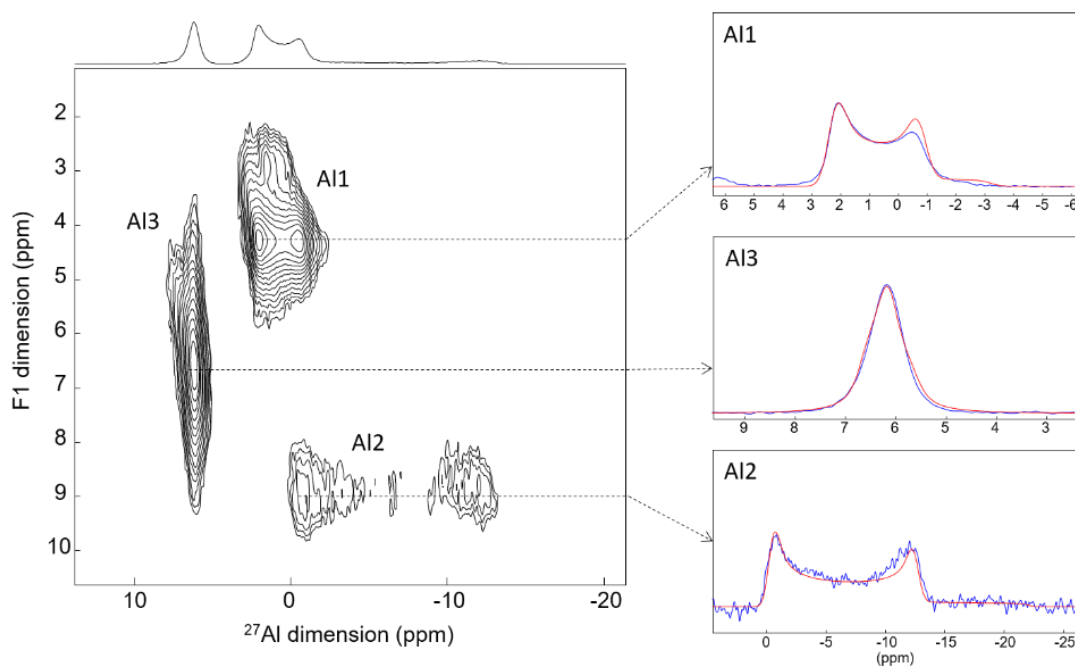


Figure 5.9:  $^{27}\text{Al}$  MQMAS NMR spectrum of MIL-96. (Source: Benzaqui *et al.*<sup>12</sup>)

Trying to reproduce the spectrum with the parameters reported by Volkringer *et al.*<sup>6,10</sup>, it noticed that an important line broadening was employed by the authors (Figure 5.8b). In contrast, the  $^{27}\text{Al}$  MQMAS of MIL-96<sup>12</sup> (Figure 5.9), which contains the same trimesate linker than MIL-100, but different inorganic building units, shows very well defined resonances. This MOF has much smaller pore size, and is therefore much more rigid than MIL-100(Al). The larger pore sizes of MIL-100(Al) and the discreet Al-triclusters (rather than infinite chains), could lead to a much more flexible 3D network, hence lead to local disorder. While a slight line broadening could appear enough to model the micron-sized MOF, this clearly could not reproduce the spectrum of the nanosized particles. Therefore, the  $^{27}\text{Al}$  MQMAS NMR spectra of micro and nanoMIL-100(Al) were deconvoluted using a Czejk-type model (Figure 5.6 and 5.7), which lead to a much better adjustment of the experimental spectra.

$^{27}\text{Al}$ six coordinated sites			<i>microMIL-100(Al)</i>	<i>microMIL-100(Al)</i>		<i>nanoMIL-100(Al)</i>	
			<i>(literature, 11.7 T at 30 kHz)</i>	<i>(9.4 T, 25 kHz)</i>	<i>(20 T, 20 kHz)</i>	<i>(9.4 T, 25 kHz)</i>	<i>(20 T, 20 kHz)</i>
<b>BULK</b>	Al (1)	%	9	43	41	26	26
		$\delta_{\text{iso}}$	3.3 ppm	4 ppm	3.95 ppm	4 ppm	3.95 ppm
		$C_Q$	1.3 MHz	3.5 MHz	3.5 MHz	3 MHz	3 MHz
		$\eta_Q$	0.04	0.61	0.61	0.61	0.61
	Al (2,3,4)	%	59	36	37	54	55
		$\delta_{\text{iso}}$	2.3 ppm	2.5 ppm	2.19 ppm	2.5 ppm	2.19 ppm
		$C_Q$	2.72 MHz	3.85 MHz	3.85 MHz	4.84 MHz	4.87 MHz
		$\eta_Q$	0	0.61	0.61	0.61	0.61
	Al (5,6,7)	%	32	21	22	16	14
		$\delta_{\text{iso}}$	1.3 ppm	0.24 ppm	0.24 ppm	0.30 ppm	0.30 ppm
		$C_Q$	5.57 MHz	4.83 MHz	4.83 MHz	5 MHz	5 MHz
		$\eta_Q$	0.27	0.65	0.65	0.65	0.65
<b>New site</b>	Al (8)	%				4	5
		$\delta_{\text{iso}}$				-1.50 ppm	-1.50 ppm
		$C_Q$				3.3 MHz	3.3 MHz
		$\eta_Q$				0.95	0.95

Table 5.1: Detailed line-shapes parameters of  $^{27}\text{Al}$  species of MIL-100(Al).

### 3. CD-P coated nanoMIL-100(Al)

The success of the coating process was confirmed by performing  $^1\text{H}$  and  $^{13}\text{C}$  MAS NMR experiments. The spectra recorded were compared with  $^1\text{H}$  and  $^{13}\text{C}$  NMR spectra of pristine  $\beta$ -cyclodextrin (CD) and pure nanoMIL-100(Al), showed in Figure 5.10 and Figure 5.11, respectively.  $^1\text{H}$  resonances belong to the CD are visible in the  $^1\text{H}$  MAS NMR spectrum of CD-P coated nanoMIL-100(Al) around 3 to 5 ppm. Identification of all  $^{13}\text{C}$  resonances of CD-P coating evidences that both the MOF and the coating part are intact after the coating process.

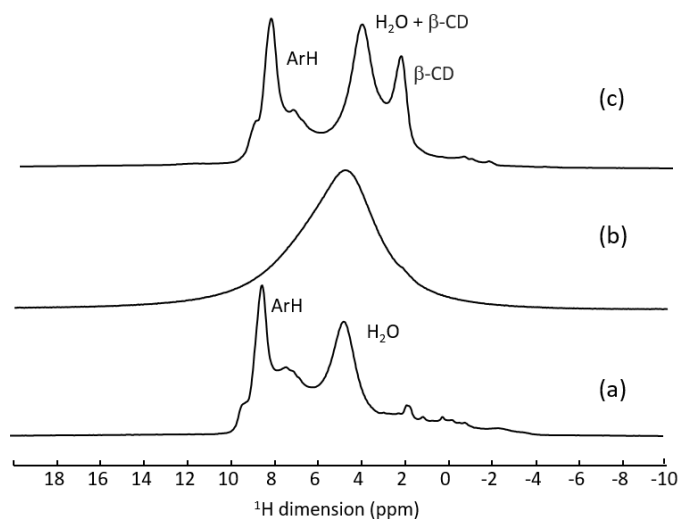


Figure 5.10:  $^1\text{H}$  MAS NMR spectra of nanoMIL-100(Al) (a), pristine  $\beta$ -CD-P (b) and CD-P coated nanoMIL-100(Al) (c), recorded at 60 kHz (20 T).

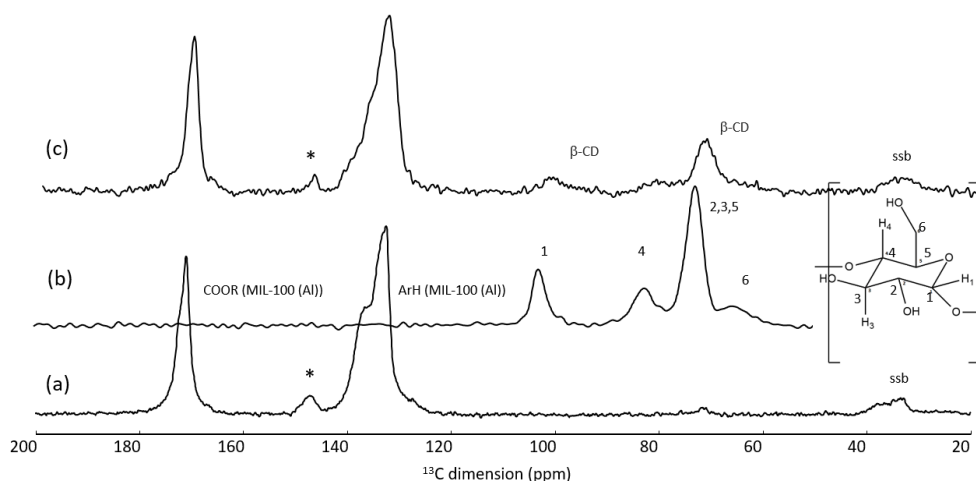


Figure 5.11:  $^{13}\text{C}$  MAS NMR spectra of nanoMIL-100(Al) (a), pristine  $\beta$ -CD-P (b) and CD-P coated nanoMIL-100(Al) (c), recorded at 10 kHz (9.4 T). The  $^{13}\text{C}$  resonances of CD are assigned based on liquid NMR spectrum<sup>13</sup>. \* indicate traces of impurities and ssb indicate the spinning sidebands.

Despite the use of high field and fast MAS, not enough information were given by the proton experiments, and also the carbon spectra does not help to have information about the interaction taking place at the surface of this complex system. Another challenge was the low quantity of the surface species of the particles. Surface enhanced solid-state NMR, such as dynamic nuclear polarization (DNP) methods can be used to detect the species on the external surface of the MOFs<sup>14-</sup>

<sup>16</sup>. DNP methods involve the use of heterogeneous radical, solvent, low temperature (100 K), that not allow studying the state of the particles as they can be potentially administered *in vivo*. Therefore, the approach chosen is to use simpler MAS NMR methods at room temperature, taking advantage of the heteroatoms present in the system. More in detail, Aluminum and Phosphorus are the two nuclei studied, because of the presence of the Aluminum only as metal center of the nanoMOF and of the phosphorus on the coating (cyclodextrin phosphate).

<sup>27</sup>Al MAS NMR spectrum of CD-P coated nanoMIL-100(Al) was recorded and compared with the one of the pristine nanoMIL-100(Al), showing a quite similar lineshape (Figure 5.12).

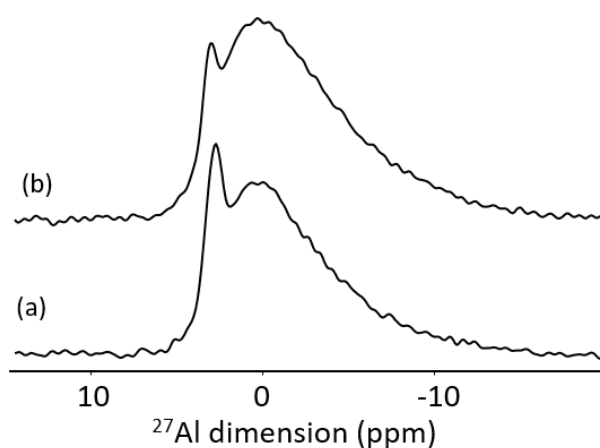


Figure 5.12: <sup>27</sup>Al MAS NMR of nanoMIL-100(Al) (a) and CD-P coated nanoMIL-100(Al) (b), recorded at 20 kHz on a 20 T spectrometer.

Careful analysis of <sup>27</sup>Al MQMAS experiment (Figure 5.13) shows that while the bulk Al signals remain similar, the new identified aluminum site is slightly modified when the NPs are coated with the CD-P (details of Al species in Table 5.2). This result indicates that probably the new Al resonance belong to the Al atoms present at or slightly below the surface of the nanoMOF since CD-P is too bulky to penetrate the pores. Another observation is the shift upon coating results, probably from interactions between some of the surface aluminum species of the NPs and the coating.

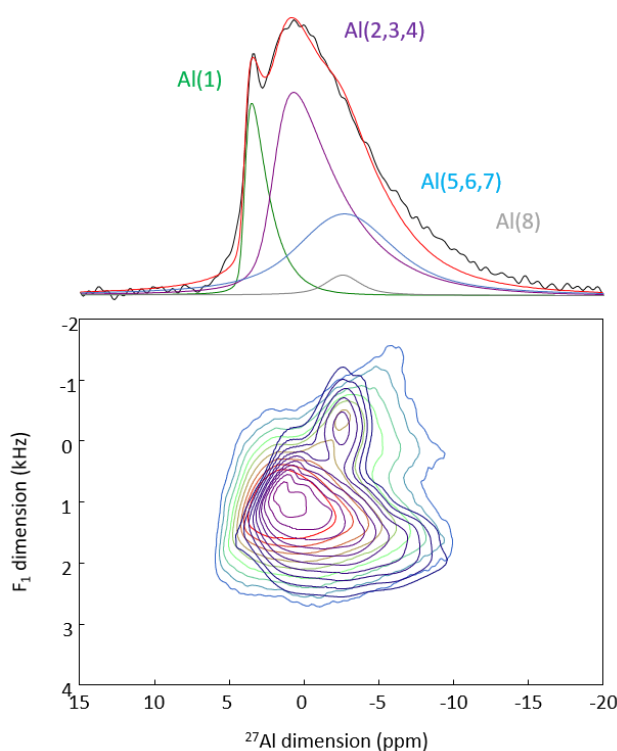


Figure 5.13:  $^{27}\text{Al}$  MQMAS NMR spectrum of the CD-P coated nanoMIL-100(Al), recorded at 20 kHz (on a 20 T spectrometer). The simulation was made using Czejk and QMAS1/2 mode on Dmfit program<sup>11</sup>.

$^{27}\text{Al}$ six coordinated sites			<i>nanoMIL-100(Al)</i>	<i>CD-P coated nanoMIL-100(Al)</i>
(20 T, 20 kHz)				
<b>BULK</b>	Al (1)	%	26	30
		$\delta_{\text{iso}}$	3.95 ppm	3.95 ppm
		$C_Q$	3 MHz	3.1 MHz
		$\eta_Q$	0.61	0.61
	Al (2,3,4)	%	55	47
		$\delta_{\text{iso}}$	2.19 ppm	2.19 ppm
		$C_Q$	4.87 MHz	4.87 MHz
		$\eta_Q$	0.61	0.61
	Al (5,6,7)	%	14	15
		$\delta_{\text{iso}}$	0.30 ppm	0.5 ppm
		$C_Q$	5 MHz	5 MHz
		$\eta_Q$	0.65	0.65
<b>SURFACE</b>	Al (8)	%	5	8
		$\delta_{\text{iso}}$	-1.50 ppm	-1.00 ppm
		$C_Q$	3.3 MHz	3.0 MHz
		$\eta_Q$	0.95	0.94

Table 5.2: Detailed line-shapes parameters of  $^{27}\text{Al}$  species of CD-P coated and pure nanoMIL-100(Al).

To understand better these interactions, through-space  $^1\text{H}$ - $^{27}\text{Al}$  (2D) *D*-HMQC MAS NMR experiment was performed trying to correlate the protons of the CD-P that are in close proximity to

the aluminum species. However, the  $^1\text{H}$  spectrum obtained is dominated by the signal of the proton of the linkers, hence no interaction with the surface aluminum species are detected (Figure 5.14).

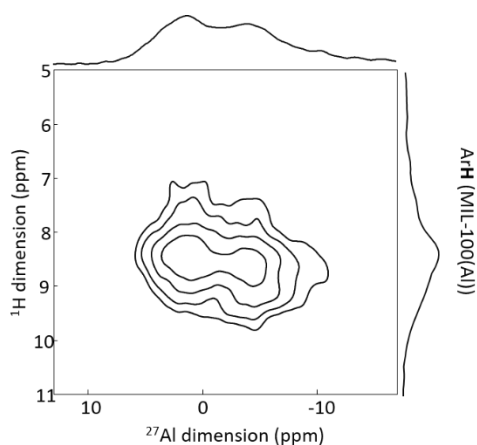


Figure 5.14:  $^{27}\text{Al}\{^1\text{H}\}$  2D D-HMQC MAS NMR spectrum of CD-P coated nanoMIL-100(Al), recorded on a 20 T spectrometer (at 60 kHz, with a recoupling time of 1.4 ms).

Another nucleus was chosen to analyze and  $^{31}\text{P}$  1D CPMAS NMR experiment was performed and compared with the one recorded for the pristine  $\beta$ -CD-P (Figure 5.15).

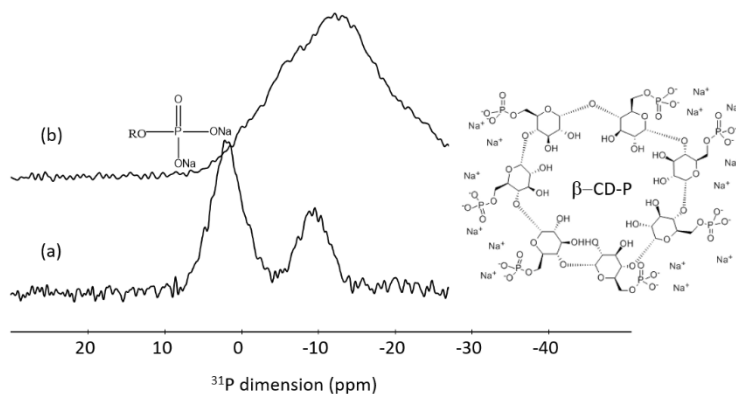


Figure 5.15:  $^{31}\text{P}$  CPMAS NMR of pristine CD-P (a), CD-P coated nanoMIL-100(Al) (b).

It seems that, in the encapsulation process, the CD-P loses the signal belong to the P-ONa, probably for a creation of an interaction with the Al of the nanoMOF, as it was already observed from the  $^{27}\text{Al}$  NMR experiment. To have a confirmation of this interaction, reminding that  $^{27}\text{Al}$ , arising solely from the nanoMOF and  $^{31}\text{P}$ , arising solely from the CD-P coating, 2D  $^{27}\text{Al}$ - $^{31}\text{P}$  heteronuclear correlation

experiment was performed, in order to selectively identify the surface aluminum species of the NPs in close proximity to the CD-P. Because of the short  $^{27}\text{Al}$  transverse relaxation time  $T_2$  (shown in Table 5.3), it was not possible to use the through-bond heteronuclear multiple-quantum ( $J$ -HMQC) experiment that requires recoupling time in the 8 ms range for optimum efficiency<sup>11,17</sup>.

<i>Sample</i>	$^{27}\text{Al } T_2 \text{ (ms, } \pm 0.1)$
nanoMIL-100(Al)	3.8
CD-P coated nanoMIL-100(Al)	3.8

Table 5.3:  $^{27}\text{Al } T_2$  measured from a spin echo experiment of the samples studied on 20 T spectrometer.

The through-space dipolar based version ( $D$ -HMQC) was employed, for which the optimum dipolar recoupling requires shorter recoupling time<sup>18</sup>. The recoupling time was kept short enough to ensure that only the aluminum in very close proximity of the  $^{31}\text{P}$  were selected. The resulting 2D  $^{27}\text{Al}$ - $^{31}\text{P}$  MAS NMR spectrum of CD-P-coated nanoMIL-100(Al) is shown in Figure 5.16. The observed  $^{27}\text{Al}$  NMR signal is at -5 ppm (as already observed in the MQMAS showed in Figure 5.13), which indicates that the observed surface Al species in the vicinity of the CD-P are in six-fold coordination. The  $^{27}\text{Al}$  chemical shift is lower than the  $^{27}\text{Al}$  chemical shifts in pristine nanoMIL-100(Al), which range between 1.1 and 3.4 ppm<sup>10</sup>. It is close to chemical shift observed in alumino-phosphate, hence we can hypothesize that the six-fold coordination is preserved by the formation of an Al-O-P bond between the Al surface sites of the nanoMOF and the phosphate group of the CD-P, which very likely substitute a water molecule (see Figure 5.1).

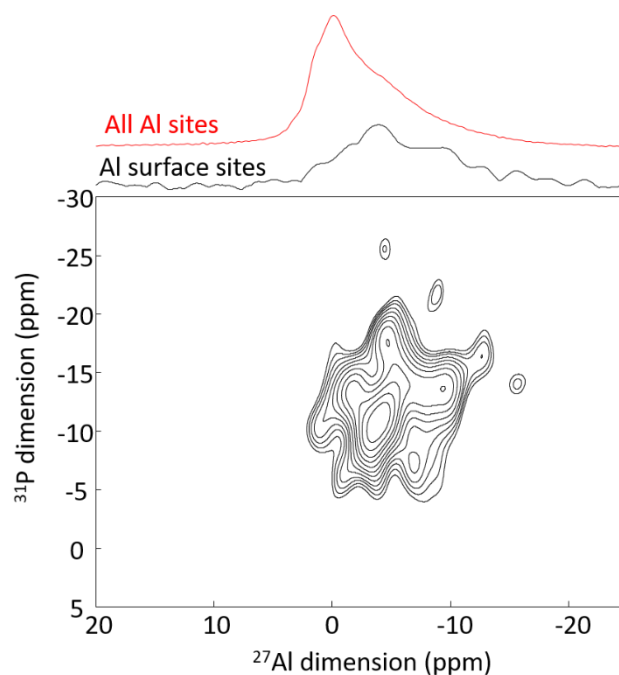


Figure 5.16: 2D  $^{27}\text{Al}\{^{31}\text{P}\}$  *D*-HMQC MAS NMR spectrum of CD-P-coated nanoMIL-100(Al), recorded at 14 kHz on a 17.6 T spectrometer. The black spectrum is the full projections on the horizontal dimension for the surface sites, while the red spectrum are the MAS NMR spectrum shown for comparison.

The identification of a new Al resonance belonging to the Al surface sites of the nanoMOF was possible to identify, thanks to a simple ssNMR methodology. It is the first time that this resonance is analyzed and it may be a useful discover for the modification of the surface of nanoMIL-100(Al) as DDS.

#### 4. ATP loaded nanoMIL-100(Al)

Due to the formation of Al-O-P bonds between the nanoMOF and the coating, an investigation of the possible interactions between a phosphate drug and the MOF was made. As already said, Adenosine Triphosphate (ATP) was selected. The investigation started with the easiest nuclei,  $^1\text{H}$  and  $^{13}\text{C}$ .  $^1\text{H}$  MAS NMR spectra (Figure 5.17) were performed at two different field (9.4 T and 20 T) and at moderate (25 kHz) and fast MAS (60 kHz), showing strong overlapping of broad resonances because of distribution of chemical shift, due to the complexity of the system. The interpretation of the spectra is difficult and even the comparison with the  $^1\text{H}$  NMR spectra performed on the pure drug does not give enough information. The only observation is the confirmation of the incorporation of the drug in

the nanoMOF, due to the presence of proton of the P-OH group of the ATP at 11 ppm in the loaded sample.

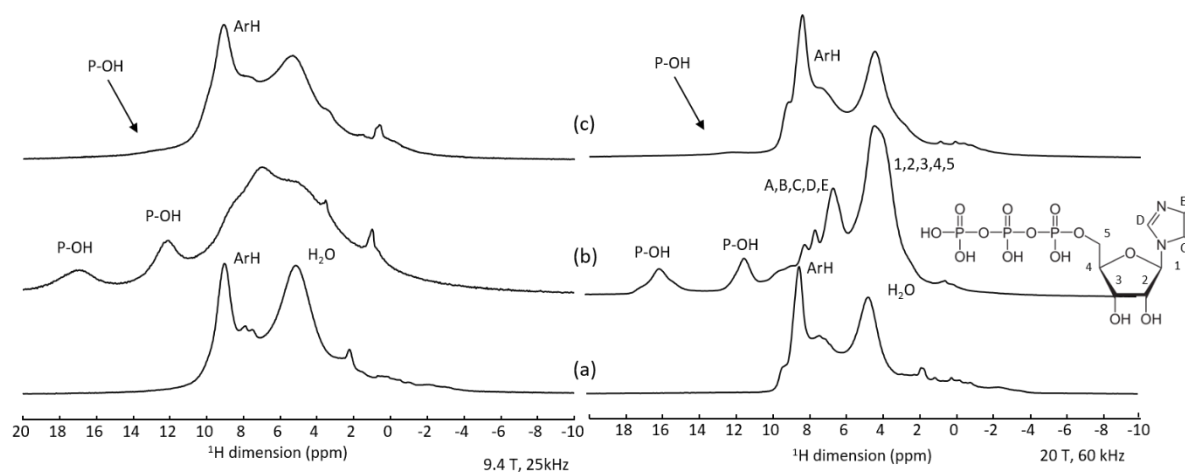


Figure 5.17:  $^1\text{H}$  MAS NMR spectra of nanoMIL-100(Al) (a), pure ATP (b), ATP loaded nanoMIL-100(Al) (c), recorded at 25 kHz (9.4 T) and 60 kHz (20 T). The lines of ATP are assigned based on the spectrum on reported database<sup>19–22</sup>.

Performing 2D homonuclear experiment (Figure 5.18) at high field and fast MAS on the loaded sample, one can see correlation peaks between the resonance belong to P-OH of the ATP and the proton of the linker around 9 ppm, showing a spatial proximity between the drug and the linker. Probably the drug is located in the pores of the nanoMOF.

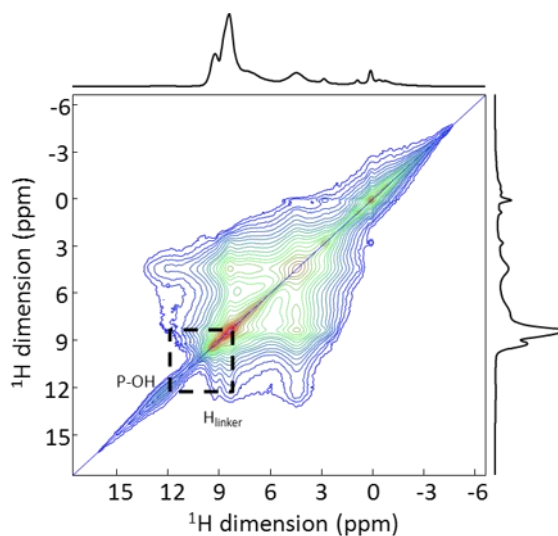


Figure 5.18: 2D  $^1\text{H}$ - $^1\text{H}$  spin diffusion NMR spectrum of ATP-loaded nanoMIL-100(Al), recorded 60 kHz, on a 20 T (mixing time of 5 ms).

The confinement of the drug is confirmed by the  $^{13}\text{C}$  CPMAS NMR spectra performed. Moreover, the drug seems intact in the nanoMOF, because all the carbon resonances of the ATP can be identified in the loaded nanoMOF (assignment showed in Figure 5.19).

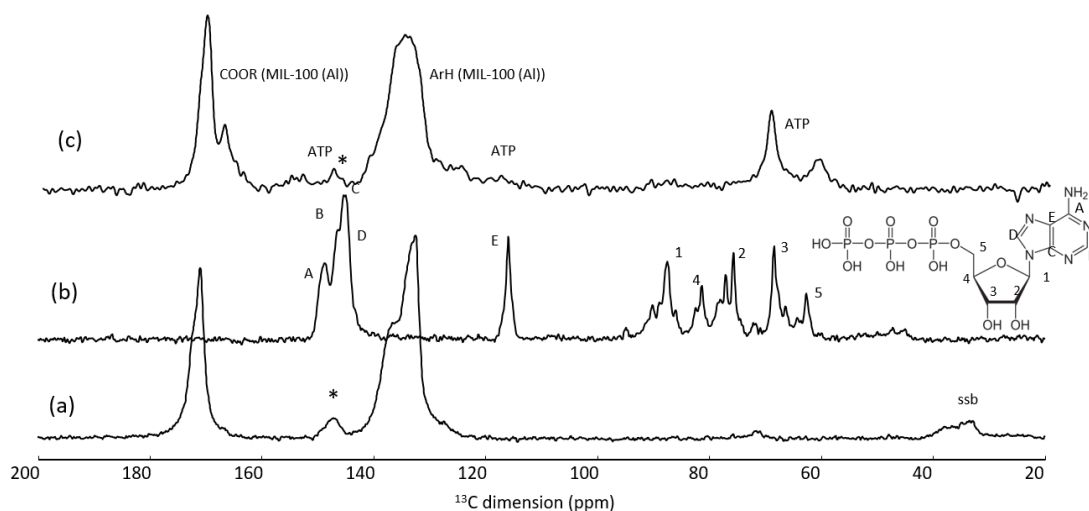


Figure 5.19:  $^{13}\text{C}$  MAS NMR spectra of nanoMIL-100(Al) (a), pure ATP (b), ATP loaded nanoMIL-100(Al) (c), recorded at 10 kHz (9.4 T). The lines of ATP are assigned based on the spectrum on reported database<sup>19–22</sup>. \* indicate traces of impurities and ssb indicate the spinning sidebands.

Even if, thanks to  $^1\text{H}$  and  $^{13}\text{C}$  NMR experiment, it is possible to affirm that the drug is intact and it is probably located in pores of the nanoMOF, any information is given on the possible interactions taking place between the drug and the MOF. Therefore, as well as for the CD-P coated nanoMIL-100(Al), the strategy adopted was to take advantage of the aluminum nuclei present in the MOF and the phosphorus nuclei belonging only to the drug molecules. Despite the use of high magnetic field (20 T), the  $^{27}\text{Al}$  MAS NMR spectrum of ATP loaded nanoMIL-100(Al) compared with the one of the pristine nanoMIL-100(Al) is quite similar (Figure 5.20).

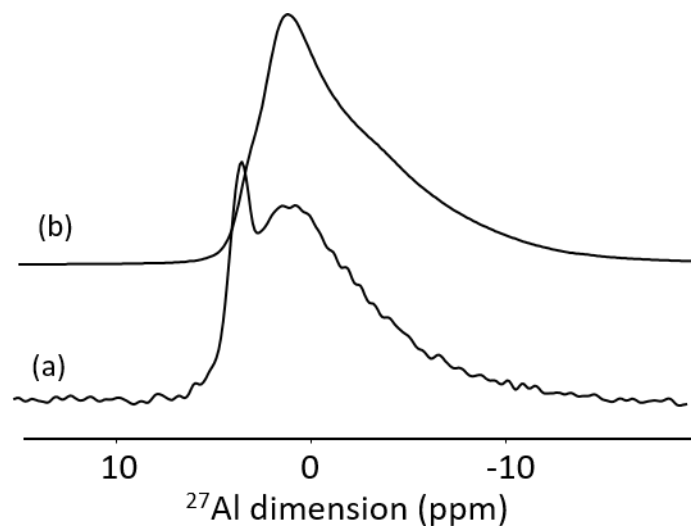


Figure 5.20:  $^{27}\text{Al}$  MAS NMR of nanoMIL-100(Al) (a) and ATP loaded nanoMIL-100(Al) (b), recorded at 20 kHz on a 20 T spectrometer.

By performing the MQMAS experiment on the ATP loaded nanoMIL-100(Al) one can notice that when the drug is loaded, the bulk Al signals are affected, indicating the successful incorporation of the drug inside the mesopores of the nanoMOF (Figure 5.21) (details of the species are given in Table 5.4).

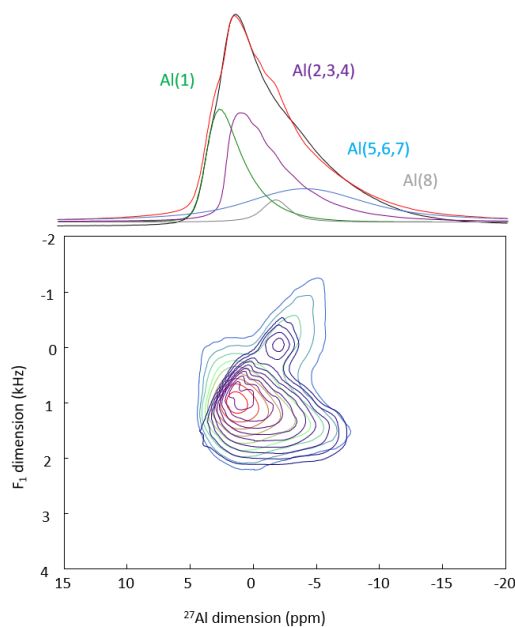


Figure 5.21:  $^{27}\text{Al}$  MQMAS NMR spectrum of ATP loaded nanoMIL-100 (Al), recorded at 20 kHz (on a 20 T spectrometer). The simulation were made using Czejk and QMAS1/2 mode on Dmfit program<sup>11</sup>.

$^{27}\text{Al}$ six coordinated sites			<i>nanoMIL-100(Al)</i>	<i>ATP loaded nanoMIL-100(Al)</i>
(20 T, 20 kHz)				
<b>BULK</b>	Al (1)	%	26	27
		$\delta_{\text{iso}}$	3.95 ppm	3.5 ppm
		$C_Q$	3 MHz	3.8 MHz
		$\eta_Q$	0.61	0.61
	Al (2,3,4)	%	55	40
		$\delta_{\text{iso}}$	2.19 ppm	2.09 ppm
		$C_Q$	4.87 MHz	4.57 MHz
		$\eta_Q$	0.61	0.61
	Al (5,6,7)	%	14	27
		$\delta_{\text{iso}}$	0.30 ppm	0.24 ppm
		$C_Q$	5 MHz	5.72 MHz
		$\eta_Q$	0.65	0.65
<b>SURFACE</b>	Al (8)	%	5	6
		$\delta_{\text{iso}}$	-1.50 ppm	-1.50 ppm
		$C_Q$	3.3 MHz	3.0 MHz
		$\eta_Q$	0.95	0.95

Table 5.3: Detailed line-shapes parameters of  $^{27}\text{Al}$  species of ATP loaded and pure nanoMIL-100(Al).

Through-space  $^1\text{H}$ - $^{27}\text{Al}$  (2D) *D* HMQC MAS NMR experiment was performed trying to correlate the protons of the ATP that are in close proximity to the aluminum species. As for CD-P coated nanoMOF, the  $^1\text{H}$  spectrum obtained is dominated by the signal of the proton of the linkers and no interaction can be noticed (Figure 5.22).

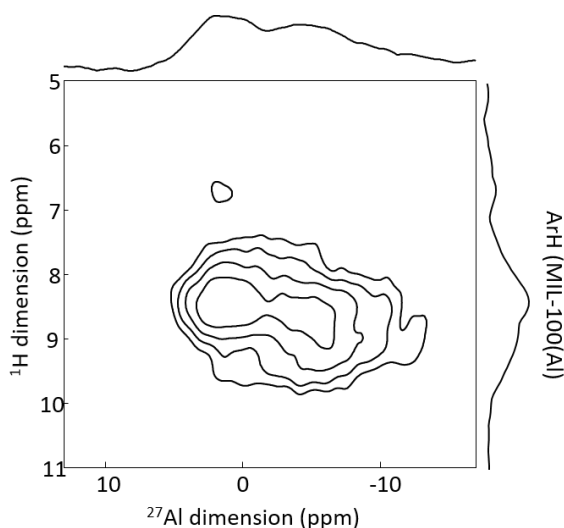


Figure 5.22:  $^{27}\text{Al}$   $\{^1\text{H}\}$  2D *D*-HMQC MAS NMR spectra of ATP loaded nanoMIL-100(Al), recorded on a 20 T spectrometer (at 60 kHz, with a recoupling time of 1.4 ms).

Study of phosphate environment of the drug was conducted. In Figure 5.21, it can be clearly seen how the phosphate signals of the ATP maintain the same shape when loaded in the nanoMOF, even if the resonances result broader due to the confinement of the drug in the pores.

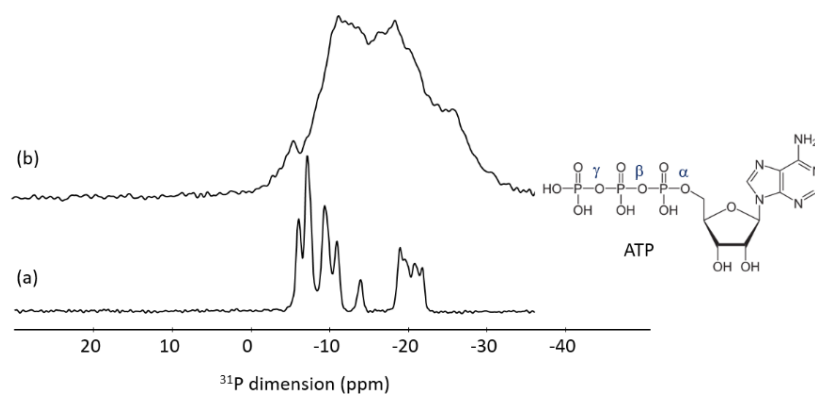


Figure 5.23:  $^{31}\text{P}$  CPMAS NMR of pure ATP (a), ATP loaded nanoMIL-100(Al) (b), recorded at 14 kHz in a 9.4 T spectrometer.

To have an idea of the assignment of the different  $^{31}\text{P}$  resonances of the ATP, 2D  $^{31}\text{P}$ - $^{31}\text{P}$  homonuclear correlation experiments (*J*-type and through space-proximity) were performed and are showed in Figure 5.24. The  $\beta$ -phosphorus atom (the middle of the tri-phosphate) is identified in both spectra, around -20 ppm, as it is the only one having correlation with other two P atoms. The other two phosphates are identified thanks to the literature<sup>23</sup> ( $\alpha$ -phosphorus around -10 ppm and  $\gamma$ -phosphorus around -5 ppm). The presence of several  $\alpha$ ,  $\beta$  and  $\gamma$  phosphates is due to the fact that the commercial ATP is a mixture of several hydration forms. Additionally, the through-space correlation experiment gives the opportunity to observe the inter-molecular interactions.

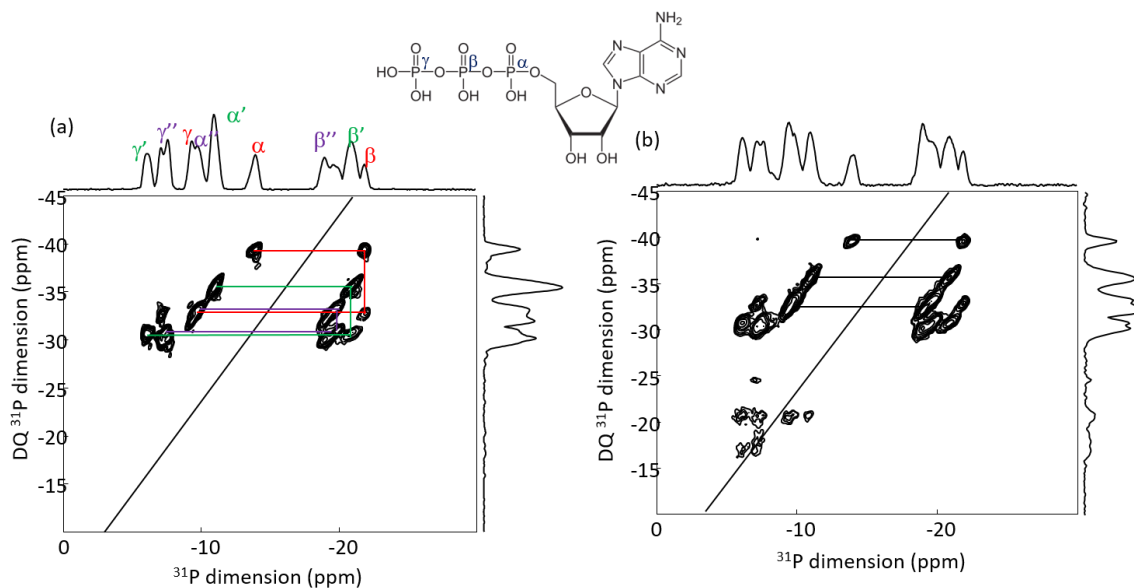


Figure 5.24:  $^{31}\text{P}$ - $^{31}\text{P}$  2D J-type (CP-INADEQUATE) (a) and through-space proximity ( $S_3$ ) (b) DQ-SQ homonuclear correlation spectra of ATP (at 14 kHz, on a 9.4 T). The lines represent the different hydrated forms of ATP present in the commercial product. Additional peaks are seen on the  $S_3$  NMR spectrum (dipolar-based), which are due to longer range interactions.

Performing the same experiment on the ATP loaded nanoMIL-100(Al) (Figure 5.25), the middle  $\beta$ -phosphate is identified as it is linked to two other phosphorus group. In addition, the triphosphate structure seems to be preserved once the ATP is loaded in the pores of the nanoMOF. One can notice a shift of the  $^{31}\text{P}$  resonances ( $\alpha$ -phosphorus around -30 ppm,  $\beta$ -phosphorus around -20 ppm and  $\gamma$ -phosphorus around -10 ppm), which very likely indicates that the drug is bent in the pores and has strong interaction with the framework aluminum sites.

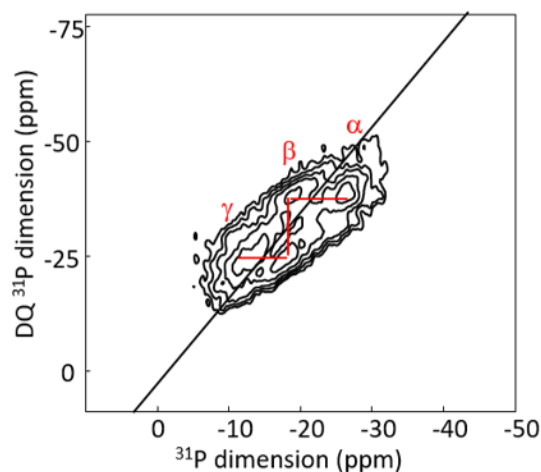


Figure 5.25:  $^{31}\text{P}$ - $^{31}\text{P}$  2D DQ-SQ homonuclear correlation spectra of ATP loaded nanoMIL-100(Al), recorded at 14 kHz, on a 9.4 T.

To go further in the characterization and trying to have more details about the interactions at the interface of the system and the drug, 2D  $^{27}\text{Al}$ - $^{31}\text{P}$  heteronuclear correlation experiment was performed. Because of the short  $^{27}\text{Al}$  transverse relaxation time  $T_2$  (around 3.4 ms), the *D*-HMQC was employed. A six-fold coordinated  $^{27}\text{Al}$  resonance around -7 ppm is observed in the ATP loaded nanoMIL-100(Al) 2D  $^{27}\text{Al}$ - $^{31}\text{P}$  *D*-HMQC MAS NMR spectrum (Figure 5.26), which suggests a formation of a Al-O-P chemical bond between Al species of the MOF framework and the terminal phosphate of the drug, which  $^{31}\text{P}$  resonance is located around -10 ppm. This allows the assignment of the  $^{31}\text{P}$  resonances in the  $^{31}\text{P}$ - $^{31}\text{P}$  homonuclear correlation experiment (Figure 5.25). The  $^{27}\text{Al}$  resonance is the signature of the grafted aluminum sites inside the pores of the MOF. Correlation of lower intensity is also observed between these Al species and the middle P of the triphosphate chain (around -20 ppm), in agreement with longer Al-P distance. Here again, the ATP very likely replaces a water molecule from the Al tricluster. Therefore, the ATP showed similar interaction with the MOF of the coating CD-P.

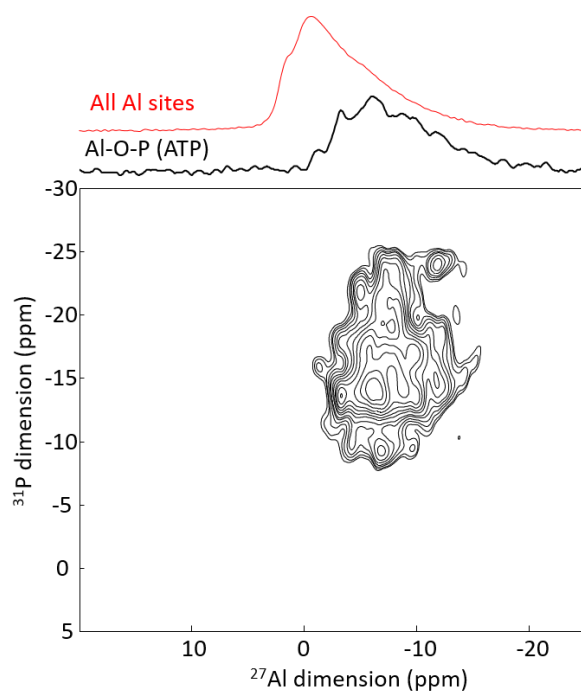


Figure 5.26: 2D  $^{27}\text{Al}\{^{31}\text{P}\}$  D-HMQC MAS NMR spectrum of ATP loaded MIL-100(Al), recoded at 14 kHz on a 17.6 T spectrometer. The black spectrum is the full projection for the interphase sites, while the red spectrum is the MAS NMR spectrum shown for comparison.

## 5. CD-P coated ATP loaded nanoMIL-100(Al)

Once the CD-P coated nanoMIL-100(Al) and the ATP loaded nanoMIL-100(Al) were analyzed, one may be wondering if the loading can influence the coating process, or *vice versa*. With this goal, the final product CD-P coated ATP loaded nanoMIL-100(Al) was analyzed following the same strategy as the previous samples.  $^1\text{H}$  and  $^{13}\text{C}$  MAS NMR spectra, shown in Figure 5.27 and 5.28 respectively, were recorded to confirm the incorporation of the drug and the success of the coating process.

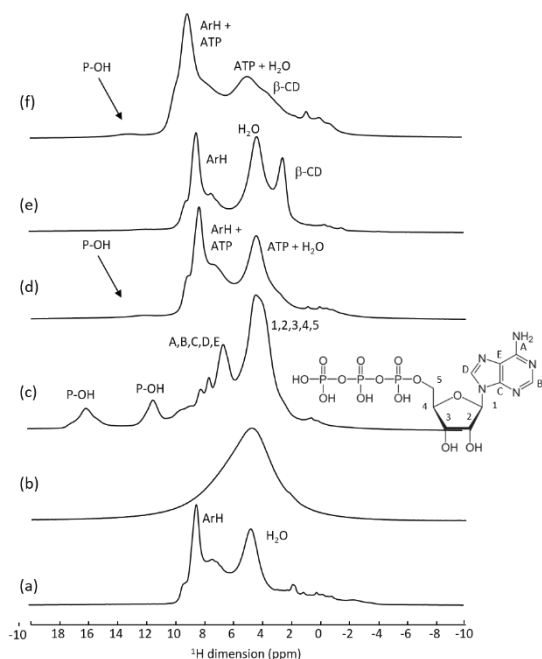


Figure 5.27:  $^1\text{H}$  MAS NMR spectra of nanoMIL-100(Al) (a), pristine CD-P (b), pure ATP (c), ATP loaded nanoMIL-100(Al) (d), CD-P coated nanoMIL-100(Al) (e) and CD-P coated ATP loaded nanoMIL-100(Al) (f), recorded at 60 kHz (20 T). The lines of ATP are assigned based on the spectrum on reported database<sup>19–22</sup>.

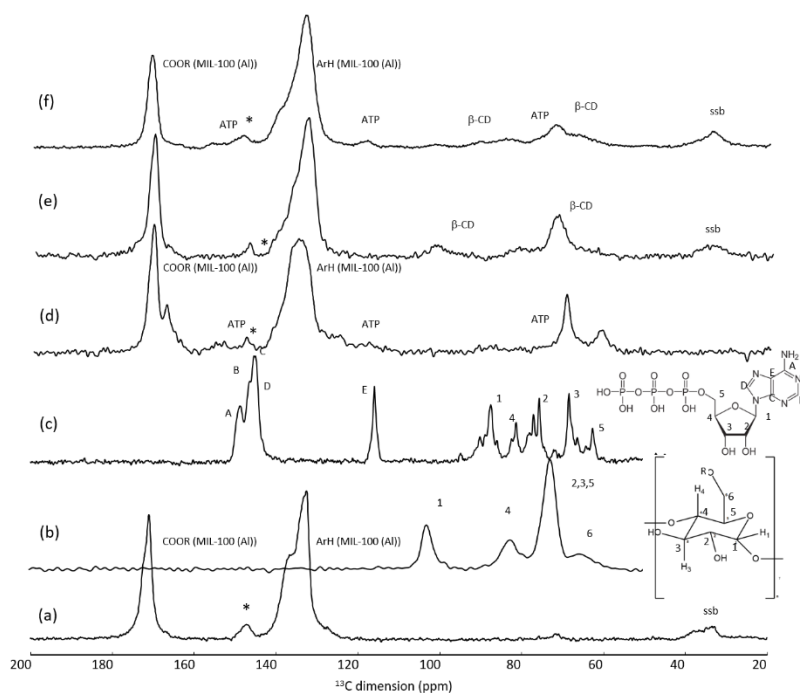


Figure 5.28:  $^{13}\text{C}$  MAS NMR spectra of nanoMIL-100(Al) (a), pristine CD-P (b), pure ATP (c), ATP loaded nanoMIL-100(Al) (d), CD-P coated nanoMIL-100(Al) (e) and CD-P coated ATP loaded nanoMIL-100(Al) (f), recorded at 10 kHz (9.4 T). The  $^{13}\text{C}$  resonances of CD are assigned based on liquid NMR spectrum<sup>13</sup>. \* indicate traces of impurities and ssb indicate the spinning sidebands.

$^1\text{H}$  NMR spectrum has a very broad lineshapes and, as for ATP loaded nanoMIL-100(Al), the presence of the resonance of P-OH is the only evidence of the incorporation of the drug. A broadening

of the resonance around 5 ppm may be a confirmation of the presence of CD-P coating.  $^{13}\text{C}$  NMR experiments confirm this hypothesis and indicate that the coating does not have any influence on the loading of the drug and vice versa, as expected.

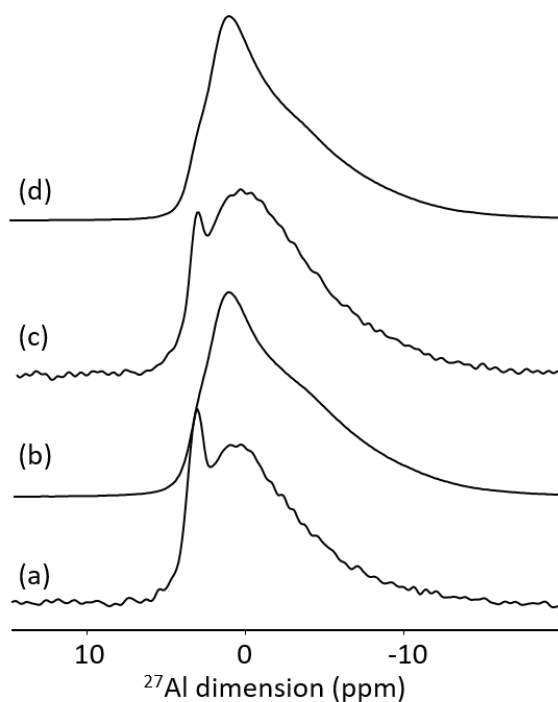


Figure 5.29:  $^{27}\text{Al}$  MAS NMR of pristine nanoMIL-100(Al) (a), ATP loaded nanoMIL-100(Al) (b), CD-P coated nanoMIL-100(Al) (c) and CD-P coated ATP loaded nanoMIL-100(Al) (d), recorded at 20 kHz on a 20 T spectrometer.

$^{27}\text{Al}$  MAS NMR spectrum was performed and any significant information could be extracted from the 1D spectra (Figure 5.29) and MQMAS experiment (Figure 5.30) was carried out to have additional information and do a comparison with the ones recorded on the previous samples. One can noticed that both Al bulk and surface species are effected, as expected. Details of Al species and differences with the other samples are given in Table 5.5.

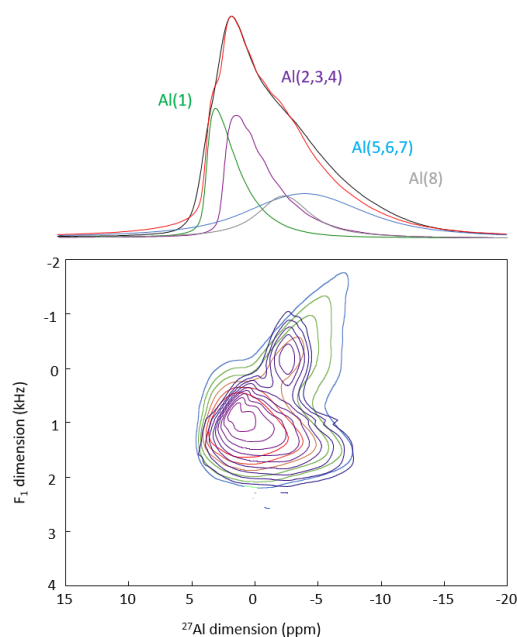


Figure 5.30:  $^{27}\text{Al}$  MQMAS NMR spectrum of CD-P coated ATP loaded nanoMIL-100 (Al) recorded at 20 kHz (on a 20 T spectrometer). The simulation were made using Czejk and QMAS1/2 mode on Dmfit program<sup>11</sup>.

$^{27}\text{Al}$ six coordinated sites		<i>CD-P coated nanoMIL-100(Al)</i>	<i>ATP loaded nanoMIL-100(Al)</i>	<i>CD-P coated ATP loaded nanoMIL-100(Al)</i>	
<i>(20 T, 20 kHz)</i>					
<b>BULK</b>	Al (1)	%	30	27	24
		$\delta_{\text{iso}}$	3.95 ppm	3.5 ppm	3.5 ppm
		$C_Q$	3.1 MHz	3.8 MHz	3.8 MHz
		$\eta_Q$	0.61	0.61	0.61
	Al (2,3,4)	%	46	40	31
		$\delta_{\text{iso}}$	2.19 ppm	2.09 ppm	2.10 ppm
		$C_Q$	4.87 MHz	4.57 MHz	4.57 MHz
		$\eta_Q$	0.61	0.61	0.61
	Al (5,6,7)	%	15	27	30
		$\delta_{\text{iso}}$	0.5 ppm	0.24 ppm	0.24 ppm
		$C_Q$	5 MHz	5.72 MHz	5.72 MHz
		$\eta_Q$	0.65	0.65	0.65
<b>SURFACE</b>	Al (8)	%	8	6	14
		$\delta_{\text{iso}}$	-1.0 ppm	-1.5 ppm	-1 ppm
		$C_Q$	3.0 MHz	3.0 MHz	3.0 MHz
		$\eta_Q$	0.94	0.95	0.94

Table 5.5: Detailed line-shapes parameters of  $^{27}\text{Al}$  species of CD-P coated, ATP loaded and CD-P coated ATP loaded nanoMIL-100(Al).

Once again the phosphorus environment was analyzed.  $^{31}\text{P}$  MAS NMR spectrum (Figure 5.31) of CD-P coated ATP loaded nanoMIL-100(Al) seems a sum of the two spectra of the CD-P coated and ATP loaded nanoMOF, in which the left part belongs to the coating and the right part to the drug.  $^{31}\text{P}$ - $^{31}\text{P}$

2D experiment performed on CD-P coated ATP loaded nanoMIL-100(Al) (Figure 5.32) seems quite similar to the one of ATP-loaded nanoMIL-100(Al), showing that the triphosphate structure of the ATP, and the phosphorus environment are not influenced by the coating process.

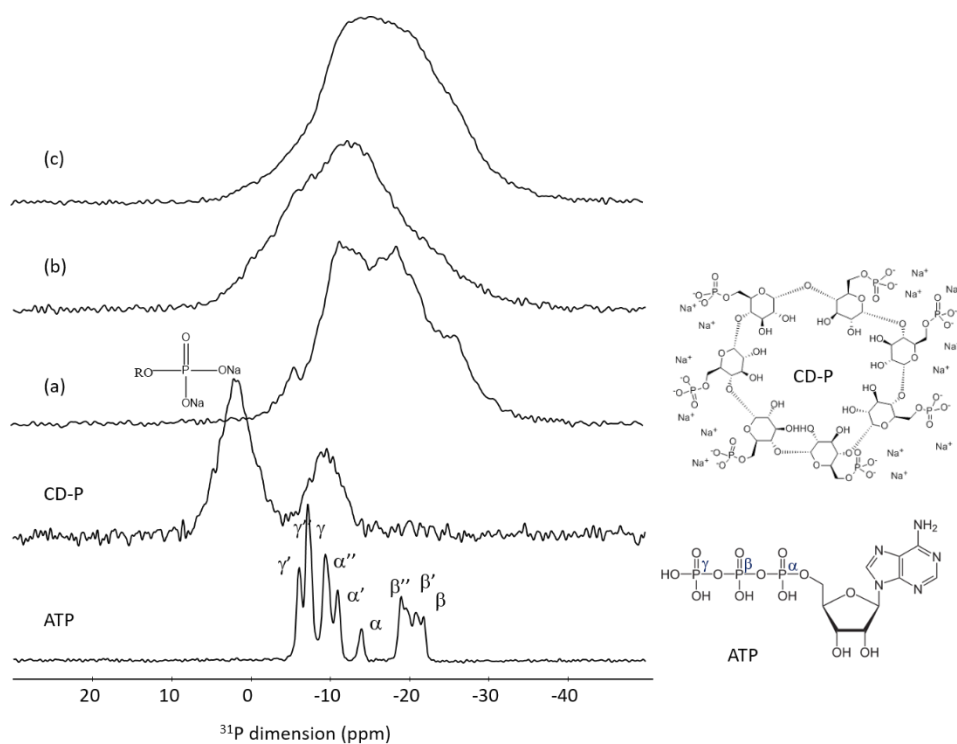


Figure 5.31:  $^{31}\text{P}$  CPMAS NMR of pure ATP, pristine CD-P, ATP loaded nanoMIL-100(Al) (a), CD-P coated nanoMIL-100(Al) (b) and CD-P coated ATP loaded nanoMIL-100(Al) (c), recorded at 14 kHz on a 9.4 T spectrometer.

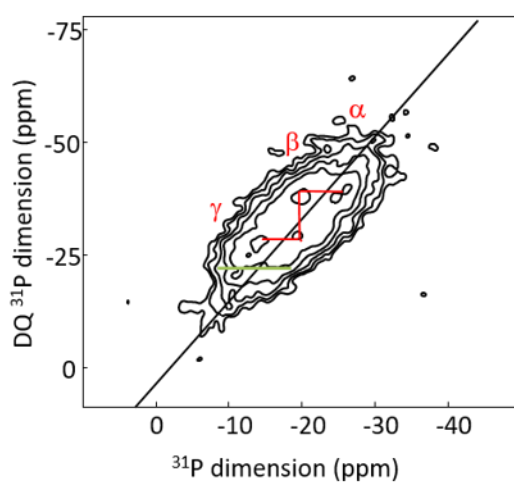


Figure 5.32:  $^{31}\text{P}$ - $^{31}\text{P}$  2D DQ-SQ homonuclear correlation spectrum of CD-P coated ATP loaded nanoMIL-100(Al) (at 14 kHz, on a 9.4 T). The phosphate resonances of the ATP are in red and the one of CD-P in green.

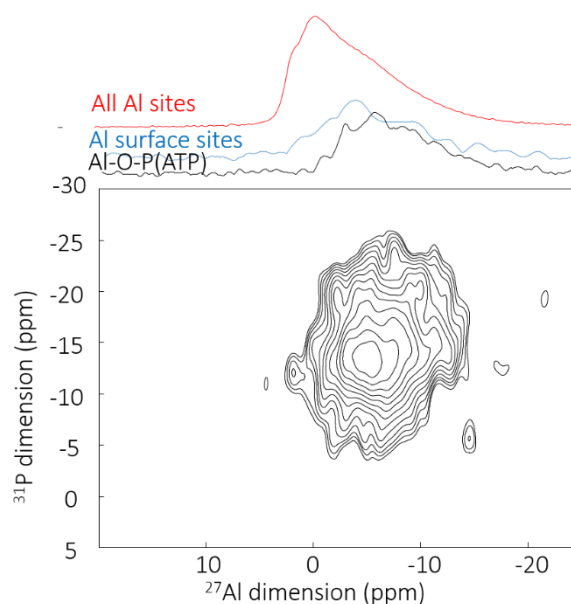


Figure 5.33: 2D  $^{27}\text{Al}\{^{31}\text{P}\}$  D-HMQC MAS NMR spectrum of CD-P coated ATP loaded MIL-100(Al), recoded at 14 kHz on a 17.6 T spectrometer. The blue spectrum is the full projection on the horizontal dimension for the surface sites, the black spectrum is the full projection for the interphase sites, while the red spectrum is the MAS NMR spectrum shown for comparison.

To have a better idea of the interactions and analyze if there is an influence between the coating and the loading process, 2D  $^{27}\text{Al}\text{-}^{31}\text{P}$  heteronuclear correlation experiment was performed also in the final product (Figure 5.33). The ATP content is much higher than the CD-P loading, hence the spectrum is dominated by the Al-O-ATP interaction. However, the  $^{31}\text{P}$  chemical shift expands to the higher ppm region (-5 to -10 ppm), characteristic of the CD-P coating. The similarity of the spectra belong to ATP loaded nanoMIL-100(Al) and CD-P coated ATP loaded nanoMIL-100(Al) confirms that the CD-P coating on the external surface of the ATP loaded nanoMOF did not affect the Al-O-ATP bond formed inside the MOF cavities.

## 6. Conclusions

The study of interaction on surface and interface of the nanoMIL-100(Al) was provided by taking advantage of distinct heteroatoms present in the nanoMOF ( $^{27}\text{Al}$ ) which surface was coated by bulky phosphate CD groups ( $^{31}\text{P}$ ) and in which a phosphate drug ( $^{31}\text{P}$ ) was loaded. Thanks to this

methodology, the low resolution of  $^1\text{H}$  MAS NMR spectroscopy was circumvented, and it was possible to show for the first time a  $^{27}\text{Al}$  NMR signature at room temperature of aluminum species present at the surface or below the surface of nanoparticles and their interaction with the CD-P coating. Moreover, the structural characterization showed the successful CD-P coating in ATP-loaded nanoMIL-100(Al), which did not modify the drug-MOF interactions. This methodology may be useful to guide in more efficient surface modification in several coating-nanoparticles, or to study the incorporation of the drug in the particles and its effect on the surface state. The formation of the strong P-O-Al covalent bonding between the CD and the MOF might be the key to ensure high stability of the core-shell nanoparticles *in vivo*.

The same set of experiments may be useful to study the degradation process of the nanoparticles in physiological medium. As shown by M. Vuong in her Master thesis<sup>8</sup>, after an initial fast release of trimesic acid, the degradation process becomes slower and reach a plateau in 48 hours (Figure 5.34).

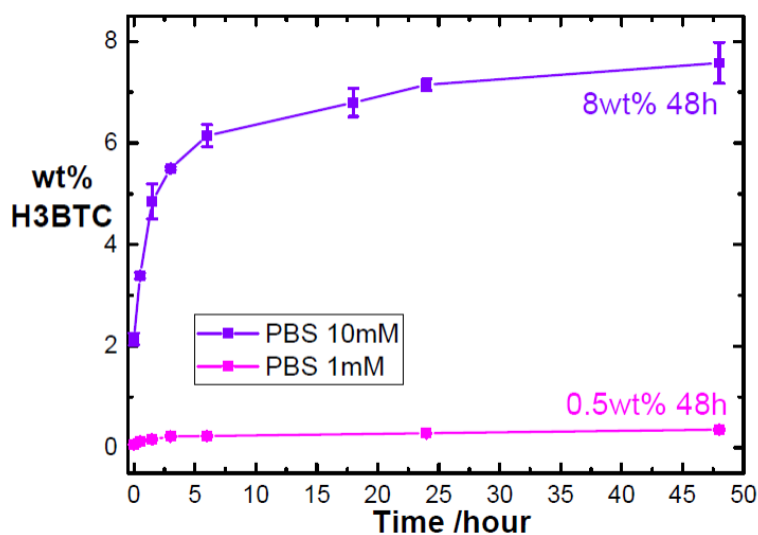


Figure 5.34: Quantitative analysis of MOF degradation by High Pressure Liquid Chromatography (HPLC). After 0, 0.5, 1.5, 3, 6, 24 and 48 hours of degradation, the amount of free trimesate linker in the supernatant collected after NPs degradation in PBS and in water was monitored. Two conditions were tested with a concentration of PBS 1 mM and 10 mM, showing that increasing the amount of PBS, the degradation is more important, but it reaches maximum the 8 wt%.

This release profile pointed out a limit of the nanoMOF degradation, which we chose to investigate by ssNMR.  $^{27}\text{Al}$  MAS NMR experiment was recorded after the degradation process (Figure 5.35a), showing a modification on coordination of  $^{27}\text{Al}$  species. Appearance of new Al five and four-coordinated species are detected around 20 and 48 ppm, respectively. In addition, a new Al six-coordinated resonance around -5 ppm is observed. Probably due to the formation of Al-O-P bond during the degradation process. To confirm this 2D  $^{27}\text{Al}$ - $^{31}\text{P}$  D-HMQC MAS NMR was recorded and is shown in Figure 5.35b, showing a strong correlation between a  $^{31}\text{P}$  resonance (around -10 ppm) and the  $^{27}\text{Al}$  resonance around -5 ppm.

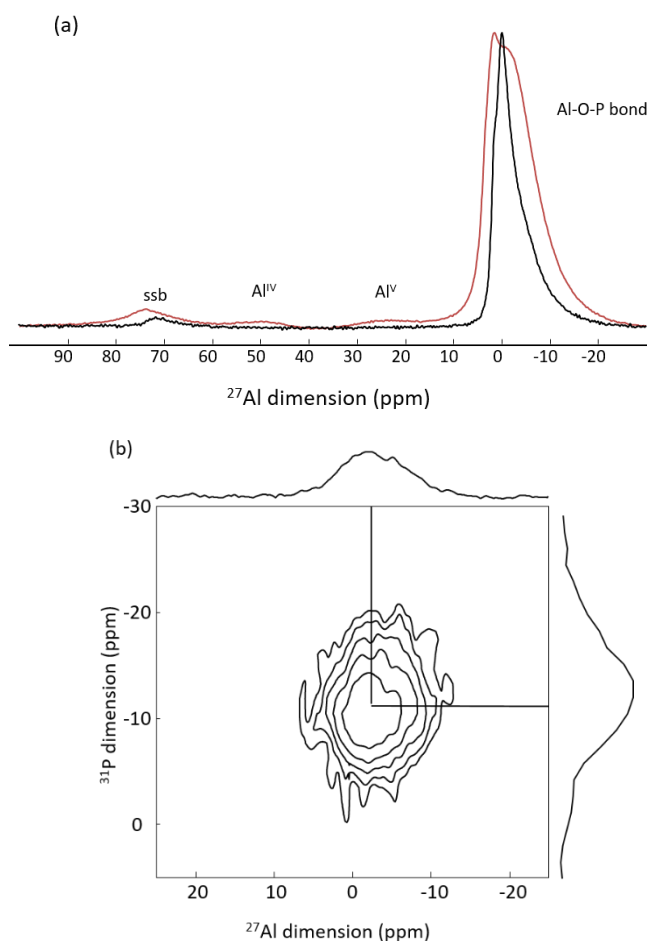


Figure 5.35: (a)  $^{27}\text{Al}$  MAS NMR of intact (black line) and degraded nanoMIL-100(Al) (red line) in phosphate buffer; (b) 2D  $^{27}\text{Al}\{^{31}\text{P}\}$  D-HMQC MAS NMR of degraded nanoMIL-100(Al), recorded on 17.6 T. ssb indicate the spinning sidebands.

Thanks to these results, a mechanism of degradation process, shown in Figure 5.36, was proposed. First, the monohydrogen phosphate and dihydrogen phosphate ions (component of PBS) replace the  $\text{H}_2\text{O}$  ligands of the Al trimer cluster, as they are the easiest ligands to substitute.

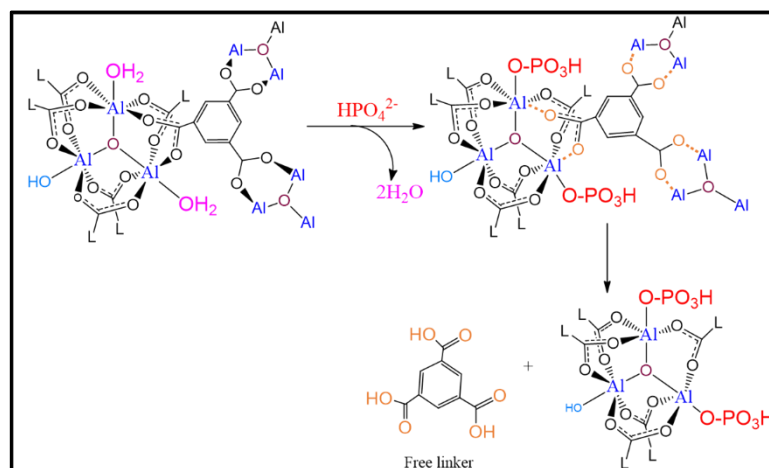


Figure 5.36: Proposed reaction between MIL-100(Al) trimer cluster with PBS.

The Al 4 and 5-coordinated intermediates could be formed when the bond Al-O-C is destroyed, to release the free trimesic acid (deprotonated or not, depends of the pH). These Al species unexpectedly keep their 4-5-coordination, and neither phosphate ion nor water molecule completes their coordination sphere. One guess is that initial degradation of nanoMIL-100(Al) at the surface leads to formation of aluminum phosphate ( $\text{AlPO}_x$ ) species, in which all water and trimesate ligands are replaced by phosphate groups. This  $\text{AlPO}_x$  layer, which consists of 4- and 5-coordinated-Al, can passivate the surface of NPs (which might explain the holes observed in TEM images). Then, the degradation reaction becomes slower and finally stops, corresponding with the plateau release of free linker trimesic acid. The same degradation profile was found in the CD-P coated nanoMIL-100(Al), showing that the coating does not prevent the nanoMOF degradation. Furthermore, the coating is strongly anchored on the nanoparticles surface even after 5 days of degradation.  $^{27}\text{Al}$  MAS NMR recorded (Figure 5.37a), shows the  $^{27}\text{Al}$  5 and 4 coordinated resonances and the additional six-coordinated one, already noticed in the degraded nanoMIL-100(Al). The formation of the Al-O-P was

confirmed by the 2D  $^{27}\text{Al}$ - $^{31}\text{P}$  D-HMQC MAS NMR recorded (Figure 5.37b), which gives the same result of the degraded nanoMIL-100(Al). Furthermore, the similar Al 4- and 5-coordinated species observed, indicative of probable formation of the  $\text{AlPO}_x$  passivation layers on NPs external surface. As CD-P covers partly the NPs surface, the bare surface can still be attacked and reacts like in non-coated-MOF. Notably, the CD-P coating does not prevent the nanoMOF degradation, but the reaching of the plateau (the not-completely degradation of the nanoMOF) can be a problem for the release of the drug. Consequently, a new type of surface modification has to be found to have a correct and controlled drug delivery and release.

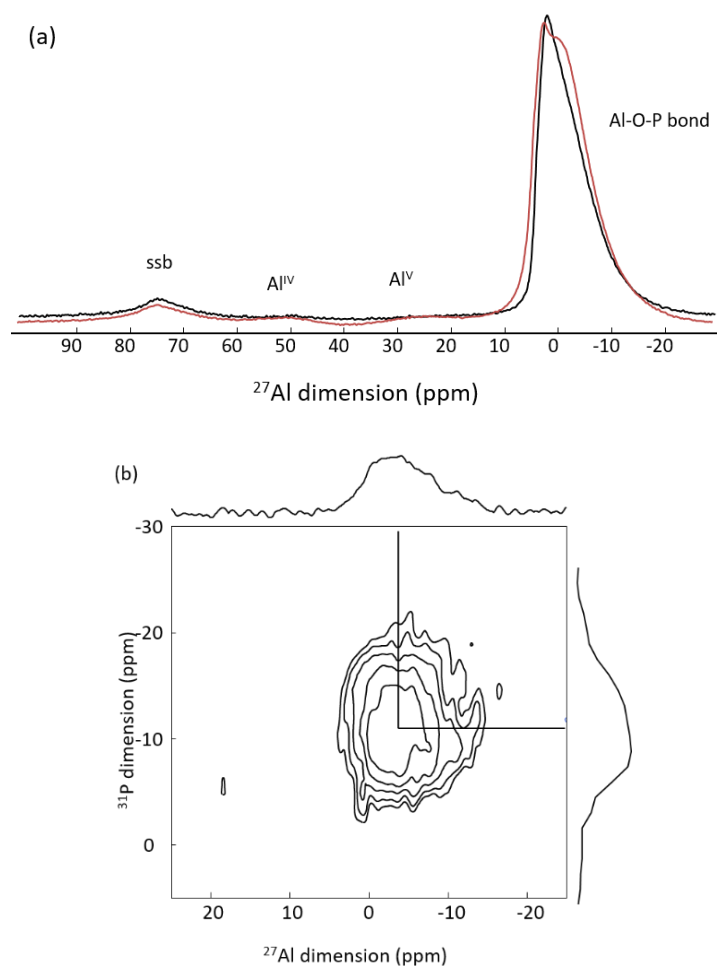


Figure 5.37: (a)  $^{27}\text{Al}$  MAS NMR of degraded CD-P coated nanoMIL-100(Al) (black line) and degraded nanoMIL-100(Al) (red line) in phosphate buffer; (b) 2D  $^{27}\text{Al}\{^{31}\text{P}\}$  D-HMQC MAS NMR of degraded CD-P nanoMIL-100(Al). ssb indicate the spinning sidebands.

## 7. Experimental ssNMR section

All the samples were finely ground into powders and packed into a zirconia rotor of the appropriate size. Then, the full rotor was dried at 40° C under vacuum for at least 12 hours prior to the NMR experiments. The NMR spectra were acquired using TopSpin 3.5 Bruker Software and processed with the Dmfit program<sup>24</sup>. The chemical shift are referred for <sup>1</sup>H and <sup>13</sup>C to TMS, to Al(NO<sub>3</sub>)<sub>3</sub> 1 M solution for <sup>27</sup>Al and to H<sub>3</sub>PO<sub>4</sub> 85 wt% solution for <sup>31</sup>P.

<i>Nucleus/i</i>	<i>Probe and MAS</i>	<i>Pulse sequence</i>	<i>Main Parameters</i>	<i>Time required</i>
<sup>1</sup> H	HXY 1.3 mm probe in double mode, with a spinning rate of 60 kHz	Hahn Echo	Recycle delay of 3 s; 90° pulse of 3.5 μs; an inter-pulse delay synchronized with one rotor period.	less than 1 minute
<sup>27</sup> Al- <sup>1</sup> H		D-HMQC	Recycle delay of 0.3 s; R421 as recoupling sequence, with 1.4 ms of recoupling time; States-TPPM procedure.	7 hours
<sup>27</sup> Al	HXY 3.2 mm probe in double mode, with a spinning rate of 20 kHz	1-pulse	Recycle delay of 0.3 s; 90° pulse of 2.2 μs (RF field of 38 kHz)	5 minutes
		z-filter MQMAS	RF field of 96 kHz for excitation of triple quantum (3Q) coherences and for 3Q->0Q conversion; All MQMAS spectra are presented after a shearing transformation.	3-14 hours

Table 5.6: NMR spectra recorded on a 850 MHz (20 T) WB Bruker NMR spectrometer.

<i>Nucleus/i</i>	<i>Probe and MAS</i>	<i>Pulse sequence</i>	<i>Main Parameters</i>	<i>Time required</i>
<sup>27</sup> Al- <sup>31</sup> P	<sup>1</sup> H- <sup>31</sup> P- <sup>27</sup> Al 4 mm probe, with a spinning rate of 14 kHz	D-HMQC	Recycle delay of 0.25 s; R421 as recoupling sequence, with 1.7 ms of recoupling time; DFS was applied to boost the <sup>27</sup> Al magnetization; States procedure;	40-45 hours

Table 5.7: NMR spectra recorded on 750 MHz (17.6 T) WB Bruker NMR spectrometer.

<i>Nucleus/i</i>	<i>Probe and MAS</i>	<i>Pulse sequence</i>	<i>Main Parameters</i>	<i>Time required</i>
<sup>13</sup> C	HX 4 mm probe, with a spinning rate of 10 kHz.	CP-MAS	Recycle delay of 5 s; 90° pulse on <sup>1</sup> H of 4 μs (RF field of 62 kHz); contact time of 3.5 ms; <sup>1</sup> H SPINAL-64 decoupling applied during acquisition (RF field of 70 kHz).	2-3 hours
<sup>27</sup> Al	HX 2.5 mm probe, with a spinning rate of 25 kHz.	z-filter MQMAS	RF field of 50 kHz for excitation of triple quantum (3Q) coherences and for 3Q->0Q conversion; All MQMAS spectra are presented after a shearing transformation.	10 hours
<sup>31</sup> P	HX 4 mm probe, with a spinning rate of 14 kHz.	CP-MAS	Recycle delay of 5 s; 90° pulse on <sup>1</sup> H of 4 μs (RF field of 62 kHz); contact time of 5 ms; <sup>1</sup> H SPINAL-64 decoupling applied during acquisition (RF field of 70 kHz).	around 30 minutes
<sup>31</sup> P- <sup>31</sup> P		CP-INADEQUATE	Recycle delay of 4 s; recoupling delay of 7 ms; <sup>1</sup> H SPINAL-64 decoupling applied during recoupling and acquisition time (RF field of 70 kHz and 79 kHz, respectively).	4 hours
		S3 with initial CP	Recycle delay of 4 s; recoupling delay of 2.8 ms; <sup>1</sup> H CW decoupling applied during recoupling time (RF field of 52 kHz) and <sup>1</sup> H SPINAL-64 decoupling applied during acquisition time (RF field of 70 kHz)	16-64 hours

Table 5.8: NMR spectra recorded on a 400 MHz (9.4 T) Bruker NMR spectrometer.

## References

- (1) Horcajada, P.; Chalati, T.; Serre, C.; Gillet, B.; Sebrie, C.; Baati, T.; Eubank, J. F.; Heurtaux, D.; Clayette, P.; Kreuz, C.; Chang, J.-S.; Hwang, Y. K.; Marsaud, V.; Bories, P.-N.; Cynober, L.; Gil, S.; Férey, G.; Couvreur, P.; Gref, R. Porous Metal–Organic–Framework Nanoscale Carriers as a Potential Platform for Drug Delivery and Imaging. *Nature Materials* **2010**, *9* (2), 172–178.
- (2) Anand, R.; Borghi, F.; Manoli, F.; Manet, I.; Agostoni, V.; Reschiglian, P.; Gref, R.; Monti, S. Host–Guest Interactions in Fe(III)-Trimesate MOF Nanoparticles Loaded with Doxorubicin. *J. Phys. Chem. B* **2014**, *118* (29), 8532–8539.
- (3) Simon-Yarza, T.; Mielcarek, A.; Couvreur, P.; Serre, C. Nanoparticles of Metal–Organic Frameworks: On the Road to In Vivo Efficacy in Biomedicine. *Advanced Materials* **2018**, *30* (37), 1707365–1707380.
- (4) Agostoni, V.; Horcajada, P.; Noiray, M.; Malanga, M.; Aykaç, A.; Jicsinszky, L.; Vargas-Berenguel, A.; Semiramoth, N.; Daoud-Mahammed, S.; Nicolas, V.; Martineau, C.; Taulelle, F.; Vigneron, J.; Etcheberry, A.; Serre, C.; Gref, R. A “Green” Strategy to Construct Non-Covalent, Stable and Bioactive Coatings on Porous MOF Nanoparticles. *Scientific Reports* **2015**, *5* (1), 7925–7933.
- (5) Férey, G.; Serre, C.; Mellot-Draznieks, C.; Millange, F.; Surblé, S.; Dutour, J.; Margiolaki, I. A Hybrid Solid with Giant Pores Prepared by a Combination of Targeted Chemistry, Simulation, and Powder Diffraction. *Angewandte Chemie* **2004**, *116* (46), 6456–6461.
- (6) Volkringer, C.; Popov, D.; Loiseau, T.; Férey, G.; Burghammer, M.; Riekkel, C.; Haouas, M.; Taulelle, F. Synthesis, Single-Crystal X-Ray Microdiffraction, and NMR Characterizations of the Giant Pore Metal–Organic Framework Aluminum Trimesate MIL-100. *Chemistry of Materials* **2009**, *21* (24), 5695–5697.
- (7) Porcino, M.; Christodoulou, I.; Dang Le Vuong, M.; Gref, R.; Martineau-Corcoc, C. New Insights on the Supramolecular Structure of Highly Porous Core–Shell Drug Nanocarriers Using Solid-State NMR Spectroscopy. *RSC Advances* **2019**, *9*, 32472–32475.
- (8) Vuong Dang Le, M. Degradation Study of Metal–Organic Framework Nanoparticles by Solid-State Nuclear Magnetic Resonance Spectroscopy, 2019.
- (9) Li, X.; Lachmanski, L.; Safi, S.; Sene, S.; Serre, C.; Grenèche, J. M.; Zhang, J.; Gref, R. New Insights into the Degradation Mechanism of Metal–Organic Frameworks Drug Carriers. *Sci Rep* **2017**, *7* (1), 13142–13153.
- (10) Haouas, M.; Volkringer, C.; Loiseau, T.; Férey, G.; Taulelle, F. Monitoring the Activation Process of the Giant Pore MIL-100(Al) by Solid State NMR. *The Journal of Physical Chemistry C* **2011**, *115* (36), 17934–17944.
- (11) Massiot, D.; Fayon, F.; Alonso, B.; Trebosc, J.; Amoureux, J.-P. Chemical Bonding Differences Evidenced from J-Coupling in Solid State NMR Experiments Involving Quadrupolar Nuclei. *Journal of Magnetic Resonance* **2003**, *164*, 160–164.
- (12) Benzaqui, M.; Pillai, R. S.; Sabetghadam, A.; Benoit, V.; Normand, P.; Marrot, J.; Menguy, N.; Montero, D.; Shepard, W.; Tissot, A.; Martineau-Corcoc, C.; Sicard, C.; Mihaylov, M.; Carn, F.; Beurroies, I.; Llewellyn, P. L.; De Weireld, G.; Hadjiivanov, K.; Gascon, J.; Kapteijn, F.; Maurin, G.; Steunou, N.; Serre, C. Revisiting the Aluminum Trimesate-Based MOF (MIL-96): From Structure Determination to the Processing of Mixed Matrix Membranes for CO<sub>2</sub> Capture. *Chem. Mater.* **2017**, *29* (24), 10326–10338.
- (13) Upreti, M.; Strassburger, K.; Chen, Y. L.; Wu, S.; Prakash, I. Solubility Enhancement of Steviol Glycosides and Characterization of Their Inclusion Complexes with Gamma-Cyclodextrin. *International Journal of Molecular Sciences* **2011**, *12* (11), 7529–7553.
- (14) Rossini, A. J.; Zagdoun, A.; Lelli, M.; Canivet, J.; Aguado, S.; Ouari, O.; Tordo, P.; Rosay, M.; Maas, W. E.; Copéret, C.; Farrusseng, D.; Emsley, L.; Lesage, A. Dynamic Nuclear Polarization Enhanced Solid-State NMR Spectroscopy of Functionalized Metal–Organic Frameworks. *Angew. Chem. Int. Ed.* **2012**, *51* (1), 123–127.

- (15) Pourpoint, F.; Thankamony, A. S. L.; Volkringer, C.; Loiseau, T.; Trébosc, J.; Aussenac, F.; Carnevale, D.; Bodenhausen, G.; Vezin, H.; Lafon, O.; Amoureux, J.-P. Probing  $^{27}\text{Al}$ – $^{13}\text{C}$  Proximities in Metal–Organic Frameworks Using Dynamic Nuclear Polarization Enhanced NMR Spectroscopy. *Chem. Commun.* **2014**, 50 (8), 933–935.
- (16) Guo, Z.; Kobayashi, T.; Wang, L.-L.; Goh, T. W.; Xiao, C.; Caporini, M. A.; Rosay, M.; Johnson, D. D.; Pruski, M.; Huang, W. Selective Host-Guest Interaction between Metal Ions and Metal-Organic Frameworks Using Dynamic Nuclear Polarization Enhanced Solid-State NMR Spectroscopy. *Chem. Eur. J.* **2014**, 20 (49), 16308–16313.
- (17) Deschamps, M.; Fayon, F.; Hiet, J.; Ferru, G.; Derieppe, M.; Pellerin, N.; Massiot, D. Spin-Counting NMR Experiments for the Spectral Editing of Structural Motifs in Solids. *Phys. Chem. Chem. Phys.* **2008**, 10, 1298–1303.
- (18) Trebosc, J.; Hu, B.; Amoureux, J. P.; Gan, Z. Through-Space R3-HETCOR Experiments between Spin-1/2 and Half-Integer Quadrupolar Nuclei in Solid-State NMR. *Journal of Magnetic Resonance* **2007**, 186, 220–227.
- (19) Wishart, D. S.; Feunang, Y. D.; Marcu, A.; Guo, A. C.; Liang, K.; Vázquez-Fresno, R.; Sajed, T.; Johnson, D.; Li, C.; Karu, N.; Sayeeda, Z.; Lo, E.; Assempour, N.; Berjanskii, M.; Singhal, S.; Arndt, D.; Liang, Y.; Badran, H.; Grant, J.; Serra-Cayuela, A.; Liu, Y.; Mandal, R.; Neveu, V.; Pon, A.; Knox, C.; Wilson, M.; Manach, C.; Scalbert, A. HMDB 4.0: The Human Metabolome Database for 2018. *Nucleic Acids Research* **2018**, 46 (D1), D608–D617.
- (20) Wishart, D. S.; Jewison, T.; Guo, A. C.; Wilson, M.; Knox, C.; Liu, Y.; Djoumbou, Y.; Mandal, R.; Aziat, F.; Dong, E.; Bouatra, S.; Sinelnikov, I.; Arndt, D.; Xia, J.; Liu, P.; Yallou, F.; Bjorn Dahl, T.; Perez-Pineiro, R.; Eisner, R.; Allen, F.; Neveu, V.; Greiner, R.; Scalbert, A. HMDB 3.0—The Human Metabolome Database in 2013. *Nucleic Acids Research* **2012**, 41 (D1), D801–D807.
- (21) Wishart, D. S.; Knox, C.; Guo, A. C.; Eisner, R.; Young, N.; Gautam, B.; Hau, D. D.; Psychogios, N.; Dong, E.; Bouatra, S.; Mandal, R.; Sinelnikov, I.; Xia, J.; Jia, L.; Cruz, J. A.; Lim, E.; Sobsey, C. A.; Shrivastava, S.; Huang, P.; Liu, P.; Fang, L.; Peng, J.; Fradette, R.; Cheng, D.; Tzur, D.; Clements, M.; Lewis, A.; De Souza, A.; Zuniga, A.; Dawe, M.; Xiong, Y.; Clive, D.; Greiner, R.; Nazyrova, A.; Shaykhtudinov, R.; Li, L.; Vogel, H. J.; Forsythe, I. HMDB: A Knowledgebase for the Human Metabolome. *Nucleic Acids Research* **2009**, 37 (Database), D603–D610.
- (22) Wishart, D. S.; Tzur, D.; Knox, C.; Eisner, R.; Guo, A. C.; Young, N.; Cheng, D.; Jewell, K.; Arndt, D.; Sawhney, S.; Fung, C.; Nikolai, L.; Lewis, M.; Coutouly, M.-A.; Forsythe, I.; Tang, P.; Shrivastava, S.; Jeroncic, K.; Stothard, P.; Amegbey, G.; Block, D.; Hau, David. D.; Wagner, J.; Miniaci, J.; Clements, M.; Gebremedhin, M.; Guo, N.; Zhang, Y.; Duggan, G. E.; MacInnis, G. D.; Weljie, A. M.; Dowlatabadi, R.; Bamforth, F.; Clive, D.; Greiner, R.; Li, L.; Marrie, T.; Sykes, B. D.; Vogel, H. J.; Querengesser, L. HMDB: The Human Metabolome Database. *Nucleic Acids Research* **2007**, 35 (Database), D521–D526.
- (23) Ben-Bashat, D.; Shinar, H.; Navon, G.  $^{31}\text{P}$  NMR Methods for the Direct Determination of ADP in the Presence of ATP. *Journal of Magnetic Resonance, Series B* **1996**, 110 (3), 231–239.
- (24) Massiot, D.; Fayon, F.; Capron, M.; King, I.; Le Calvé, S.; Alonso, B.; Durand, J.-O.; Bujoli, B.; Gan, Z.; Hoatson, G. Modelling One- and Two-Dimensional Solid-State NMR Spectra: Modelling 1D and 2D Solid-State NMR Spectra. *Magn. Reson. Chem.* **2002**, 40 (1), 70–76.

## Chapter 6

Surface modified nanoMIL-100(Al) as  
drug carrier for Doxorubicin



## 1. Introduction

Surface modification is an essential step to improve the long-term colloidal stability of DDSs. CD-P coating, as illustrated in detail in Chapter 5, showed a great ability of stabilization of nanoparticles, but it does not allow the complete degradation of the nanoMOF, that can be a potential problem for the release of the drug. To improve this aspect, a new CD-based coating was developed by Prof R. Gref. The goal was to increase the amount of CD at the surface of the NPs and to combine the carrier effect of CD and the nanoMOF to potentially increase the drug loading. Furthermore, the different interactions of the drug with the CD or with the nanoMOF could lead to a two-step release process, interesting aspect in view therapeutic comfort. In the first part of this chapter, the new coating and its interaction with the nanoMIL-100(Al) is presented. In the second part, the efficiency of the new DDS to incorporate doxorubicin (DOX) drug (Figure 6.1) is investigating.

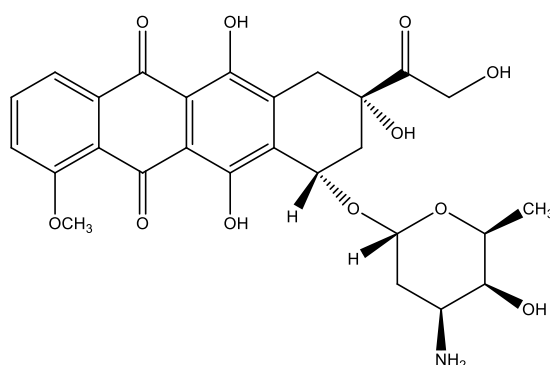


Figure 6.1: Chemical Structure of Doxorubicin.

Doxorubicin (DOX) is a very potent cytotoxic anticancer, belonging to the anthracycline family and used to treat leukemia and other solid tumors. DOX directly inhibits topoisomerase II and nucleic acid synthesis. As a result, the proliferation of cancer cells will be terminated. However, doxorubicin has limited use because of its severe side effects such as cardiotoxicity like as dysrhythmia and heart failure<sup>1</sup>. Moreover, in water solution the DOX molecules have tendency to self-associate each other and this affect cell uptake and may affect cell uptake and may cause cancer cell drug resistance<sup>2</sup>. The cardiotoxicity of anthracyclines has been related to their redox activity and thought to be controllable

by delivering the drugs as Fe(III) complexes. NanoMIL-100(Fe) gives the possibility of Fe complexes formation to reduce the cardiotoxicity as well as tendency to overcome the self-association of DOXO complex that affect cell uptake and may cause cancer cell drug resistance. The maximal DOX payload in nanoMIL-100(Fe) was reported as 32.5 wt%, while polymeric nanoparticles, such as poly lactic-co-glycolic acid (PLGA) nanoparticles (NPs), DOX payload was less than 15 wt%, whatever the preparation method<sup>3-6</sup> and DOX payload in the commercial Doxil® (doxorubicin loaded liposome) was only around 12 wt%<sup>7,8</sup>. Among all the DDS used<sup>1,2,9</sup> to deliver Doxorubicin drug, biodegradable  $\gamma$ -CD-citrate oligomers (CD-CO) (Figure 6.2)<sup>10</sup> showed a good deliver profile of the drug in breast cell tumor, with a complete preservation of the drug<sup>9</sup>.

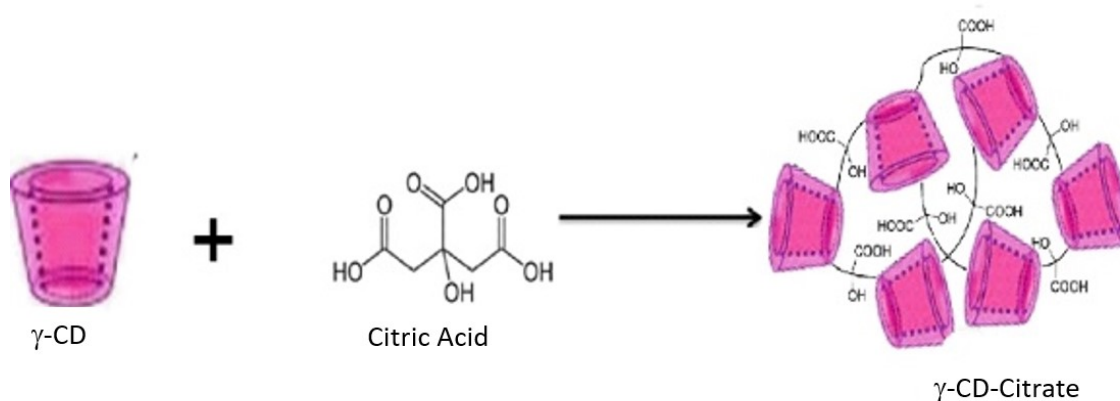


Figure 6.2: Schematic representation of  $\gamma$ -CD-citrate oligomers.

Coating the surface of the nanoMIL-100(Fe) with the CD-CO polymer may therefore be a strategy to improve the performance of both DDSs and have a safe delivery of the DOX drug. The synthesis of CD-CO coated nanoMIL-100(Al) and the DOX incorporation were carried out by Dr. Lisa Xue in the group of Prof. Ruxandra Gref. The CD-CO oligomers were synthesized by adapting a previously reported method<sup>10</sup> and by simply incubating the nanoMOFs in aqueous DOX solutions under agitation, at room temperature for 1~6 days, the drug was loaded. Figure 6.3 reports the kinetics of DOX encapsulation obtained by fluorescence spectroscopy.

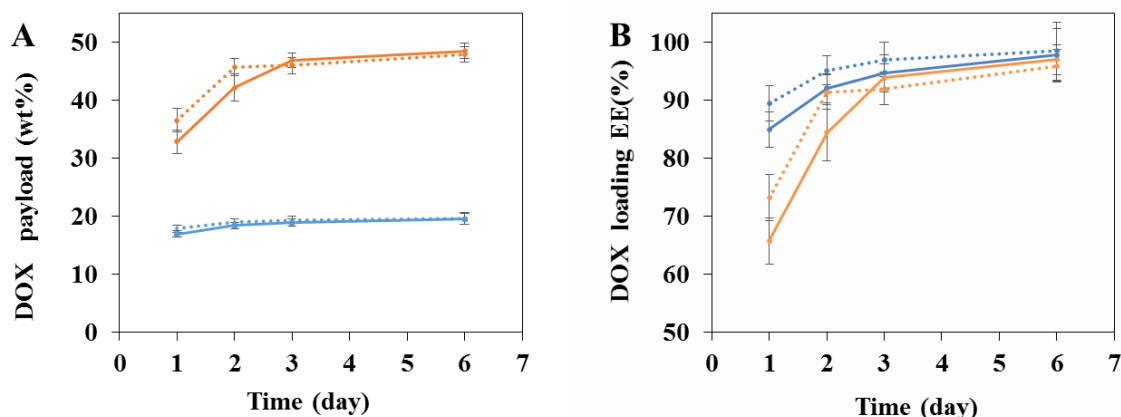


Figure 6.3: DOX payload (A) and encapsulation efficiency (EE, B) in nanoMIL-100(Fe) (straight line) and CD-CO@nanoMIL-100(Fe) (dotted line) at different TDL (blue: 20%; orange: 50%).

Noteworthy, the nanoMOFs kept the same morphology with faceted-type structures before and after DOX encapsulation, whatever the payloads, as shown by TEM images (Figure 6.4).

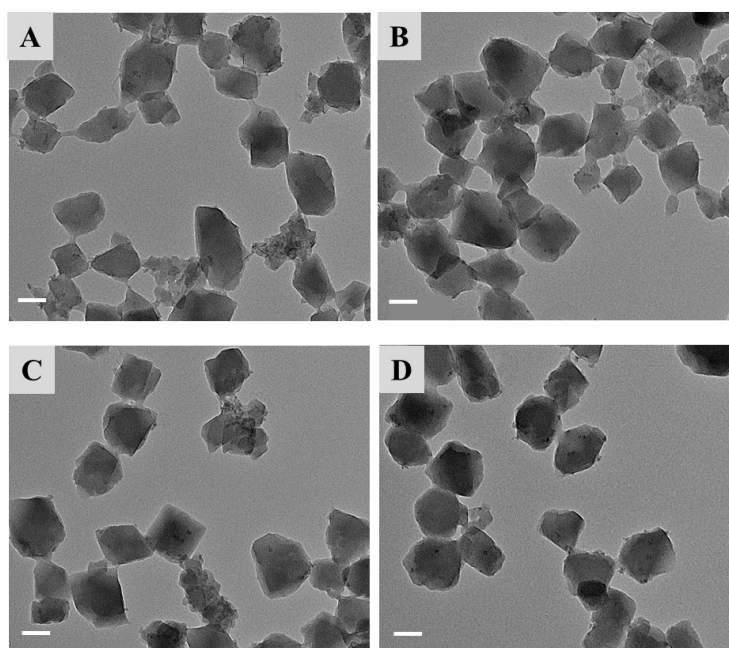


Figure 6.4: TEM images of MIL-100 (Fe) nanoMOFs (A), CD-CO@nanoMOFs (B), DOX loaded nanoMOFs (C) and DOX loaded CD-CO@nanoMOFs (D) (scale bar: 100 nm).

After surface modification with CD-CO, the colloidal stability of Dox loaded nanoMIL-100(Fe) was significantly improved and no aggregation was observed after three weeks storage at 4°C at lower loadings (DOX payload of  $19.6 \pm 0.9$  wt%). Surprisingly, at high loadings (TDL of 50% or 100%), the DOX-loaded CD-CO coated nanoMil-100(Fe) aggregated immediately after DOX loading.

DOX release studies in PBS were also conducted. DOX loaded nanoMOFs were diluted in PBS solution and incubated at 37°C after centrifugation and quantified by fluorescent spectroscopy. Interestingly, the DOX release behavior was found to be dependent on the DOX payloads. When DOX payload of  $19.6\pm 0.9$  wt%, DOX release from bare nanoMOFs reached around  $31\pm 2.3\%$  within 3 days and  $56\pm 4.0\%$  in 30 days (Figure 6.5).

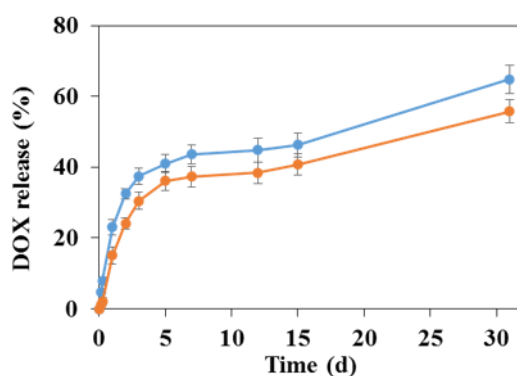


Figure 6.5. DOX release in PBS of DOX loaded nanoMIL-100(Fe) (orange) and DOX loaded CD-CO coated nanoMIL-100(Fe) (blue). The CD-CO coating accelerated DOX release ( $56\pm 4.0\%$  &  $65\pm 3.7\%$  in 30 days for nanoMOFs and CD-CO@nanoMOFs, respectively).

When less DOX was loaded, in the case of DOX payload of  $9.7\pm 0.8$  wt%, more DOX was released in the same condition ( $76\pm 3.2\%$  &  $56\pm 4.0\%$  in 30 days for TDL of 10% and 20%, respectively). When more DOX was loaded in nanoMOFs, they were possibly more packed in the pores or on the surface of nanoMOFs. This phenomenon has been reported in the case of topotecan, of which the monomers aggregate inside the pores of nanoMOFs in a “ship in a bottle” fashion<sup>11</sup>. In this study, it appears that the advantage of CD coating is to better extract DOX from the cores, although the effect is not very strong. In conclusion, CD coating accelerates the loading process and allows to better extract DOX. If fluorescence spectroscopy provides quantitative information about drug loading and release, it is essential to understand the interactions playing at atomic level. As already reported in the Chapter 5, we chose to investigate by ssNMR spectroscopy the diamagnetic analog of nanoMIL-100(Fe), namely nanoMIL-100(Al), assuming similar drug/host interactions could occur in both systems. We first report the interactions of the new CD-CO coating with the MOF nanoparticles and its role on the degradability

of the MOF. In the second part, the loading of the drug in the CD-CO coating, in the MOF and in the MOF covered with the CD-CO coating are shown. Contrary to the CD-P reported in Chapter 5, there is no heteroatom present in large quantity on the coating, making the NMR investigation much more challenging. Therefore, the isotopic labelling strategy used to tackle this challenge is illustrated.

## 2. CD-CO coating on nanoMIL-100(Al)

To understand the affinity of the covering CD-CO groups and the MOF surface,  $^1\text{H}$ ,  $^{27}\text{Al}$  and  $^{13}\text{C}$  MAS NMR were recorded on nanoMIL-100(Al) and CD-CO coated nanoMIL-100(Al). The  $^{27}\text{Al}$  MAS NMR of both samples are similar (Figure 6.6), with all Al atoms in six-fold coordination.

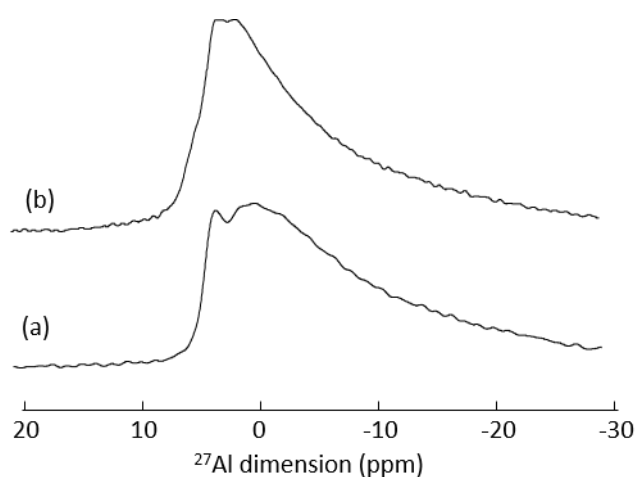


Figure 6.6:  $^{27}\text{Al}$  MAS NMR of nanoMIL-100(Al) (a) and CD-CO coated nanoMIL-100(Al) (b), recorded at 10 kHz on a 9.4 T spectrometer.

In the  $^{13}\text{C}$  CPMAS NMR spectra (Figure 6.7), the  $^{13}\text{C}$  resonances corresponding to the CD-CO can be identified: the CD part is located in the 60-80 ppm region, while the citrate carboxyl atoms appear in the 180 ppm region, the  $\text{CH}_2$  around 40 ppm and  $\text{CH-OH}$  around 100 ppm. Note in Figure 6.7b that the  $^{13}\text{C}$  resonances of the free  $\text{COOH}$  and the ester  $\text{COOCD}$  have similar chemical shift, as a single broad resonance is observed. One can notice an unfortunate overlap of the carboxylic  $^{13}\text{C}$  resonances with those of the carboxylic carbon atoms from the MOF linker in the 170-180 ppm region. Due to the small proportion of coating with respect to the NP size, the signals of the CD-CO have low intensity and it is therefore difficult to distinguish between the ester ( $\text{COOCD}$ ) and the free  $\text{COOH}$  of

the citric acid moieties, but it is possible to notice a new  $^{13}\text{C}$  resonance around 180 ppm, not present in the pure coating and pristine nanoMOF.

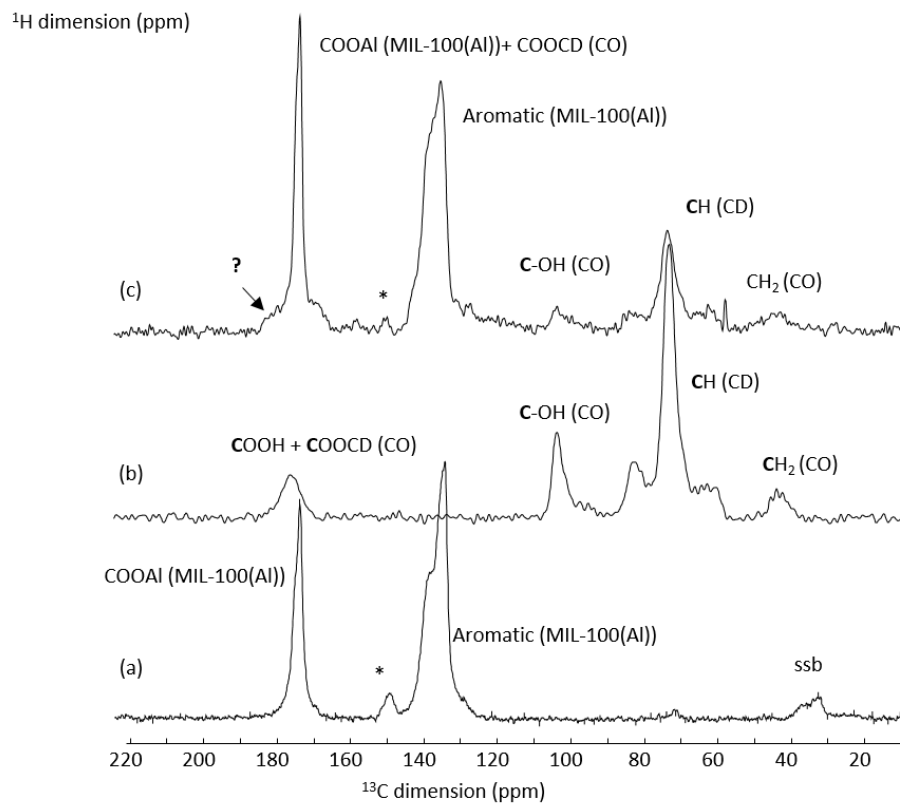


Figure 6.7:  $^{13}\text{C}$  CPMAS NMR of nanoMIL-100(Al) (a), CD-CO polymer (b) and CD-CO coated nanoMIL-100(Al) (c), recorded at 10 kHz on a 9.4 T spectrometer. The lines are assigned. \* indicate traces of impurities and ssb indicate the spinning sidebands.

$^1\text{H}$  MAS NMR spectra were also recorded and are shown in Figure 6.8.

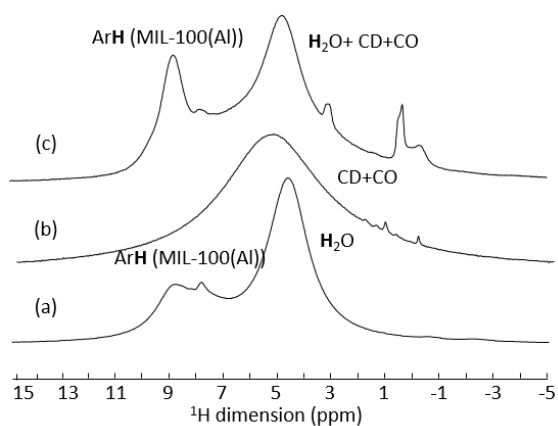


Figure 6.8:  $^1\text{H}$  MAS NMR of nanoMIL-100(Al) (a), CD-CO polymer (b) and CD-CO coated nanoMIL-100(Al), recorded at 10 kHz on a 9.4 T spectrometer. The lines are assigned.

However, as was already observed for MIL-100(Al) NPs coated with CD-P (see Chapter 5), due to the presence of numerous protons both in the MOF and in the coating (the  $^1\text{H}$  spectrum is dominated by the broad peak of the  $\text{CH}_2$  protons of the CD), no useful information could be extracted. In CD-P coated nanoMIL-100(Al), the strategy of take advantage of the heteroatoms present either in the MOF only (i.e.,  $^{27}\text{Al}$ ) or in the coating only ( $^{31}\text{P}$ ), allowed clear probing of the coating-MOF interactions. In the system under study here, while the MOF still contains a heteroatom ( $^{27}\text{Al}$ ), the coating only contains  $^1\text{H}$  and non-abundant  $^{13}\text{C}$  (ca. 1% natural abundance).

Therefore, we chose to  $^{13}\text{C}$ -label the CD-CO polymer. This was performed by using 1,5- $^{13}\text{C}_2$ -citric acid in the polymer synthesis. This way,  $^{27}\text{Al}$  was selectively present in the MOF, while  $^{13}\text{C}$  is present in significant quantity in both the coating and the nanoparticles. The  $^1\text{H}$  and  $^{27}\text{Al}$  NMR spectra recorded on labeled and non-labeled coated nanoMOF are quite similar, showing that the enrichment of the coating did not influence the polymer-MOF interactions (Figure 6.9).

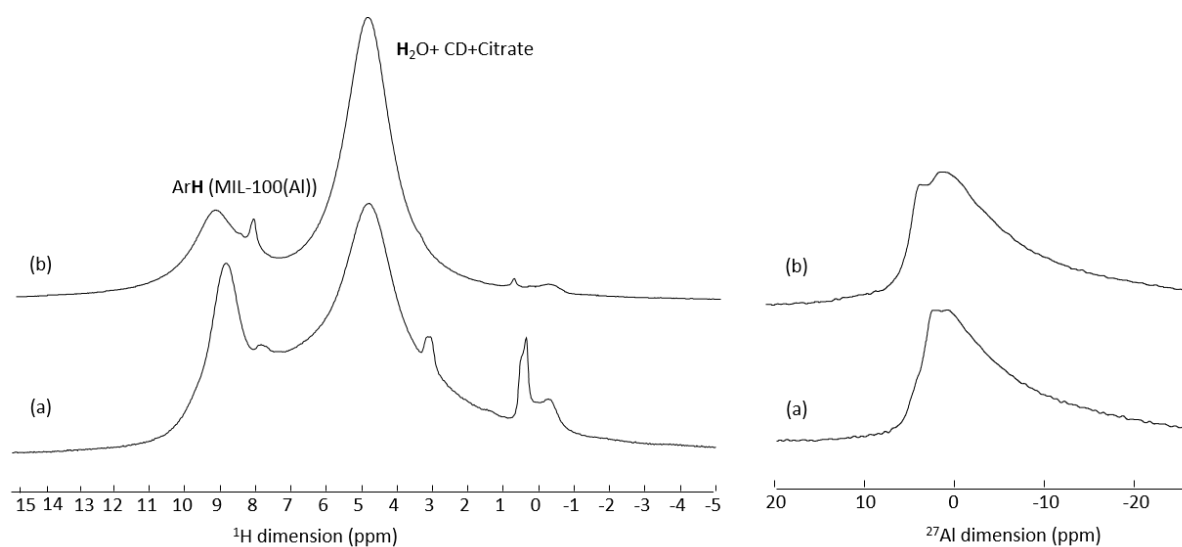


Figure 6.9:  $^1\text{H}$  MAS NMR of CD-CO coated nanoMIL-100(Al) (a) and CD- $^{13}\text{C}_2$  coated nanoMIL-100(Al) (b), recorded at 10 kHz on a 9.4 T spectrometer.

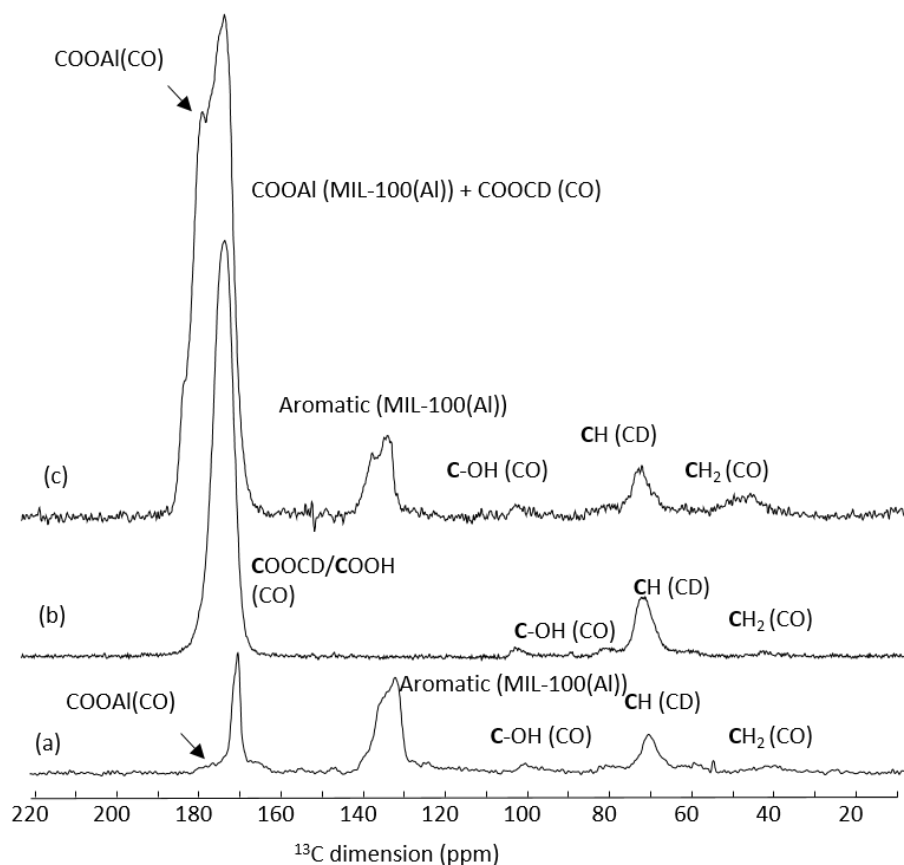


Figure 6.10:  $^{13}\text{C}$  CPMAS NMR of CD-CO coated nanoMIL-100(Al) (a), CD- $^{13}\text{C}$ O polymer (b) and CD- $^{13}\text{C}$ O coated nanoMIL-100(Al) (c), recorded at 10 kHz on a 9.4 T spectrometer. The lines are assigned.

The evidence of the enrichment was clearly visible on the  $^{13}\text{C}$  NMR spectrum recorded at 9.4 T (Figure 6.10). In contrast with the CD-CO coated nanoMOF, the labeled sample presents, clearly, two  $^{13}\text{C}$  signals in the region around 180-170 ppm. A comparison with the  $^{13}\text{C}$  NMR recorded on the polymer evidences that the resonance around 175 ppm belongs to the COOCD and COOH of the citrate as long as the COOAl of the nanoMIL-100(Al) and that the second resonance around 180 ppm is a new  $^{13}\text{C}$  species, probably formed from the interaction (chemical bond) between the COOH of the citrate and the Al surface sites of the nanoMOF.

To probe this hypothesis,  $^{27}\text{Al}$ - $^{13}\text{C}$  2D *D*-HMQC experiment was performed and compared with one recorded on pure nanoMIL-100(Al) (Figure 6.11). As already said in Chapter 5, through-space HMQC has to be used, because of the short  $^{27}\text{Al}$  transverse relaxation time  $T_2$  (shown in Table 5.3). These experiments show the spatial proximity between carbon and aluminum atoms. Correlation peaks of

strong intensity are observed between the CD-CO ( $^{13}\text{C}$  resonance at 180 ppm) and the surface Al sites, confirming that the CD-CO polymer has high affinity with the surface of the nanoparticles.

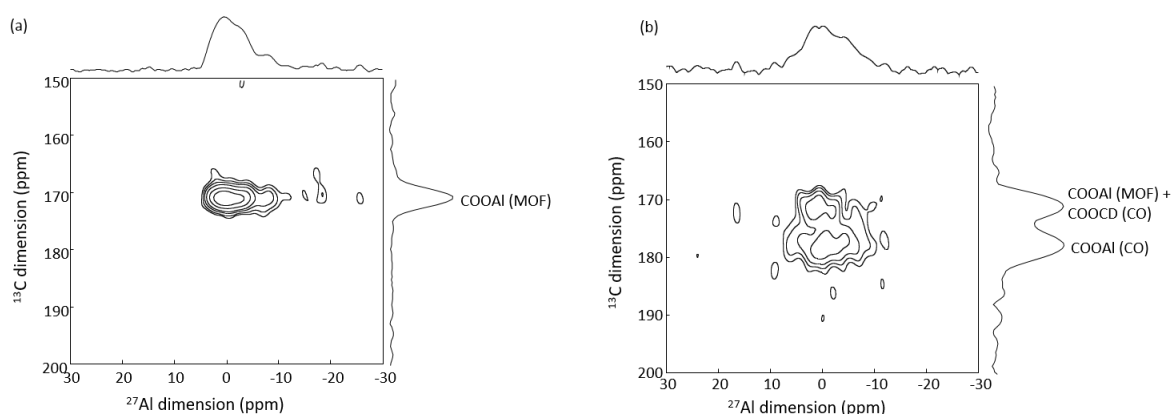


Figure 6.11:  $^{27}\text{Al}\{^{13}\text{C}\}$  2D *D*-HMQC NMR of nanoMIL-100(Al) (a) and CD- $^{13}\text{C}$ O coated nanoMIL-100(Al) (b), recorded at 12.5 kHz on a 9.4 T spectrometer.

$^{13}\text{C}$ - $^{27}\text{Al}$  double-resonance RESPDOR NMR spectra were further recorded (Figure 6.12), to try identifying the structural differences between the two peaks observed in the carboxylic region, since  $^{13}\text{C}$ - $^{27}\text{Al}$  RESPDOR experiments can provide indication about the relative C-Al internuclear distances. In a RESPDOR experiment, a larger dephasing indicates shorter Al-C distance. For CD-CO coated nanoMIL-100(Al), the spectra show that the  $^{13}\text{C}$  resonance at 180 ppm (line 2) has shorter distance to the Al than the  $^{13}\text{C}$  resonance at 175 ppm (line 1). Note that the  $^{13}\text{C}$  resonance at 175 ppm contains both the carboxylic group of the trimesate linker of the MOF (not labeled, but present in large quantity) and the COO-CD of the CD- $^{13}\text{C}$ O coating. This supports further the hypothesis that this additional peak results from a chemical bond formed between some of the free COOH groups of the CD-CO polymers and the Al atoms located at the surface of the MOF NPs.

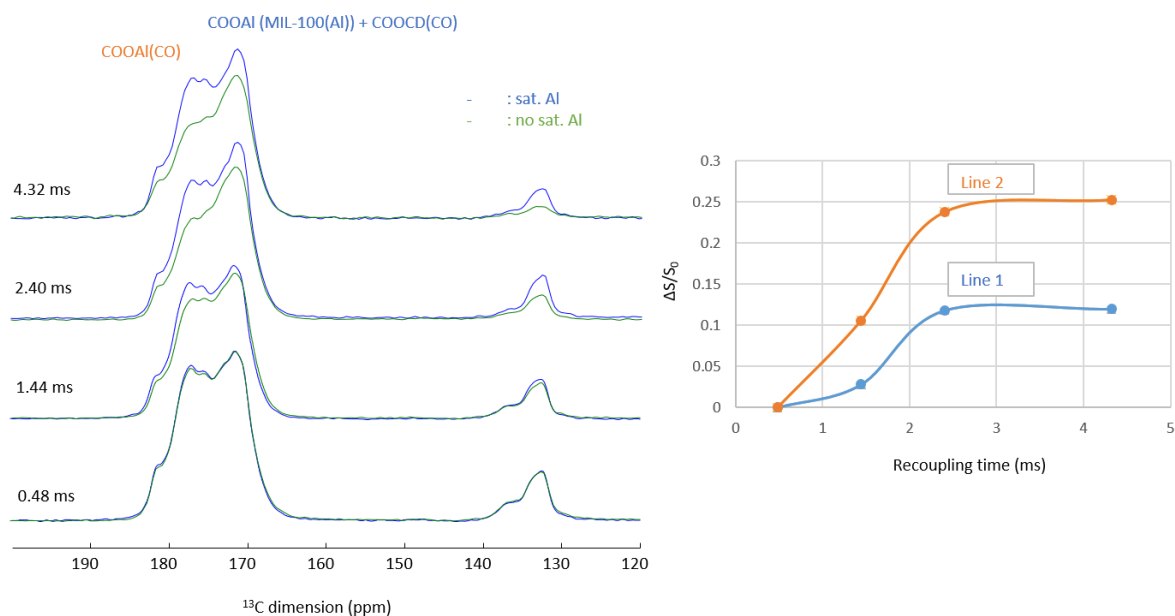


Figure 6.12:  $^{13}\text{C}$ - $^{27}\text{Al}$  CP-RESPDOR NMR spectra (left) with non (green) and saturation (blue) of Al nuclei, recorded at 12.5 kHz (9.4 T) at different recoupling time; RESPDOR curves of Line 2 (corresponding to COOAl (CO) and shown in orange) and Line 1 (corresponding to COOAl (MIL-100(Al)) + COOCD (CO) and shown in blue).

Knowing the interactions taking place, degradation reaction of CD- $^{13}\text{C}$  coated nanoMOF in mimetic physiological medium, as phosphate buffer PBS, as shown by M. Vuong in her Master thesis<sup>12</sup>, was performed to investigate the degradation profile and compare the two different coating (CD-P and CD-CO).

$^1\text{H}$  and  $^{13}\text{C}$  MAS NMR experiments (Figure 6.13) were recorded on the solid recovered, filtered and dried after the degradation. If little change are noticed in the  $^1\text{H}$  NMR spectra, it is possible to notice on the  $^{13}\text{C}$  CPMAS NMR spectrum small fraction of citrate release after the degradation from the  $^{13}\text{C}$  resonance belonging to the COO<sup>-</sup> of the Citrate. The  $^{31}\text{P}$  CPMAS NMR spectrum (Figure 6.14) shows a broad resonance centered at -10 ppm. On the  $^{27}\text{Al}$  NMR spectrum of the degraded product, one can notice the increase of intensity of the resonance located around -5 ppm.

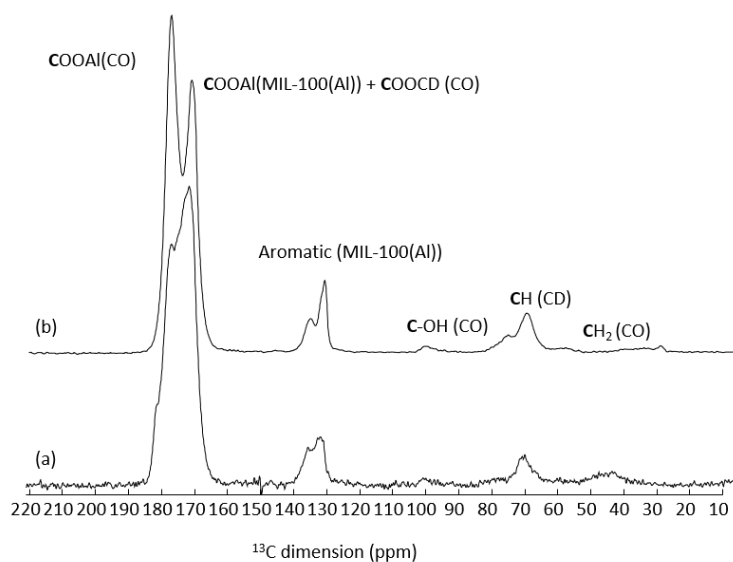
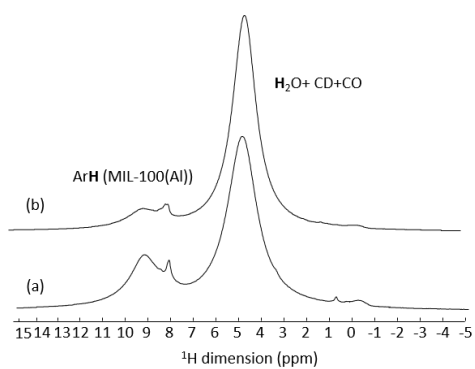


Figure 6.13:  $^1\text{H}$  MAS (up) and  $^{13}\text{C}$  CPMAS (bottom) NMR of  $\text{CD-}^{13}\text{CO}$  coated nanoMIL-100(Al) (a) and degraded  $\text{CD-}^{13}\text{CO}$  coated nanoMIL-100(Al) (b), recorded at 10 kHz on a 9.4 T spectrometer. The lines are assigned.

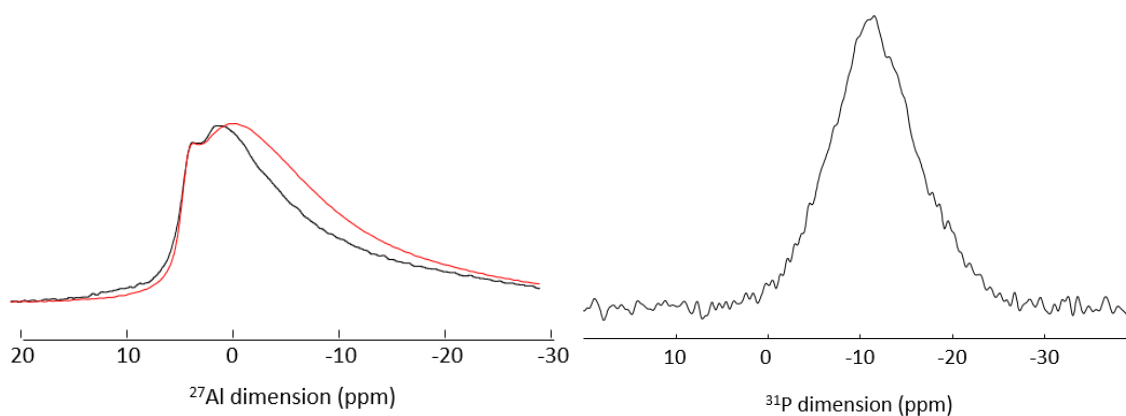


Figure 6.14:  $^{27}\text{Al}$  MAS NMR of  $\text{CD-}^{13}\text{CO}$  coated nanoMIL-100(Al) (black) and degraded  $\text{CD-}^{13}\text{CO}$  coated nanoMIL-100(Al) (red) (left) and  $^{31}\text{P}$  CPMAS NMR spectrum of degraded  $\text{CD-}^{13}\text{CO}$  coated nanoMIL-100(Al) (right), recorded at 12.5 kHz and 14 kHz, respectively, on a 9.4 T spectrometer.

This was already observed in the degraded nanoMIL-100(Al) and was characteristic of the formation of Al-O-P bonds between the framework aluminum atoms and the phosphate species of the PBS. Formation of this bond is confirmed by the 2D  $^{27}\text{Al}$ - $^{31}\text{P}$  *D*-HMQC MAS NMR recorded (Figure 6.15). On this spectrum, similarly to the degraded CD-P coated nanoMIL-100(Al), a peak of strong intensity is observed between the phosphorus species and the new resonances at -5 ppm. As mentioned in Chapter 5, the degraded CD-P coated nanoMIL-100(Al) showed the presence of 4 and 5 coordinated Al species, that were hypothetically thought to be related to the formation of an  $\text{AlPO}_x$  passivation layers on NPs external surface. These species are absent in the CD-CO coated nanoMIL-100(Al). This may be due to the much larger covering obtained with the CD-CO polymers coating, preventing the phosphate species from attacking the external surface of the particles. The following step is to measure the linker release of this CD-CO coated nanoMIL-100(Al) and try to understand whether the new coating allows better degradation of the particles.

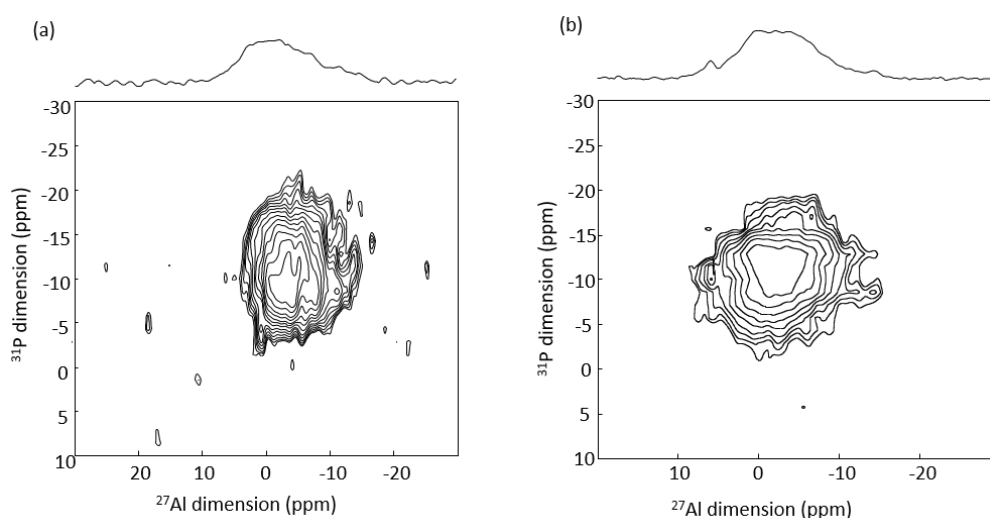


Figure 6.15: 2D  $^{27}\text{Al}\{^{31}\text{P}\}$  *D*-HMQC MAS NMR spectra of degraded CD-P coated MIL-100(Al) (a) and degraded CD- $^{13}\text{C}$ O coated nanoMIL-100(Al) (b), recorded at 14 kHz on a 17.6 T spectrometer.

Finally, a 2D  $^{27}\text{Al}$ - $^{13}\text{C}$  *D*-HMQC MAS NMR was recorded and compared with the one recorded on the non degraded sample (Figure 6.16). On the indirect  $^{13}\text{C}$  projection, one can notice the difference of intensity between the two  $^{13}\text{C}$  carbonyl resonances, notably with a decrease of the peak corresponding to the ester of the nanoMOF, as consequence of the degradation process. The presence

of the interaction between the Al sites and the CO polymer ( $^{13}\text{C}$  resonance at 180 ppm) evidences that the polymer seems stable even after the degradation process. Probably, only a few percentage is released. This result can be important in the rate of the drug release process.

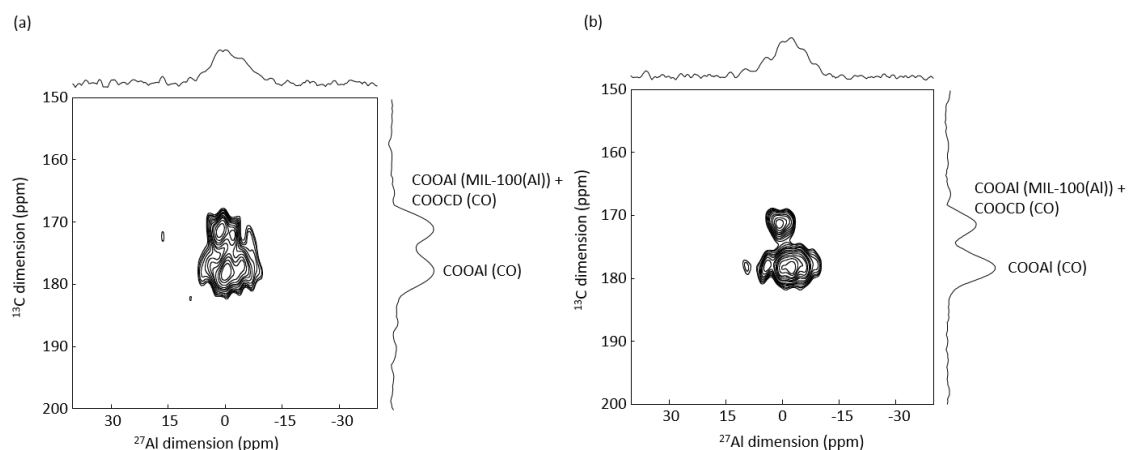


Figure 6.16:  $^{27}\text{Al}\{^{13}\text{C}\}$  2D *D*-HMQC NMR of CD- $^{13}\text{C}$ O coated nanoMIL-100(Al) (a) and degraded CD- $^{13}\text{C}$ O coated nanoMIL-100(Al) (b), recorded at 12.5 kHz on a 9.4 T spectrometer.

Now that the good interaction of the CD-CO coating with the MOF surface is ascertained, DOX loading was investigated in a step by step manner. We first show the DOX loading in nanoMIL-100(Al) and CD-CO polymer separately and eventually in the target DDS, CD-CO coated nanoMIL-100(Al).

### 3. DOX loaded in nanoMIL-100(Al)

Figure 6.17 reports the  $^{13}\text{C}$  CPMAS NMR spectra of MIL-100(Al) nanoparticles loaded with various amount of DOX. All the spectra show the presence of the DOX molecules, confirming the success of the loading process. One can notice differences between the positions of some carbon resonances of the DOX loaded compared to those of pure crystalline DOX. It turns out that the chemical shift of the  $^{13}\text{C}$  resonances of the loaded DOX are very similar to those of DOX in solution, notably in the 110-140 ppm region (Figure 6.17e). The difference between DOX molecules in the crystalline phase and in solution is the presence of  $\pi$ - $\pi$  interactions in the crystal that generates particular  $^{13}\text{C}$  shifts in the aromatic region. In Figure 6.18 are shown the  $^{13}\text{C}$  solid and the liquid simulated NMR spectra of the Doxorubicin drug with assignment of all the  $^{13}\text{C}$  resonances. The fact that the DOX molecules loaded in the MOF NPs have chemical shifts similar to that in solution indicates the absence of  $\pi$ - $\pi$  stacking

once incorporated in the MOF. MIL-100(Al) nanoparticles were loaded with increasing amount of DOX, from 5 to 50 wt%. While a clear increase of the  $^{13}\text{C}$  DOX resonance intensity is observed between the 5 and 20% loading (Figures 6.17 b and c), no difference is observed between 20 and 50% loading (Figures 6.17 c and d). This very likely shows that the amount of DOX loading inside the pores of the MOF is limited to ca 20%. One possible explanation for the fact that the  $^{13}\text{C}$  signal of the excess DOX molecules is not seen, could be an accumulation of DOX molecules on the surface of the particles. If this external layer of DOX is amorphous, it will generate very broad  $^{13}\text{C}$  resonances that could be difficult to detect because lying under the peaks of the crystalline phase.

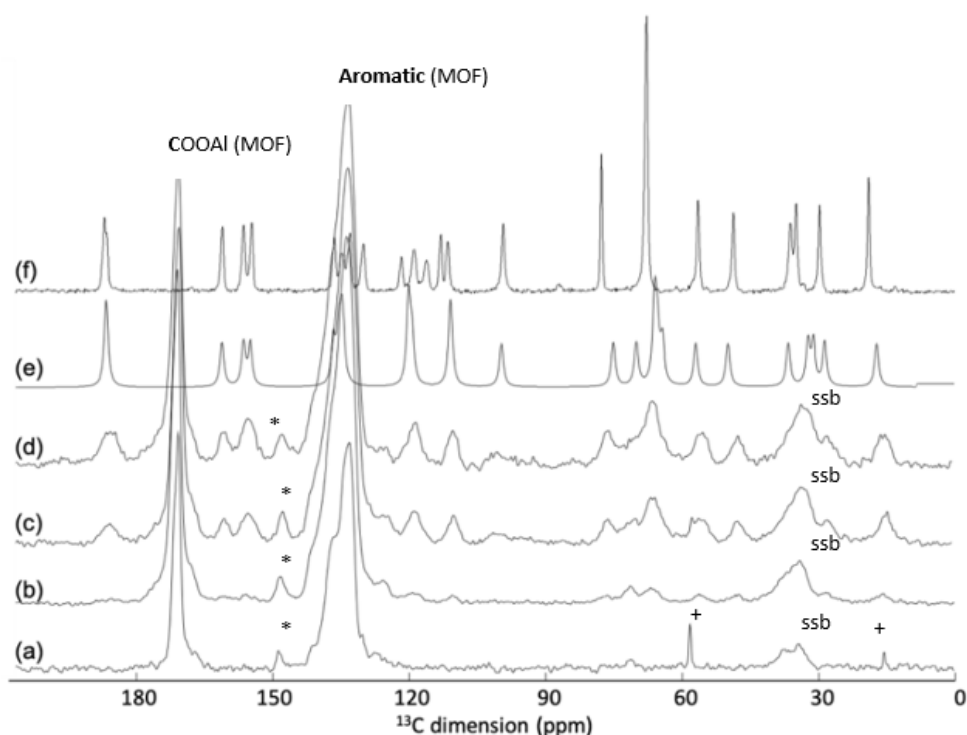


Figure 6.17:  $^{13}\text{C}$  CPMAS NMR spectra of (a) MIL-100(Al) and MIL-100(Al) loaded with (b) 5% DOX, (c) 20% DOX and (d) 50% DOX. In (e) and (f) are shown the  $^{13}\text{C}$  NMR spectra of DOX in solution and in the solid-state, respectively. Unlabeled lines correspond to the DOX signals. \* indicate traces of impurities, + indicate traces of EtOH and ssb indicate the spinning sidebands.

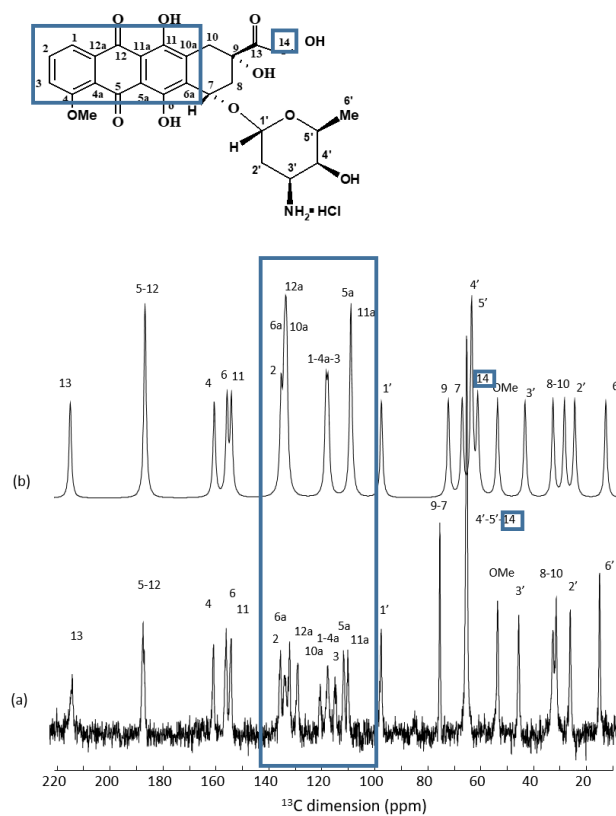


Figure 6.18:  $^{13}\text{C}$  CPMAS (a) and liquid simulated by MNova (b) NMR spectra of doxorubicin drug. The lines are assigned and the difference are highlighted by the blue square.

$^{27}\text{Al}$  MQMAS experiment was recorded and it is shown in Figure 6.19. The  $^{27}\text{Al}$  parameters are shown in Table 6.1. As reported for the ATP loaded nanoMIL-100(Al), only a variation of the Al bulk species is detected, evidencing the incorporation of the drug in the pores of the MOF.

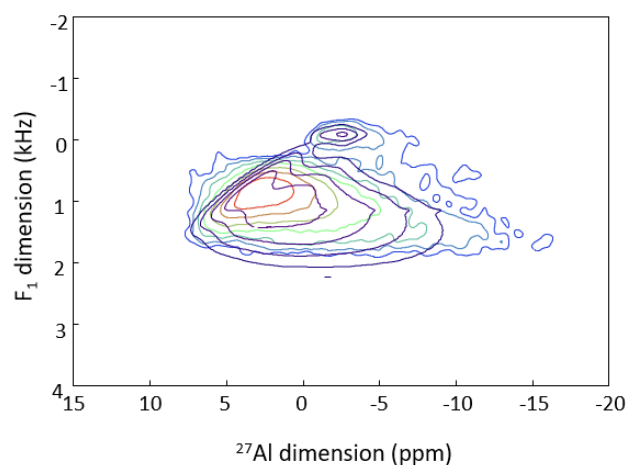


Figure 6.19:  $^{27}\text{Al}$  MQMAS NMR spectra of the DOX loaded nanoMIL-100(Al), recorded at 12.5 kHz (on a 11.7 T spectrometer). The simulation were made using Czejk and QMAS1/2 mode on Dmfit program<sup>13</sup>.

$^{27}\text{Al}$ six coordinated sites			<i>nanoMIL-100(Al)</i>	<i>DOX loaded nanoMIL-100(Al)</i>
			(20 T, 20 kHz)	(11.7 T, 12.5 kHz)
<b>BULK</b>	Al (1)	%	26	30
		$\delta_{\text{iso}}$	3.95 ppm	4 ppm
		$C_Q$	3.0 MHz	3.0 MHz
		$\eta_Q$	0.61	0.61
	Al (2,3,4)	%	54	42
		$\delta_{\text{iso}}$	2.19 ppm	2.5 ppm
		$C_Q$	4.87 MHz	4.57 MHz
		$\eta_Q$	0.61	0.61
	Al (5,6,7)	%	16	19
		$\delta_{\text{iso}}$	0.30 ppm	0.24 ppm
		$C_Q$	5 MHz	5.3 MHz
		$\eta_Q$	0.65	0.65
<b>SURFACE</b>	Al (8)	%	4	7
		$\delta_{\text{iso}}$	-1.50 ppm	-1.50 ppm
		$C_Q$	3.3 MHz	3.0 MHz
		$\eta_Q$	0.95	0.95

Table 6.1: Detailed line-shapes parameters of  $^{27}\text{Al}$  species of ATP loaded and pure nanoMIL-100(Al).

$^1\text{H}$ - $^1\text{H}$  2D MAS NMR experiment (Figure 6.20) was carried, showing correlation between OH of DOX and the aromatic protons of the MIL-100(Al), which confirmed the presence of the drug in the pores of the nanoMIL-100(Al).

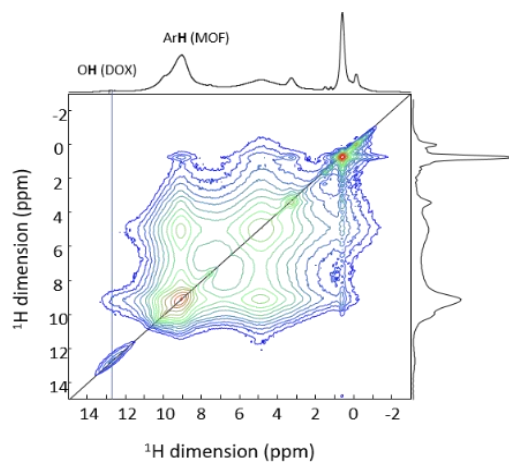


Figure 6.20: 2D  $^1\text{H}$ - $^1\text{H}$  spin diffusion NMR spectrum NMR of DOX loaded nanoMIL-100(Al) recorded with mixing time of 5 ms with a spinning speed of 50 kHz in a 17.6 T spectrometer.

Knowing the location of the DOX on the nanoparticles, incorporation of the DOX molecules in the  $^{13}\text{C}$ -labeled polymer was also achieved and despite the limited quantity of DOX loading and DOX-polymer interaction could be expected and it will be illustrated in the next section.

## 4. DOX loaded in the CD-CO polymer

The  $^1\text{H}$  and  $^{13}\text{C}$  MAS NMR spectra of DOX loaded  $^{13}\text{C}$ -labeled CD-CO polymer are shown (Figure 6.21 and 6.22). The resonance of the DOX molecules are seen, albeit with small intensity related to the small loading rate (<25 wt%). They have chemical shift similar to the DOX molecules incorporation in the nanoMIL-100(Al) shown earlier, indicating here also the absence of  $\pi$ - $\pi$  stacking interactions.

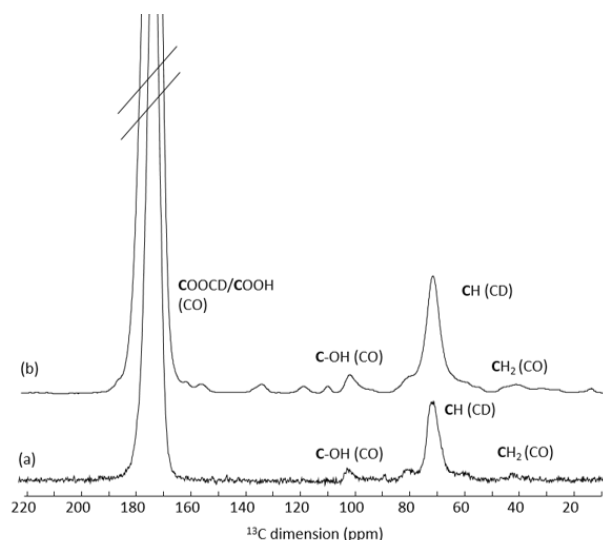


Figure 6.21:  $^{13}\text{C}$  CPMAS NMR spectra of CD-CO and DOX loaded CD- $^{13}\text{C}$ O polymer, recorded at 10 kHz in a 9.4 T spectrometer. Small-unlabeled lines correspond to the DOX signals. The strong signal of the labeled  $^{13}\text{C}$  citrate is truncated for sake of clarity.

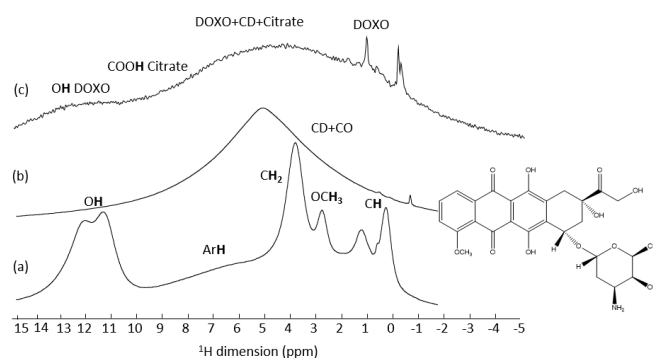


Figure 6.22:  $^1\text{H}$  MAS NMR spectra of pure DOX (a) CD- $^{13}\text{C}$ O polymer (b) and DOX loaded CD- $^{13}\text{C}$ O polymer (c), recorded at 10 kHz on a 9.4 T spectrometer. The lines are assigned. The  $^1\text{H}$  resonances of the DOX were assigned compared with liquid NMR data<sup>14</sup>.

$^1\text{H}$ - $^1\text{H}$  2D MAS NMR experiments were carried out (Figure 6.23) to probe spatial proximities between the protons of the CD-CO and those of the DOX. The spectra show cross-correlation peaks

between the OH of DOX and the broad peaks of the CD, indicating close contact between the DOX and the CD-CO in the particles.

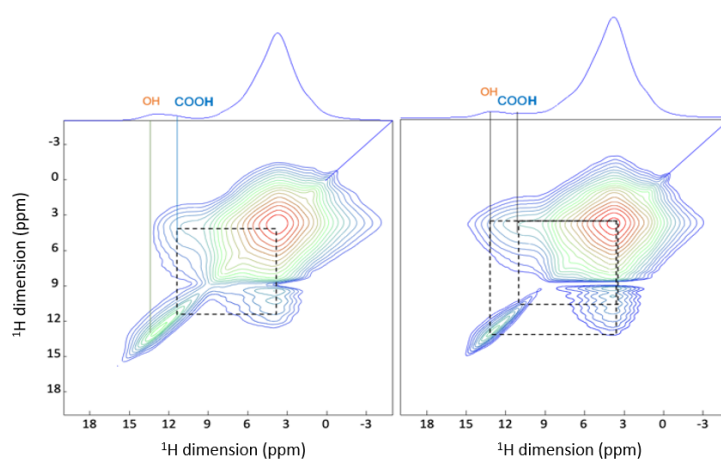


Figure 6.23: 2D  $^1\text{H}$ - $^1\text{H}$  spin diffusion NMR spectra of DOX loaded CD- $^{13}\text{C}$ O polymer recorded with mixing time of 5 ms (left) and 15 ms (right) on a 17.6 T spectrometer with a spinning speed of 50 kHz.

Taking advantage of the  $^{13}\text{C}$ -labelling of the citrate moieties (that significantly increases the sensitivity of  $^{13}\text{C}$  NMR experiments),  $^{13}\text{C}$ - $^1\text{H}$  proximity was probed through  $^{13}\text{C}$ - $^1\text{H}$  *D*-HMQC experiment. In this experiment, the magnetization of the  $^{13}\text{C}$ -citrate was selectively chosen and transferred to its surrounding protons. The intensity of the resulting protons resonances as a function of transfer time is shown in Figure 6.24. Short proximities are dominant at short recoupling time, while longer C-H distances appear at longer transfer time. In this figure, at short recoupling time, mostly the protons of the CD and citrate moieties are seen, as expected since the  $^{13}\text{C}$  label tag is present on the CD-CO polymer only. For longer magnetization transfer time, the protons of the DOX start also to be observed. This confirms the close mixing of the DOX molecules within the CD-CO polymer. Interestingly, the aromatic protons of the DOX have much higher intensity on the  $^1\text{H}$  NMR spectrum after transfer from the  $^{13}\text{C}$ -citrate than in the normal  $^1\text{H}$  MAS NMR spectrum. This indicates that the DOX molecules have a preferential interaction with the CD- $^{13}\text{C}$ O polymer through their rigid aromatic part.

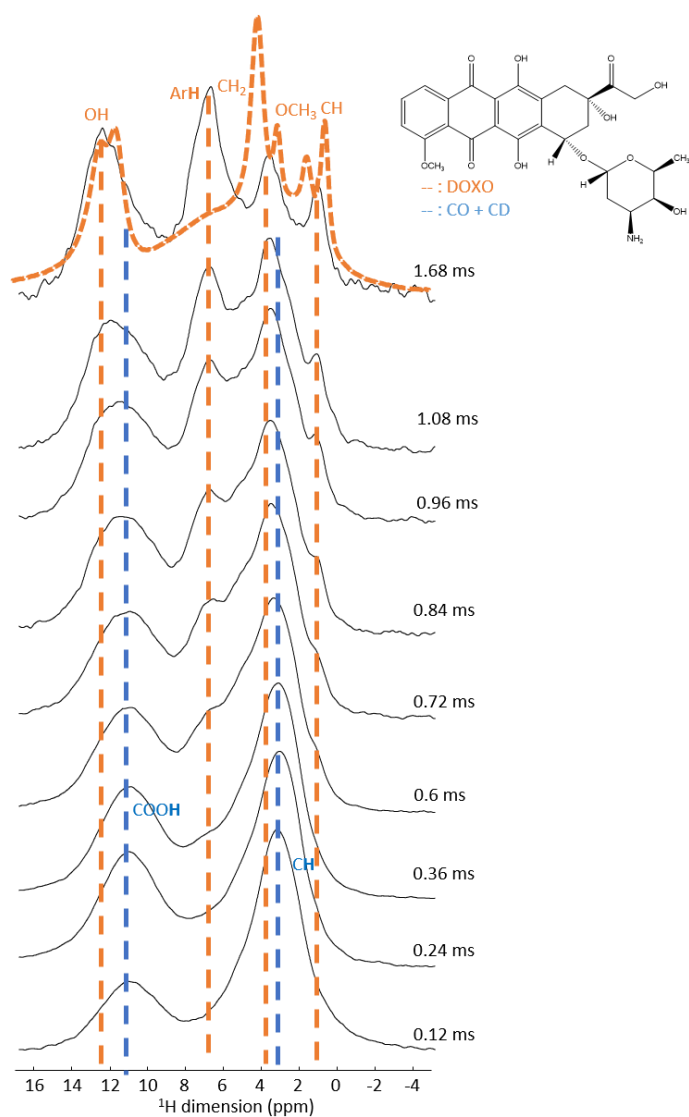


Figure 6.24:  $^1\text{H} \{^{13}\text{C}\}$   $D$ -HMQC NMR spectrum of DOX loaded CD-CO polymer, recorded for recoupling times ranging from 0.12 to 1.68 ms, at 50 kHz on a 17.6 T spectrometer. For comparison, the  $^1\text{H}$  MAS NMR spectrum of pure DOX is shown in orange dash line. The vertical blue dash lines indicate the position of  $^{13}\text{C}$  resonances from the CD-CO moieties, while the vertical orange dash lines indicate those of the DOX molecules.

In this section, it was shown that DOX has great affinity both with the CD-CO polymer and the nanoMIL-100(Al). In the next section, the final target DDS system, *i.e.* DOX-loaded CD- $^{13}\text{C}$ O nanoMIL-100(Al) is investigated.

## 5. DOX loaded CD-<sup>13</sup>C coated nanoMIL-100(Al)

Investigation of the structure and of the possible interactions was carried out for the DOX loaded CD-<sup>13</sup>C coated nanoMIL-100(Al). It is important to remind that the DOX showed a good affinity for both the polymer and the MOF (see the previous section) and that the CD-<sup>13</sup>C polymer is too bulky to interact with the pores of the nanoMOF, consequently it is present only on the surface of the nanoparticles.

The <sup>13</sup>C CPMAS NMR spectra are presented in Figure 6.25. In the DOX loaded CD-<sup>13</sup>C coated nanoMIL-100(Al), the <sup>13</sup>C signals of the DOX molecules are seen and are similar to the solution state <sup>13</sup>C NMR spectrum of DOX, indicating the absence of  $\pi$ - $\pi$  interactions, as was already observed in the DOX loaded nanoMIL-100(Al). No other significant differences are observed, hence at first sight, the DOX loading did not seem to affect the nanoparticles.

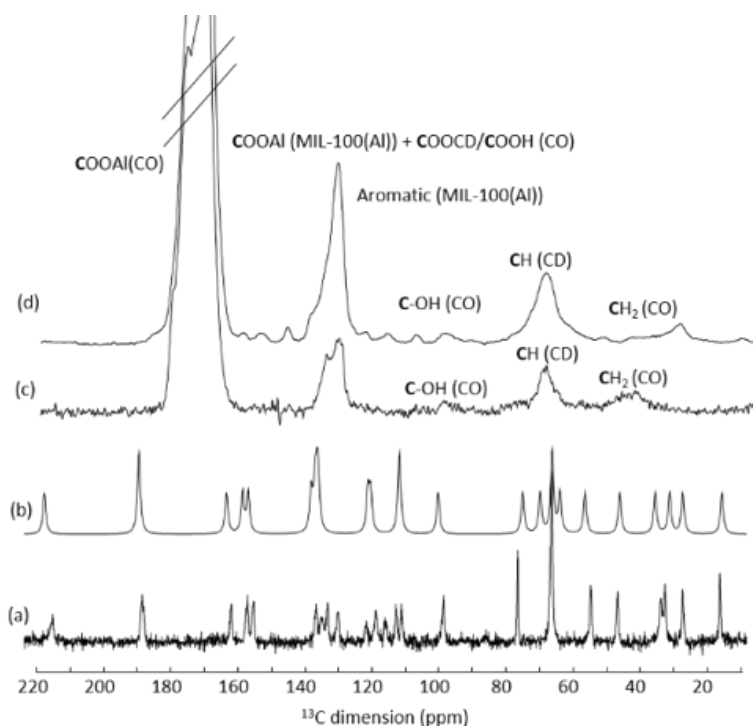


Figure 6.25: <sup>13</sup>C CPMAS NMR spectra of pure DOX (a), CD-<sup>13</sup>C coated nanoMIL-100(Al) (c) and DOX loaded CD-<sup>13</sup>C coated nanoMIL-100(Al) (d). Small-unlabeled lines correspond to the DOX signals and the liquid NMR simulated spectrum (b) is shown for comparison. The strong signal of the labeled <sup>13</sup>C citrate is truncated for sake of clarity and the lines are assigned.

$^1\text{H}$  and  $^{27}\text{Al}$  MAS NMR spectra do not show either any significant difference with the non-loaded sample (Figure 6.26). The presence of the DOX is confirmed by  $^1\text{H}$  resonances belong to the aromatic part and OH groups of the molecules.

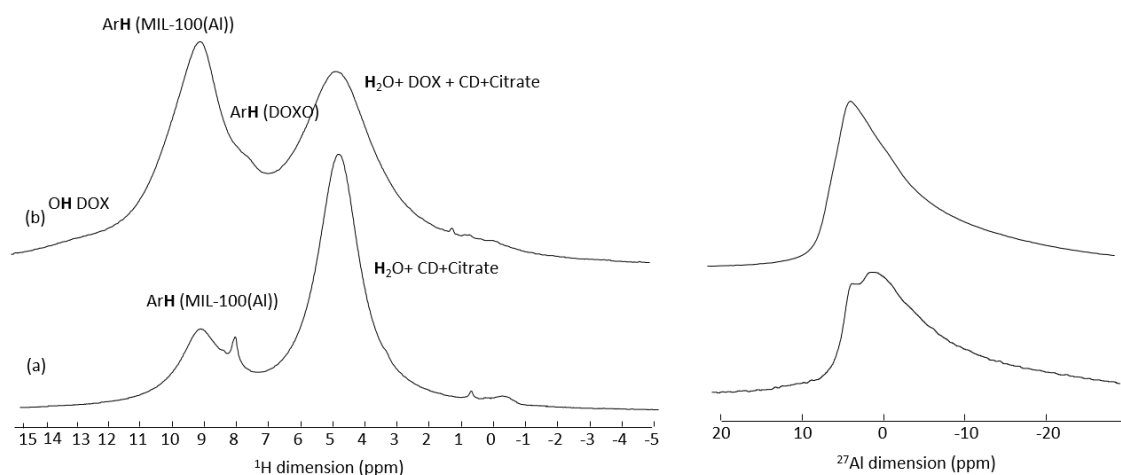


Figure 6.26:  $^1\text{H}$  (left) and  $^{27}\text{Al}$  (right) of  $\text{CD-}^{13}\text{CO}$  coated nanoMIL-100(Al) (a) and DOX loaded  $\text{CD-}^{13}\text{CO}$  coated nanoMIL-100(Al) (b), recorded at 10 kHz on a 9.4 T spectrometer.

$^1\text{H}$ - $^1\text{H}$  MAS NMR spectrum was recorded at high field and fast MAS (Figure 6.27). The sample was dried at 40 °C under vacuum, prior to perform the experiment in order to remove the water, which  $^1\text{H}$  resonance overlaps with the  $^1\text{H}$  resonance of cyclodextrin and citrate. Even if the resonances result are still broad, the OH resonance of the DOX is visible. The resulting 2D spectrum evidences the interaction of the DOX molecules with both the coating and the pores of nanoMIL-100(Al).

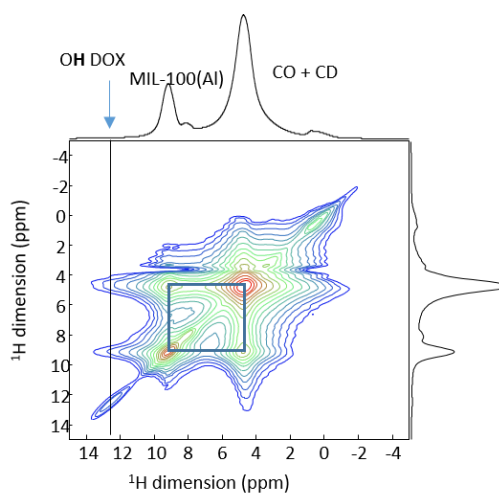


Figure 6.27: 2D  $^1\text{H}$ - $^1\text{H}$  spin diffusion NMR spectrum of DOX loaded  $\text{CD-}^{13}\text{CO}$  coated nanoMIL-100(Al) recorded with mixing time of 5 ms on a 17.6 T spectrometer with a spinning speed of 50 kHz.

$^1\text{H} \{^{13}\text{C}\}$  *D*-HMQC was performed to try to have more details about the interactions seen on the 2D  $^1\text{H}$ - $^1\text{H}$  spectra. The intensity of the resulting protons resonances as a function of transfer time is shown in Figure 6.28. At short recoupling time, mostly the protons of the CD and citrate moieties are seen, as expected since the  $^{13}\text{COO}^-$ , but also the aromatic proton of the MOF are visible, since the  $\text{COO}^-$  of the MIL-100(Al) as the same chemical shift and it is present in larger quantity than the coating  $\text{CD-}^{13}\text{CO}$ . For longer magnetization transfer time, the protons of the DOX start also to be observed. Differently from the results of the DOX loaded in the polymer, the first interactions seen are with the  $^1\text{H}$  resonance of the  $-\text{OCH}_3$  groups, evidencing that probably the preferential interaction of the polymer and the MOF with the drug is still with the rigid aromatic part.

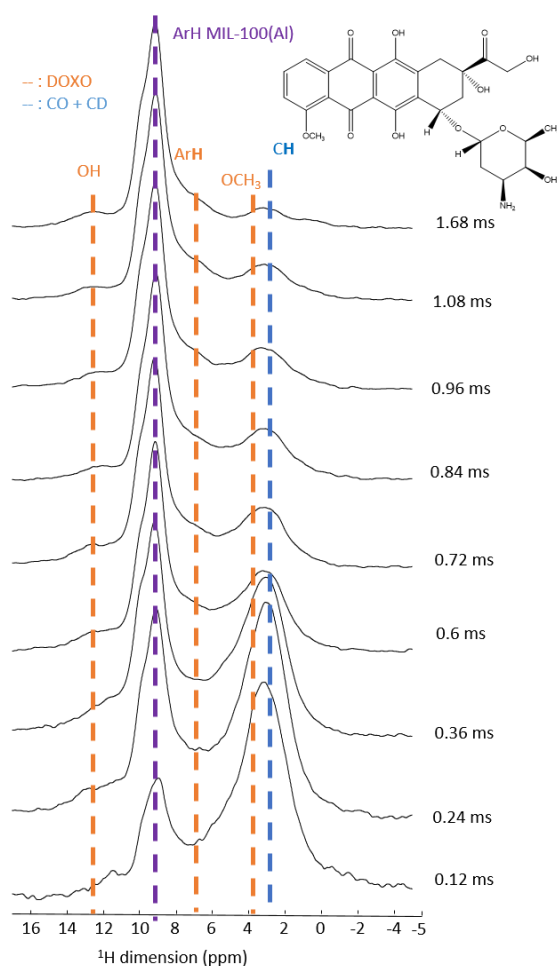


Figure 6.28:  $^1\text{H} \{^{13}\text{C}\}$  *D*-HMQC spectra of DOX loaded  $\text{CD-}^{13}\text{CO}$  coated nanoMIL-100(Al) (b), recorded for recoupling times ranging from 0.12 to 1.68 ms, at 50 kHz on a 17.6 T spectrometer. The vertical blue dash lines indicate the position of  $^{13}\text{C}$  resonances from the  $\text{CD-CO}$  moieties, while the vertical orange and purple dash lines indicate those of the DOX molecules and nanoMIL-100(Al), respectively.

Taking advantage of the  $^{13}\text{C}$ -enrichment strategy,  $^{13}\text{C}$ - $^{13}\text{C}$  2D DQ-SQ homonuclear correlation experiments were carried out on the DOX loaded CD- $^{13}\text{C}$ O polymer and DOX loaded CD- $^{13}\text{C}$ O coated nanoMIL-100(Al) (Figure 6.29). The goal was to try to correlate the  $^{13}\text{C}$  resonances of the enriched citrate with the DOX and comparing with the loaded-coated nanoMOF to see if any difference can be noticed. Unfortunately, even after 4 days of acquisition only the  $^{13}\text{C}$  resonance of the  $^{13}\text{COO}^-$  of the citrate were visible in both samples. The only information that can be extracted, it is the presence of the new resonance that we identified as the carboxylic group interacting with the Al of the nanoMOF at the surface.

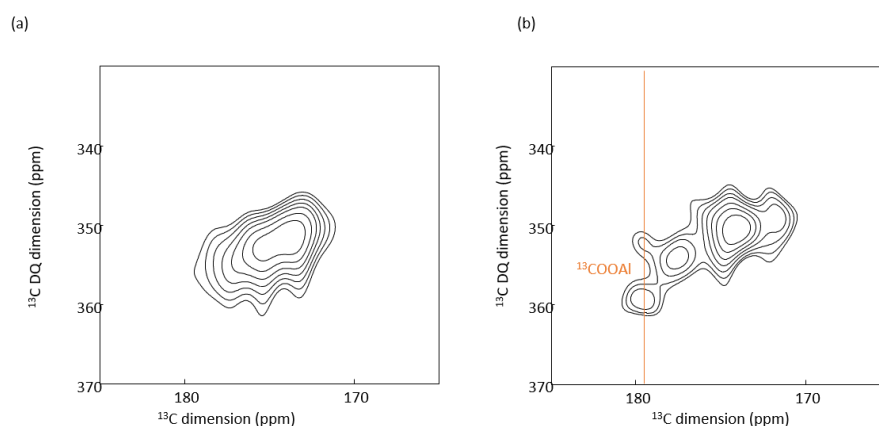


Figure 6.29:  $^{13}\text{C}$ - $^{13}\text{C}$  2D DQ/SQ MAS NMR spectra of DOX loaded CD- $^{13}\text{C}$ O polymer (a) and DOX loaded CD- $^{13}\text{C}$ O coated nanoMIL-100(Al) (b), recorded at 11 kHz on a 9.4 T spectrometer.

Having not the information needed from the  $^{13}\text{C}$ - $^{13}\text{C}$  2D NMR,  $^{27}\text{Al}\{^{13}\text{C}\}$  2D *D*-HMQC NMR experiment was recorded to evaluate if the loading process leads to sweeping change on the interaction between the coating and the surface of nanoMOF. The  $^{13}\text{C}$ - $^{27}\text{Al}$  2D MAS NMR spectrum (Figure 6.30) shows that the coating and the NP are still in strong interaction. However, the relative intensity between the two resonances are different. This indicates that, in addition to going in the pores of the MOF as shown earlier, the DOX molecules also interact significantly with the CD-CO coating. Notably, since the intensity of COOAl (CO) has decreased, it very likely indicates that part of the  $^{13}\text{COO-Al}$  bonds formed between the citric acid moieties and the surface Al sites have been broken, but the NPs are still stables.

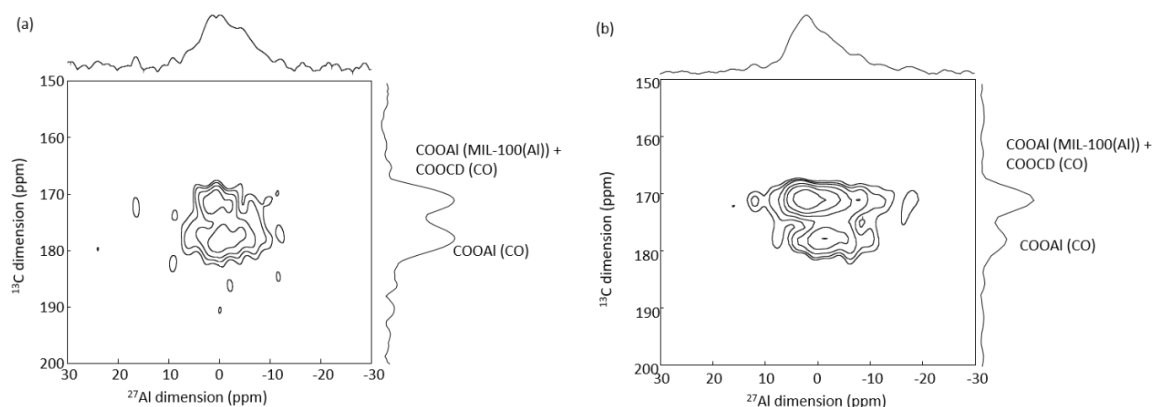


Figure 6.30:  $^{27}\text{Al}\{^{13}\text{C}\}$  2D *D*-HMQC NMR spectra of CD- $^{13}\text{C}$ O coated nanoMIL-100(Al) (a) and DOX loaded CD- $^{13}\text{C}$ O coated nanoMIL-100(Al) (b), recorded at 12.5 kHz on a 9.4 T spectrometer.

## 6. Conclusions

A new NP coating was proposed to try to perform a better release of the DOX drug. CD-CO polymer showed good affinity for the anticancer drug, Doxorubicin as well as nanoMIL-100(Al). CD-CO polymer was selected to cover MIL-100(Al) nanoparticles and build a new drug carrier for the DOX. The systems were studied by ssNMR spectroscopy.  $^1\text{H}$  NMR spectra are very broad and very few information can be extracted by them. Therefore, the strategy adopted to get information about the structure of this complex systems and the interaction between the drug and the two carriers as well as the nanoMOF with its coating, was to use in the synthesis of the coating a citric acid enriched in  $^{13}\text{C}$ . Thanks to this and aluminum present only in the nanoMOF,  $^{27}\text{Al}$ - $^{13}\text{C}$  heteronuclear correlation experiments were performed. The results obtained give the possibility to confirm the good interaction of the DOX with both the polymer and the MOFs, showing that in the DOX loaded CD- $^{13}\text{C}$ O coated nanoMIL-100(Al), the DOX is placed in the pores of the MOF as well as formed inclusion complex with CD-CO polymer. The interaction of the DOX with the coating reduces the interaction of the citrate with the Al of the surface, but does not affect the stability of the coated nanoparticles. The next step is to study the release of the drug, to validate the better efficiency of the system.

## 7. Experimental ssNMR section

All the samples were finely ground into powders and packed into a zirconia rotor of the appropriate size. The NMR spectra were acquired using TopSpin 3.5 Bruker Software and processed with the Dmfit program<sup>15</sup>. The chemical shift are referred for  $^1\text{H}$  and  $^{13}\text{C}$  to TMS, to  $\text{Al}(\text{NO}_3)_3$  1 M solution for  $^{27}\text{Al}$  and to  $\text{H}_3\text{PO}_4$  85 wt% solution for  $^{31}\text{P}$ .

<i>Nucleus/i</i>	<i>Probe and MAS</i>	<i>Pulse sequence</i>	<i>Main Parameters</i>	<i>Time required</i>
$^1\text{H}$	HXY 1.3 mm probe in double mode, with a spinning rate of 50 kHz	Hahn Echo	Recycle delay of 3 s; $90^\circ$ pulse of 1.1 $\mu\text{s}$ ; an inter-pulse delay synchronized with one rotor period.	less than 1 minute
$^1\text{H}$ - $^1\text{H}$	HXY 1.3 mm probe in double mode, with a spinning rate of 50 kHz	Exchange	Recycle delay of 3 s; $^1\text{H}$ $90^\circ$ pulse of 1.1 $\mu\text{s}$ ; two different mixing times (5 ms and 15 ms); 250 $t_1$ slices with 128 transients were co-added; States procedure for 2D sensitive; The samples were dried under vacuum at $40^\circ\text{C}$ before to perform the experiments.	Around 26 hours
$^1\text{H}$ - $^{13}\text{C}$	HXY 1.3 mm probe in double mode, with a spinning rate of 50 kHz	<i>D</i> -HMQC	Recycle delay of 0.25 s; $R4^2_1$ as recoupling sequence, with different recoupling times; States procedure for 2D sensitive.	20 min
$^{27}\text{Al}$ - $^{31}\text{P}$	$^1\text{H}$ - $^{31}\text{P}$ - $^{27}\text{Al}$ 4 mm probe , with a spinning rate of 14 kHz	<i>D</i> -HMQC	Recycle delay of 0.25 s; $R4^2_1$ as recoupling sequence, with 1.7 ms of recoupling time; DFS was applied to boost the $^{27}\text{Al}$ magnetization; States procedure for 2D sensitive.	40-45 hours

Table 6.2: NMR spectra recorded on 750 MHz (17.6 T) WB Bruker NMR spectrometer.

<i>Nucleus/i</i>	<i>Probe and MAS</i>	<i>Pulse sequence</i>	<i>Main Parameters</i>	<i>Time required</i>
<sup>1</sup> H	HX 4 mm probe, with a spinning rate of 10 kHz.	Hahn Echo	Recycle delay of 5 s; 90° pulse on <sup>1</sup> H of 4 μs; an inter-pulse delay synchronized with one rotor period.	1 minute
<sup>13</sup> C	HX 4 mm probe, with a spinning rate of 10 kHz.	CP-MAS	Recycle delay of 5 s; 90° pulse on <sup>1</sup> H of 4 μs (RF field of 62 kHz); contact time of 3.5 ms; <sup>1</sup> H SPINAL-64 decoupling applied during acquisition (RF field of 70 kHz).	2-3 hours
<sup>27</sup> Al	HX 4 mm probe, with a spinning rate of 12.5 kHz.	1-pulse	Recycle delay of 0.3 s; 90° pulse of 3.33 μs (RF field of 25 kHz)	around 6 minutes
<sup>31</sup> P	HX 4 mm probe, with a spinning rate of 14 kHz.	CP-MAS	Recycle delay of 5 s; 90° pulse on <sup>1</sup> H of 4 μs (RF field of 62 kHz); contact time of 5 ms; <sup>1</sup> H SPINAL-64 decoupling applied during acquisition (RF field of 70 kHz).	around 30 minutes
<sup>13</sup> C- <sup>27</sup> Al	HX 4 mm probe, using REDOR BOX, with a spinning rate of 12.5 kHz.	CP-RESPDOR	Recycle delay of 2.5 s; 90° pulse on <sup>1</sup> H of 4 μs (RF field of 62 kHz); contact time of 3.5 ms; <sup>1</sup> H SPINAL-64 decoupling applied during acquisition (RF field of 70 kHz).	6 hours
<sup>27</sup> Al- <sup>13</sup> C	HX 4 mm probe, using REDOR BOX, with a spinning rate of 12.5 kHz.	D-HMQC	Recycle delay of 0.3 s; R4 <sub>2</sub> <sup>1</sup> as recoupling sequence, with 2.4 ms of recoupling time; DFS was applied to boost the <sup>27</sup> Al magnetization; States procedure for 2D sensitive; All spectra are treated with 100 Hz LB apodization in both dimensions.	21-42 hours
<sup>13</sup> C- <sup>13</sup> C	HX 4 mm probe, with a spinning rate of 11 kHz	SC14 with initial CP	Recycle delay of 1 s; RF field <sup>1</sup> H for CP of 61 kHz; contact time of 1.5 ms; <sup>1</sup> H CW and SPINAL-64 decoupling applied during recoupling and acquisition, respectively (RF field of 50 kHz and 98.77 kHz, respectively). excitation and reconversion times of 3 ms each with a RF field of 37.7 kHz; States-TPPI procedure for 2D sensitive.	3-4 days

Table 6.3: NMR spectra recorded on a 400 MHz (9.4 T) Bruker NMR spectrometer.

<i>Nucleus/i</i>	<i>Probe and MAS</i>	<i>Pulse sequence</i>	<i>Main Parameters</i>	<i>Time required</i>
<sup>1</sup> H- <sup>1</sup> H	HX 4 mm probe, with a spinning rate of 12.5 kHz.	Exchange	Recycle delay of 1.5 s; <sup>1</sup> H 90 pulse of 3 us; 256 t <sub>1</sub> slices with 16 transients were co-added; States procedure for 2D sensitive.	Around 2 hours
<sup>27</sup> Al		z-filter MQMAS	RF field of 50 kHz for excitation of triple quantum (3Q) coherences and for 3Q->0Q conversion; <i>MQMAS spectrum</i> are <i>presented</i> after a <i>shearing</i> transformation	4 hours

Table 6.4: NMR spectra recorded on a Bruker 500 MHz (11.6 T) WB NMR spectrometer.

## References

- (1) Ngan, Y.; Gupta, M. A Comparison between Liposomal and Nonliposomal Formulations of Doxorubicin in the Treatment of Cancer: An Updated Review. *Archives of Pharmacy Practice* **2016**, *7* (1), 1–13.
- (2) Anand, R.; Borghi, F.; Manoli, F.; Manet, I.; Agostoni, V.; Reschiglian, P.; Gref, R.; Monti, S. Host–Guest Interactions in Fe(III)-Trimesate MOF Nanoparticles Loaded with Doxorubicin. *J. Phys. Chem. B* **2014**, *118* (29), 8532–8539.
- (3) Tabatabaei Mirakabad, F. S.; Nejati-Koshki, K.; Akbarzadeh, A.; Yamchi, M. R.; Milani, M.; Zarghami, N.; Zeighamian, V.; Rahimzadeh, A.; Alimohammadi, S.; Hanifehpour, Y.; Joo, S. W. PLGA-Based Nanoparticles as Cancer Drug Delivery Systems. *Asian Pacific Journal of Cancer Prevention* **2014**, *15* (2), 517–535.
- (4) Betancourt, T.; Brown, B.; Brannon-Peppas, L. Doxorubicin-Loaded PLGA Nanoparticles by Nanoprecipitation: Preparation, Characterization and *in Vitro* Evaluation. *Nanomedicine* **2007**, *2* (2), 219–232.
- (5) Yoo, H. S.; Lee, K. H.; Oh, J. E.; Park, T. G. In Vitro and in Vivo Anti-Tumor Activities of Nanoparticles Based on Doxorubicin–PLGA Conjugates. *Journal of Controlled Release* **2000**, *68* (3), 419–431.
- (6) Park, H.; Yang, J.; Lee, J.; Haam, S.; Choi, I.-H.; Yoo, K.-H. Multifunctional Nanoparticles for Combined Doxorubicin and Photothermal Treatments. *ACS Nano* **2009**, *3* (10), 2919–2926.
- (7) Bulbake, U.; Doppalapudi, S.; Kommineni, N.; Khan, W. Liposomal Formulations in Clinical Use: An Updated Review. *Pharmaceutics* **2017**, *9* (4), 1–33.
- (8) Gabizon, A. A. Pegylated Liposomal Doxorubicin: Metamorphosis of an Old Drug into a New Form of Chemotherapy. *Cancer Investigation* **2001**, *19* (4), 424–436.
- (9) Anand, R.; Malanga, M.; Manet, I.; Manoli, F.; Tuza, K.; Aykaç, A.; Ladavière, C.; Fenyvesi, E.; Vargas-Berenguel, A.; Gref, R.; Monti, S. Citric Acid– $\gamma$ -Cyclodextrin Crosslinked Oligomers as Carriers for Doxorubicin Delivery. *Photochem. Photobiol. Sci.* **2013**, *12* (10), 1841.
- (10) Martel, B.; Ruffin, D.; Weltrowski, M.; Lekchiri, Y.; Morcellet, M. Water-Soluble Polymers and Gels from the Polycondensation between Cyclodextrins and Poly(Carboxylic Acid)s: A Study of the Preparation Parameters. *J. Appl. Polym. Sci.* **2005**, *97* (2), 433–442.
- (11) di Nunzio, M. R.; Wang, Y.; Douhal, A. Spectroscopy and Dynamics of Topotecan Anti-Cancer Drug Comprised within Cyclodextrins. *Journal of Photochemistry and Photobiology A: Chemistry* **2013**, *266*, 12–21.
- (12) Vuong Dang Le, M. Degradation Study of Metal–Organic Framework Nanoparticles by Solid-State Nuclear Magnetic Resonance Spectroscopy, 2019.
- (13) Massiot, D.; Fayon, F.; Alonso, B.; Trebosc, J.; Amoureux, J.-P. Chemical Bonding Differences Evidenced from J-Coupling in Solid State NMR Experiments Involving Quadrupolar Nuclei. *Journal of Magnetic Resonance* **2003**, *164*, 160–164.
- (14) Piorecka, K.; Stanczyk, W.; Florczak, M. NMR Analysis of Antitumor Drugs: Doxorubicin, Daunorubicin and Their Functionalized Derivatives. *Tetrahedron Letters* **2017**, *58* (2), 152–155.
- (15) Massiot, D.; Fayon, F.; Capron, M.; King, I.; Le Calvé, S.; Alonso, B.; Durand, J.-O.; Bujoli, B.; Gan, Z.; Hoatson, G. Modelling One- and Two-Dimensional Solid-State NMR Spectra: Modelling 1D and 2D Solid-State NMR Spectra. *Magn. Reson. Chem.* **2002**, *40* (1), 70–76.

# Conclusions and Perspectives



During this thesis, several drug/carrier DDSs were investigated by ssNMR spectroscopy. The low resolution of  $^1\text{H}$  nucleus was circumvented using heteronuclei (such as  $^{19}\text{F}$ ,  $^{27}\text{Al}$ ,  $^{31}\text{P}$ ,  $^{13}\text{C}$ ,  $^2\text{H}$ ,  $^{17}\text{O}$ , etc). Although there was an important loss of sensitivity, it provided much greater selectivity than  $^1\text{H}$  NMR spectroscopy.

A first system consisting of antitubercular prodrug Lansoprazole loaded in  $\gamma$ -CD-MOF was investigated. The affinity competition of the CD with the surfactant, necessary to obtain MOF particles with homogeneous size, and the drug was analyzed with ssNMR. Using the  $^{19}\text{F}$  nucleus as a spy, the drug could be located with respect to the CD. Protonation state of the drug, an important parameter for drug delivery, could be obtained by  $^{15}\text{N}$  NMR spectroscopy at natural abundance using the newly developed Bruker CryoProbe that provided the required sensitivity. Complemented with molecular modeling, a fine understanding of the system could be obtained.

The second system under investigation was a DDS based on nanoMIL-100(Al) as drug carrier. In a first step, surface coating and loaded drugs containing phosphorus atoms were selected because they were shown to have great affinity with the Fe-based MOF analog, and Al-O-P chemical bonds are known to be energetically favorable. Using  $^{27}\text{Al}$   $\{^{31}\text{P}\}$  2D *D*-HMQC experiments, we confirmed the expected great affinity between the phosphated coating (phosphate  $\beta$ -CD) and drug (adenosine triphosphate) with the surface and/or bulk aluminum cations of the MOF.  $^{27}\text{Al}$   $\{^{31}\text{P}\}$  2D *D*-HMQC experiments were further used to analyze the degradation of the MOF in a biological medium (phosphate buffer). It was found that little degradation, hence drug delivery, was obtained, possibly because of the formation of an aluminophosphate type layer on the external surface of the MOF.

Therefore, another more covering surface coating was considered:  $\gamma$ -CD-citrate oligomers (CD-CO). It was further chosen because  $\gamma$ -CD was expected to show more affinity towards the drug than  $\beta$ -CD (which is smaller), hence potentially leading to greater drug payload. Here, the drug selected was Doxorubicin (DOX) because of its known affinity with CD-CO. In this system, the strategy adopted was to synthesize the CD-CO polymer using  $^{13}\text{C}$ -labeled citrate as precursor. This way, using  $^{27}\text{Al}$   $\{^{13}\text{C}\}$  2D *D*-

HMQC,  $^{13}\text{C}$   $\{^{27}\text{Al}\}$  RESPDOR and  $^1\text{H}$   $\{^{13}\text{C}\}$  D-HMQC experiments, the good interaction of new coating with the nanoMIL-100(Al) surface was confirmed, as well as the loading of the DOX both in the pores of the MOFs and in the coating was validated. Drug release study are still under way.

The ensemble of data reported in this thesis has shown that using heteroatoms to investigate DDS at the molecular level was a nice alternative to  $^1\text{H}$  NMR spectroscopy, at the cost of lower sensitivity but with the advantage of greater selectivity. This methodology is being continued by M. V. D. Le in her thesis. In particular, the effect of the length of the phosphate chain of the drug (mono- vs tri-phosphate) on its affinity and drug delivery is being assessed.

If only few nuclei were studied in this work ( $^{19}\text{F}$ ,  $^{27}\text{Al}$ ,  $^{31}\text{P}$ ,  $^{13}\text{C}$ ,  $^{15}\text{N}$ ), there are other that could be considered.

Deuterium is a new 'a la mode' nucleus in the development of drugs. The C-D bond is indeed stronger than the C-H bond. This stronger bond results in less destruction of the drug in the body, hence enhanced bioavailability and lower drug administration. Furthermore, D replacing H in a known molecule, the development time of the drug is considerably reduced. So far a single deuterated drug has been FDA approved (Austedo<sup>®</sup> from Teva), but a dozen other are under study at different stages (I to III)<sup>1</sup>. From an NMR spectroscopy point of view, Deuterium dilutes the protons, which simplifies the  $^1\text{H}$  MAS NMR spectra and it modifies the hydrogen bonds. Therefore, D<sub>2</sub>O can be used to play on the drug/carrier interactions. As an example, Vancomycin (VCM) drug was loaded inside nanoparticles of PLGA, in which PVA is intermingled within the PLGA at the surface. Due to the strong overlap of the proton resonances and the presence of water molecules, deuteration strategy was used to try to simplify the  $^1\text{H}$  NMR spectra. In Figure 1, we compare the effect of the pH on the NP loaded with the drug. The spectra of the pure Vancomycin and the pristine PLGA are showed for the assignment of the resonances. If no difference can be notice in the carbon spectra performed in the samples at different pH, in the proton spectra, it is possible to notice an increase of intensity of the resonances belong to the Vancomycin protons (OH, NH). This can be better notice in Figure 2, in which the spectra of the

samples at different pH are compared also with the sample synthesized in D<sub>2</sub>O. A zoom of the part between 6.5 and 13 ppm is shown on the left part of the Figure 2. One can notice that the resonances belong to OH and NH are more intense in the deuterated sample and in the one at pH=7.5. At pH=4 we have interactions, made by H-bonds, between the drug and the polymers. Once that we change the pH, going to a neutral ones (as pH=7.5), the drug crystallizes inside the polymer, and losing these interactions, the peaks appear narrower. The same narrow lines can be noticed in the spectrum of deuterated sample, because the deuteration strategy “modifies” the H-bond and so, the interactions between the drug and the polymer.

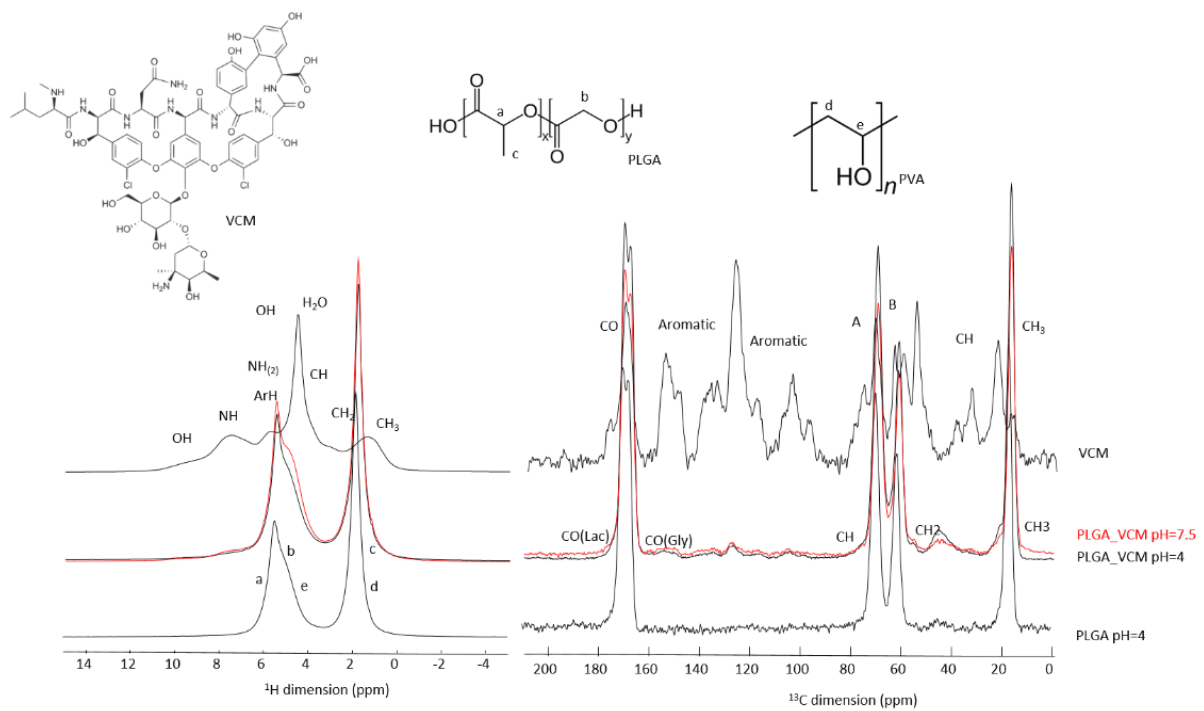


Figure 1: <sup>1</sup>H (left) and <sup>13</sup>C (right) MAS NMR spectra of pristine PLGA, pure VCM and PLGA\_VCM at two different pH, recorded at 60 kHz in a 20 T spectrometer. The assignment of the resonances are reported.

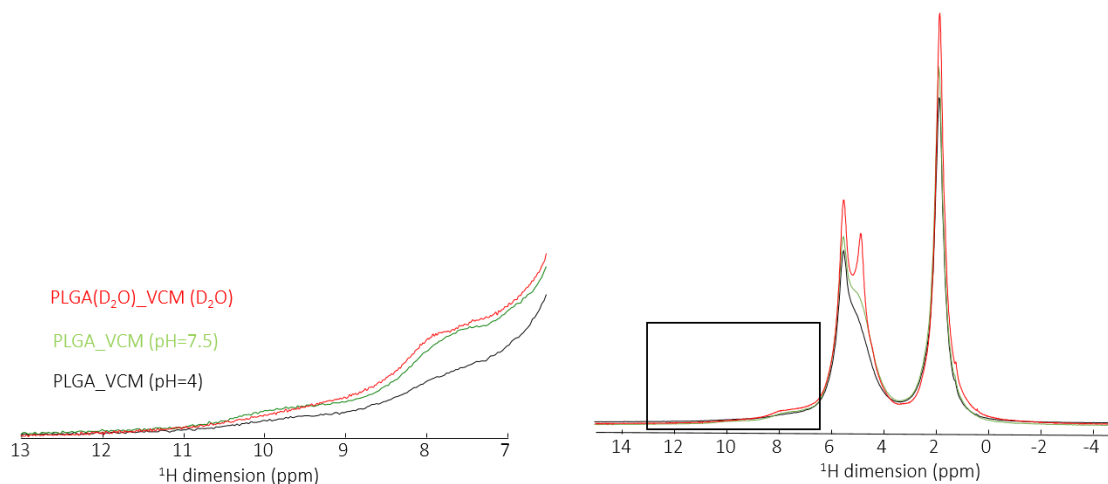


Figure 2.  $^1\text{H}$  MAS NMR spectra of PLGA\_VCM at two different pH and deuterated, recorded at 60 kHz in a 20 T spectrometer. The left spectrum shows a zoom on the OH and NH protons of VCM.

Finally, another present atom in DDS is Oxygen. The only NMR-active isotope of oxygen is  $^{17}\text{O}$ , which is a spin 5/2 and has an abundance of 0.037 %. This low natural abundance requires (often) expensive labeling. In Figure 3, is shown the  $^{17}\text{O}$  MAS NMR spectrum of NOTT-400(Sc) $^2$  which was selectively labeled with  $^{17}\text{O}$  i) introduced in the last step of the synthesis, ii) NOTT-400(Sc) left for 3 weeks in  $\text{H}_2^{17}\text{O}$ . This type of labeling method requires large quantity of expensive water.

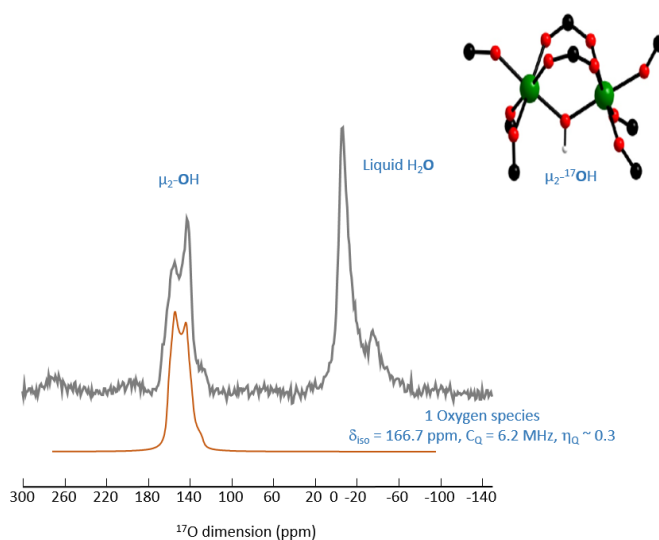


Figure 3:  $^{17}\text{O}$  MAS NMR spectrum of NOTT-400, recorded at 10 kHz on a 7.0 T spectrometer. In red is shown the deconvolution spectrum made by Dmfit program<sup>3</sup>.

Recently, new labeling strategies using minor amount of labeled water were proposed: i) in ball milling, ii) using simple impregnation in labeled water. This last strategy was successfully applied for zeolites<sup>4,5</sup>. Because the MOFs bearing chemical similarities with zeolites, this strategy was also attempted on a MOF, NOTT-400(Sc). In Figure 4 is shown the <sup>17</sup>O MAS NMR spectrum of NOTT-400(Sc)<sup>2</sup> which was selectively labeled with <sup>17</sup>O with this new cheaper method. This shows that the oxo functions of the MOFs are highly labile and can be easily exchanged. This is very important as these oxo functions are usually the most reactive sites of the MOFs, being for catalysis, gas adsorption, or drug delivery.

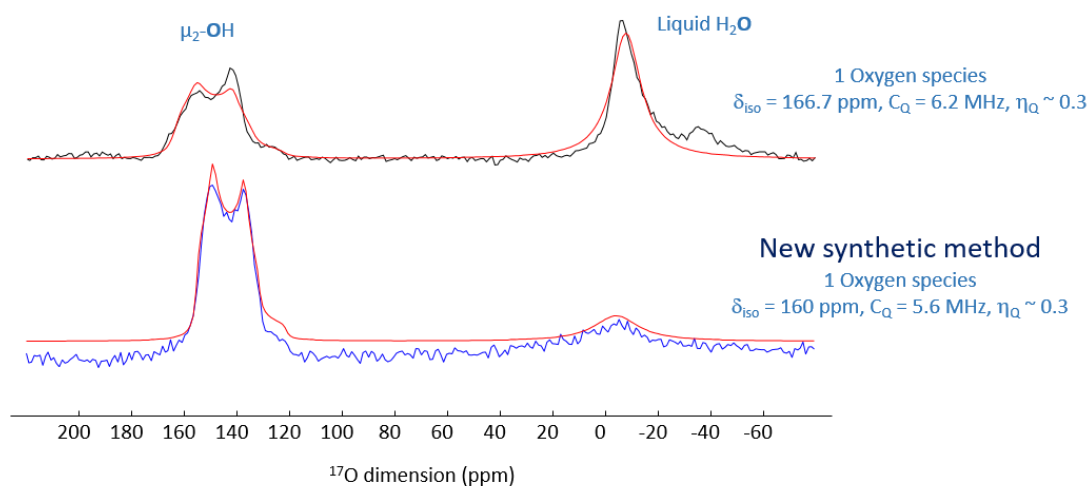


Figure 4: <sup>17</sup>O MAS NMR spectrum of NOTT-400 labeled with the new synthetic method, recorded at 30 kHz on a 20 T spectrometer and compared with the previous synthetic method. In red are shown the deconvolution spectra made by Dmfit program<sup>3</sup>.

In conclusion, ssNMR spectroscopy is an important analytical tool to understand DDSs at the atomic level, and represent an important guide for the design of DDSs with improved performances.

## References

- (1) DeWitt, S. H.; Maryanoff, B. E. Deuterated Drug Molecules: Focus on FDA-Approved Deutetrabenazine: Published as Part of the *Biochemistry* Series “Biochemistry to Bedside.” *Biochemistry* **2018**, *57* (5), 472–473.
- (2) Álvarez, J. R.; Peralta, R. A.; Balmaseda, J.; González-Zamora, E.; Ibarra, I. A. Water Adsorption Properties of a Sc(III) Porous Coordination Polymer for CO<sub>2</sub> Capture Applications. *Inorg. Chem. Front.* **2015**, *2* (12), 1080–1084.
- (3) Massiot, D.; Fayon, F.; Capron, M.; King, I.; Le Calvé, S.; Alonso, B.; Durand, J.-O.; Bujoli, B.; Gan, Z.; Hoatson, G. Modelling One- and Two-Dimensional Solid-State NMR Spectra: Modelling 1D and 2D Solid-State NMR Spectra. *Magn. Reson. Chem.* **2002**, *40* (1), 70–76.
- (4) Heard, C. J.; Grajciar, L.; Rice, C. M.; Pugh, S. M.; Nachtigall, P.; Ashbrook, S. E.; Morris, R. E. Fast Room Temperature Lability of Aluminosilicate Zeolites. *Nat. Commun.* **2019**, *10* (1), 4690–4697.
- (5) Pugh, S. M.; Wright, P. A.; Law, D. J.; Thompson, N.; Ashbrook, S. E. Facile, Room-Temperature <sup>17</sup>O Enrichment of Zeolite Frameworks Revealed by Solid-State NMR Spectroscopy. *J. Am. Chem. Soc.* **2020**, *142* (2), 900–906.

# Publications





## Efficient incorporation and protection of lansoprazole in cyclodextrin metal-organic frameworks

Xue Li<sup>a</sup>, Marianna Porcino<sup>b</sup>, Charlotte Martineau-Corcoc<sup>b,c,d</sup>, Tao Guo<sup>e</sup>, Ting Xiong<sup>f</sup>, Weifeng Zhu<sup>f</sup>, Gilles Patriarche<sup>g</sup>, Christine Péchoux<sup>h</sup>, Barbara Perronne<sup>i</sup>, Alia Hassan<sup>i</sup>, Rainer Kümmerle<sup>j</sup>, Alexandre Michelet<sup>j</sup>, Anne Zehnacker-Rentien<sup>a</sup>, Jiwen Zhang<sup>e,f</sup>, Ruxandra Gref<sup>a,\*</sup>

<sup>a</sup> Université Paris-Saclay, CNRS, Institut des Sciences Moléculaires d'Orsay, 91405 Orsay, France

<sup>b</sup> Université d'Orléans, CEMHTI UPR CNRS 3079, F-45071 Orléans, France

<sup>c</sup> Université Paris Saclay, ILV UMR CNRS 8180, Université de Versailles St-Quentin en Yvelines, 78035 Versailles, France

<sup>d</sup> Institut Universitaire de France (IUF), 75005 Paris, France

<sup>e</sup> Center for Drug Delivery Systems, Shanghai Institute of Materia Medica, Chinese Academy of Sciences, 201210 Shanghai, China

<sup>f</sup> Key Laboratory of Modern Preparation of TCM, Ministry of Education, Jiangxi University of Traditional Chinese Medicine, 330004 Nanchang, China

<sup>g</sup> Université Paris-Saclay, CNRS, Centre de Nanosciences et de Nanotechnologies, 91120 Palaiseau, France

<sup>h</sup> Université Paris-Saclay, INRAE, AgroParisTech, GABI, 78350 Jouy-en-Josas, France

<sup>i</sup> Bruker Biospin Corporation, 8117 Fällanden, Switzerland

<sup>j</sup> PerkinElmer, 16 avenue du Québec, 91140 Villebon sur Yvette, France

### ARTICLE INFO

#### Keywords:

Cyclodextrin  
Metal-organic frameworks  
Lansoprazole  
Inclusion complex  
Drug stability

### ABSTRACT

Lansoprazole (LPZ) is an acid pump inhibitor, which readily degrades upon acidic or basic conditions and under heating. We investigated here LPZ stability upon incorporation in particles made of cyclodextrin metal-organic frameworks (CD-MOFs). LPZ loaded CD-MOFs were successfully synthesized, reaching high LPZ payloads of  $23.2 \pm 2.1$  wt%, which correspond to a molar ratio of 1:1 between LPZ and  $\gamma$ -CD. The homogeneity of LPZ loaded CD-MOFs in terms of component distribution was confirmed by elemental mapping by STEM-EDX. Both CTAB, the surfactant used in the CD-MOFs synthesis, and LPZ compete for their inclusion in the CD cavities. CTAB allowed obtaining regular cubic particles of around 5  $\mu\text{m}$  with 15 wt% residual CTAB amounts. When LPZ was incorporated, the residual CTAB amount was less than 0.1 wt%, suggesting a higher affinity of LPZ for the CDs than CTAB. These findings were confirmed by molecular simulations. Vibrational circular dichroism studies confirmed the LPZ incorporation inside the CDs. Solid-state NMR showed that LPZ was located in the CDs and that it remained intact even after three years storage. Remarkably, the CD-MOFs matrix protected the drug upon thermal decomposition. This study highlights the interest of CD-MOFs for the incorporation and protection of LPZ.

### 1. Introduction

Cyclodextrin-based metal-organic frameworks (CD-MOFs) have emerged as one of the latest classes of crystalized porous MOFs particles. Since their discovery in 2010 (Smaldone et al., 2010), CD-MOFs have attracted growing interest due to their useful applications in separation, gas storage, sensing, catalysis, and in biomedicine (Arima et al., 2015; Han et al., 2018). Assembled mostly using metals and non-toxic  $\gamma$ -CDs widely used for biomedical applications (Loftsson and Brewster, 1996; Loftsson and Duchêne, 2007), they advantageously display high surface areas, adjustable chemical functionality, and

structural diversity (Arima et al., 2015; Han et al., 2018; Qiu et al., 2020; Smaldone et al., 2010; Qiu et al., 2018). CD-MOFs were shown to incorporate a large variety of anticancer (e.g., doxorubicin, fluorouracil, methotrexate, quercetin), anti-inflammatory (e.g., ibuprofen, furbiprofen, fenbufen, ketoprofen), antihypertensive (captopril, azilsartan) drugs, acid pump inhibitor (lansoprazole ( $\pm$ )-(LPZ), named LPZ for simplicity reasons), and various other pharmaceutical ingredients (e.g., salicylic acid, ferulic acid, pseudolaric acid, folic acid, glycyrrhizic acid, etc) (Liu et al., 2017; Lv et al., 2016; Michida et al., 2015; Moussa et al., 2016; Smaldone et al., 2010; Abuçafy et al., 2018; Rajkumar et al., 2019; Xu et al., 2019). As shown in Fig. 1 upper panel, CD-MOFs delimit

\* Corresponding author.

E-mail address: [ruxandra.gref@universite-paris-saclay.fr](mailto:ruxandra.gref@universite-paris-saclay.fr) (R. Gref).

<https://doi.org/10.1016/j.ijpharm.2020.119442>

Received 29 April 2020; Received in revised form 14 May 2020; Accepted 15 May 2020

Available online 21 May 2020

0378-5173/ © 2020 Elsevier B.V. All rights reserved.

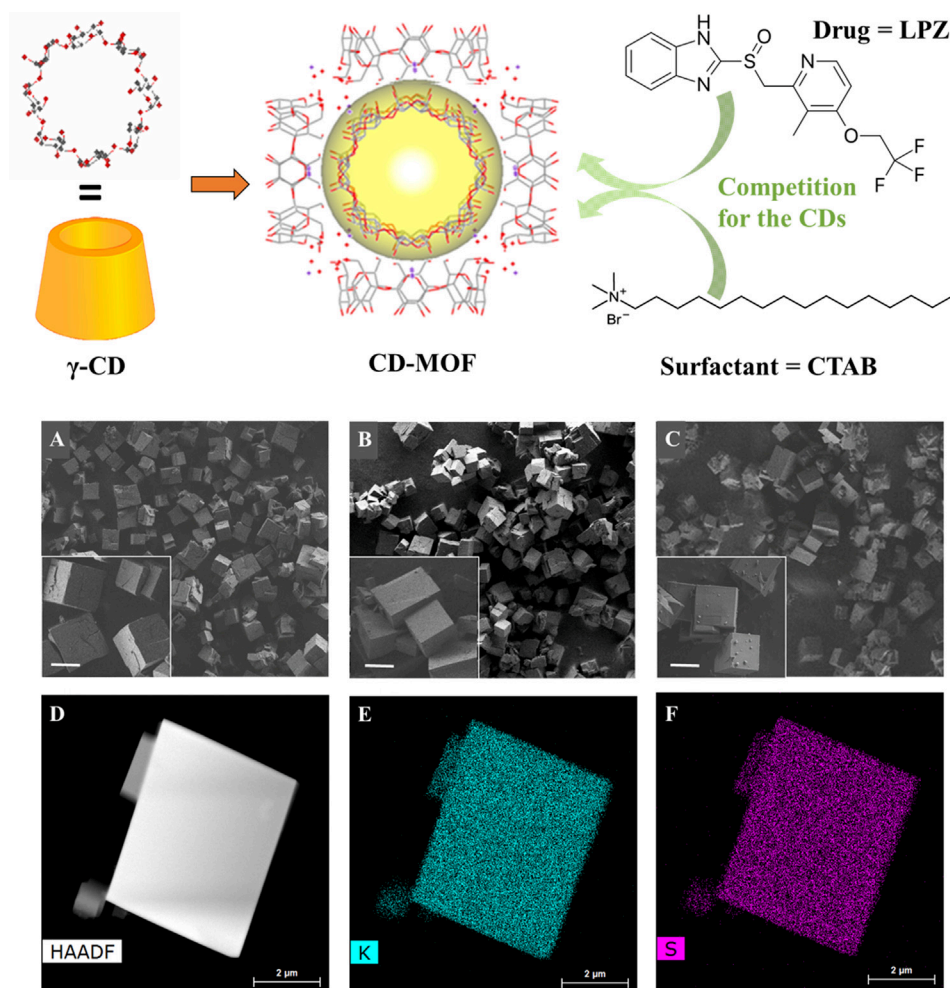


**Fig. 1.** Upper panel: Schematic representation of the synthesis of CD-MOFs starting from the building units ( $\gamma$ -CDs) and K ions (red dots). The cell unit comprises a cavity (yellow) of around 1.7 nm which is surrounded by 6 CDs. During synthesis, both the drug (LPZ) and the surfactant (CTAB) compete for the CD cavities. **Lower panel:** SEM micrographs of empty CD-MOF (A), racemic LPZ loaded CD-MOF (B) and (R)-LPZ loaded CD-MOF (C) scale bar: 5  $\mu$ m; HAADF-STEM images (D) and EDX mapping (E: K mapping and F: S mapping) of racemic LPZ loaded CD-MOF crystals. (For interpretation of the references to colour in this figure legend, the reader is referred to the web version of this article.)

an extended framework incorporating the symmetric cyclic  $\gamma$ -CD oligosaccharide, and are based on the coordination of the K<sup>+</sup> alkali metal cations to alternating  $\alpha$ -1,4-linked D-glucopyranosyl units on the primary and secondary faces of the  $\gamma$ -CD tori (Smaldone et al., 2010). Drugs were mainly loaded by impregnation inside the porosity and loadings reached at best 12.6 wt% in the case of captopril (Liu et al., 2016). The loadings were increased when the molecules of interest were co-crystallized with CD-MOFs. For instance, rhodamine B could be incorporated with loadings of 18.5 wt% (Smaldone et al., 2010).

One remarkable result was the incorporation of LPZ in CD-MOFs with loadings as high as  $23 \pm 2$  wt% (Li et al., 2017). The crystallized particles of around 6  $\mu$ m were prepared using cetyltrimethyl ammonium bromide (CTAB) as stabilizer and had regular shapes (Furukawa et al., 2012). When CD-MOFs were prepared in the absence of CTAB, they had irregular shapes and high polydispersity, but the LPZ loadings were still in the range 21–23 wt%. The high LPZ loadings correspond to a 1:1 M ratio between LPZ and  $\gamma$ -CDs in the matrix. However, the role played by CTAB in building regular crystalline supramolecular structures without affecting drug loading is still to be uncovered. Indeed, both CTAB and LPZ compete for the CD cavities inside the CD-MOFs (Fig. 1, upper panel). Moreover, LPZ is a fragile molecule which readily degrades in both acidic (DellaGreca et al., 2006; Ekpe and Jacobsen, 1999; Gupta et al., 2007) and basic conditions (Battu and Pottabathini, 2015; DellaGreca et al., 2006; Liu et al., 2005), even during storage at 4  $^{\circ}$ C (DiGiacinto et al., 2000). It was interesting to study here whether the integrity of the drug was preserved upon incorporation in CD-MOFs and long-term storage.

To gain information on LPZ chemical stability as well as LPZ and CTAB respective locations, we employed a set of complementary

techniques. First, LPZ distribution inside the CD-MOFs was characterized by scanning transmission electron microscope (STEM) associated with energy-dispersive X-ray spectroscopy (EDX), which is a powerful tool to detect compositional distribution in single particles. In particular, the detection of sulfur (present only in LPZ) enabled studying drug distribution in these slices of CD-MOFs with high resolution. In addition, vibrational circular dichroism (VCD) enabled studying conformational changes of LPZ inside the CD-MOFs.

The <sup>1</sup>H nuclear magnetic resonance (NMR) spectroscopy is often used to study CD-drug inclusions in liquid (Cheng et al., 2018; Di Nunzio et al., 2013; Kundu and Roy, 2017; Rajendiran et al., 2014; Ye et al., 2013) or in solid phase (Ferreira et al., 2015; Skorupska et al., 2014; Upreti et al., 2011; Vogt and Strohmeier, 2012; Wulff et al., 2002). Here, although it proved much more challenging, we choose to employ solid-state NMR spectroscopy to directly study the LPZ-loaded CD-MOFs in their final state, as crystalline dried powders.

Using state-of-the-art NMR equipment and methods, including high-field magnets (up to 20 T), ultra-fast (up to 60 kHz) magic-angle (MAS) <sup>1</sup>H NMR spectroscopy, complemented by <sup>1</sup>H-<sup>19</sup>F-<sup>13</sup>C triple-resonance NMR and <sup>15</sup>N NMR at natural abundance, new atomic-level insights about the interactions between CTAB/LPZ and CD-MOFs, as well as the localization and configuration of CTAB and LPZ in CD-MOFs have been obtained. A special attention has been attributed to the competition of LPZ and CTAB for the CDs in CD-MOFs. These data were further supported by molecular simulation, which allowed comparing the respective interactions between LPZ, CTAB and the CD-MOFs. In a nutshell, the experimental data corroborated the simulations enabling gaining insights on the mechanism of formation and locations of individual constituents.

Finally, thermogravimetric analysis coupled to Fourier transform infrared spectroscopy (TGA-FTIR) was used to investigate the thermal decomposition of LPZ as free drug or incorporated in CD-MOFs. The thermal stability of the drug molecules was preserved after three years storage.

## 2. Experimental

### 2.1. Materials and reagents

The chemical compounds, including  $\gamma$ -CD, CTAB, potassium hydroxide (KOH), methanol, isopropanol and ethanol were purchased from Sigma-Aldrich Co. Ltd (France). (R)-LPZ, used only for VCD studies, was provided by Toronto Research Chemicals and racemic LPZ was provided by Zhuhai Rundu Co. Ltd (China). Water was filtered by a Milli-Q system (18.4 M $\Omega$  cm, Millipore, Milford, MA, USA). All chemicals were used without further purification.

### 2.2. Synthesis of CD-MOF crystals with or without LPZ

CD-MOF crystals were synthesized as previously reported (Li et al., 2017). Briefly, CD-MOFs were prepared by reacting  $\gamma$ -CD (0.125 mM) with KOH (200 mM). The solution was filtered through a 0.45  $\mu$ m membrane to remove any possible dust. Then, methanol was allowed to diffuse in this reaction mixture placed in a vial at 50 °C for 6 h. To obtain monodispersed crystals, 6.0 mL of the supernatant was transferred into another vial with 48.0 mg of CTAB, then the suspension was incubated for 3 h at room temperature. The crystals were finally harvested, washed three times with isopropanol and dried at 50 °C overnight under vacuum. LPZ loaded CD-MOFs crystals were synthesized in a similar way, except that racemic LPZ or (R)-LPZ (80 mM) was added in the aqueous solution of  $\gamma$ -CD (0.125 mM) and KOH (200 mM). After purification, the CD-MOFs loaded or not with LPZ were stored at 4 °C in closed vials until further use.

The drug payload is defined as the percentage of LPZ in the drug-loaded CD-MOFs and was calculated as Equation:

$$\text{Payload (\%)} = \frac{\text{Encapsulated Drug (mg)}}{\text{Drug loaded CD - MOF (mg)}} \times 100$$

### 2.3. Characterization of CD-MOFs crystals before or after LPZ encapsulation

The morphologies of all synthesized CD-MOF crystals were observed by scanning electron microscopy (SEM). SEM images were acquired on a Zeiss SUPRA 55 VP field emission gun scanning electron microscope fitted with an EDAX EDS analytical system. It was set to a low voltage (1 kV) and low current (a few pA) in order not to damage the samples and to avoid any conductive coating that could bother direct observation of the samples. Secondary electron type detector was used to record the images.

STEM associated with elemental chemical Energy-dispersive X-ray spectroscopy (EDX) cartography was employed to characterize the elemental (C, H, N, S, and Br) distribution in the particles. The MOFs samples were placed on a copper grid covered with a pure carbon membrane. The observations in STEM were made on a Titan Themis 200 microscope (FEI/Thermo Fischer Scientific) equipped with a geometric aberration corrector on the probe. This microscope was also equipped with the "Super-X" systems for EDX analysis with a detection angle of 0.9 sr. The observations were made at 200 kV with a probe current of about 70 pA and a half-angle of convergence of 24 mrad. High-angle annular dark-field (HAADF)-STEM images were acquired with a camera length of 110 mm (inner/outer collection angles were respectively 69 mrad and 200 mrad).

The synthesized particles were further cut into thin sections for

further STEM observations. Briefly, the dried CD-MOFs powder samples were embedded in epoxy resin (Delta microscopie – France) and polymerized 48 h at 56 °C. Sections were performed in an ultramicrotome (Leica UC6) using a diamond trim (LFG France). The section thickness was between 100 and 200 nm and the sections were directly collected on 300 mesh carbon grids.

Elemental analysis was performed to quantify the C, H, N, S, and Br elemental weight contents in the CD-MOFs particles loaded or not with LPZ. LPZ and CTAB powders were used as controls. N and S are present only in LPZ but not in CD-MOFs. Moreover, N and Br are in CTAB but not in CD-MOFs. Therefore, the amounts of Br and N found in empty CD-MOFs was used to quantify CTAB content. The amount of S was used to determine the amount of LPZ, and Br for CTAB in LPZ loaded CD-MOFs. The amounts of C, H, and N were used to confirm the results. Briefly, the determination of C, H, N was performed with a combustion method using an Elemental Analyzer (Perkin-Elmer 2400 CHNS/O Series II System). Sample elements were converted to gases at 1050 °C. The quantification of Br was performed using a combustion method to decompose organic samples. Then a potentiometric titration was applied using Titroprocessor (835 Titrand) and ion chromatography analysis was performed on Dionex IC system. Sulfur was determined by a combustion method, followed by gravimetric titration and ion chromatography analysis (Dionex IC system). Inductively coupled plasma mass spectrometry (ICP-MS) analysis was used to further confirm the payload. After CD-MOFs digestion using aqua regia (15 min under ultrasonic bath), an ICP-MS equipped with a triple quadrupole (Agilent 8800, Agilent Technologies, Japan) was used for the analysis. Operation conditions were daily optimized using a tuning solution. S isotopes were detected using "mass shift mode" ( $^{48}\text{SO}^+$ ,  $^{49}\text{SO}^+$  and  $^{50}\text{SO}^+$ ) after their reaction with oxygen in the cell. Dwell time for each of the targeted isotopes was 1 s. S was quantified using external calibration prepared with certified 1000 mg L $^{-1}$  S standard (Merck, Germany).

The vibrational infrared (IR) absorption and VCD spectra of CD-MOFs were measured using a Fourier-transform infrared spectroscopy (FTIR) spectrometer (Vertex 70, Bruker) equipped with a VCD module (PMA 50, Bruker). The IR radiation was filtered by a low-pass filter cutting at 2000 cm $^{-1}$ , linearly polarized, and then modulated by a 50 kHz ZnSe photo-elastic modulator (Hinds). The signal was measured by a Mercury-Cadmium-Telluride (MCT) IR detector equipped with a BaF $_2$  window and cooled with liquid nitrogen then demodulated using a lock-in amplifier (Stanford Research Systems SR 830). A spectral resolution of 4 cm $^{-1}$  was used for both absorption and VCD spectra. The alignment of the spectrometer was controlled by checking the mirror-image relation between the VCD spectra of the two enantiomers of camphor (0.3 M in CCl $_4$ ). The samples were prepared by mixing the studied system with KBr with a mortar and pestle and pressing 200 mg pellets. KBr was first grinded in a mixer mill (MM 400 Retsch) at 20 Hz during 30 min and kept dry in an oven at 80 °C, as usually done for the studies of solid samples (Declerck et al., 2019; Pérez-Mellor and Zehnacker, 2017). Two concentrations were used for each system, with the following amounts for 1 g of KBr: 3.8 or 4.3 mg for LPZ, 2.5 or 5 mg for bare CD-MOF, and 4.5 or 5.5 mg for CD-MOF loaded with LPZ. The artefacts due to the birefringence were eliminated following the procedure proposed by Merten (Merten et al., 2008), derived from that introduced by Buffeteau (Buffeteau et al., 2005). It consists in rotating the sample in the plane perpendicular to the light propagation axis for each side of the pellet and averaging the spectra obtained for the pellets at 0°, 90°, 180°, 270°. The measurements were repeated twice. The final spectrum was obtained by adding 2100 scans for each sample position and averaging all the positions so that the total acquisition time was 4 h.

#### 2.4. Solid-state NMR characterization of CD-MOFs crystals with or without LPZ

The  $^1\text{H} \rightarrow ^{19}\text{F} \rightarrow ^{13}\text{C}$  cross polarized magic angle spinning (CPMAS) NMR spectra were recorded on a Bruker 500 MHz WB NMR spectrometer using a  $^1\text{H}$ - $^{19}\text{F}$ -X triple-resonance 2.5 mm probe (Martineau et al., 2011). The initial  $^1\text{H} \rightarrow ^{19}\text{F}$  CP was used to reduce the repetition delay, taking advantage of short  $T_1(^1\text{H})$  compared to  $T_1(^{19}\text{F})$  (Yu et al., 2015). The  $^{13}\text{C}$  CP experiments were recorded on a 9.4 T magnet ( $^1\text{H}$  and  $^{13}\text{C}$  Larmor frequency of 400 and 100 MHz, respectively) with a Bruker spectrometer, using a 4 mm double resonance MAS probe. The  $^{13}\text{C}$  chemical shifts are referenced to TMS. The contact time was set to 3.5 ms, the recycle delay was set at 3 s, the initial  $90^\circ$  pulse on  $^1\text{H}$  to 2.5  $\mu\text{s}$  with a Radio Frequency (RF) field of 70 kHz.  $^1\text{H}$  SPINAL-64 decoupling was applied during the  $^{13}\text{C}$  acquisition. The  $^1\text{H}$  MAS NMR spectra were recorded at a magnetic field of 20 T, using a Bruker 850 MHz WB NMR spectrometer and a HXY 1.3 mm probe in double-resonance mode. The spectra were acquired using Hahn echo pulse sequence, with a  $90^\circ$  pulse duration of 2.5  $\mu\text{s}$ , an inter-pulse delay synchronized with one rotor period and a spinning rate of 60 kHz. The recycle delay was set to 5 s and 16 transients were recorded for each sample. The  $^1\text{H}$  chemical shifts were referenced to TMS. The  $^1\text{H}$ - $^1\text{H}$  2D MAS exchange NMR experiment was recorded with a recycle delay of 2 s and two different mixing times (5 and 10 ms). 700  $t_1$  slices with 16 transients were co-added. The States procedure provides a phase sensitive 2D NMR spectrum.

$^{15}\text{N}$  CPMAS NMR spectra were recorded on a Bruker 400 WB NMR spectrometer using a 4 mm probe head and spinning at 10 kHz. 10,240 and 75,776 transients were accumulated for LPZ and LPZ loaded CD-MOF, respectively. Similar  $^{15}\text{N}$  CPMAS NMR spectra were recorded at 8 kHz MAS frequency on a Bruker 600 SB NMR spectrometer using a novel cryogenically cooled 3.2 mm HCN CPMAS probe (Biosolids CryoProbe™) (Hassan et al., 2020). 528 and 122 888 transients were accumulated for LPZ and LPZ loaded CD-MOF, respectively. In all cases, acquisition time is 20 ms. No apodization was applied on the LPZ spectrum, while a 30 Hz Lorentzian apodization was applied on  $^{15}\text{N}$  CPMAS NMR spectrum of LPZ loaded CD-MOFs. All the samples were finely ground into powders and packed into a zirconia rotor of the appropriate size. The NMR spectra were acquired using TopSpin 3.5 Bruker Software and processed with the DMfit program (Massiot et al., 2002).

#### 2.5. Molecular simulation

The crystal structure of CD-MOFs was extracted from the single crystal structure of MOF-1 as reported in the literature (Forgan et al., 2012). In the docking model, an expanded non-periodic structure was used, where the  $\text{OH}^-$  ion was replaced by  $\text{H}_2\text{O}$  and the  $\text{K}^+$  ion was deleted in PyMOL 2.2.0. The molecular structure of  $\gamma$ -CD was extracted from reported CD-MOFs structures (Forgan et al., 2012). The structure of CTAB was obtained from the PubChem of National Center for Biotechnology Information (PubChem CID: 5974; <https://pubchem.ncbi.nlm.nih.gov>). AutoDock was then applied using docking program AutoDock Vina 1.1.2 (Allouche, 2012) to optimize their molecular structures.

Lamarckian Genetic Algorithm (LGA) in combination with a grid-based energy evaluation method was used to pre-calculate grid maps according to the interatomic potentials of all atom types present in the host and guest molecules, including the Lennard-Jones potentials for van der Waals interactions and Coulomb potentials for electrostatic interactions. A grid map of dimensions  $30 \text{ \AA} \times 30 \text{ \AA} \times 30 \text{ \AA}$  and  $10 \text{ \AA} \times 10 \text{ \AA} \times 10 \text{ \AA}$ , with a grid spacing of 0.375  $\text{ \AA}$ , was placed to cover the CD-MOF and  $\gamma$ -CD models, respectively. With the help of AutoDockTools (Zhao and Sanner, 2007), the atomic partial charges were calculated by the Gasteiger-Marsili method (Gasteiger and Marsili, 1980). The parameters used for the global search were an initial

population of 50 individuals, with a maximal number of energy evaluations of 1,500,000 and a maximal number of generations of 50,000 as an end criterion. Other docking parameters were set as default.

#### 2.6. Thermal degradation analysis

Thermal decomposition of LPZ loaded CD-MOFs was investigated using a PerkinElmer thermogravimetric analysis Fourier transform infrared spectroscopy (TGA-FTIR) system which consists of a TGA 4000 coupled to a FTIR (Spectrum Two) by TL8000 interface. Samples masses ranging from 6 to 10 mg were heated from 25 to 600  $^\circ\text{C}$  at a rate of 10  $^\circ\text{C}/\text{min}$  in a  $\text{N}_2$  atmosphere. The flow rate was approximately 60 mL/min applied by the TGA 4000 internal mass flow controller and further monitored by TL8000 to ensure the constant flow rate and avoid the gas mixing in the cell. The heated line that transfers evolved gases from the TGA to the FTIR was set at 260  $^\circ\text{C}$  and the IR gas cell was held at 270  $^\circ\text{C}$ . IR spectra were recorded with a 4  $\text{cm}^{-1}$  resolution in the range of 4,000–500  $\text{cm}^{-1}$ . Pure LPZ and CD-MOF particles were used as controls.

### 3. Results and discussions

#### 3.1. Synthesis and characterization of LPZ loaded CD-MOFs

CD-MOFs crystals were successfully obtained displaying a crystal-line structure with regular cubic morphology and diameters around 5  $\mu\text{m}$  (Fig. 1A), in agreement with previously reported data (Li et al., 2017). The racemic LPZ or (*R*)-LPZ loaded CD-MOFs were prepared with a similar procedure except the addition of the drug directly in the reaction mixture composed of  $\gamma$ -CD, KOH and CTAB.

LPZ was reported to degrade rapidly within 6–8 h in basic conditions, especially at high temperature (e.g. 60  $^\circ\text{C}$  (Battu and Pottabathini, 2015) or 80  $^\circ\text{C}$  (Shankar et al., 2017)). In this study, LPZ was incorporated in CD-MOFs at lower temperature (50  $^\circ\text{C}$ ) and during a 6 h procedure, in the presence of KOH (200 mM). LPZ was extracted from the prepared CD-MOFs and its integrity was assessed by HPLC, showing exactly the same retention time peak without the appearance of degradation products, out ruling a possible degradation during CD-MOF preparation. Possibly, CDs played a protective role, as it has been observed in previous studies (Pasic, 2008).

Three complementary methods were used to assess drug loading: i) elemental analysis (determination of “N” and “S” contents in loaded samples) showed that the LPZ payload reached  $21 \pm 2 \text{ wt\%}$  (Table 1); ii) HPLC-UV-vis allowed determining payloads of  $22 \pm 2 \text{ wt\%}$  and iii) ICP-MS showed payloads of  $20 \pm 2 \text{ wt\%}$ . It was concluded that there is a good agreement between the three methods. Moreover, no significant drug loading differences were observed when (*R*)-LPZ was incorporated instead of LPZ (less than 2% differences, as quantified by ICP-MS, showing (*R*)-LPZ payload of  $20 \pm 1.5 \text{ wt\%}$ ). Interestingly, despite the high LPZ loadings, the CD-MOFs' morphology and size were not affected by LPZ incorporation (Fig. 1B and C).

HAADF-STEM images confirmed the regular morphologies of the CD-MOFs possessing sharp edges, loaded or not with the drug (Fig. 1D). When coupled with EDX, this method gave insights on the element distribution inside the particles. The homogeneous distribution of K in the CD-MOFs (Fig. 1E) indicates their homogeneity in terms of composition. Indeed, sulfur (S) is only present in LPZ and not in the CD-MOFs matrix. Fig. 1F shows the high homogeneity in terms of drug distribution in the particles. Control samples (Fig. S1) shows that there is no residual S in the empty CD-MOFs. Fluor (F) is a lighter element compared to S, present in LPZ and not in CD-MOFs. Fig. S2 shows that this element diffracted more at the particle edges in thick samples, as confirmed also by the mapping of C and O.

Thus, to circumvent possible artefacts due to the thickness of the samples and gain deeper insights on the element distribution inside the CD-MOFs, these were cut into slices of 100–200 nm thick and analyzed

**Table 1**  
Elemental analysis of CD-MOFs loaded or not with LPZ. Free LPZ and CTAB were used as controls.

Sample	C (%)		H (%)		S (%)		N (%)		Br (%)		LPZ (%)		CTAB (%)	
	A <sup>a</sup>	A	A	B <sup>b</sup>	A	B	A	B	A	B	A	B	A	B
LPZ	51.8 ± 0.4	3.3 ± 0.3	9.1 ± 0.3	8.7 ± 0.3	11.15 ± 0.3	–	98 ± 3 (N)	100 ± 3 (S)	–	–	–	–	–	–
CTAB	62.9 ± 0.4	12.2 ± 0.3	–	–	3.8 ± 0.1	22.4 ± 0.5	–	–	–	–	–	–	100 ± 3 (N)	101 ± 2 (Br)
CD-MOF	42.4 ± 0.4	6.8 ± 0.3	–	–	0.6 ± 0.1	3.1 ± 0.3	–	–	–	–	–	–	14.8 ± 3 (N)	14.1 ± 2 (S)
LPZ loaded CD-MOF	42.0 ± 0.4	5.5 ± 0.3	2.0 ± 0.3	2.1 ± 0.1	2.6 ± 0.1	0.3 ± 0.1	23 ± 3 (S)	24 ± 3 (S)	–	–	–	–	0.05 ± 0.02 (N)	1.4 ± 0.5 (Br)

A: The experiments were performed with a combustion method using an elemental analyzer; B: The results were obtained by ICP-MS.

again by HAADF-STEM. Fig. S3 shows the mapping of all the CD-MOF components (F, C, O, S, K), supporting the homogeneous drug distribution within their structure.

It has been previously reported (Li et al., 2017) by some of us that the Raman spectra of different individual CD-MOFs particles perfectly superimposed, suggesting the homogenous composition of the drug loaded CD-MOFs particles. However, element mapping (Fig. S3) gave even deeper and clearer insight.

As reported by Furukawa et al (Furukawa et al., 2012), the addition of CTAB during the synthesis of the particles is needed to control their size and achieve regular cubic morphologies. However, no study has been performed yet to elucidate the possible interference of CTAB with drug loading inside CD-MOFs. To do so, CTAB residual amounts in empty and loaded CD-MOFs was determined by both elemental analysis and ICP-MS (Table 1).

As described in materials and method section, CTAB contains Br and N, whereas CD-MOFs do not. Elemental analysis of control samples (CTAB and LPZ) shows that their composition can be retrieved from elemental analysis data (Table 1). Therefore, the accurate quantification of Br and N in the synthesized CD-MOFs allows for determining their residual CTAB content.

The amount of CTAB in empty CD-MOF crystals was as high as 15 ± 1.4 wt% (corresponding to molar ratio of 2:3 between CTAB and  $\gamma$ -CD). This suggests that CTAB was incorporated in high amounts in CD-MOFs, possibly poisoning crystals growing and thus allowing for the formation of small crystals. Surprisingly, the amount of residual CTAB in LPZ loaded CD-MOFs was practically undetectable (less than 0.1 wt %) despite the fact that the same amount of CTAB was used in the preparation procedure as in the case of empty CD-MOFs.

In contrast, the contents of LPZ in the CD-MOFs were similar, whether CTAB was used or not in their preparation procedure (payloads of 21 ± 2 wt% and 23 ± 2 wt%, respectively).

It can be concluded that the addition of LPZ during the CD-MOF formation competed with CTAB, and LPZ substituted CTAB in the final particle.

### 3.2. Solid-state NMR characterization

Magic-angle spinning (MAS) solid-state NMR spectroscopy measurements were performed in order to get further information about the interaction of CTAB and CD-MOF as well as the modification of LPZ structure upon encapsulation.

#### 3.2.1. Solid-state NMR characterization of CD-MOF

Fig. 2 displays the 1D <sup>1</sup>H and <sup>13</sup>C solid-state NMR spectra of pristine  $\gamma$ -CD and of the CD-MOF. The <sup>1</sup>H MAS spectrum of  $\gamma$ -CD shows a single broad featureless resonance while the spectrum of the CD-MOF, acquired under the same experimental conditions, contains three sets of peaks: the hydroxyl protons at 5.20 ppm, the CH groups and the CH<sub>2</sub> groups at 3.49 and 3.06 ppm, respectively (Bekiroglu et al., 2003). <sup>1</sup>H-<sup>13</sup>C 2D NMR experiments validate our line assignment (Fig. S5). The

lines corresponding to the  $\gamma$ -CD appear narrower on the CD-MOF. This might be due to the intrinsic porosity of the CD-MOF, which increases the <sup>1</sup>H-<sup>1</sup>H distances, hence reduces the homonuclear dipolar interaction and the linewidth. An additional set of peaks is noticed at 1 ppm which corresponds to the aliphatic protons of the CTAB used in the CD-MOF synthesis and trapped in their final structure. This is confirmed by the <sup>13</sup>C CPMAS NMR spectrum, which contains, in addition to the peaks of the  $\gamma$ -CD (at 102.2, 82.3, 73.5 and 61.8 ppm), peaks of smaller intensity that correspond to the CTAB. This validates the incorporation of CTAB in the CD-MOFs detected by the elemental analysis (Table 1).

<sup>1</sup>H-<sup>1</sup>H 2D MAS NMR homonuclear correlation spectra were recorded to get further insights into the possible location of the CTAB in the CD-MOFs. The 2D <sup>1</sup>H-<sup>1</sup>H NMR spectrum of the CD-MOFs recorded with a short mixing time (Fig. 3A) contains cross-correlation peaks of high intensity between the CTAB and the CH/CH<sub>2</sub> of the  $\gamma$ -CD, while the intensity of the cross-peaks between the CTAB and the OH of the  $\gamma$ -CD are of a much smaller intensity. This is due to shorter distance of the CTAB with the inside protons of the  $\gamma$ -CD, which indicates that part of the CTAB is very likely located inside the  $\gamma$ -CD cavity.

#### 3.2.2. Solid state NMR characterization of LPZ loaded CD-MOF

The <sup>1</sup>H and <sup>13</sup>C MAS NMR spectra of LPZ loaded CD-MOFs were displayed in Fig. 4 along with those of pure LPZ. The first observation was that the intensity of the CTAB resonances has strongly decreased (in the 25 ppm region and slightly above 50 ppm), indicating that the drug loading process has expelled most CTAB molecules from the system, as observed by elemental analysis (Table 1).

Several <sup>13</sup>C NMR experiments were performed to identify and quantify the various carbon atoms (Fig. S6): a CP with short contact time (50  $\mu$ s) allows selection of the proton bearing carbon atoms while a quantitative CP (Johnson and Schmidt-Rohr, 2014) allows the determination of the number of carbon atoms contributing to each <sup>13</sup>C resonance (which can arise from the overlap of several C atoms). Careful analysis of these experiments showed that all <sup>13</sup>C resonances of the drug are found in the LPZ loaded CD-MOF sample, supporting the HPLC data which showed that the drug remained intact after the encapsulation process, presumably because it was stabilized inside the MOF particles. Stability of LPZ inside the particles is further supported by the <sup>13</sup>C liquid-state NMR spectrum of the CD-MOF dissolved in D<sub>2</sub>O, which shows the absence of degraded LPZ (Fig. S4).

Finally, the quantitative analysis <sup>1</sup>H-<sup>1</sup>H and <sup>1</sup>H-<sup>13</sup>C 2D NMR data (Fig. S7) indicate a ratio between the LPZ and  $\gamma$ -CD close to 1:1, corroborating the ICP-MS, elemental analysis and HPLC data.

One can notice that the <sup>13</sup>C resonances corresponding to the carbon atoms C11 and C20 (overlapped with one CD resonance) of the LPZ have different chemical shifts in the pure and loaded drug (Figs. 4 and 5). Notably, C11 and C20 are flexible sp<sup>3</sup> carbon atoms, the observed shifts hence very likely correspond to a bending of the drug once it is loaded in the CD-MOFs.

Besides C11 and C20, C5 and C6, which belong to the imidazole ring, also show significant shift of their <sup>13</sup>C resonance upon loading.

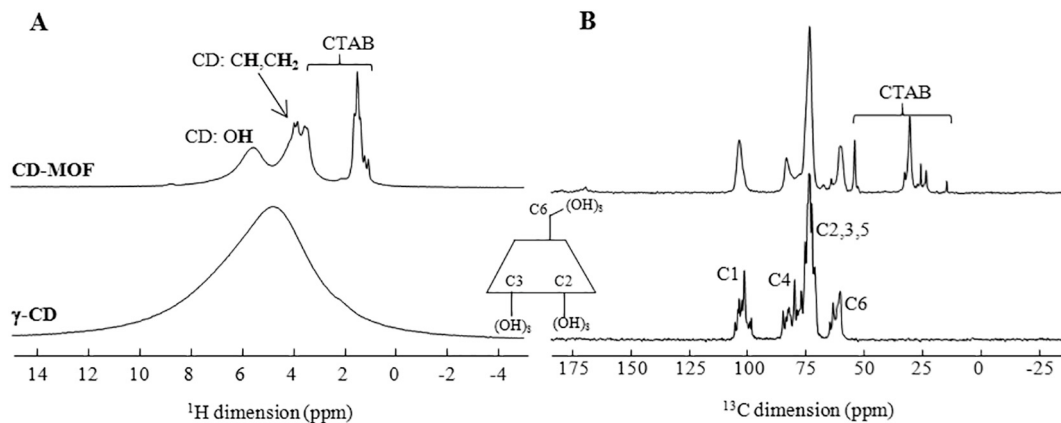


**Fig. 2.**  $^1\text{H}$  MAS (A) and  $^{13}\text{C}$  CPMAS (B) NMR spectra of CD-MOF (top) and  $\gamma$ -CD (bottom). The CTAB and CD molecules are shown on the right. The NMR lines are assigned.

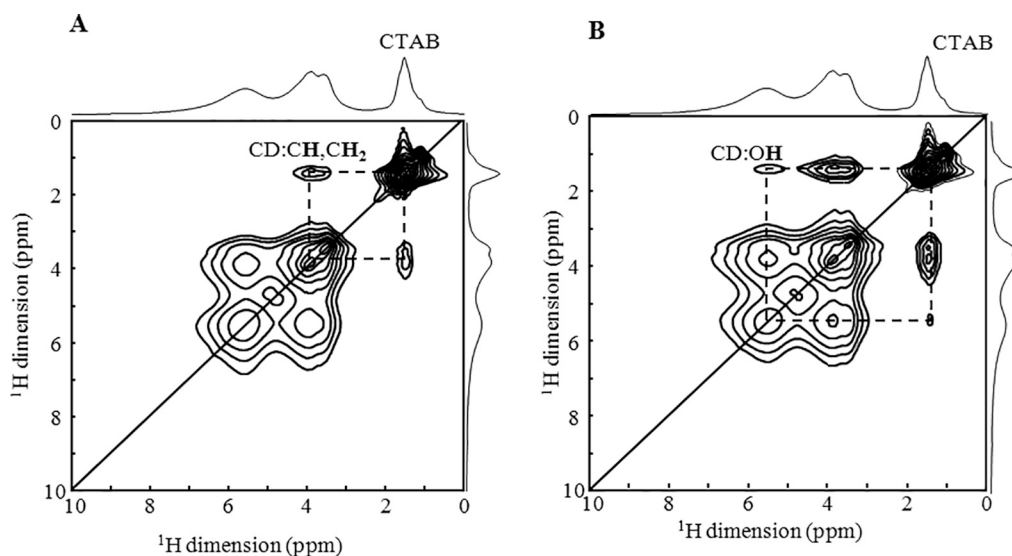


**Fig. 3.**  $^1\text{H}$ - $^1\text{H}$  2D MAS NMR correlation spectra of CD-MOF recorded with mixing time of 5 ms (A) and 10 ms (B). The dash lines indicate spatial proximity between the protons of the CTAB and those of the  $\gamma$ -CD.

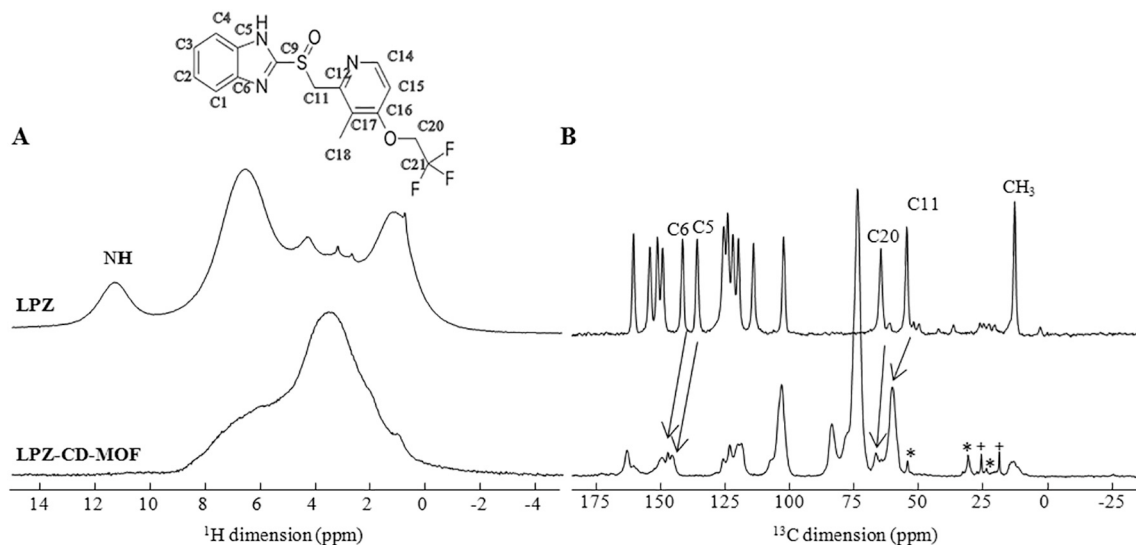


**Fig. 4.**  $^1\text{H}$  MAS (A) and  $^{13}\text{C}$  CPMAS (B) NMR spectra of pure LPZ (top) and LPZ loaded CD-MOF (bottom). The lines are assigned comparing with LPZ solution (in  $\text{DMSO-}d_6$ ) NMR studies (Table S1) (Ramulu et al., 2013). The molecule of LPZ with carbon atoms numbered is shown. \* indicate traces of CTAB together with traces of ethanol.

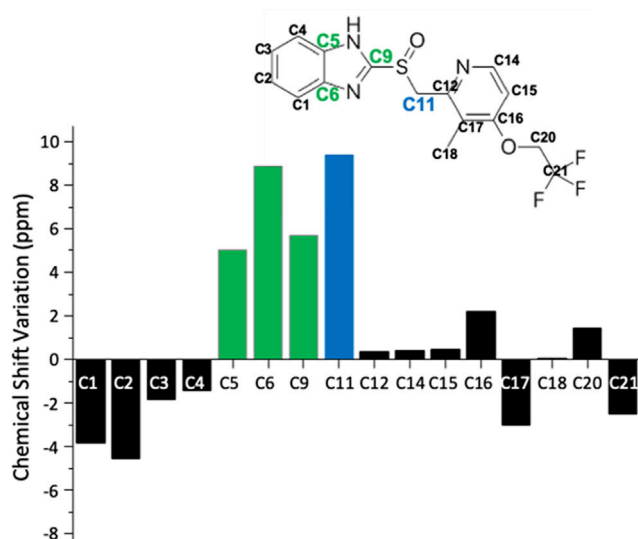


Fig. 5. <sup>13</sup>C chemical shift variation (ppm) of the carbon atoms of LPZ pure and loaded in the CD-MOFs.

These shifts are correlated to the disappearance of the N–H proton of the pure drug (<sup>1</sup>H chemical shift of 11.5 ppm Fig. 4A), when it is loaded in the CD-MOF and with a strong shift of the <sup>15</sup>N resonance in the <sup>15</sup>N CPMAS NMR spectrum (Fig. 6). All these features indicated that the LPZ molecules are deprotonated when loaded in the CD-MOF, possibly because of their basic inner microenvironment.

Despite the relatively small amount of drug loaded (below 25%) and broadness of the signals (due to chemical shift distributions), the <sup>15</sup>N CPMAS NMR spectrum of the drug-loaded samples could be obtained at natural abundance in less than 48 h due to significant signal enhancement provided by the novel cryogenically cooled 3.2 mm HCN CPMAS probe (see experimental section), while no signal could be obtained in a week in an usual NMR spectrometer (Fig. S8). In formulated drugs,

significant <sup>15</sup>N NMR sensitivity gain have been obtained using dynamic nuclear polarization (DNP-MAS) NMR (Ni et al., 2017). However, CD-MOFs are unstable in the solvents that are required for performing DNP-MAS studies. Hence, the cryoprobe technology is so far the only technology that allows probing the state of a low API content in formulations that are not amenable to DNP-MAS NMR. Note that the CPMAS CryoProbe has been used so far for biomolecules (Hassan et al., 2020), and we reported here its first use in the field of materials science.

Despite using a high magnetic field (20.0 T) and fast MAS (60 kHz), the <sup>1</sup>H MAS NMR spectrum of LPZ loaded CD-MOFs only showed broad peaks with extremely low resolution (Fig. 4A and S9), hence 2D <sup>1</sup>H–<sup>1</sup>H NMR appeared of limited use. Therefore, to get insights into the interactions between the drug and the CD-MOFs, we used the <sup>19</sup>F nucleus as a spy. The advantage of <sup>19</sup>F is that there is only one fluorine atom in the compound, which belongs to the drug. We therefore recorded, using a dedicated <sup>1</sup>H–<sup>19</sup>F-X probe, a <sup>1</sup>H–<sup>19</sup>F–<sup>13</sup>C double CPMAS NMR experiment. The initial <sup>1</sup>H–<sup>19</sup>F was used to benefit from the shorter relaxation T<sub>1</sub> of <sup>1</sup>H (shorter than 1 s) compared to the one of <sup>19</sup>F (> 5 s). This experiment allows the selection of the carbon atoms in the vicinity of the fluorine atom. The resulting <sup>13</sup>C NMR spectrum (Fig. 7) was compared to the <sup>1</sup>H–<sup>13</sup>C CPMAS NMR spectrum, in which all <sup>13</sup>C atoms are present (since both the drug and the γ-CD have protons to transfer magnetization to the carbon atoms). The spectra were normalized to the CD peak at 73 ppm. In the <sup>19</sup>F–<sup>13</sup>C CPMAS, one can notice that the CF<sub>3</sub> and C20 carbons of the LPZ have higher intensity, which is an expected result as these are the closest C atoms to the <sup>19</sup>F nuclei. There is also a significant signal for the <sup>13</sup>C of the γ-CD, indicating its close spatial proximity to the drug. Among the <sup>13</sup>C signals of the γ-CD, the one labeled C6 in Fig. 2 (which corresponds to the CH<sub>2</sub>OH) has higher intensity than the other γ-CD carbon atoms (Fig. 7). This indicates that the CF<sub>3</sub> is in close contact with the CH<sub>2</sub>OH of the γ-CD, i.e., the molecule is most probably bend so that the CF<sub>3</sub> groups get located outside of the CD cavity.

To investigate the fate of the LPZ molecules once incorporated in CD-MOF crystals, the synthesized particles were characterized by VCD spectroscopy. (R)-LPZ loaded particles were successfully synthesized,

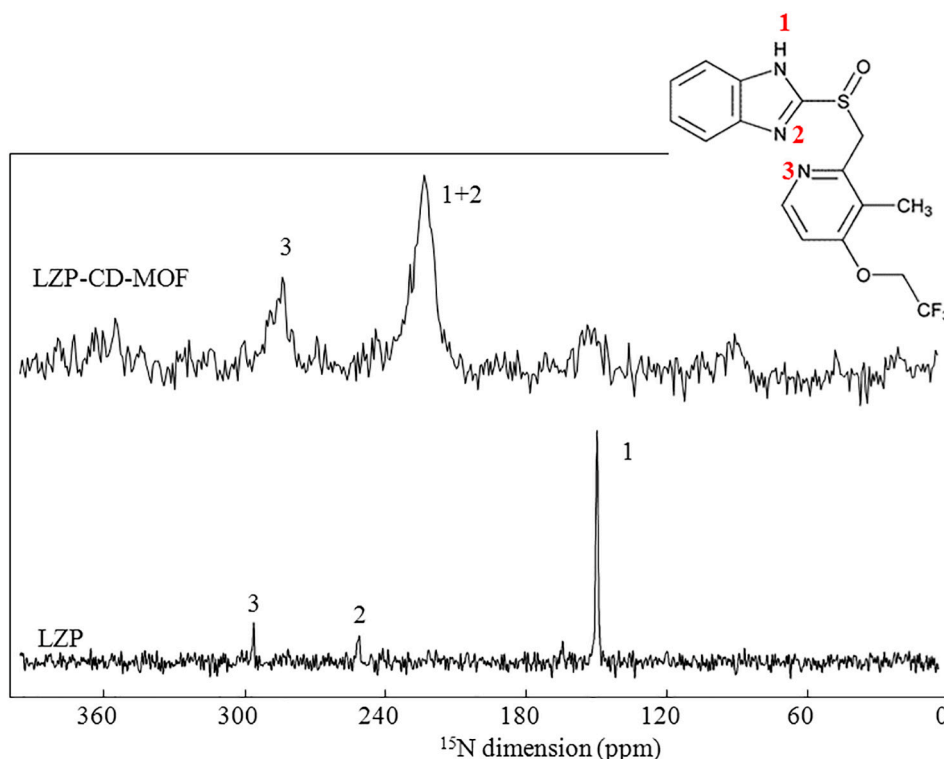


Fig. 6. <sup>15</sup>N-CPMAS NMR spectra of pure LPZ and loaded LPZ showing the deprotonation of the imidazole ring upon drug loading in the CD-MOF.

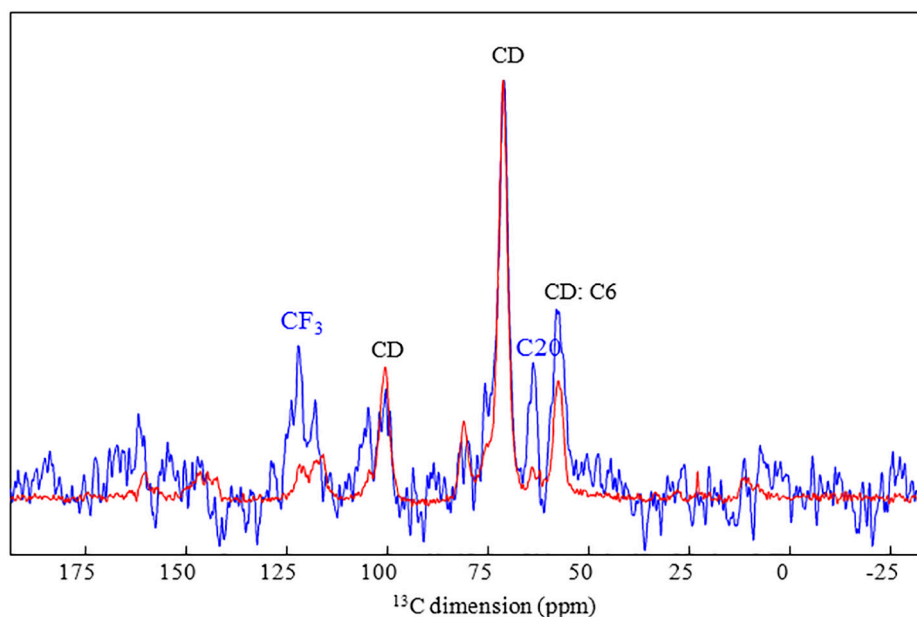


Fig. 7.  $^1\text{H} \rightarrow ^{13}\text{C}$  (red) and  $^{19}\text{F} \rightarrow ^{13}\text{C}$  (blue) CPMAS NMR spectra of LPZ loaded CD-MOF. The spectra are normalized to the  $^{13}\text{C}$  resonance of  $\gamma$ -CD at 73 ppm. The lines are assigned. (For interpretation of the references to colour in this figure legend, the reader is referred to the web version of this article.)

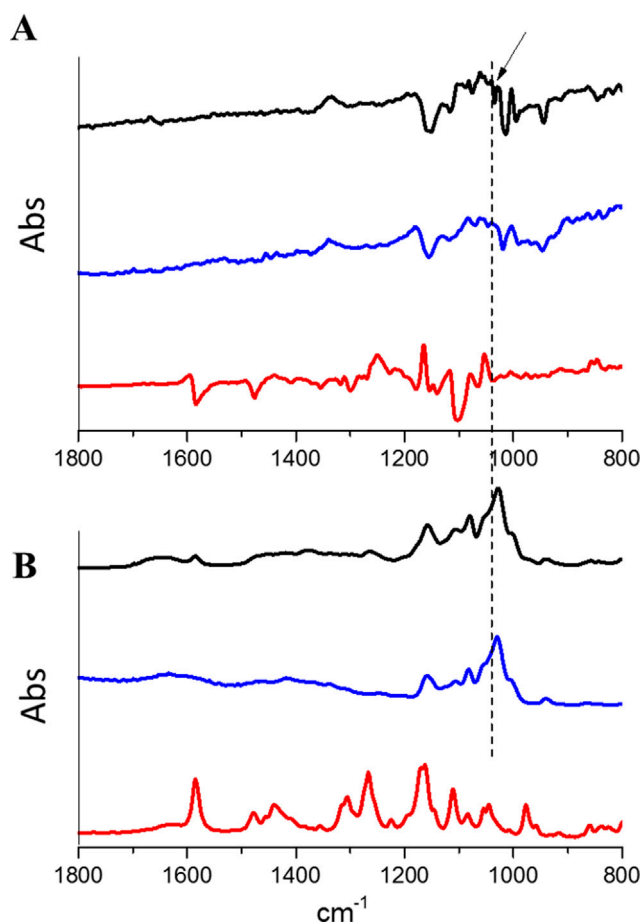


Fig. 8. (A) VCD spectrum of (R)-LPZ (red), bare CD-MOF (blue), and (R)-LPZ loaded CD-MOF (black), together with their absorption spectrum (B). The vertical scale of the VCD spectra is multiplied by  $10^4$ . (For interpretation of the references to colour in this figure legend, the reader is referred to the web version of this article.)

reaching the payload of  $20 \pm 1.5$  wt%. Prior to the VCD spectra, IR spectra were recorded for (R)-LPZ, empty CD-MOFs, and drug loaded CD-MOFs. All the bands of CD-MOFs appear unmodified in the IR absorption spectrum of loaded MOF, indicating that the structure of the crystals was preserved after LPZ loading. Several intense bands of (R)-LPZ also appeared in this spectrum, at 1167, 1267 and  $1585\text{ cm}^{-1}$  (Fig. S11). They were not modified in frequency or intensity relative to (R)-LPZ. This confirmed the successful drug loading in the particles. In contrast, the region of other intense bands of (R)-LPZ, between the bands at 1040 and  $1115\text{ cm}^{-1}$ , was modified in the loaded CD-MOF relative to the pure drug (R)-LPZ. This observation points to a modification of the structure of LPZ upon inclusion in the CD-MOFs.

The VCD spectra of (R)-LPZ, bare CD-MOF, and loaded CD-MOF were recorded. As shown in Fig. 8, the spectrum of (R)-LPZ is intense, of the order of  $5 \times 10^4$ . Indeed, intense VCD spectra are often observed for crystalline samples. Most bands present in the VCD spectrum of the drug-loaded MOF are due to the CD-MOF itself, further proving that the structure of CD-MOF was kept intact. For example, the IR absorption band of (R) LPZ at  $1167\text{ cm}^{-1}$  (shown in Fig. S11) corresponds to an intense negative band in the VCD spectrum of (R)-LPZ. Although this band is observed in the IR absorption of loaded CD-MOF, it is absent in its VCD spectrum. These data indicate again that the LPZ structure was changed upon inclusion in CD-MOFs. HPLC and NMR data clearly ruled out a possible degradation of the drug. A possible explanation of VCD data could be LPZ deprotonation, as is suggested by the solid-state NMR data.

### 3.3. Molecular simulation

Molecular simulation was carried out to gain insights into the competition between CTAB and LPZ to insert into the available cavities of CD-MOFs. First, the interaction of the two molecules with free  $\gamma$ -CDs were studied. Fig. 9 (A,B) shows that both LPZ and CTAB crouch in the hydrophobic  $\gamma$ -CD cavity [14].

In contrast, inside the CD-MOF structures, both LPZ and CTAB preferentially locate in the  $\gamma$ -CD pairs of CD-MOF rather than in the cage of CD-MOF (yellow sphere in Fig. 9 C, D).

As shown in Fig. 9, part of the CTAB molecule is nonetheless located inside the CD-cavity of CD-MOF, which is in agreement with the  $^1\text{H}$ - $^1\text{H}$  MAS NMR spectra reported in Fig. 4. When one LPZ molecule is inserted

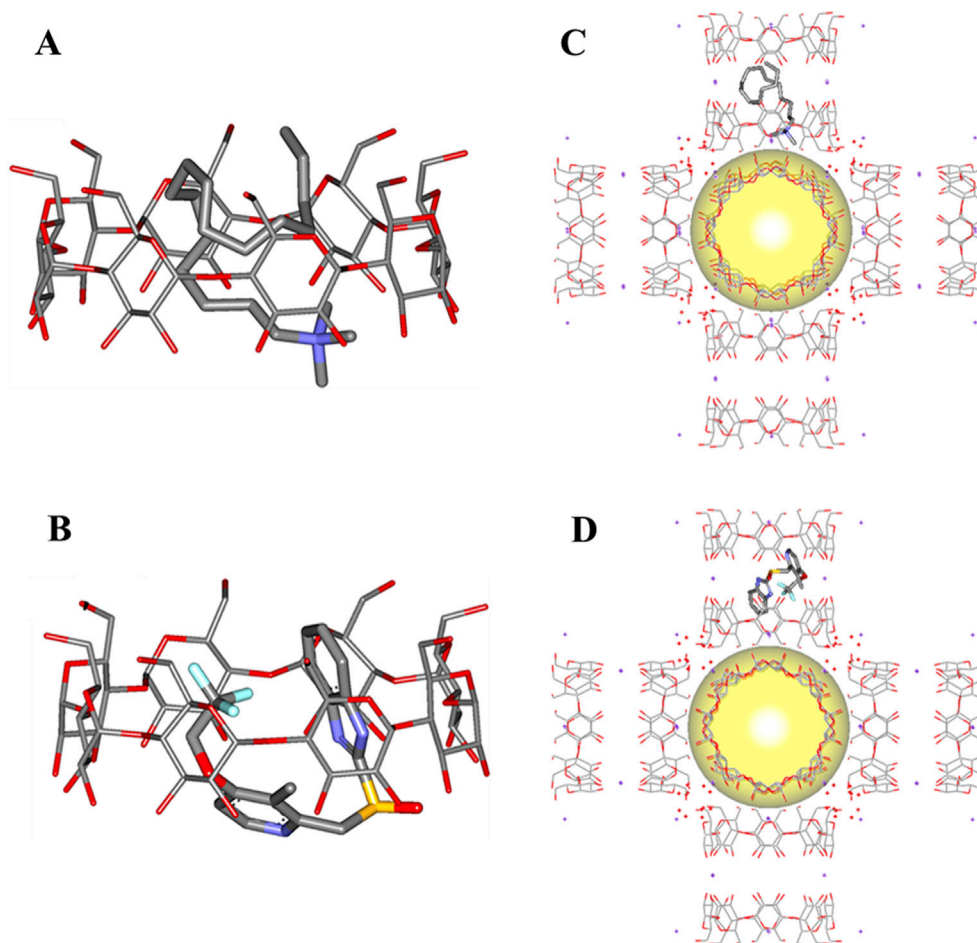


**Fig. 9.** Simulated configurations of CTAB (A, C) and LPZ (B, D) in monomeric  $\gamma$ -CD (A, B) and in  $\gamma$ -CD-MOF (C, D). K ions were indicated as purple spots in the structure of the CD-MOF. For the simulation, two LPZ molecules were placed in contact with two CD cavities of the CD-MOFs. (For interpretation of the references to colour in this figure legend, the reader is referred to the web version of this article.)

in the system, the  $\text{CF}_3$  group tend to locate outside the  $\gamma$ -CDs of CD-MOF, in between two of them, which is also in agreement with the  $^{19}\text{F}$ - $^{13}\text{C}$  CPMAS NMR experiments.

LPZ possessed a stronger interaction free energy with both  $\gamma$ -CD ( $-5.3 \text{ kcal}\cdot\text{mol}^{-1}$ ) and CD-MOF ( $-7.5 \text{ kcal}\cdot\text{mol}^{-1}$ ) than CTAB ( $-2.9 \text{ kcal}\cdot\text{mol}^{-1}$  and  $-4.0 \text{ kcal}\cdot\text{mol}^{-1}$  for  $\gamma$ -CD and CD-MOF, respectively).

In summary, the interaction free Gibbs energy of CTAB is weaker than that of LPZ either with CD-MOF or with  $\gamma$ -CD, which explains the experimental observations that LPZ molecules are preferentially incorporated in the CD-MOFs when both CTAB and LPZ are used for their preparation. This is likely due to the presence of more nonpolar alkyl groups in CTAB than in LPZ. Moreover, simulations were performed to study the competition between LPZ and CTAB molecules for the CD cavities in CD-MOFs. To do so, one LPZ molecule and one CTAB molecule was placed in contact with one CD inside the CD-MOF. Based on the free Gibbs energies  $\Delta G$  and the Eq. (1), at a temperature of 300 K, with  $R = 8.314 \text{ J mol}^{-1} \text{ K}^{-1}$  and  $e = 2.71828$ , the probability that LPZ forms an inclusion complex was 40 times higher than for the CTAB:CD complex. This again supports the fact that during CD-MOF synthesis, LPZ molecules replace CTAB ones and only trace CTAB is found in the final LPZ loaded CD-MOFs.

$$K = e^{-\frac{\Delta G}{RT}} \quad (1)$$

#### 3.4. Thermal stability of LPZ as free or encapsulated form

Once demonstrated that LPZ was embedded inside the  $\gamma$ -CDs of the CD-MOFs, it was interesting to study if this peculiar configuration allows improving its stability inside the dried particles stored at room temperature up to three years. To do so, thermal decomposition was investigated by TGA-FTIR analysis, combining the TGA ability to accurately measure weight loss during heating and FTIR allowing to chemically identify the nature of the gas evolved from the sample decomposition.

TGA weight loss thermograms and the corresponding derivative curves (DTG) for LPZ, CD-MOF, and LPZ loaded CD-MOF crystals are shown in Fig. 10A and B. Free LPZ degraded in two steps, with specific temperatures of around 190 °C and 315 °C, respectively. Total IR absorbance spectra were recorded when these degradation events occurred (Fig. S12). As illustrated in Fig. 10C, the FTIR spectra corresponding to the first gas departure at 190 °C corresponds well to 2,2,2-trifluoroethanol ( $\text{C}_2\text{H}_3\text{F}_3\text{O}$ ). The FTIR spectra of the second departure at around 315 °C showed bands at around  $1476 \text{ cm}^{-1}$ , which were assigned to the departure of LPZ aromatic rings (Fig. S13).

In contrast to LPZ, CD-MOF crystals exhibited different thermal degradation stages with two weight loss regions at around 55 °C and 300 °C. First gas departure at around 55 °C in CD-MOFs thermograms was attributed to isopropanol traces (Fig. S14), as this solvent was used to wash the particles. CD-MOF particles decomposed at around 300 °C.

Finally, three decomposition steps were observed for LPZ loaded CD-MOFs (Fig. 10, blue curves). The first departure corresponds to

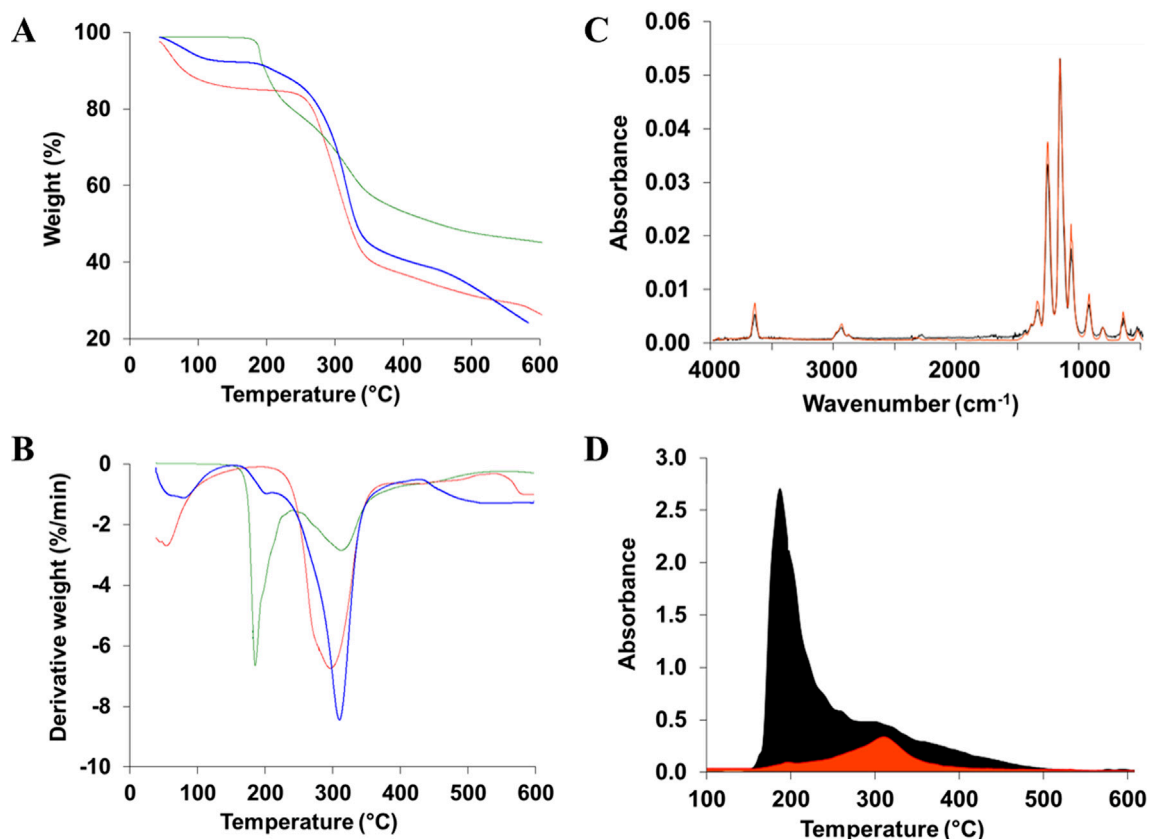


**Fig. 10.** TGA (A) and DTG (B) curves for LPZ (green), CD-MOFs (red), and LPZ loaded CD-MOFs (blue); FTIR spectra (C) of LPZ evolved gas at 190 °C (black) and the spectrum of 2,2,2-trifluoroethanol from the database (orange); 2,2,2-trifluoroethanol departure (D) from pure LPZ (black) and LPZ loaded CD-MOFs (orange). (For interpretation of the references to colour in this figure legend, the reader is referred to the web version of this article.)

isopropanol traces, as in the case of empty CD-MOFs. The 2,2,2-trifluoroethanol vapor production corresponding to LPZ decomposition was identified in both second and third departures (around 200 and 310 °C, respectively). Remarkably, the departure of 2,2,2-trifluoroethanol from LPZ loaded CD-MOFs was dramatically delayed as compared to the pure LPZ (190 °C & 310 °C for pure LPZ and LPZ loaded CD-MOFs, respectively). This delay corresponds to an increased in the stability of the drug upon decomposition which could be attributed to its embedding inside the CD-MOF matrix. These results are in line with the protective effects of LPZ embedding in native CDs upon thermal decomposition of LPZ (Lu et al., 2012).

#### 4. Conclusion

LPZ loaded CD-MOFs were successfully synthesized displaying regular cubic morphology, uniform size of around 5  $\mu\text{m}$  and high LPZ payloads up to  $23 \pm 2$  wt%, which corresponds to a molar ratio of 1:1 between LPZ and  $\gamma$ -CD in the CD-MOFs. The drug was uniformly distributed inside the particles as assessed by STEM-EDX in the whole particles and in thin slices of them. Solid NMR enabled deciphering drug location and configuration inside CD-MOFs, which was well corroborated by molecular simulations and VCD studies.

The drug LPZ was well incorporated inside the constitutive  $\gamma$ -CDs cavities of the CD-MOFs, filling practically all of them. LPZ competes for the  $\gamma$ -CDs with the CTAB surfactant used to modulate the size of the CD-MOFs and replaces it, leading to the formation of crystals devoid of CTAB, but maintaining their high LPZ payloads, which is an advantage for biomedical applications.

Remarkably, the CD-MOF matrix protected the drug upon degradation, even after three years storage at room temperature.

#### Declaration of Competing Interest

The authors declare that they have no known competing financial interests or personal relationships that could have appeared to influence the work reported in this paper.

#### Acknowledgements

This work was supported by the French National Research Agency (ANR-10-LABX-0035, ANR-14-CE08-0017 and EuronanoMedIII PCInano) and the National Science and Technology Major Projects for “Major New Drugs Innovation and Development” (2018ZX09721002-009). We thank Pierre Florian (CEMHTI Orléans) for help in the  $^{15}\text{N}$ -NMR experiments, financial support from the IR-RMN-THC Fr3050 CNRS, the MIMA2-MET platform (<https://doi.org/10.15454/1.5572348210007727E12>) and the Ile-de-France DIM RESPORE. We are grateful to Dr. Borja Moreira-Alvarez, Dr José M. Costa Fernandez and Dr. Jorge R. Encinar (University of Oviedo, Spain) for ICP-MS experiments. MP thanks the Région Centre-Val de Loire for a PhD fellowship. We thank Dr. Mohamed Haouas (ILV, Versailles) for the acquisition of the  $^{13}\text{C}$  liquid NMR spectrum.

#### Appendix A. Supplementary data

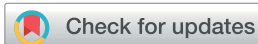
Supplementary data to this article can be found online at <https://doi.org/10.1016/j.ijpharm.2020.119442>.

#### References

Abuqafy, M.P., Caetano, B.L., Chiari-Andréo, B.G., Fonseca-Santos, B., do Santos, A.M., Chorilli, M., Chiavacci, L.A., 2018. Supramolecular cyclodextrin-based metal-organic

- frameworks as efficient carrier for anti-inflammatory drugs. *Eur. J. Pharm. Biopharm.* 127, 112–119.
- Allouche, A., 2012. Software news and updates gabedit: a graphical user interface for computational chemistry softwares. *J. Comput. Chem.* 31, 174–182.
- Arima, H., Hayashi, Y., Higashi, T., Motoyama, K., 2015. Recent advances in cyclodextrin delivery techniques. *Expert Opin.* 12, 1425–1441.
- Battu, S., Pottabathini, V., 2015. Hydrolytic degradation study of lansoprazole, identification, isolation and characterisation of base degradation product. *Am. J. Anal. Chem.* 06, 145–155.
- Bekiroglu, S., Kenne, L., Sandström, C., 2003. <sup>1</sup>H NMR studies of maltose, maltoheptaose,  $\alpha$ -,  $\beta$ -, and  $\gamma$ -cyclodextrins, and complexes in aqueous solutions with hydroxy protons as structural probes. *J. Org. Chem.* 68, 1671–1678.
- Buffeteau, T., Lagugné-Labarthe, F., Sourisseau, C., 2005. Vibrational circular dichroism in general anisotropic thin solid films: measurement and theoretical approach. *Appl. Spectrosc.* 59, 732–745.
- Cheng, J.G., Yu, H.J., Chen, Y., Liu, Y., 2018. Selective binding and controlled release of anticancer drugs by polyanionic cyclodextrins. *Bioorganic Med. Chem.* 26, 2287–2290.
- Declerck, V., Pérez-Mellor, A., Guillot, R., Aitken, D.J., Mons, M., Zehnacker, A., 2019. Vibrational circular dichroism as a probe of solid-state organisation of derivatives of cyclic  $\beta$ -amino acids: cis- and trans-2-aminocyclobutane-1-carboxylic acid. *Chirality* 31, 547–560.
- DellaGreca, M., Iesce, M.R., Previtiera, L., Rubino, M., Temussi, F., Brigante, M., 2006. Degradation of lansoprazole and omeprazole in the aquatic environment. *Chemosphere* 63, 1087–1093.
- Di Nunzio, M.R., Wang, Y.L., Douhal, A., 2013. Spectroscopy and dynamics of topotecan anti-cancer drug comprised within cyclodextrins. *J. Photochem. Photobiol. A Chem.* 266, 12–21.
- DiGiacinto, J.L., Olsen, K.M., Bergman, K.L., Hoie, E.B., 2000. Stability of suspension formulations of lansoprazole and omeprazole stored in amber-colored plastic oral syringes. *Ann. Pharmacother.* 34, 600–605.
- Ekpe, A., Jacobsen, T., 1999. Effect of various salts on the stability of lansoprazole, omeprazole, and pantoprazole as determined by high-performance liquid chromatography. *Drug Dev. Ind. Pharm.* 25, 1057–1065.
- Ferreira, M.J.G., García, A., Leonardi, D., Salomon, C.J., Lamas, M.C., Nunes, T.G., 2015. <sup>13</sup>C and <sup>15</sup>N solid-state NMR studies on albendazole and cyclodextrin albendazole complexes. *Carbohydr. Polym.* 123, 130–135.
- Forgan, R.S., Smaldone, R.A., Gassensmith, J.J., Furukawa, H., Cordes, D.B., Li, Q., Wilmer, C.E., Botros, Y.Y., Snurr, R.Q., Slawin, A.M.Z., Stoddart, J.F., 2012. Nanoporous carbohydrate metal-organic frameworks. *J. Am. Chem. Soc.* 134, 406–417.
- Furukawa, Y., Ishiwata, T., Sugikawa, K., Kokado, K., Sada, K., 2012. Nano- and micro-sized cubic gel particles from cyclodextrin metal-organic frameworks. *Angew. Chem. Int. Ed.* 124, 10718–10721.
- Gasteiger, J., Marsili, M., 1980. Iterative partial equalization of orbital electronegativity—a rapid access to atomic charges. *Tetrahedron* 36, 3219–3228.
- Gupta, H.P., Saini, K., Dhingra, P., Pandey, R., 2007. Study of acid catalyzed reactions of proton pump inhibitors at D.M.E. *Port. Electrochim. Acta* 26, 433–448.
- Han, Y., Liu, W., Huang, J., Qiu, S., Zhong, H., Liu, D., 2018. Cyclodextrin-based metal-organic frameworks (CD-MOFs) in pharmaceuticals and biomedicine. *Pharmaceutics* 10, 1–21.
- Hassan, A., Quinn, C.M., Struppe, J., Sergeyev, I.V., Zhang, C., Guo, C., Runge, B., Theint, T., Dao, H.H., Jaroniec, C.P., Berbon, M., Lends, A., Habenstein, B., Loquet, A., Kuemmerle, R., Perrone, B., Gronenborn, A.M., Polenova, T., 2020. Sensitivity boosts by the CPMAS CryoProbe for challenging biological assemblies. *J. Magn. Reson.* 311, 106680.
- Johnson, R.L., Schmidt-Rohr, K., 2014. Quantitative solid-state <sup>13</sup>C NMR with signal enhancement by multiple cross polarization. *J. Magn. Reson.* 239, 44–49.
- Kundu, M., Roy, M.N., 2017. Preparation, interaction and spectroscopic characterization of inclusion complex of a cyclic oligosaccharide with an antidepressant drug. *J. Incl. Phenom. Macrocycl. Chem.* 89, 177–187.
- Li, X., Guo, T., Lachmanski, L., Manoli, F., Menendez-Miranda, M., Manet, I., Guo, Z., Wu, L., Zhang, J., Gref, R., 2017. Cyclodextrin-based metal-organic frameworks particles as efficient carriers for lansoprazole: Study of morphology and chemical composition of individual particles. *Int. J. Pharm.* 531, 424–432.
- Liu, B., He, Y., Han, L., Singh, V., Xu, X., Guo, T., Meng, F., Xu, X., York, P., Liu, Z., Zhang, J., 2017. Microwave-assisted rapid synthesis of  $\gamma$ -cyclodextrin metal-organic frameworks for size control and efficient drug loading. *Cryst. Growth Des.* 17, 1654–1660.
- Liu, B., Li, H., Xu, X., Li, X., Lv, N., Singh, V., Stoddart, J.F., York, P., Xu, X., Gref, R., Zhang, J., 2016. Optimized synthesis and crystalline stability of  $\gamma$ -cyclodextrin metal-organic frameworks for drug adsorption. *Int. J. Pharm.* 514, 212–219.
- Liu, K.H., Kim, M.J., Jung, W.M., Kang, W., Cha, I.J., Shin, J.G., 2005. Lansoprazole enantiomer activates human liver microsomal cyp2C9. *Pharmacology* 33, 209–213.
- Loftsson, T., Brewster, M.E., 1996. Pharmaceutical applications of cyclodextrins. 1. Drug solubilization and stabilization. *J. Pharm. Sci.* 85, 1017–1025.
- Loftsson, T., Duchêne, D., 2007. Cyclodextrins and their pharmaceutical applications. *Int. J. Pharm.* 329, 1–11.
- Lu, Y., Guo, T., Qi, J., Zhang, J., Wu, W., 2012. Enhanced dissolution and stability of lansoprazole by cyclodextrin inclusion complexation: preparation, characterization, and molecular modeling. *AAPS PharmSciTech* 13, 1222–1229.
- Lv, N., Guo, T., Liu, B., Wang, C., Singh, V., Xu, X., Li, X., Chen, D., Gref, R., Zhang, J., 2016. Improvement in thermal stability of sucralose by  $\gamma$ -cyclodextrin metal-organic frameworks. *Pharm. Res.* 34, 269–278.
- Martineau, C., Engelke, F., Taulelle, F., 2011. Multiple resonance heteronuclear decoupling under MAS: dramatic increase of spectral resolution at moderate magnetic field and MAS frequencies. *J. Magn. Reson.* 212, 311–319.
- Massiot, D., Fayon, F., Capron, M., King, I., Le Calvé, S., Alonso, B., Durand, J.O., Bujoli, B., Gan, Z., Hoatson, G., 2002. Modelling one- and two-dimensional solid-state NMR spectra. *Magn. Reson. Chem.* 40, 70–76.
- Merten, C., Kowalik, T., Hartwig, A., 2008. Vibrational circular dichroism spectroscopy of solid polymer films: Effects of sample orientation. *Appl. Spectrosc.* 62, 901–905.
- Michida, W., Ezaki, M., Sakuragi, M., Guan, G., Kusakabe, K., 2015. Crystal growth of cyclodextrin-based metal-organic framework with inclusion of ferulic acid. *Cryst. Res. Technol.* 50, 556–559.
- Moussa, Z., Hmadeh, M., Abiad, M.G., Dib, O.H., Patra, D., 2016. Encapsulation of curcumin in cyclodextrin-metal organic frameworks: dissociation of loaded CD-MOFs enhances stability of curcumin. *Food Chem.* 212, 485–494.
- Ni, Q.Z., Yang, F., Can, T.V., Sergeyev, I.V., D'Addio, S.M., Jawla, S.K., Li, Y., Lipert, M.P., Xu, W., Williamson, R.T., Leone, A., Griffin, R.G., Su, Y., 2017. In situ characterization of pharmaceutical formulations by dynamic nuclear polarization enhanced MAS NMR. *J. Phys. Chem. B* 121, 8132–8141.
- Pasic, M., 2008. Study to design stable lansoprazole pellets (Ph.D. thesis). Univ. Basel.
- Pérez-Mellor, A., Zehnacker, A., 2017. Vibrational circular dichroism of a 2,5-diketopiperazine (DKP) peptide: evidence for dimer formation in cyclo LL or LD diphenylalanine in the solid state. *Chirality* 29, 89–96.
- Qiu, C., Wang, J., Qin, Y., Fan, H., Xu, X., Jin, Z., 2018. Green synthesis of cyclodextrin-based metal-organic frameworks through the seed-mediated method for the encapsulation of hydrophobic molecules. *J. Agric. Food Chem.* 66, 4244–4250.
- Qiu, J., Li, X., Gref, R., Vargas-Berenguel, A., 2020. Carbohydrates in metal organic frameworks: Supramolecular assembly and surface modification for biomedical applications. In: Mozafari, M. (Ed.), *Metal Organic Frameworks for Biomedical Applications*. pp. 445–465.
- Rajendiran, N., Sankaranarayanan, R.K., Saravanan, J., 2014. A study of supramolecular host-guest interaction of dothiepin and doxepin drugs with cyclodextrin macrocycles. *J. Mol. Struct.* 1067, 252–260.
- Rajkumar, T., Kukkar, D., Kim, K.H., Sohn, J.R., Deep, A., 2019. Cyclodextrin-metal-organic framework (CD-MOF): From synthesis to applications. *J. Ind. Eng. Chem.* 72, 50–66.
- Ramulu, K., Rao, B.M., Someswara Rao, N., 2013. Identification, isolation and characterization of potential degradation product in idebenone drug substance. *Rasayan J. Chem.* 6, 324–333.
- Shankar, G., Borkar, R.M., Suresh, U., Guntuku, L., Naidu, V.G.M., Nagesh, N., Srinivas, R., 2017. Forced degradation studies of lansoprazole using LC-ESI HRMS and <sup>1</sup>H-NMR experiments: in vitro toxicity evaluation of major degradation products. *J. Mass Spectrom.* 52, 459–471.
- Skorupska, E., Jeziorna, A., Kazmierski, S., Potrzebowski, M.J., 2014. Recent progress in solid-state NMR studies of drugs confined within drug delivery systems. *Solid State Nucl. Magn. Reson.* 57–58, 2–16.
- Smaldone, R.A., Forgan, R.S., Furukawa, H., Gassensmith, J.J., Slawin, A.M.Z., Yaghi, O.M., Stoddart, J.F., 2010. Metal-organic frameworks from edible natural products. *Angew. Chem. Int. Ed.* 49, 8630–8634.
- Upreti, M., Strassburger, K., Chen, Y.L., Wu, S., Prakash, I., 2011. Solubility enhancement of steviol glycosides and characterization of their inclusion complexes with  $\gamma$ -cyclodextrin. *Int. J. Mol. Sci.* 12, 7529–7553.
- Vogt, F.G., Strohmeier, M., 2012. 2D solid-state NMR analysis of inclusion in drug-cyclodextrin complexes. *Mol. Pharm.* 9, 3357–3374.
- Wulff, M., Aldén, M., Tegenfeldt, J., 2002. Solid-state NMR investigation of indomethacin-cyclodextrin complexes in PEG 6000 carrier. *Bioconjug. Chem.* 13, 240–248.
- Xu, J., Wu, L., Guo, T., Zhang, G., Wang, C., Li, H., Li, X., Singh, V., Chen, W., Gref, R., Zhang, J., 2019. A “Ship-in-a-Bottle” strategy to create folic acid nanoclusters inside the nanocages of  $\gamma$ -cyclodextrin metal-organic frameworks. *Int. J. Pharm.* 556, 89–96.
- Ye, Y., Sun, Y., Zhao, H., Lan, M., Gao, F., Song, C., Lou, K., Li, H., Wang, W., 2013. A novel lactoferrin-modified  $\beta$ -cyclodextrin nanocarrier for brain-targeting drug delivery. *Int. J. Pharm.* 458, 110–117.
- Zhao, Yong, Sanner, Michel F., 2007. FLIPDock: docking flexible ligands into flexible receptors. *Proteins. Struct. Funct. Bioinformatics* 68, 726–737.
- Yu, C., Bourrelly, S., Martineau, C., Saidi, F., Bloch, E., Lavrard, H., Taulelle, F., Horcajada, P., Serre, C., Llewellyn, P.L., Magnier, E., Devic, T., 2015. Functionalization of Zr-based MOFs with alkyl and perfluoroalkyl groups: the effect on the water sorption behavior. *Dalt. Trans.* 44, 19687–19692.



Cite this: *RSC Adv.*, 2019, 9, 32472

# New insights on the supramolecular structure of highly porous core–shell drug nanocarriers using solid-state NMR spectroscopy†

 Marianna Porcino,<sup>a</sup> Ioanna Christodoulou,<sup>b</sup> Mai Dang Le Vuong,<sup>bc</sup> Ruxandra Gref<sup>id</sup> \*<sup>b</sup> and Charlotte Martineau-Corcus<sup>id</sup> \*<sup>c</sup>

Nano-sized metal–organic frameworks (nanoMOFs), with engineered surfaces to enhance the targeting of the drug delivery, have proven efficient as drug nanocarriers. To improve their performances a step further, it is essential to understand at the molecular level the interactions between the nanoMOF interfaces and both the surface covering groups and the drug loaded inside the micropores. Here we show how solid-state NMR spectroscopy allows us to address these issues in an aluminum-based nanoMOF coated and loaded with phosphorus-containing species.

Received 13th September 2019

Accepted 4th October 2019

DOI: 10.1039/c9ra07383c

rsc.li/rsc-advances

Since their recent discovery, iron-based nanoMOFs have attracted increasing interest due to their potential for medical applications, owing to the versatility of their structural features, *in vivo* biocompatibility and biodegradability, properties as contrast agents and possibility to tailor their surface functionalities.<sup>1,2</sup> Among them, iron trimesate nanoMOF MIL-100(Fe) (MIL stands for Material of Institute Lavoisier) is among the most promising candidates for efficient drug incorporation by a one-step organic solvent-free method and for surface coating with cyclodextrin (CD) molecules which can be further engineered by linking phosphates (CD-P), targeting moieties or polymers.<sup>3,4</sup> The interactions of surface-modified iron trimesate nanoMOFs with cancer cells were increased by means of these versatile “Lego”-type coatings.<sup>3</sup> If the potential applications of the CD-P coated nanoMOFs have been demonstrated,<sup>1,5</sup> little information is known about the interactions at the atomic level between the CD-P coating and the nanoparticle (NP) surface sites. It was hypothesized that, in contrast to drug molecules which cross the windows of the MOFs and adsorb inside the pores, CD-Ps are too bulky and supposed not to bypass windows of around 9 Å in diameter and effectively remain adsorbed onto the external surface (Fig. 1). Having a direct proof of this hypothesis could help guide further CD-P engineering. Understanding the interactions at the molecular level between the

drug and the host solid is also crucial, as these interactions have a strong influence on the delivery processes. This study addresses these important aspects by using up-to-date complementary solid-state spectroscopic methodologies.

In the past decades, magic-angle spinning (MAS) solid-state nuclear magnetic resonance (ssNMR) spectroscopy, sensitive to short-range order, has proven an essential technique to get information about the structure of MOFs,<sup>6</sup> including drug-carrier MOFs.<sup>7</sup> Although it appeared ideally suited to address the questions mentioned above, we faced the presence of strong paramagnetic centers (Fe<sup>3+</sup> cations)

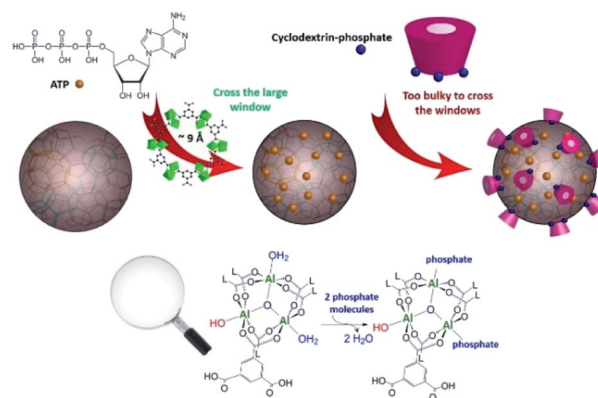


**Fig. 1** Upper panel: schematic representation of the highly porous MIL-100(Al) nanoparticles loaded with ATP and then coated with CD-P. Bottom panel: close up of Al trimers coordinated to trimesate ligands (L). Two molecules of bound water can be replaced either by phosphates from the drug or by phosphate grafted onto the cyclodextrin molecules. Phosphates bound to CD can only access sites located close to the external MOF surface. CD dimensions: cage 6–6.5 Å, external diameter 15.4 Å, height ~8 Å. ATP molecule has about 7 Å radius.

<sup>a</sup>CNRS, CEMHTI UPR 3079, Université d'Orléans, 1d Avenue de la recherche scientifique, 45071 Orléans, France

<sup>b</sup>ISMO, UMR 8214 CNRS, Université Paris Sud, Université Paris Saclay, 91400 Orsay, France. E-mail: ruxandra.gref@u-psud.fr

<sup>c</sup>MIM, Institut Lavoisier de Versailles (ILV), UMR CNRS 8180, Université de Versailles St-Quentin en Yvelines (UVSQ), 45 Avenue des Etats-Unis, 78035 Versailles Cedex, France. E-mail: charlotte.martineau@uvsq.fr

† Electronic supplementary information (ESI) available: Experimental section, additional <sup>31</sup>P, <sup>1</sup>H and <sup>1</sup>H–<sup>27</sup>Al NMR spectra. See DOI: 10.1039/c9ra07383c



that severely reduces the relaxation times hence the amount of available information on the NMR spectra. We therefore have chosen to focus our study on the diamagnetic analogue of nanoMIL-100(Fe), namely nanoMIL-100(Al). The MIL-100(Al) topology<sup>8</sup> is similar to that of MIL-100(Fe),<sup>9</sup> it was shown that large amounts of drugs can be incorporated in this material, and that the NP surface (Fig. 1) can also be efficiently coated by CD-P.<sup>3</sup> Drug of interest here is adenosine triphosphate (ATP), a neurotransmitter with a crucial role in metabolism, which is believed to have a strong affinity with the aluminium species of the nanoMOF framework.

During our investigation, we were confronted to several challenges, including: (i) the complexity of the system, which yields broad overlapping <sup>1</sup>H MAS NMR spectra even at high field (20 T) and fast-MAS (60 kHz, Fig. S1, ESI†), and (ii) the low quantity of the surface species despite the reduced size (150 nm) of the particles. To circumvent the latter difficulty, surface enhanced solid-state NMR spectroscopy such as dynamic nuclear polarization (DNP) methods have been developed. They have proven their efficiency to detect the species present at the external surfaces of silica nanoparticles<sup>10</sup> and the applicability of the method for MOFs was shown.<sup>11</sup> However, DNP-MAS requires the use of a heterogeneous radical, solvent, low temperature (100 K), hence it does not represent the state of NPs as they can potentially be administered *in vivo* in patients. Therefore, we chose to work at room temperature and with simpler MAS NMR methods, namely <sup>27</sup>Al, <sup>31</sup>P and 2D <sup>27</sup>Al–<sup>31</sup>P correlation spectroscopy, that did not involve the use of external molecules such as solvents or radicals.

The <sup>27</sup>Al MAS NMR spectra of pristine and CD-P surface coated nanoMIL-100(Al) (Fig. S2, ESI†) are essentially similar despite the use of high magnetic field (20 T). For quadrupolar nuclei such as <sup>27</sup>Al, greater resolution can often be obtained using the multiple-quantum MAS (MQ-MAS) NMR experiment that separates the aluminium species in the indirect (vertical) dimension. The <sup>27</sup>Al MQMAS NMR spectrum of the nanoMIL-100(Al) recorded at moderate static magnetic field (9.4 T, Fig. S2, ESI†) is similar to that reported earlier for micron-sized MIL-100(Al) recorded at 11.7 T.<sup>12</sup> The <sup>27</sup>Al MQMAS NMR spectrum of nanoMIL-100(Al) recorded at 20 T interestingly has increased resolution which reveals the presence of an additional peak located at around –5 ppm (Fig. 2a). While the bulk Al signals remain similar, the new aluminium sites are in turn slightly modified when the NPs are coated with the CD-P (Fig. 2b), which indicates (i) that this aluminium resonance is due to the Al atoms present at or slightly below the surface of the NPs since CD-P is too bulky (see Fig. 1) to penetrate the open 3D-MOF structure, (ii) the shift of the resonance upon coating results from interactions between some of the surface aluminium species of the NPs and the CD-P coating. In the drug loaded samples (Fig. 2c and d), the bulk Al signals are more affected, indicating the successful incorporation of the drug inside the micropores of the nanoMOF.

To understand further these interactions, through-space <sup>1</sup>H–<sup>27</sup>Al two-dimensional (2D) MAS NMR experiments were performed in an attempt to correlate the protons of the CD-P that are in close proximity to the aluminium species. However

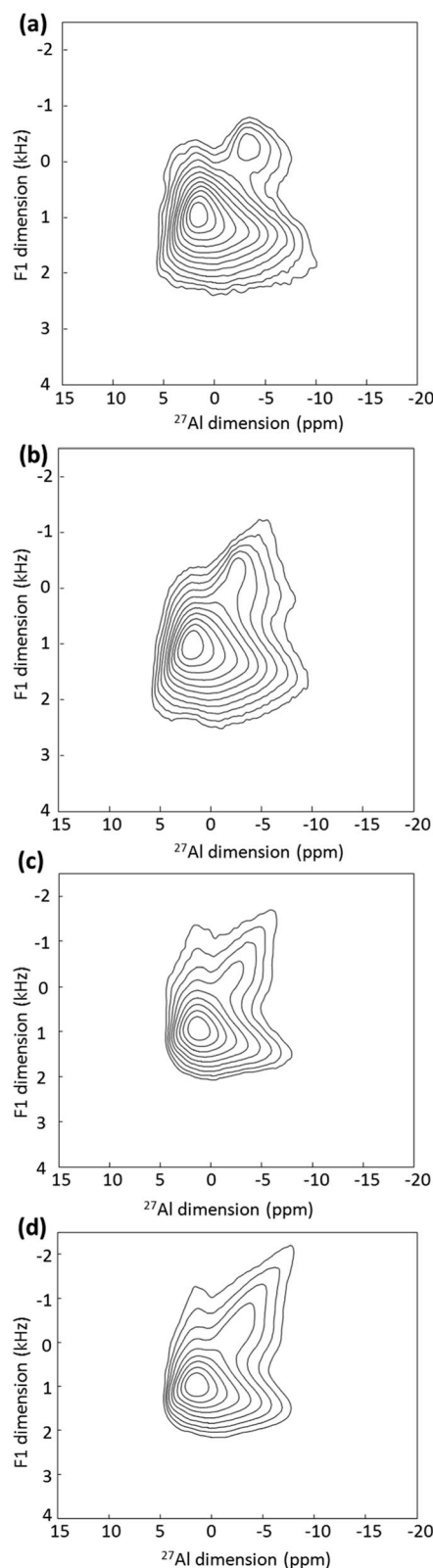
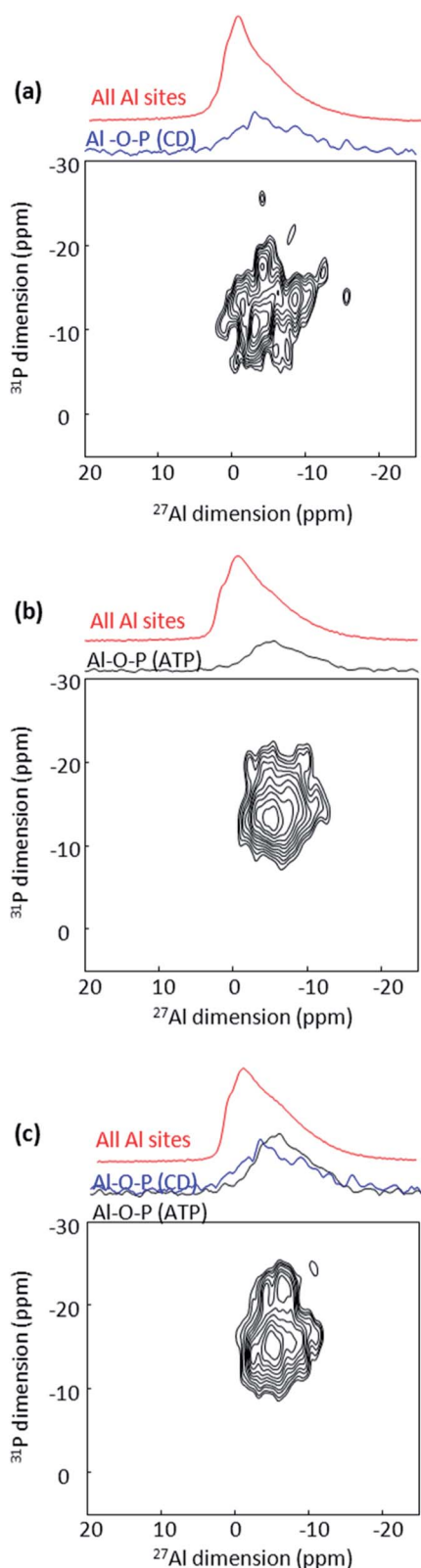


Fig. 2 <sup>27</sup>Al MQMAS NMR spectra of (a) pristine nanoMIL-100(Al) and nanoMIL-100(Al) (b) coated with CD-P, (c) loaded with ATP and (d) loaded with ATP and coated with CD-P.

the <sup>1</sup>H NMR spectrum is dominated by the signal of proton of the linkers, hence only the <sup>1</sup>H–<sup>27</sup>Al correlations from the bulk of the NPs were detected (Fig. S3, ESI†).





**Fig. 3**  $^{27}\text{Al}\{^{31}\text{P}\}$  MAS D-HMQC NMR spectra of CD-P coated (a), ATP loaded (b) and CD-P coated ATP loaded nanoMIL100(Al) (c). The top blue spectra are the full projections on the horizontal dimension for the surface sites, the black spectra are the full projection for the interphase sites, while the red spectra are the MAS NMR spectra shown for comparison.

The  $^{31}\text{P}$  MAS NMR signatures of ATP and CD-P are well distinct (Fig. S5, ESI†).  $^{31}\text{P}$ - $^{31}\text{P}$  double-quantum single-quantum (DQ-SQ) NMR experiments were performed, which allow probing the spatial proximity between the phosphate groups. In CD-P, the  $^{31}\text{P}$  DQ-SQ NMR spectrum shows the phosphate groups grafted on the CD cavity. In ATP, such a spectrum allows the distinction of the middle phosphate of the tri-phosphate chain, which is the only  $^{31}\text{P}$  resonance that has two other P neighbours (Fig. S4, ESI†). In both ATP-loaded and ATP-loaded and coated nanoMIL-100(Al), the  $^{31}\text{P}$  DQ-SQ NMR correlations are similar to pure ATP, showing that the triphosphate moieties are preserved after loading (Fig. S6, ESI†). One can notice a shift of the  $^{31}\text{P}$  resonances, which very likely indicates strong interaction with the framework aluminium sites.

To go further in the characterization, we took advantage of the heteronuclei present in the CD-P coated nanoMIL-100(Al):  $^{27}\text{Al}$ , arising solely from the nanoMOF and  $^{31}\text{P}$ , arising solely from the CD-P coating. By recording 2D NMR spectrum between  $^{31}\text{P}$  and  $^{27}\text{Al}$  nuclei, the surface aluminium species of the NPs in close proximity to the CD-P and the bulk aluminium sites located in the vicinity of the loaded drug are expected to be selectively detected. Because of the short  $^{27}\text{Al}$  transverse relaxation time  $T_2$  (Table S1, ESI†), we could not use the through-bond heteronuclear multiple-quantum (J-HMQC) experiment that requires recoupling time in the 8 ms range for optimum efficiency.<sup>13</sup> Instead we employed the through-space dipolar-based version (D-HMQC), for which the optimum dipolar recoupling requires shorter recoupling time.<sup>14</sup> The recoupling time was kept short enough to ensure that only the Al in very close proximity to the  $^{31}\text{P}$  were selected. The resulting 2D  $^{27}\text{Al}$ - $^{31}\text{P}$  MAS NMR spectrum of CD-P-coated nanoMIL-100(Al) is shown Fig. 3a. The  $^{27}\text{Al}$  NMR signal is at  $-5$  ppm (*i.e.*, chemical shift similar to that of the surface peak observed in the MQMAS NMR spectra Fig. 2), which indicates that the observed surface Al species in the vicinity of the CD-P are in six-fold coordination. The  $^{27}\text{Al}$  chemical shift is lower than the  $^{27}\text{Al}$  chemical shifts in pristine MIL-100(Al) which range between 1.1 and 3.4 ppm.<sup>12</sup> It is close to chemical shift observed in aluminophosphate, hence we can hypothesize that the six-fold coordination is preserved by the formation of an Al-O-P bond between the Al surface sites of the nanoMOF and the terminal phosphate groups of the CD-P, which very likely substitute a water molecule (Fig. 1).

A similar six-fold coordinated  $^{27}\text{Al}$  resonance around  $-7$  ppm is observed in the ATP loaded nanoMIL-100(Al) 2D  $^{27}\text{Al}$ - $^{31}\text{P}$  D-HMQC MAS NMR spectrum (Fig. 3b), which suggests a close proximity (formation of a Al-O-P chemical bond) between Al species of the MOF framework and the terminal phosphate of the drug, which  $^{31}\text{P}$  resonance is located at  $-10$  ppm. This  $^{27}\text{Al}$  resonance is the signature of the grafted aluminium sites inside the pores of the MOF. Correlation of lower intensity is also observed between these Al species and the middle P of the triphosphate chain ( $-20$  ppm), in agreement with longer Al-P distance. Here again, the ATP very likely replaces a water molecule from the Al tricluster.

Finally, we performed the same 2D  $^{27}\text{Al}$ - $^{31}\text{P}$  NMR experiment in the target CD-P coated nanoMIL-100(Al) loaded with ATP



(Fig. 3c). The ATP content is much higher than the CD-P loading, hence the spectrum is dominated by the Al–O–ATP interaction. However, the  $^{31}\text{P}$  chemical shift expands to the higher ppm region (–5 to –10 ppm), characteristic of the CD-P coating. The similarity of the spectra in Fig. 3b and c clearly confirms that the CD-P coating on the external surface of the ATP-loaded nanoMOF did not affect the Al–O–ATP bond formed inside the MOF cavities.

In conclusion, by taking advantage of distinct heteroatoms present in an aluminium-based nanoMOF ( $^{27}\text{Al}$ ) which surface was coated by bulky phosphated CD groups ( $^{31}\text{P}$ ), we could circumvent the low resolution of  $^1\text{H}$  MAS NMR spectroscopy and provide for the first time a  $^{27}\text{Al}$  NMR signature at room temperature of aluminium species present at the surface or below the surface of MOF NPs and their interaction (*i.e.*, the formation of Al–O–P covalent bonds) with the CD-P coating. The formation of this strong covalent bonding between the CD and the MOF might be the key to ensure high stability of the core-shell NP *in vivo*. Using the same NMR methodology, we have shown the strong interaction of the triphosphate-drug ATP with the Al atoms of the MOF framework. Finally, we have shown the successful CD-P coating in a ATP-loaded nanoMIL-100(Al), which did not modify the MOF-drug interactions. This set of ssNMR experiment represents an essential characterization tool to guide towards more efficient surface modifications of these NPs, better targeting drugs (mono, di or tri-phosphate) and to help in understanding the effect of drug incorporation on the surface state of the nanoMOF. It could also be very useful in the investigation of nanoMIL-100(Al) NPs degradation in physiological medium (phosphate buffer) in which Al–O–P interactions might occur and be at the origin of the drug release processes. The methodology presented here consisting in covering the surface of porous NPs by bulky groups (unable to penetrate in the porosity of the particles) containing heteroatoms easily accessible by ssNMR (like  $^{31}\text{P}$  or  $^{19}\text{F}$ ) could also become a general strategy to probe surface species of MOF NPs without need of expensive DNP-MAS experiments.

## Conflicts of interest

There are no conflicts to declare.

## Acknowledgements

MP thanks the Région Centre-Val de Loire for a PhD fellowship. CMC is grateful for financial support from the Institut Universitaire de France (IUF). Financial support from the IR-RMN-THC Fr3050 CNRS for conducting the research is gratefully acknowledged. This work was also supported by the Paris Ile-de-France Region – DIM “Respire” and by the Labex NanoSaclay. MP and CMC thank Dr. Franck Fayon (CEMHTI Orléans) for fruitful discussions about the  $^{31}\text{P}$ - $^{31}\text{P}$  DQ-SQ NMR experiments.

## Notes and references

- 1 P. Horcajada, T. Chalati, C. Serre, B. Gillet, C. Sebrie, T. Baati, J. F. Eubank, D. Heurtaux, P. Clayette, C. Kreuz, J. S. Chang, Y. K. Hwang, V. Marsaud, P. N. Bories, L. Cynober, S. Gil, G. Ferey, P. Couvreur and R. Gref, *Nat. Mater.*, 2010, **9**, 172.
- 2 T. Baati, L. Njim, F. Neffati, A. Kerkeni, M. Bouttemi, R. Gref, M. F. Najjar, A. Zakhama, P. Couvreur, C. Serre and P. Horcajada, *Chem. Sci.*, 2013, **4**, 1597.
- 3 V. Agostoni, P. Horcajada, M. Noiray, M. Malanga, A. Aykac, L. Jicsinszky, A. Vargas-Berenguel, N. Semiramo, S. Daoud-Mahammed, V. Nicolas, C. Martineau, F. Taulelle, J. Vigneron, A. Etcheberry, C. Serre and R. Gref, *Sci. Rep.*, 2015, **5**, 7925.
- 4 A. Aykac, M. Noiray, M. Malanga, V. Agostoni, J. M. Casas-Solvas, E. Fenyvesi, R. Gref and A. Vargas-Berenguel, *Biochim. Biophys. Acta*, 2017, **1861**, 1606.
- 5 (a) T. Simon-Yarza, T. Baati, A. Paci, L. L. Lesueur, A. Seck, M. Chiper, R. Gref, C. Serre, P. Couvreur and P. Horcajada, *J. Mater. Chem. B*, 2016, **4**, 585; (b) T. Simon-Yarza, M. Gimenez-Marques, R. Mrimi, A. Mielcarek, R. Gref, P. Horcajada, C. Serre and P. Couvreur, *Angew. Chem., Int. Ed.*, 2017, **56**, 15565.
- 6 C. Martineau-Corcoc, *Curr. Opin. Colloid Interface Sci.*, 2018, **33**, 35.
- 7 S. Devautour-Vinot, C. Martineau, S. Diaby, M. Ben-Yahia, S. Miller, C. Serre, P. Horcajada, D. Cunha, F. Taulelle and G. Maurin, *J. Phys. Chem. C*, 2013, **117**, 11694.
- 8 G. Ferey, C. Serre, C. Mellot-Draznieks, F. Millange, S. Surble, J. Dutour and I. Margiolaki, *Angew. Chem., Int. Ed.*, 2004, **43**, 6296.
- 9 C. Volkringer, D. Popov, T. Loiseau, G. Ferey, M. Burghammer, C. Riekel, M. Haouas and F. Taulelle, *Chem. Mater.*, 2009, **21**, 5695.
- 10 A. J. Rossini, A. Zagdoun, M. Lelli, A. Lesage, C. Copéret and L. Emsley, *Acc. Chem. Res.*, 2013, **46**, 1942.
- 11 (a) A. J. Rossini, A. Zagdoun, M. Lelli, J. Canivet, S. Aguado, O. Ouari, P. Tordo, M. Rosay, W. E. Maas, C. Coperet, D. Farrusseng, L. Emsley and A. Lesage, *Angew. Chem., Int. Ed.*, 2012, **51**, 123; (b) F. Pourpoint, A. S. L. Thankamony, C. Volkringer, T. Loiseau, J. Trébosc, F. Aussenac, D. Carnevale, G. Bodenhausen, H. Vezin, O. Lafon and J.-P. Amoureux, *Chem. Commun.*, 2014, **50**, 933; (c) Z. Y. Guo, T. Kobayashi, L. L. Wang, T. W. Goh, C. X. Xiao, M. A. Caporini, M. Rosay, D. D. Johnson, M. Pruski and W. Y. Huang, *Chem.–Eur. J.*, 2014, **20**, 16308.
- 12 M. Haouas, C. Volkringer, T. Loiseau, G. Ferey and F. Taulelle, *J. Phys. Chem. C*, 2011, **115**, 17934.
- 13 (a) D. Massiot, F. Fayon, B. Alonso, J. Trebosc and J. P. Amoureux, *J. Magn. Reson.*, 2003, **164**, 160; (b) M. Deschamps, F. Fayon, J. Hiet, G. Ferru, M. Derieppe, N. Pellerin and D. Massiot, *Phys. Chem. Chem. Phys.*, 2008, **10**, 1298.
- 14 J. Trebosc, B. Hu, J. P. Amoureux and Z. Gan, *J. Magn. Reson.*, 2007, **186**, 220.





**Marianna PORCINO**

## **La spectroscopie de résonance magnétique nucléaire à l'état solide : un outil pour la caractérisation des systèmes poreux de délivrance de médicaments**

Les systèmes d'administration de médicaments (Drug Delivery Systems (DDSs)) sont des formulations ou des dispositifs utilisés pour améliorer les performances de médicaments peu efficaces. Les Metal-Organic Frameworks (MOFs) de taille nanométrique sont des vecteurs de médicaments potentiellement intéressants car par leur capacité à incorporer de grandes quantités de principes actifs dans leurs pores, et dont la surface peut être modifiée, leur donnant une meilleure stabilité et efficacité. L'analyse de la structure d'un DDS est une étape clé pour guider les chimistes vers la synthèse de matériaux toujours plus performants. La spectroscopie RMN à l'état solide est une technique idéale pour l'analyse de ces architectures supramoléculaires car elle fournit des informations sur la localisation du médicament, l'interaction médicament-MOF et la structure du MOF, ainsi que sur le processus de dégradation, qui conduit à la libération du médicament. Dans cette thèse, nous avons exploré les potentialités de la RMN du solide associée, quand nécessaire, au marquage isotopique pour la caractérisation poussée de DDSs à base de MOFs. Une attention particulière a été portée sur l'utilisation des hétéronoyaux ( $^{19}\text{F}$ ,  $^{27}\text{Al}$ ,  $^{31}\text{P}$ ,  $^{13}\text{C}$ ,  $^{17}\text{O}$ ) présents dans le principe actif ou dans le nanovecteur et qui, au prix d'une sévère perte de sensibilité, offre beaucoup plus d'information que le noyau  $^1\text{H}$ .

Mots clés : délivrance de médicaments, RMN à l'état solide, composés microporeux.

## **Solid state nuclear magnetic resonance spectroscopy: a tool for the characterization of porous drug delivery systems**

Drug delivery systems (DDSs) are formulations used to improve the performance of drugs with low efficacy and safety. Nanosized porous Metal-Organic Frameworks (MOFs) are considered as promising drug carriers, as large amount of drug can be incorporated in their pores and their surface can be coated with specific ligand, increasing their stability and efficacy. Analysis of the structure of a DDS is an essential step to guide the synthesis efforts towards particles with improved properties. Solid-state NMR spectroscopy is uniquely suited to study these supramolecular assemblies as it provides information at the atomic scale about drug location, drug-carrier interaction, and carrier structure and about the process of degradation, which allows the delivery of the drug. In this thesis, we have explored the potential of ssNMR spectroscopy associated to, when required, isotope labeling for the in-depth characterization of selected MOF-based DDSs. A particular focus was put on the use of heteronuclei ( $^{19}\text{F}$ ,  $^{27}\text{Al}$ ,  $^{31}\text{P}$ ,  $^{13}\text{C}$ ,  $^{17}\text{O}$ ) that are present in the drug and/or the carrier, and which, at the cost of severe sensitivity drop, provide much more information than  $^1\text{H}$  nucleus.

Keywords: drug delivery systems, solid-state NMR, microporous materials.



**Condition Extrêmes et Matériaux : Haute  
Température et Irradiation  
CEMHTI UPR 3079 CNRS  
1D, Avenue de la Recherche Scientifique 45071  
Orléans Cedex 2**

